

Magnetic Resonance Imaging of the Brain in Prenatal Alcohol Exposure and Advances in Measuring  
Cortical Microstructure

by

Graham Taylor Little

A thesis submitted in partial fulfillment of the requirements for the degree of

Doctor of Philosophy

Department of Biomedical Engineering  
University of Alberta

© Graham Taylor Little, 2020

## Abstract

Fetal alcohol spectrum disorder (FASD) encompasses a large spectrum of physical, cognitive and behavioral deficits resulting from prenatal alcohol exposure. Studies using magnetic resonance imaging (MRI) have shown structural and functional brain alterations in children and adolescents with FASD. This thesis addresses the following three absences in the neurodevelopment / FASD literature. 1) The most common differences reported in structural brain imaging studies of FASD is reductions in regional brain volumes associated with prenatal alcohol exposure. However, most studies of regional brain volume have examined individual brain regions separately, ignoring complex relationships between structures that may be able to better discriminate individuals with FASD. 2) Previous studies of brain function in FASD populations have largely employed task-based functional MRI (fMRI) with few studies using resting-state fMRI (rs-fMRI) a method that measures intrinsic functional connectivity between brain structures at rest. The few studies of resting-state functional connectivity in FASD have used samples limited in size and have reported contradictory findings of increased / decreased functional connectivity in FASD justifying the need for studies of larger cohorts of children/adolescents with FASD. 3) Most MRI studies of neurodevelopment of the human cortex rely on indirect measures of brain structure (e.g. thickness) and function (e.g. blood oxygen level dependent signal), results of which infer but do not explicitly measure microstructural changes. In-vivo studies using diffusion MRI of the adult human cortex have shown promise in differentiating regions with known microstructural differences but have relied on long-acquisitions (~1 hour) along with anatomical registration to a T1-weighted image prone to registration errors. This thesis aims to address these fundamental challenges by first using machine learning to classify children/adolescents with FASD from controls and investigate whether patterns (i.e. multivariate analysis) of regional volumetric brain reductions can better discriminate those with FASD relative to analysis of any individual brain region. Secondly, resting-state functional connectivity is investigated in a large multisite cohort of children/adolescents with FASD and compared to controls. This project also required an additional analysis of between-site reliability and correction of functional connectivity measurements using data acquired from the same 8 individuals at the same 4 sites used in the multisite FASD cohort. Thirdly, a framework for diffusion analysis of the cortex is proposed that segments the cortex in native

diffusion tensor imaging space (removing the need for additional anatomical imaging/registration) and applied to diffusion data acquired at 1.5mm isotropic resolution.

Data presented in this thesis present novel information about patterns of regional brain volume differences in FASD, demonstrating that an FASD classification model generated from multiple regional brain volumes can more accurately discriminate individuals with FASD from controls (accuracy 77%, sensitivity 64%, specificity 88%) when compared to models generated from any brain region independently. Additional evidence is provided showing differences in FASD related regional brain volume change between males and females, suggesting that FASD classification models should be created separately for males and females. Functional connectivity analysis revealed decreased internetwork connectivity between regions primarily associated with the salience network, frontal-parietal network and language network and suggests underlying deficits in the functional network brain architecture are associated with prenatal alcohol exposure. Both the classification and functional connectivity findings provide evidence of altered brain structure and function in individuals with FASD and this knowledge has the potential to inform diagnostic and medical interventions for this population in the future. Furthermore, this thesis proposes a framework for in-vivo analysis of diffusion tensor imaging (DTI) of the cortex. Results here show accurate segmentation of the cortex on native DTI. Additionally, surface-based diffusion measurements extracted from the cortex revealed values in line with other higher-resolution (1.0 mm - 1.25 mm isotropic) acquisitions. Given the short scan time (~3.5 minutes) the proposed technique could be a useful approach for the study of clinical or neurodevelopmental populations. Overall, this thesis provides novel contributions to the understanding of the effects of prenatal alcohol exposure on the developing brain and provides methodological advances for future studies of the development of cortical microstructure.

## Preface

This thesis is an original work by Graham Taylor Little. The four research chapters of the thesis contain novel contributions to the international MRI research community. Chapter 4 of this thesis has been published as Little G, Beaulieu C. “Multivariate models of brain volume for identification of children and adolescents with fetal alcohol spectrum disorder”. *Hum Brain Mapp.* 2019;1–14. Data for chapter was acquired under a large collaborative multisite study (NeuroDevNet, N=160) and by former/current lab members as part of their thesis work (Dr. Sarah Treit, and Dr. Catherine Lebel, N=141). I was responsible for all other aspects of the work, including concept formation, analysis, and wrote the manuscript with guidance from C. Beaulieu. Chapter 5 is an original contribution to this thesis and has not been published elsewhere, however a version of this work has been presented at the international Organization for Human Brain Mapping Conference (Hawaii, USA, 2015). Data for this chapter was collected under the multisite NeuroDevNet project, and I was responsible for all other aspects of the work including analysis, figure creation, and wrote the chapter with guidance from C. Beaulieu. Chapter 6 of this thesis has been published as Little G, Reynolds J, Beaulieu C. “Altered Functional Connectivity Observed at Rest in Children and Adolescents Prenatally Exposed to Alcohol”. *Brain Connectivity.* 2018;8(8):503-15. Data for this chapter was collected under the multisite NeuroDevNet project, and I was responsible for all other aspects of the work, including concept formation, analysis, and wrote the manuscript with guidance from C. Beaulieu and J. Reynolds. Chapter 7 is an original contribution to this thesis and has not been published elsewhere. Data for this chapter was collected by myself in collaboration with other members from the lab (Dr. Sarah Treit, Dr. Pascal Tetreault, and Emily Stolz). I was responsible for all other aspects of the work, including method development, image analysis, and wrote the manuscript with guidance from C. Beaulieu.

All research projects for which this thesis was a part received ethics approval from the University of Alberta Research Ethics Board. Chapters 4, 5 and 6 used data collected under a large multisite collaborative research project (NeuroDevNet) and received research ethics approval from all research institutions involved, namely human research ethics boards at University of Alberta, Children’s Hospital of Eastern Ontario, University of Manitoba, and the University of British Columbia.

## Acknowledgements

This work was funded by Canadian Institutes of Health Research (CIHR) and the Networks of Centres of Excellence (NCE) via NeuroDevNet. Specifically, I would like to thank NeuroDevNet, Brain Canada and the Women and Children's Health Research Institute (WCHRI) for providing support for my salary.

I would like to thank all the students and faculty in the Department of Biomedical Engineering at the University of Alberta. Everyone was always generous with their time and open to helping in anyway they could. Thanks to Maisie Goh and Carol Hartle for keeping me up to date and on track with all the administrative duties over the years. Thanks to Peter Seres for all the help trouble shooting new acquisition protocols. Thanks to all those current and former members of the Beaulieu lab who provided help with my research, especially Dr. Pascal Tetreault and Dr. Sarah Treit whose discussions on Neuroscience and Fetal Alcohol Spectrum Disorder (FASD) helped inform my research projects and focus on scientifically/clinically important questions. Many thanks to my supervisory committee for providing feedback. CHRISTIAN! Thanks for the independence to execute my own research ideas, the thorough feedback which I have come to enjoy and the personal support to accomplish my goals.

Finally, thanks to my friends and family for all the support over the years. Especially to my Mom and Dad who instilled in me both the value of education and the belief I could pursue anything. Most importantly, I would like to thank my wife Jen, who I am so lucky to share my life with. Your strength and support over the last years has been invaluable and I could not have accomplished this without you. Thanks for keeping me sane and keeping real life together while I pursued a dream. Finally, thanks to Jude for clearing my head when I came home from a busy workday, the way you look at the world with wonder inspires me every day. To Jude and any future "Littles", stay curious, the world only gets more beautiful the more you try to understand it.

## Table of Contents

<b>List of Tables</b> .....	x
<b>List of Figures</b> .....	xi
<b>Introduction</b> .....	1
1 Brain Development and Structure .....	5
1.1 Organization of the Human Brain from Microstructure to Macrostructure.....	5
1.1.1 Cerebral Cortex .....	6
1.1.2 Subcortical and Limbic Grey Matter Structures .....	7
1.1.3 White Matter Organization Leading to Large-Scale Functional Networks .....	8
1.1.4 In Utero Brain Development .....	10
1.1.5 Altered Brain Development in Fetal Alcohol Spectrum Disorder .....	12
2 Magnetic Resonance Imaging and Analysis Methods.....	16
2.1 Nuclear Magnetic Resonance Signal and Relaxation .....	16
2.2 Generating a Magnetic Resonance Image .....	18
2.3 Structural Brain Imaging Acquisition and Analysis.....	21
2.3.1 MPAGE - Structural Brain Imaging Acquisition.....	22
2.3.2 Automated Volumetric Brain Image Analysis.....	23
2.4 Echo Planar Imaging for Functional and Diffusion MRI .....	26
2.5 Functional Magnetic Resonance Imaging .....	27
2.5.1 Resting-State Functional Magnetic Resonance Imaging Analysis .....	28
2.6 Diffusion Magnetic Resonance Imaging.....	31
2.6.1 Diffusion Tensor Parameters.....	34
2.7 Statistical Analysis.....	36
2.7.1 Measurement of Repeatability and Reproducibility .....	36
2.7.2 Machine Learning Approaches for Multivariate Analysis.....	37
3 MRI in Fetal Alcohol Spectrum Disorder.....	40
3.1 Volumetric / Classification Studies in FASD .....	40
3.2 Functional MRI Studies in FASD .....	42
3.3 Studies of Cortical Microstructure in the Human Brain.....	45
<b>Research</b> .....	48
4 Multivariate Models of Brain Volume for the Identification of Individuals Prenatally Exposed to Alcohol .....	48
4.1 Introduction .....	49

4.2 Materials and Methods.....	51
4.2.1 FASD / Typically Developing Subjects Training and Testing Datasets .....	51
4.2.2 Cognitive Testing .....	53
4.2.3 Image Acquisition .....	55
4.2.4 Automated Brain Segmentation.....	56
4.2.5 Predictive Model Training .....	57
4.2.6 Model Evaluation / Interpretation .....	57
4.2.7 Sensitivity of Model to Participant Demographics .....	58
4.2.8 Sex Specific Modelling .....	58
4.3 Results .....	59
4.3.1 FASD Classification Model / Performance.....	59
4.3.2 Diagnostic, Demographic, and Cognitive Associations to FASD Classification Model.....	63
4.3.3 Sex Specific Models .....	64
4.4 Discussion.....	68
4.4.1 FASD Classification .....	68
4.4.2 Relating Multivariate and Univariate Analysis of FASD Regional Brain Volumes .....	69
4.4.3 FASD Classification with Sex Specific Models.....	72
4.4.4 Study Limitations and Future Directions .....	74
4.4.5 Conclusions.....	75
Appendix A.....	76
5 Inter-site Reproducibility of Functional Connectivity Relative to Intra-site Repeatability .....	78
5.1 Introduction .....	79
5.2 Materials and Methods.....	80
5.2.1 Participants / Image Acquisition.....	80
5.2.2 Pre-Processing .....	81
5.2.3 Functional Connectivity ROI Based Analysis.....	82
5.2.4 Repeatability and Reproducibility Analysis of Functional Connectivity .....	82
5.2.5 Evaluation of Proposed Site Correction Technique.....	83
5.3 Results .....	84
5.3.1 Temporal Signal to Noise Ratio and Qualitative Reproducibility Analysis.....	84
5.3.2 Within-site Repeatability Analysis.....	88
5.3.3 Between-site Reproducibility Analysis and Multisite Correction .....	91
5.4 Discussion.....	94
5.4.1 Reproducibility of Functional Connectivity Measures Between Sites .....	94

5.4.2 Multisite Correction .....	95
5.4.3 Limitations .....	95
5.5 Conclusions .....	96
6 Altered Functional Connectivity Observed at Rest in Children and Adolescents Prenatally Exposed to Alcohol .....	98
6.1 Introduction .....	99
6.2 Materials and Methods.....	101
6.2.1 FASD / Typically Developing Participants .....	101
6.2.2 Cognitive Testing .....	104
6.2.3 Image Acquisition .....	104
6.2.4 Intersite Correction Participants .....	105
6.2.5 Pre-Processing .....	105
6.2.6 Functional Connectivity ROI Based Analysis.....	106
6.2.7 Multisite Correction .....	108
6.2.8 Spatial Overlap of Connected Regions .....	108
6.2.9 Group Comparison / Network Matrices Analysis .....	109
6.3 Results.....	109
6.3.1 Cognitive and Behavioral Differences in FASD .....	109
6.3.2 Spatial Characteristics of Connectivity in FASD.....	111
6.3.3 Functional Connectivity Differences in FASD: .....	113
6.3.4 Potential Confounding Variables and Cognitive Associations.....	115
6.4 Discussion.....	118
6.4.1 Spatial Patterns of Resting State Networks in FASD.....	118
6.4.2 Functional Connectivity Differences in FASD .....	118
6.4.3 Regional Functional Alterations in FASD .....	120
6.4.4 Functional Connectivity may be Associated with Structural/Metabolic Alterations in FASD .....	121
6.4.5 Correlations to Cognitive Scores .....	122
6.4.6 Limitations.....	123
6.4.7 Conclusions.....	125
Appendix B .....	126
7 Anisotropy of the Human Cerebral Cortex Segmented on Diffusion MRI.....	130
7.1 Introduction .....	131
7.2 Materials and Methods.....	133
7.2.1 Participants, Data Acquisition and Pre-processing.....	133

7.2.2 Voxel-Based White Matter Segmentation.....	135
7.2.3 Surface-Based Inner and Outer Cortical Boundary Segmentation.....	139
7.2.4 Surface-based Diffusion Measurements.....	142
7.2.5 Spherical Registration and Regional Analysis.....	142
7.2.6 Test-retest Analysis.....	143
7.3 Results.....	145
7.3.1 Cortical Segmentations on Native DTI.....	145
7.3.2 Diffusion Measurements in Native Imaging Space.....	147
7.3.3 Test-retest repeatability.....	151
7.4 Discussion.....	154
7.4.1 Cortical Segmentation on Native DTI.....	154
7.4.2 Regional Variation in Surface-Based Diffusion Measurements.....	156
7.4.3 Diffusion MRI Acquisition Considerations for Measuring Cortical Anisotropy.....	157
7.4.4 Conclusions.....	159
8 Summary & Conclusions.....	160

## List of Tables

<b>Table 3.1.</b> Summary of FASD machine learning classification literature using biologically based measurements .....	42
<b>Table 3.2.</b> Summary of resting-state functional connectivity studies in FASD .....	45
<b>Table 3.3.</b> Summary of high-resolution (~1mm isotropic) in-vivo diffusion MRI studies of the cortex .....	47
<b>Table 4.1.</b> Participant characteristics and demographics for training “NeuroDevNet” data .....	54
<b>Table 4.2.</b> Participant characteristics and demographics for testing “CIHR” data .....	55
<b>Table 5.1.</b> Within-site repeatability for ROI functional connectivity at four sites .....	90
<b>Table 5.2.</b> Between-site reproducibility for ROI functional connectivity across four sites .....	93
<b>Table 6.1.</b> Participant characteristics and demographics for FASD and control groups .....	103
<b>Table 6.2.</b> Regions of interest used for functional connectivity analysis .....	107
<b>Table 6.3.</b> Behavioral and cognitive scores for control and FASD groups .....	110
<b>Table 6.4.</b> Associations of potential confounds in the FASD group to functional connectivity .....	115

## List of Figures

<b>Figure 1.1.</b> General tissue composition of the brain .....	6
<b>Figure 1.2.</b> Microstructural and large scale organization of the cortex .....	7
<b>Figure 1.3.</b> Subcortical grey matter structures.....	8
<b>Figure 1.4.</b> Functional and structural connectivity of the Default Mode Network .....	10
<b>Figure 1.5.</b> Stages of embryonic development.....	11
<b>Figure 1.6.</b> Facial features characteristic of Fetal Alcohol Syndrome (FAS) .....	15
<b>Figure 2.1.</b> T1 and T2 relaxation curves.....	17
<b>Figure 2.2.</b> Typical gradient echo MRI sequence to k-space .....	20
<b>Figure 2.3.</b> T1-weighted and T2-weighted images of the brain .....	21
<b>Figure 2.4.</b> FreeSurfer segmentation pipeline.....	26
<b>Figure 2.5.</b> Functional connectivity analysis techniques .....	30
<b>Figure 2.6.</b> Stejskal and Tanner pulsed gradient spin echo sequence.....	32
<b>Figure 2.7.</b> Diffusion tensor model.....	33
<b>Figure 2.8.</b> FA, MD and primary eigenvector maps.....	36
<b>Figure 2.9.</b> Support Vector Machine .....	39
<b>Figure 4.1.</b> Regional brain volume FASD classification model visualizations .....	60
<b>Figure 4.2.</b> Multivariate FASD classification vs univariate brain volume classification .....	62
<b>Figure 4.3.</b> FASD classification sensitivity/specificity vs caudate volume. ....	63
<b>Figure 4.4.</b> FASD classification separated by sex.....	65
<b>Figure 4.5.</b> Visualization of FASD classification models for males and females .....	67
<b>Figure 5.1.</b> Temporal signal to noise ratio maps for the same subject at four sites .....	86
<b>Figure 5.2.</b> Functional connectivity matrices for the same subject at four sites.....	87
<b>Figure 5.3.</b> Within-site repeatability of functional connectivity matrices.....	89
<b>Figure 5.4.</b> Between-site reproducibility of functional connectivity matrices .....	92
<b>Figure 6.1.</b> Seed-based functional connectivity maps for FASD and controls.....	112
<b>Figure 6.2.</b> Decreased functional connectivity observed in FASD .....	114
<b>Figure 6.3.</b> Relationship between functional connectivity and stimulants in FASD .....	117
<b>Figure 6.4.</b> Functional connectivity cognitive correlations in FASD .....	124
<b>Figure 7.1.</b> Mean DWI, FA, MD and primary eigenvector maps.....	136
<b>Figure 7.2.</b> Cortical segmentation analysis workflow in native DTI space.....	138
<b>Figure 7.3.</b> Tensor-based force visualization.....	141
<b>Figure 7.4.</b> Cortex segmentations .....	146
<b>Figure 7.5.</b> Surface maps of FA, MD, and radiality .....	149
<b>Figure 7.6.</b> FA, MD and radiality values for cortical regions.....	150
<b>Figure 7.7.</b> Test-retest of surface-based FA, MD and radiality maps .....	152
<b>Figure 7.8.</b> Test-retest of regional FA, MD, and radiality values .....	153

## List of Symbols and Abbreviations

ACC : Anterior Cingulate Cortex.....	8
ADC : apparent diffusion coefficient .....	33
ADHD : attention deficit hyperactivity disorder .....	47
ARND : alcohol related neurodevelopmental disorder .....	12
b : b-value .....	33
B <sub>0</sub> : main static magnetic field .....	15
B <sub>1</sub> : RF magnetic field.....	15
BOLD : blood oxygen level dependent .....	29
BRIEF : behavior rating inventory of executive function .....	98
DMN : Default Mode Network.....	8
DWI : diffusion weighted imaging .....	28
EPI : echo planar imaging.....	28
FA : fractional anisotropy .....	36
FAE : fetal alcohol effect.....	50
FAS : Fetal Alcohol Syndrome .....	12
FASD : Fetal Alcohol Spectrum Disorder.....	1
FDR : false discovery rate .....	103
FLAIR : fluid-attenuated inversion recovery .....	54
fMRI : functional magnetic resonance imaging .....	8
FN : false negative .....	61
G : gradient amplitude.....	33
GRE : gradient recalled echo.....	22
H <sub>2</sub> O : water molecule.....	15
ICC : intra class correlation .....	77
MD : mean diffusivity .....	36
MPRAGE : magnetization prepared rapid acquisition with gradient echo.....	22
MRF : markov random field .....	23
MRI : Magnetic Resonance Imaging .....	1
M <sub>xy</sub> : transverse magnetization .....	16
M <sub>z</sub> : longitudinal magnetization .....	16
NBD:AE : neurobehavioral disorder alcohol exposed.....	50
NEPSY-II : developmental neuropsychological assessment.....	98
NMR : nuclear magnetic resonance.....	15
PAE : prenatal alcohol exposure .....	49
pFAS : partial fetal alcohol syndrome.....	12
PPC : posterior parietal cortex.....	107
pSTG : posterior superior temporal gyrus .....	107
RF : radio frequency.....	15
ROI : region of interest .....	30
rs-fMRI : resting-state function magnetic resonance imaging .....	29
S <sub>0</sub> : baseline signal without diffusion weighting .....	34
SE:AE : static encephalopathy alcohol exposed.....	50
SNR : signal to noise ratio .....	21
SVC : support vector classifier .....	26

SVM : Support Vector Machine .....	1
T1 : longitudinal relaxation time.....	16
T2 : transverse relaxation time.....	16
TE : echo time .....	19
TI : inversion time .....	22
TP : true positive.....	61
TR : repetition time.....	19
WI-III ACH : Woodcock Johnson III tests of achivement.....	98
WMTB-C : working memory test battery for children .....	98
WRMT-R : Woodcock reading mastery tests.....	51
$\gamma$ : gyromagnetic ratio.....	15
$\delta$ : gradient duration.....	33
$\Delta$ : time allowed for diffusion .....	33
$\epsilon_1$ : primary eigenvector .....	34
$\lambda_1$ : primary eigenvalue.....	34
$\omega_0$ : Larmor frequency.....	15

## Introduction

Brain development is a complex process involving changes to brain structure and function throughout life. Many studies using in-vivo magnetic resonance imaging (MRI) have sought to characterize typical changes in brain structure and function throughout life, providing a baseline in which to compare atypical patterns of human brain development. Typical patterns of brain development are sensitive to a variety of environmental factors resulting in downstream consequences to structural and functional developmental trajectories. Fetal alcohol spectrum disorder (FASD) is an umbrella term that encompasses the cognitive and behavioral deficits associated with prenatal exposure to alcohol. Animal studies of FASD have shown the neurotoxic effects of in-utero exposure to alcohol on the developing fetus. Furthermore, in-vivo MRI studies of children / adolescents with FASD have demonstrated that differences in brain structure and function associated with prenatal alcohol exposure persist throughout development and consistently report decreased total brain volume with disproportionate volumetric reductions in subcortical grey matter structures. However, at the commencement of this thesis project no studies had examined patterns (i.e. multivariate analysis) of volumetric reductions observed in FASD using machine learning combined with structural MRI, only a few studies that were limited in sample size examined differences in functional connectivity between brain regions in FASD using resting-state functional MRI (rs-fMRI) and no studies had examined cortical microstructure using diffusion MRI using an acquisition/analysis method appropriate (short acquisition with high-resolution) for the study of neurodevelopment and FASD. Overall, this thesis aims to use MRI acquisition / analysis methods not typically applied in the FASD literature to better understand the associated structural and functional differences observed in children / adolescents prenatally exposed to alcohol.

Multiple MRI studies have assessed volumetric differences in total and regional brain volume in FASD with the most consistently reported finding being reduced total brain volume associated with prenatal exposure to alcohol (Donald et al., 2015; Lebel et al., 2011). Furthermore, studies of regional brain volumes have observed disproportionate reductions in children and adolescents with FASD in some subcortical brain volumes (e.g. putamen, caudate and hippocampus) in children (Nardelli et al., 2011; Roussotte et al., 2012) as well as regions of the cortex (e.g. regions of the parietal, temporal and frontal lobes) (Astley et al., 2009a; Chen et al., 2012). However, all previous volumetric studies of FASD have relied on univariate analysis ignoring potential relationships

between brain structures that may aid in discriminating controls from FASD. The first aim of this thesis was to use a machine learning classification model (i.e. multivariate analysis) generated from regional brain volumes to identify child / adolescents prenatally exposed to alcohol. Based on the added discriminative information provided by including multiple variables here it was hypothesized that classification using the machine learning approach would more accurately discriminate individuals with FASD relative to univariate analysis which has been the traditional approach in cross-sectional FASD studies of regional brain volume difference. The results in Chapter 4 show that the classification model generated from a support vector machine (SVM) is more accurate compared to classification models generated for each of 87 brain regions separately. In addition, this work examines differences in model weights (a measure of predictive importance) between brain regions showing that the multivariate model primarily favors regions with previously reported volumetric reductions in individuals with FASD. Furthermore, results from this chapter suggest that a marked classification imbalance in sensitivity and specificity between males and females can be improved by generating models separately for males and females suggesting that sex should be accounted for in brain volume classification studies of FASD, and further supports the notion that prenatal alcohol exposure affects regional brain volumes differently in males compared to females.

Task-based functional MRI studies of observed alterations in brain function associated with prenatal alcohol exposure. Few studies have examined alterations in functional connectivity at rest in individuals with FASD and only three were published at the start of this thesis work (Santhanam et al., 2011; Wozniak et al., 2016, 2013). Given the limited sample size of these studies only individual connections (a priori selected connections, not whole brain), individual networks or global connectivity measures (not regionally specific) were investigated. The second aim of this thesis was to investigate alterations in functional connectivity associated with prenatal exposure to alcohol in a large multisite cohort of individuals using a whole-brain analysis of individual functional connections. Given previous observations of structural and functional alterations associated with FASD it was hypothesized that a whole-brain functional analysis of a large cohort of children / adolescents with FASD, would similarly detect altered functional connectivity in children and adolescents with FASD. In Chapter 6 results are presented from a functional connectivity analysis of a large multisite cohort (N=133) of children / adolescents with FASD and controls. As part of this multisite study rs-fMRI data was acquired for the same individuals scanned twice at each

site, and in Chapter 5 a reproducibility analysis is presented along with a proposed strategy for the correction of between site variability in functional connectivity measurements. The FASD cross-sectional analysis in Chapter 6 (using the proposed site corrections from Chapter 5) revealed decreased internetwork connectivity between regions primarily associated with the salience network, frontal-parietal network, and language network and suggests underlying deficits in the functional network brain architecture are associated with prenatal alcohol exposure.

At the time this thesis commenced, in-vivo studies using diffusion MRI of the cortex primarily relied on long diffusion MRI acquisitions (~ 1 hour in length, plus acquisition of T1-weighted anatomical image for delineation of the cortex) to achieve diffusion data appropriate for analyzing the microstructural organization of the human cortex. The third and final aim of this thesis was to design a method that enabled surface-based analysis of diffusion MRI across the cortex in native diffusion tensor imaging space, for the eventual application to in-vivo studies of neurodevelopment. It was hypothesized that by using software designed to analyze the cortex in native diffusion tensor imaging (DTI) space on 1.5mm isotropic images, measurement of diffusion in the cortex would show primarily radially oriented diffusion relative to the cortex along with regional variability in other diffusion parameters such as fractional anisotropy and mean diffusivity. Notably, both findings would be in line with previous higher resolution (1.0 – 1.25 mm isotropic) studies of diffusion MRI of the cortex. The analysis pipeline presented in Chapter 7 uses diffusion data acquired in 3.5 minutes and presents an algorithm to automatically segment the cortical surface on diffusion data in native imaging space, removing the need for additional anatomical imaging and problematic registration between modalities. Results from this analysis show that similar diffusion tensor values and regional variability across the cortex compared to previous studies using longer and higher resolution acquisitions. Importantly, the presented acquisition / analysis framework has the potential for use in future studies of the development of cortical microstructure in neurodevelopmental populations given that only a single diffusion acquisition is needed and avoids problematic registration between modalities.

Overall, this thesis presents novel information about the effects of prenatal alcohol exposure on the structure and function of the childhood / adolescent brain, along with methodological advances for application in

future studies focused on the development of cortical microstructure. Following these research chapters, a brief discussion is presented of the potential impact and future directions of these three diverse research projects.

## **1 Brain Development and Structure**

### **1.1 Organization of the Human Brain from Microstructure to Macrostructure**

Much of the brain is composed of two types of cells namely, neurons and glial cells. Neurons are the primary contributor to brain function and pass information through a network of interconnected neurons via electrical and chemical signaling. On the other hand, glial cells primarily play a supporting role in brain function through several tasks including but not limited to, insulating neighboring neurons from each other, and providing structural and metabolic support to neurons. Although individual neurons vary in shape and size across the brain they all consist of three fundamental parts; a cell body which has a nucleus to carry out synthesis for almost all neuronal proteins and membranes; dendrites which receive and integrate input from other neurons and a myelinated axon that is the output of the neuron. There are approximately 100 billion neurons distributed across the brain and arranged in a pattern that allows for long range communication between brain regions. For example, myelinated axons are arranged in bundles within areas deemed “white matter” for its colored appearance and connects “grey matter” regions primarily consisting of cell bodies, glia and dendrites. The regional discrepancy in microstructural composition as well as the involvement of brain regions in cognitive and behavioral functions is the criteria used for segregating the brain into distinct regions. In general, the brain is organized into 3 primary structures, the cerebrum and cerebellum which each have left and right hemispheres and the brain stem (Figure 1.1). Components of the cerebrum (the region of focus for this thesis) are summarized in the following sections.

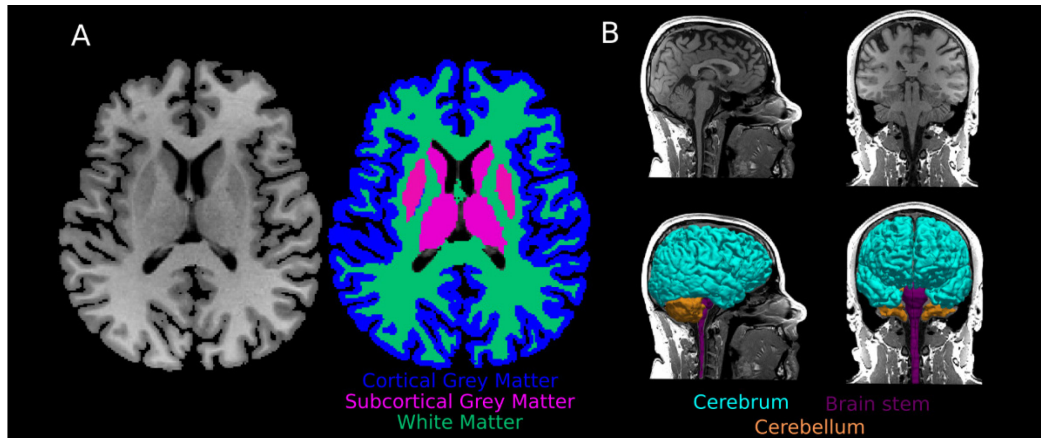


**Figure 1.1.** A) Brain tissue segmentation of a structural brain image classified into cortical grey matter (blue), subcortical grey matter (pink) and white matter (green). B) On a large scale the brain is organized into three fundamental structures, the cerebrum (cyan), cerebellum (orange) and brain stem (purple).

### 1.1.1 Cerebral Cortex

The cerebral cortex is a region of grey matter surrounding each cerebral hemisphere. Neurons within the cortex have an architectural organization comprised of 6 layers oriented parallel (tangential) to the cortical surface and cortical columns oriented perpendicular (radial) to the cortical surface. Connections between neurons within the cortex mainly run tangentially between neurons within the same cortical layers and radially to neurons within the same cortical columns through adjacent cortical layers. The cortex also has a folded geometry consisting of gyri (the ridge of the folds) and sulci (the depression of the folds). Among individuals the folding of the brain is largely variable however consistent sulci can be identified between individuals that separate the 4 primary functional regions of the cortex, namely the frontal, parietal, occipital and temporal lobes of each hemisphere (Figure 1.2). The frontal lobe extends from the most anterior portion of the cerebrum to the central sulcus and is associated with high-level cognitive functions such as emotional processing and problem solving. Notably, the frontal lobe also contains the motor cortex located on the anterior bank of the central sulcus and is the primary region associated with motor control. The parietal lobe is located on the posterior side of the central sulcus and is primarily associated with sensory processes. The occipital lobe is located in the posterior portion of the brain and is associated with visual processes, whereas the temporal lobe is located on the lateral portions of each hemisphere and is involved in auditory and memory processes.

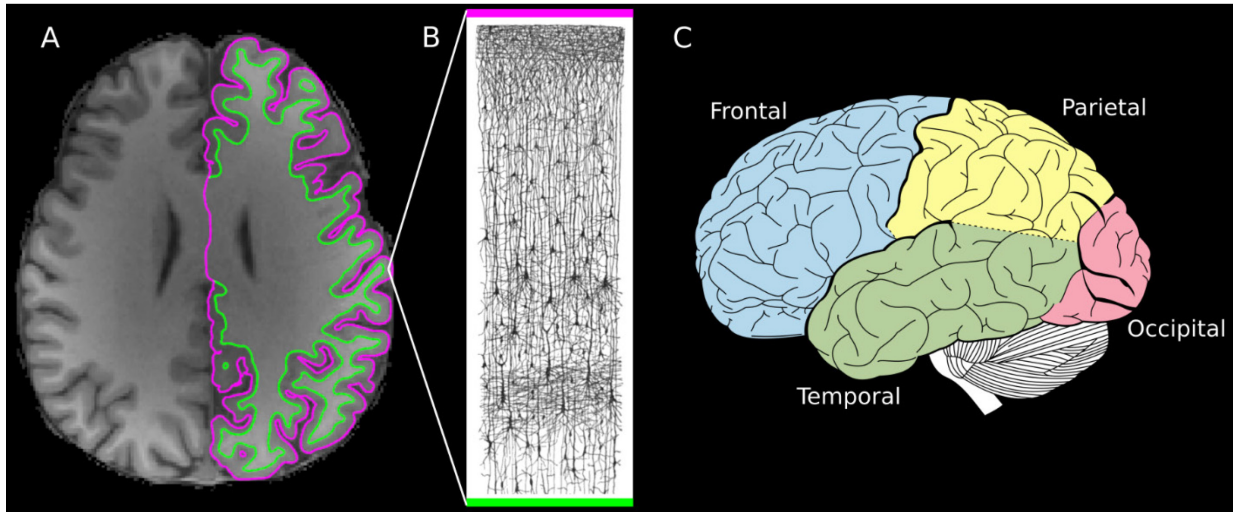


**Figure 1.2.** A) Segmentation of the inner (green) and outer (pink) cortical boundaries shown on an axial slice of a post processed structural brain MRI. B) Histological section of the cortex Golgi stained to highlight the cell soma and dendrites. The cortex has a primarily radial (columnar up-down) and tangential (left-right) microstructural organization. C) At a large scale the cortex is organized into lobes; frontal, temporal, parietal, and occipital. Images B and C modified from Wikimedia Commons (public domain).

### 1.1.2 Subcortical and Limbic Grey Matter Structures

A series of grey matter structures are located underneath the cortex within each of the cerebral hemispheres and referred to as deep grey matter structures given their location within the brain. One of these regions is the thalamus which is situated above the brain stem and has the primary role of transferring sensory input to the cortex. The basal ganglia is a family of smaller grey matter structures namely, the striatum (consisting of caudate nucleus, putamen and nucleus accumbens), globus pallidus, subthalamic nucleus and substantia nigra. Degradation of the basal ganglia nuclei is often linked to distinct movement disorders (e.g. Huntington's disease, Parkinson's disease), and regions of the basal ganglia have been associated with motor (e.g. putamen) and higher-level cognitive functions (e.g. caudate). Two grey matter structures located within the medial temporal lobe are the amygdala and the hippocampus and are differentiated from the cortex based a difference in internal microstructure. Both regions are integrated components of the limbic system and are associated with crucial functions of human behavior, for example the amygdala is largely implicated in emotional processing whereas the hippocampus is associated with the consolidation and recall of memories.

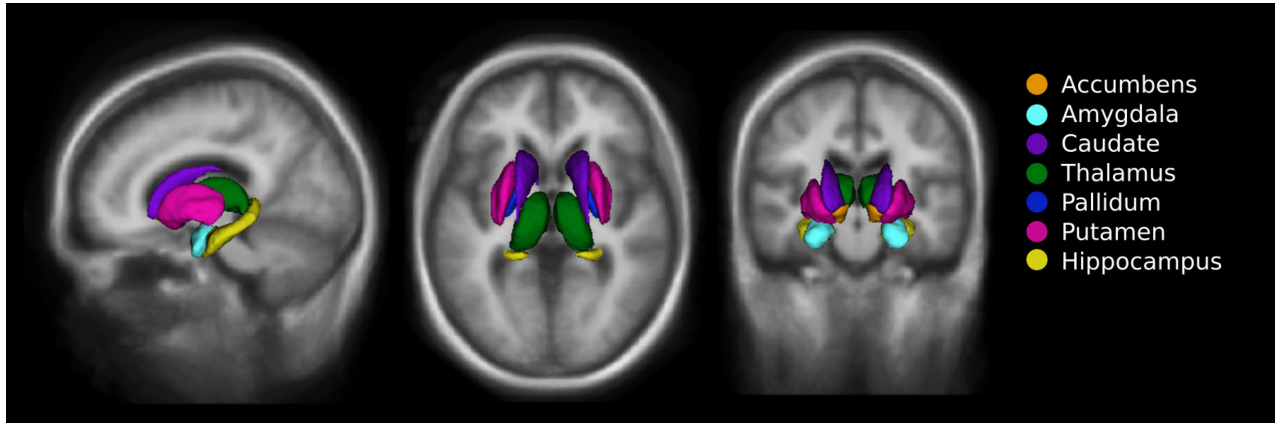


**Figure 1.3.** 3D rendering of the multiple subcortical grey matter structures shown on an average structural brain MRI template.

### 1.1.3 White Matter Organization Leading to Large-Scale Functional Networks

The white matter of the cerebrum is primarily composed of myelinated axons that are the basis for long range connections between regions of the cortex. Bundles of axons form tracts that either connect regions in opposite cerebral hemispheres (commissural fibers), connect regions within the same hemisphere (association fibers), or contain bundles of projection fibers that connect the central nervous system (cerebrum and cerebellum) to the body's peripheral nervous system via the spinal cord. Large white matter tracts can be segmented with diffusion MRI and are often studied individually. The largest white matter structure in the brain is the corpus callosum and is the primary commissural tract between the left and right hemispheres. Association tracts connect grey matter regions within each hemisphere with the most commonly reported tracts in MRI studies being the arcuate fasciculus, uncinate fasciculus, superior fronto-occipital fasciculi, inferior fronto-occipital fasciculi, cingulum, superior longitudinal fasciculi, and inferior longitudinal fasciculi. Furthermore, the anterior limb of the internal capsule and the corticospinal tract are the predominantly reported projection tracts in in-vivo studies of the human brain. Although tracts in the cerebral white matter can be segmented and investigated individually, together they form the underlying framework of large-scale functional networks within the brain.

Investigations of the in-vivo brain function using any of electroencephalography, magnetoencephalography, or functional MRI (fMRI) (pertinent to this thesis, see Section 2.4 for details) have

revealed a distinct topology of functional brain networks. Conventionally, regions of functional brain networks are referred to as nodes and connections between regions are referred to as edges in line with language used in the mathematical field of graph theory. Neurons within the nodes of functionally connected brain networks activate together and the strength (i.e. correlation) of activation patterns within and between functional brain networks is task dependent. The most commonly reported functional network is the default mode network (DMN) and is primarily composed of five cortical regions the posterior cingulate cortex, precuneus, medial prefrontal cortex, and left/right lateral parietal lobe which are connected via underlying white matter tracts (left / right superior frontal-occipital fasciculus, cingulum, and genu of corpus callosum) (Heuvel et al., 2009) (visualization in Figure 1.4). The DMN was originally referred to as the task negative network because it was activated in the absence of a behavioral task with strong synchrony of activation between regions. Since then, multiple “resting-state” functional networks have been consistently reported in studies by acquiring fMRI while a subject is at rest. While there are many methods that attempt to categorize brain regions into networks based on their structural and functional connectivity, in general there are seven (including the DMN) commonly reported groupings of these regions (Yeo et al., 2011). The frontoparietal network consists of the left / right lateral prefrontal cortex and the left / right posterior parietal cortex and primarily / connected via the superior longitudinal fasciculus. The sensorimotor network is connected by the body of the corpus callosum and consists of precentral / postcentral gyrus and the supplementary motor area. The salience network consists of the anterior cingulate cortex (ACC), left / right anterior insula, left / right rostral prefrontal cortex, and the left /right supramarginal gyrus. The language network consists of the left and right posterior superior temporal gyri that are involved in language processing, as well as the bilateral inferior frontal gyrus and these regions are primarily connected in each hemisphere through the arcuate fasciculus association tract. The network implicated in visual processing is connected via the splenium of the corpus callosum and contains regions of the primary, ventral and dorsal visual systems. Finally, the dorsal attention network is composed of the left / right frontal eye fields and the left / right intraparietal sulcus and is structurally connected through a branch of the superior longitudinal fasciculus and connected to each hemisphere through the corpus callosum.

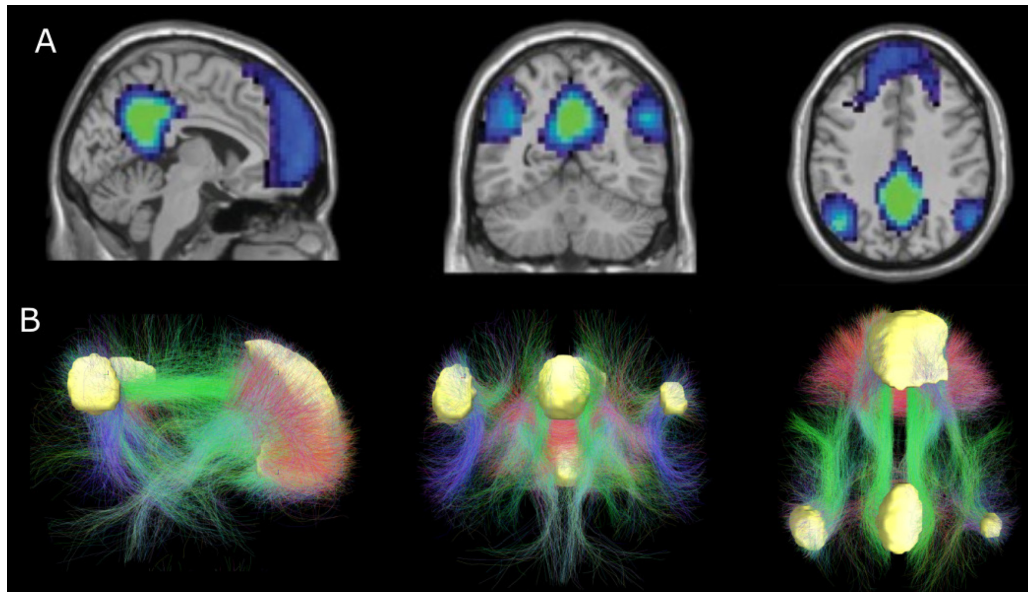


**Figure 1.4.** Functional and structural connectivity of the Default Mode Network (DMN) A) Regions of the DMN that have strongly synchronized functional activity at rest. B) Primary white matter tracts connecting the distant regions of the DMN. All images adapted from Wikimedia Commons (public domain).

### 1.1.4 In Utero Brain Development

The complex organization of the human central nervous system arises from a much simpler structure during embryonic development (for general overview see (Vanderah and Gould, 2015) where information for this section was obtained). The start of this process begins around the third week of the gestational period when a band of ectoderm thickens to form the neural plate. The plate begins to fold and close in on itself and forms the neural tube by the end of the fourth week of development. At this point the neural tube already has begun to separate into three primary vesicles; the prosencephalon (forebrain); the mesencephalon (midbrain), and the rhombencephalon (hindbrain) (Figure 1.5a). During week five the primary vesicles subdivide into five secondary vesicles namely the telencephalon (“end brain”); diencephalon (“in-between brain”); mesencephalon a primary vesicle that does not split during this stage of development; the metencephalon; and the myelencephalon (Figure 1.5b). Importantly for the focus of this thesis, the telencephalon eventually becomes the cerebral hemispheres, and the diencephalon becomes the thalamus, as well as other structures in the brain. In short, the other secondary vesicles eventually become inferiorly located structures of the central nervous system. The metencephalon becomes the cerebellum as well as the pons which is a critical structure in the brain stem, whereas the

myelencephalon and the mesencephalon become the medulla and the midbrain of the brain stem respectively. At six weeks the left and right portions of the telencephalon expand forming the basis of the two separate cerebral hemispheres.

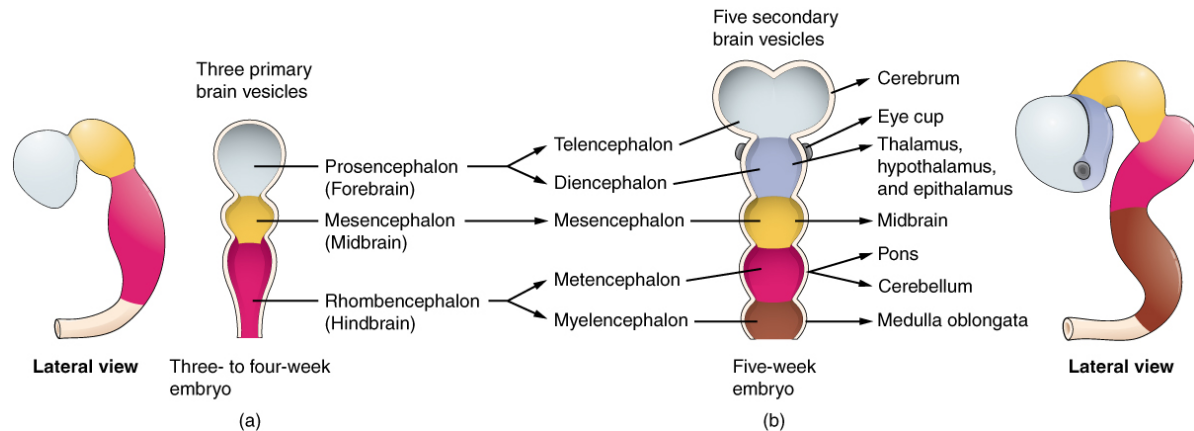


**Figure 1.5.** Initial stages of embryonic development including the development of (a) the Forebrain, Midbrain and Hindbrain, followed by (b) the further subdivision of these structures into the Telencephalon, Diencephalon, Mesencephalon, Metencephalon and Myelencephalon. Image from Wikimedia Commons (public domain).

After these initial stages of embryonic development, rapid growth of the telencephalon is observed, and the diencephalon begins to form the thalamus and hypothalamus. Around the same time the base of the telencephalon thickens becoming the basal ganglia. The telencephalon continues to grow and eventually folds down over the diencephalon and these two secondary vesicles join to form the cerebrum. At this point the surface of cerebral hemispheres are smooth structures containing the ventricle zone but attain a progressively folded shape throughout development. The development of this folded geometry occurs after the widespread proliferation and migration of neurons and glial cells from the ventricular zone into layers of cortical grey matter during months three to five of development. Neurons follow the orientation of radial glial fibers into the cortex and settle into the deep layers of the cortex first followed by subsequently formed neurons settling in superior layers of the cortex. As soon as a neuron stops migrating the process of forming connections with other neurons begins. Axons from each neuron will grow in the direction of molecular signals generated from target neurons starting a period of rapid synaptogenesis (the formation of synapses between neurons) in the brain. The specific timing and location of molecular signaling gives rise to the intricate network structure of the cortical white matter

tracts as well as the neuronal connections within the cortex. The process of rapid growth and synaptogenesis in the developing brain continues through the second (weeks 13 to 26) and third trimesters (weeks 27 to end of pregnancy) until birth.

The process of human brain development requires the successful completion of a complex series of events. Errors in the early developmental stages can affect the composition of structures that are formed in later stages of development. Interestingly, congenital malformations of brain structure are often associated with abnormal development of the nervous system during specific developmental stages. For example, between the fourth and eighth week of development the prosencephalon may fail to separate into the secondary vesicles, the telencephalon and diencephalon, resulting in a family of malformations called holoprosencephaly. Notably, the timing of this altered development coincides with the generation of facial structure, thus holoprosencephaly is usually associated with facial malformations as well. Importantly for the work in this thesis, environmental insult from alcohol during critical developmental periods has been shown to alter the typical developmental processes in both brain and facial structure.

### **1.1.5 Altered Brain Development in Fetal Alcohol Spectrum Disorder**

Alcohol is a teratogen meaning that exposure to alcohol in-utero can disrupt the typical development of an embryo or fetus. Experimental studies using animal models enable the study of altered neurodevelopment as it relates to the frequency, quantity, and timing of prenatal alcohol exposure. Through these studies a multitude of candidate mechanisms have been proposed (for review see (Goodlett et al., 2005)) that relate alcohol exposure to the disruption of naturally occurring processes that form the brain in-utero such as neurogenesis and myelination. Given the intricate sequence of events it is likely that multiple mechanisms could play a role in affecting brain development including but not limited to oxidative stress: decreased growth factor-signaling: gene expression and cell-cell interactions (Goodlett et al., 2005). Notably, these mechanisms could be onset by interactions with ethanol itself or neurotoxic metabolites that are produced during metabolism of ethanol. In addition, the dosage and timing of exposure play a role in the degree and pattern of altered brain development (Guerri et al., 2009) and

there is strong evidence that exposure during day 7, 8 and 9 in mice pups (associated with weeks 3 and 4 in humans) is associated with the craniofacial abnormalities frequently observed in humans who were prenatally exposed to alcohol (Sulik, 2005).

In 1973, the first observations were reported linking clinically confirmed prenatal alcohol exposure to common physical and behavioral deficits observed in children born to women who were severe chronic alcoholics during pregnancy (Jones et al., 1973; Jones and Smith, 1973). Consistent presentation of growth deficits, intellectual disabilities and abnormal craniofacial features led to the criteria for a diagnosis of fetal alcohol syndrome (FAS). Since then the FAS diagnosis has been recognized as a more severe subtype of a larger spectrum of disorders deemed fetal alcohol spectrum disorder (FASD) where individuals present with varying levels of the three anomalies initially observed. More specifically, various diagnostic criteria exist for FASD (Astley, 2004; Cook et al., 2016) but all involve a multidisciplinary medical assessment of the following four criteria: 1) confirmation of prenatal alcohol exposure during pregnancy; 2) growth deficiencies (weight or height); 3) central nervous system dysfunction requiring evaluation of both hard (e.g. abnormally small head circumference) or soft (e.g. poor performance on behavioral assessment) neurological signs; 4) identification of characteristic facial features including short palpebral fissures, thin vermilion border and smooth philtrum (see Figure 1.6). Notably, subtypes of FASD other than FAS, require the confirmation of a subset of the mentioned criteria. For example, a diagnosis of partial fetal alcohol syndrome (pFAS) can be obtained if the individual has confirmed prenatal alcohol exposure, behavioral and cognitive deficiencies but only presents with a subset of the facial characteristics needed for a full FAS diagnosis. On the other end of the spectrum a diagnosis of alcohol related neurodevelopmental disorder (ARND) could be given to an individual not exhibiting physical deficiencies or craniofacial abnormalities but had confirmed prenatal alcohol exposure and showed striking behavioral/cognitive deficiencies that could not be explained otherwise (Chudley et al., 2005; Eugene Hoyme et al., 2005). Additional subtypes of FASD have been proposed in the original Canadian diagnostic guidelines (see (Chudley et al., 2005)) and these guidelines were used to diagnosis the cohort analyzed in Chapter 6. More recently these guidelines have been updated (Cook et al., 2016) to include broader subcategories of the FASD diagnosis (e.g. diagnosis of FASD with sentinel facial features, and FASD without sentinel facial features) that are utilized to categorize individuals in the analysis included in

Chapter 4 of this thesis. Importantly, all modern diagnostic guidelines (Astley, 2004; Chudley et al., 2005; Cook et al., 2016; Eugene Hoyme et al., 2005) require the assessment of CNS dysfunction evaluated by behavioral testing or head circumference and do not require the assessment of CNS structural abnormalities via imaging. Although abnormal behavioral and head circumference potentially relate to regionally specific damage to the CNS these measurements are largely indirect and inadequate for the understanding of the effect prenatal alcohol exposure has on developing brain structure and function. Early attempts to understand the impact of prenatal alcohol exposure on brain structure relied on post-mortem studies of small samples of individuals. Autopsy of individuals who had been heavily exposed to alcohol have shown striking microencephaly (smaller brain), agenesis (failure in development) of the corpus callosum (Clarren et al., 1978; Jones and Smith, 1973). Although informative at the time, post-mortem studies of prenatal alcohol exposure largely select for individuals who are most severely exposed and thus do not represent the far larger population of individuals prenatally exposed to alcohol that live well into their adulthood. In contrast, in-vivo studies of brain structure and function using MRI can provide an understanding of the down-stream effects prenatal alcohol exposure has on the developing brain by capitalizing on larger samples of individuals more reflective of the broader FASD community. This knowledge is critical for the development of future interventions that could be tailored to individuals that fall under the FASD umbrella as well as for the overall advancement of our understanding of this diverse category of neurodevelopmental disorders.

## Facial features of FAS

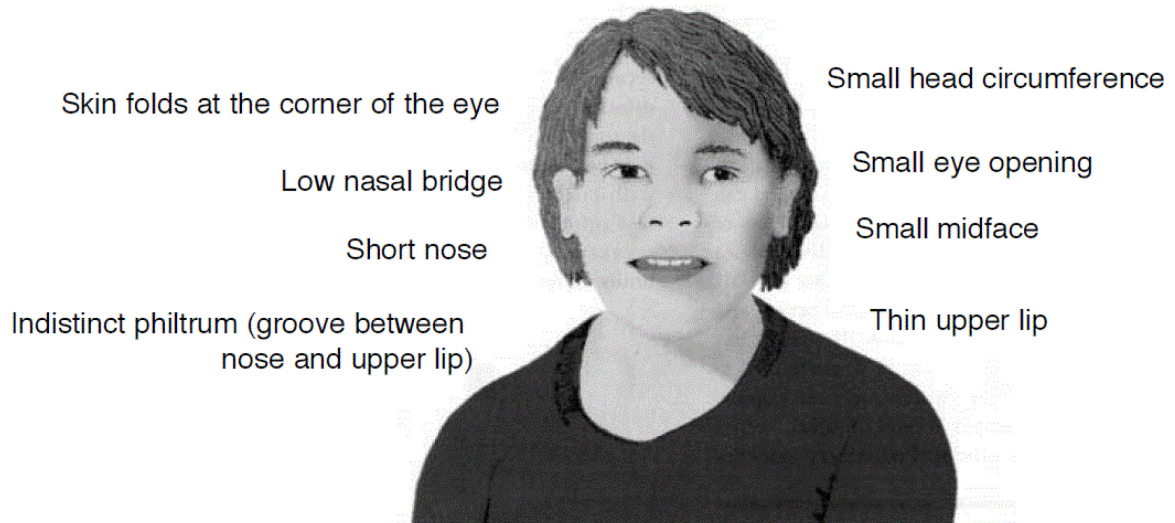


**Figure 1.6.** Facial features characteristic of Fetal Alcohol Syndrome (FAS). Image modified from Wikimedia Commons (public domain).

## 2 Magnetic Resonance Imaging and Analysis Methods

### 2.1 Nuclear Magnetic Resonance Signal and Relaxation

Nuclear magnetic resonance (NMR) and magnetic resonance imaging (MRI) experiments primarily rely on two fundamental nuclear phenomenon; 1) a non-zero magnetic moment observed from atoms that contain an odd number of protons and/or neutrons and 2) atomic particles possess intrinsic spin angular momentum (or spin). When exposed to an external magnetic field ( $B_0$ ) the non-zero magnetic moment of a nuclei will align parallel (spin up) or anti-parallel (spin down) with the external magnetic field. If a population of nuclei are exposed to an external magnetic field, slightly more nuclei will align parallel to the magnetic field because it is a lower energy state. This imbalance in orientation results in a non-zero magnetic moment parallel to  $B_0$  (longitudinal magnetization) and is the foundation of the signal that is ultimately measured in an MRI experiment. Importantly, the ratio between the spin angular momentum and the net-magnetization referred to as the gyromagnetic ratio ( $\gamma$ ) differs between nuclear species. Once the magnetization is aligned with  $B_0$  the net-magnetization precesses around  $B_0$  at the rate defined by the Larmor frequency ( $\omega_0$ ) which is proportional to the gyromagnetic ratio and strength of the external magnetic field (equation 2.1).

$$\omega_0 = \gamma B_0 \quad (2.1)$$

Water molecules consisting of two hydrogen atoms and one oxygen atom ( $H_2O$ ) are abundant in human tissue and for this reason the proton within each hydrogen nuclei ( $\gamma$  for  $^1H = 42.58 \text{ MHz / Tesla}$ ) are the primary source of signal for most MRI techniques. During an MRI experiment a radio frequency (RF) pulse (also referred to as  $B_1$ ) is applied orthogonally to  $B_0$  at a specific amplitude and frequency. The frequency of the RF pulse is selected as the Larmor (resonant) frequency for hydrogen protons and in turn protons absorb this energy causing the net magnetization to “tip” into the transverse plane (orthogonal to  $B_0$ ). The amplitude of the RF pulse determines the amount of energy received by the magnetic spins causing the net-magnetization to rotate by a differing amount into the transverse plane. An RF pulse applied in this manner is considered an “excitation pulse” and from a high level can be described by “flip angle” rather than the pulse amplitude. After the application of an excitation pulse the net magnetization is flipped into an orientation with components in both the transverse and longitudinal planes, for example a flip angle of  $90^\circ$  converts all longitudinal magnetization into the transverse plane. The

magnetization can be described by a 3-dimensional vector  $M$  composed of  $M_x$  and  $M_y$  (or together as  $M_{xy}$ ) that describe the magnetization in the transverse plane and  $M_z$  which describes the magnetization in the longitudinal plane (direction aligned with the static magnetic field). As soon as  $M$  is flipped by any amount the magnetization begins to relax back to equilibrium ( $M_z = M_0$  and  $M_{xy} = 0$ , i.e. where  $M$  is realigned with  $B_0$ ) at a rate described by two relaxation time constants  $T_1$  and  $T_2$ . This process was quantified in a mathematical analysis performed by Felix Bloch in 1946 (Bloch, 1946) and in this seminal work the Bloch equations were proposed and in the presence of a static background magnetic field (i.e.  $B_0$ ) can be solved to explain the evolution of longitudinal (equation 2.2) and transverse (equation 2.3) net magnetization as a function of time.

$$M_z(t) = M_0 + (M_z(0) - M_0)e^{-t/T_1} \quad (2.2)$$

$$M_{xy}(t) = M_{xy}(0)e^{-t/T_2} \quad (2.3)$$

In biological tissue  $T_1$  is the spin-lattice relaxation constant which is the time for nuclear spins to exchange energy with the surrounding environment a process that causes  $M_z$  to return to  $M_0$ .  $T_2$  is the spin-spin relaxation constant which describes the process of dephasing that individual spins encounter when they pass through the magnetic moments of neighboring atoms, in turn this causes  $M_{xy}$  to return to 0.  $T_1$  and  $T_2$  times differ between types of biological tissues and thus are the primary source of image contrast for MRI in the human brain (Figure 2.1).

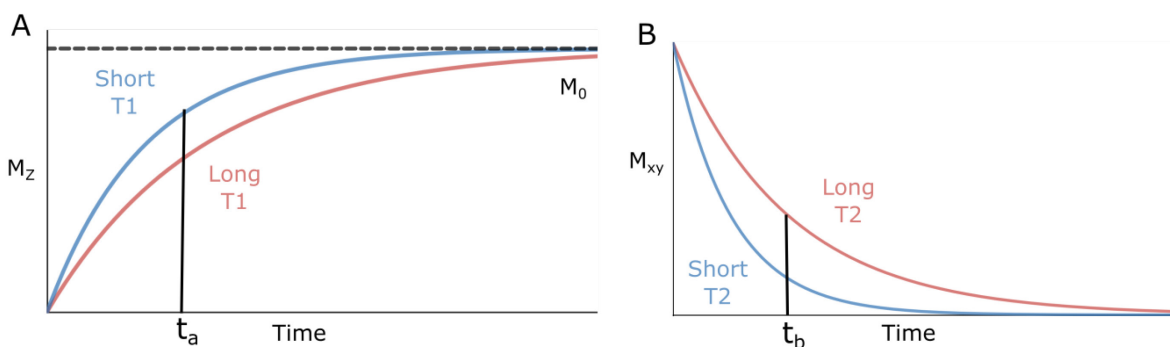


**Figure 2.1.**  $T_1$  (A) and  $T_2$  (B) relaxation curves based on a  $90^\circ$  flip angle for two theoretical tissues with differing relaxation rates. Note that if a measurement is taken at time  $t_a$  or  $t_b$  a contrast in signal amplitude is generated between the two tissues.

An additional component of relaxation is magnetic susceptibility of the tissue being measured which can cause additional dephasing of spins and a loss in the received signal leading to an increase in the transverse relaxation time ( $T_2^*$  in equation 2.4).

$$\frac{1}{T_2^*} = \frac{1}{T_2} + \frac{1}{T_2'} \quad (2.4)$$

Notably, the effects of signal loss resulting from magnetic susceptibility can be reversed by applying a  $180^\circ$  refocusing pulse halfway between the time of excitation and the time the signal is read. This spin-echo pulse effectively reverses the effect of susceptibility by allowing an equal amount of time for the spins to dephase (before the refocusing pulse) and then rephase (after the refocusing pulse) allowing for a measurement relative to  $T_2$  rather than  $T_2^*$ .

## 2.2 Generating a Magnetic Resonance Image

Generating an MR image requires the magnetically induced signal to be encoded spatially by varying the magnetic field in 3 dimensional locations. Practically this is achieved by applying magnetic fields in addition to  $B_0$  and  $B_1$  called gradients that vary the magnetic field along the X,Y and Z dimensions. In general, gradients are used to spatially select and encode the magnetic signal during the three fundamental steps of acquiring an MR image. The first step in typical 2D MRI is to select a slice and is accomplished by applying a slice select gradient (any combination of X, Y or Z gradients) along the axis perpendicular to the imaging slice. The slice select gradient effectively varies the precession frequency of the spins along the chosen axis. At the same time as the slice select gradient is applied an excitation RF pulse is applied that is designed to have a specific frequency center and range. The center frequency of this pulse is chosen to match the frequency of the spatially varying magnetic field at desired slice location and the transmit bandwidth of the pulse is chosen in a particular range that corresponds to a band of frequencies (width) along the gradient direction. By applying a linearly varying gradient and a excitation pulse at the same time only the magnetic spins within the selected frequency range (around the frequency center)

absorb the transmitted energy from the excitation pulse, effectively selecting a slice with a thickness corresponding to the frequency band and a location corresponding to the frequency center.

Following slice selection, the signal is then encoded along the other two dimensions using frequency and phase encoding respectively. The two major contributors to this technique were Paul Lauterbur (Lauterbur, 1973) and Peter Mansfield (Mansfield, 1977) whom shared the Nobel prize in Medicine in 2003 for their respective contributions to the field. When nuclear spins are exposed to a magnetic gradient of strength  $G$  (in the slice select direction) their resonance frequency ( $\omega$ ) changes as a function of their location ( $r$ ) along the gradient (equation 2.5) in the rotating frame of reference. Typically, in frequency encoding the gradient strength is left constant while the signal is read out in increments of time to acquire a set of data points over the entire frequency range. In addition to being able to temporarily manipulate signal frequency in a spatially dependent manner, gradients can be used to alter the phase of the magnetically induced signal. After a spin is exposed to a gradient (i.e. gradient turns off) the resulting spins will have acquired a phase shift ( $\phi$ ) proportional to both the strength  $G$  and the time ( $\tau$ ) that the gradient is left on (equation 2.6).

$$\omega(r) = \gamma\{B_0 + G \bullet r\} \quad (2.5)$$

$$\phi(r) = \gamma\{G \cdot r \cdot \tau\} \quad (2.6)$$

In practice phase and frequency encoding of a volume is achieved using iterations of two steps. First, a phase encode gradient is applied for a fixed length of time and secondly a frequency encoding fixed gradient strength is applied at the same time the signal is read out. Importantly, in a gradient echo sequence prior to reading out the signal a gradient is applied in the opposite direction of the frequency encode gradient for half the time (relative to the duration of the frequency encode gradient). Because gradients cause dephasing of protons by applying an initial reversed gradient prior to the readout the signal will rephase (be maximal) at the center of the readout creating an “echo”. The sequence of phase encoding followed by frequency encoding is repeated in steps with each step varying the phase encoding gradient strength to fully sample a 2D frequency space “k-space” that is the Fourier transformation of a 2D image (i.e. slice). Thus, in a simple 2D MR imaging acquisition slice selection is combined in sequence with phase encoding and frequency encoding to acquire a stack of 2D k-space slices which

are transformed separately using an inverse Fourier transformation to attain a final 3D volume (Figure 2.2). In addition to the sequence of events, the timing of events can give rise to drastically different contrast in an MR image. The echo time (TE) is the time from slice excitation to the center the readout and the repetition time (TR) is the time between excitations of the same slice. If TR is kept short relative to T1 relaxation times  $M_0$  will not fully recover and if TE is also kept short differences in T2 relaxation will not have time to evolve (i.e. minimize T2-weighting) resulting in a T1-weighted image. Whereas, if TE is kept long relative to T2 relaxation times differences in T2 relaxation between tissues will have time to evolve and if TR is also kept long  $M_0$  will fully recover (i.e. minimize T1-weighting) resulting in a T2-weighted image.

Notably, the fundamental principles of MRI acquisition (slice selection, phase encoding, frequency encoding) as well as the basic MRI pulse sequence parameters (TR, TE) are used to describe the variety of MRI sequences that are used to image brain structure, function and microstructure in this thesis work and are summarized in the following sections.

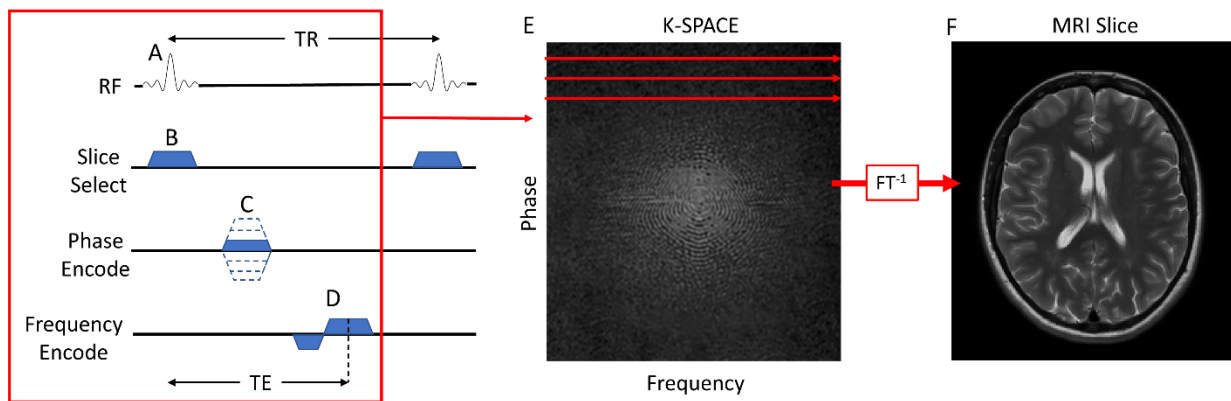


**Figure 2.2.** Typical gradient echo MRI sequence consisting of a slice excitation (A) played out simultaneously with a slice selection pulse (B). A phase encoding gradient (C) is then applied and followed by a frequency encoding gradient (D) to read out a single line of k-space. This sequence is then repeated with varying phase encode amplitudes to readout all of k-space (E). An inverse Fourier transform ( $FT^{-1}$ ) is applied to k-space to attain a single MRI slice (F).

## 2.3 Structural Brain Imaging Acquisition and Analysis

As mentioned in the previous section the image contrast generated in MR images often results from differing T1 or T2 relaxation rates between biological tissue. In typically used proton imaging the difference between relaxation rates between structures arises largely from the differing microenvironments between tissue types and is strikingly apparent in the human brain. For example, grey matter (primarily composed of cell bodies, glia and dendrites) in the brain has a longer T2 relaxation time relative to white matter (primarily composed of myelinated axons) causing a T2-weighted image to have lower intensity in regions of white matter relative to grey matter (Figure 2.3).

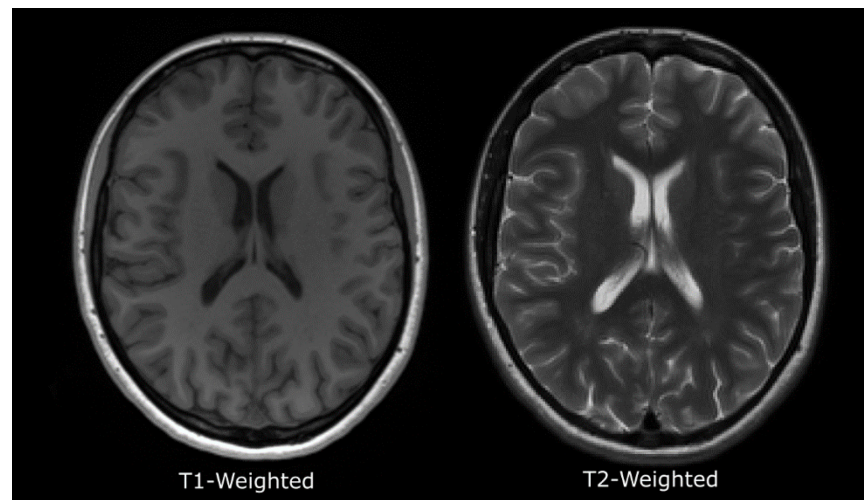


**Figure 2.3.** T1- weighted and T2-weighted images of the brain. Note the marked differences in tissue contrast between the images.

Regional differences in signal intensity are not limited to large scale tissue types alone. Some subcortical regions can also be distinguished based on differences in T2-weighted signal intensity, for example the putamen has a much higher signal intensity than the globus pallidus that likely reflects the greater iron accumulation within globus pallidus (Schenker C et al., 1993). Regional differences in T1-weighted and T2-weighted signal intensity between grey matter structure have led to the use of manual and automated segmentation techniques that parcellate the brain for the purpose of volumetric analysis of individual brain structures. Given the small size of

subcortical and cortical brain structure, segmentation techniques are usually applied to images acquired with 3D MRI sequences that enable high-resolution imaging with a slice thickness on the order of  $\sim 1$  mm. Changes in total brain volume as well as unique regional trajectories of subcortical and cortical grey matter development during childhood / adolescence have been reported in a multitude of studies using volumetric analysis (Giedd et al., 1999; Narvacan et al., 2017). Additionally, altered regional brain volumes have been reported in multiple neurodevelopmental disorders relative to controls such as FASD (Donald et al., 2015; Lebel et al., 2011), ADHD (Friedman and Rapoport, 2015), and Autism (Ha et al., 2015). Mechanisms for observed volumetric change have been suggested to be unique for individual grey matter structures, for example reductions in putamen volume are associated with iron accumulation late in life (Daugherty and Raz, 2016), whereas atrophy of the cortex during aging is likely driven by cellular shrinkage and a reduction in dendritic arborization (Morrison and Hof, 1997). The following sections detail the acquisition and analysis methods applied in the volumetric analysis presented in research Chapter 4.

### **2.3.1 MPRAGE - Structural Brain Imaging Acquisition**

Volumetric analysis of regional brain structure requires high-resolution ( $\sim 1$  mm isotropic) imaging with whole brain coverage. In typical 2D MRI the thickness of a slice is inversely related to the strength of the gradient and linearly related to the bandwidth of the applied excitation pulse. Given that RF pulses are typically chosen to be of a short duration (i.e. large bandwidth) the gradient strength becomes a limiting factor in attaining a  $\sim 1$  mm slice thickness. To this end, 3D MRI sequences have become the most common technique in volumetric studies of the human brain structure in-vivo. In contrast to 2D MR sequences which include a single phase encode step, 3D MR imaging adds additional phase encoding in the slice select direction after an initial slab selection (thicker than conventional 2D MRI slice). By adding spatial encoding along the slab select direction, 3D MRI bypasses the need to excite thin slices and can attain submillimeter spatial resolution within each slab. In addition to resolution, 3D MRI has an advantage in the signal to noise ratio (SNR) attained within each voxel. Signal to noise ratio in MRI is proportional to the (total acquisition time)<sup>1/2</sup> and 3D MRI acquires more data points relative to 2D MRI yielding an increase in SNR proportional to the (number of slices within each slab)<sup>1/2</sup> for 3D MRI compared to 2D MRI. The

benefits in resolution and SNR make 3D MRI advantageous for imaging small structures leading to this category of MR acquisition being commonly applied in studies of whole brain volumetric analysis.

The most commonly used 3D-T1-weighted sequence for whole brain imaging is the magnetization prepared rapid acquisition with gradient echo (MPRAGE) (Mugler and Brookeman, 1991) that adds two modifications to a standard 3D gradient echo sequence to attain a primarily T1-weighted contrast in a short acquisition time. To generate a T1-weighted contrast, MPRAGE applies an initial  $180^\circ$  inversion RF pulse prior to slab select and encoding steps. After the inversion pulse longitudinal magnetization recovers towards equilibrium for a specified inversion time (TI) typically between 600-900ms generating a T1-weighted signal. After the chosen TI time the signal is read out with a spoiled gradient recalled echo (GRE) which uses successive iterations of a excitation pulse with a low flip angle ( $5^\circ$  - $12^\circ$ ) followed by phase encoding in two dimensions within the excited slab. In 3D MRI phase encode steps in the slice select direction are less than in-plane phase encode direction, thus to reduce the acquisition time all phase encode lines in the slice select direction are acquired after the inversion pulse and then inversion/spoiled GRE steps are repeated for each in-plane phase encode step. Notably, the short data collection time following the inversion creates a heavily T1-weighted contrast that delineates the boundaries of subcortical and cortical brain structures.

### **2.3.2 Automated Volumetric Brain Image Analysis**

Volumetric analysis has historically used manual segmentation techniques that require an expert anatomist or trained technician to manually label and trace single or all brain structures within an anatomical image. Manual segmentation involves the detailed labeling of multiple brain structures on every imaging slice based on the image intensity of the structure, the overall position of the structure, as well as the position of the structure relative to other nearby brain structures. Thus, manual tracing of all subcortical/cortical brain structure on high-resolution imaging ( $\sim 1$  mm isotropic) can be an extensive process that can require days of work per subject. To enable volumetric analysis in large cohorts (for example greater than 100 subjects) automated segmentation methods have been developed that use image processing algorithms to parcellate a whole-brain

image into sub structures based on image intensity and spatial priors. Automated segmentation techniques have the advantage of being user independent resulting in highly reproducible volumetric measurements that can be compared between studies. The most common automated segmentation software used in volumetric studies of the brain is FreeSurfer (Fischl, 2012) and is the method applied in the volumetric analysis in the current thesis work. FreeSurfer is a software package that generates both subcortical and cortical grey matter segmentations allowing for a whole brain volumetric analysis.

Whole brain segmentation (Fischl et al., 2002) in FreeSurfer labels voxels from native imaging space for each tissue class (e.g. grey matter, white matter or CSF) as well as subcortical (e.g. hippocampus) and cortical (e.g. superior frontal gyrus) brain structures. To model the likelihood of a given voxel being assigned a structural label FreeSurfer uses a spatially varying Markov Random Field (MRF) which is a Bayesian approach that enables the inclusion of spatial priors during automated labelling. To attain label probabilities, whole brain T1-weighted images for each subject are registered to a probabilistic atlas generated from 39 manually traced healthy adults. From this atlas each voxel is assigned a probability of belonging to a specific anatomical class (e.g. putamen, hippocampus, white matter, or cortical grey matter) that is derived from the voxel image intensity and the frequency with which that voxel was identified as an anatomical structure in the 39 manual tracings. To favor anatomically correct segmentations (e.g. amygdala always is anterior to the hippocampus) the chosen label of a given voxel is also dependent on both the anatomical label and spatial relationship (anisotropic weighting of probabilities) of neighboring voxels. All probabilities are encoded into an MRF which is solved using an iterative process whereby voxels are sequentially updated at each location to maximize the probability of the segmentation, then this process is repeated until no labels are changed. The result of this algorithm is a whole brain segmentation consisting of anatomic labels for left/right cortical grey matter, left/right cortical white matter and left/right subcortical structures (e.g. caudate, putamen). Note that this initial segmentation does not parcellate the cortical grey matter into sub regions and rather cortical segmentation is handled by an additional surface-based segmentation.

In the human cortex, brain regions involved in similar cognitive functions are often anatomically bordered by large sulcal folds along the cortical surface. Thus, automated techniques for parcellating the cortex are aided by

considering regional differences in sulcal depth, a surface-based measurement that requires the boundaries of the cortex to be modelled as surfaces (Dale et al., 1999) rather than a contiguous set of individual voxels. FreeSurfer accomplishes this in following steps. Firstly, FreeSurfer creates a pseudo-white matter mask that contains a combination of voxels labeled as cerebral white matter plus subcortical and ventricular structure that is superficial to the cortical grey matter. The pseudo-white matter mask is then tessellated to generate a 3D surface mesh consisting of vertices and edges along the outside of the mask. This initial surface model is then deformed to areas of large image contrast along the border of the WM/cortex, by moving vertices incrementally along the image gradient (i.e. first derivative of the image) to a target WM/cortex image intensity while at the same time constraining the curvature and vertex spacing of the surface. This surface deformation results in a smooth surface that is located on the WM/cortex boundary. The surface deformation algorithm is then repeated to attain a surface that is located on the cortex/CSF by moving the WM/cortex vertices outward along the image gradient to a cortex/CSF target intensity while restricting movement when the vertices are within proximity of each other (i.e. in sulcal folds where walls of the surface will face each other). The WM/cortex surface is then inflated (Fischl et al., 1999) to attain a measurement of sulcal depth at each vertex which is used to perform spherical registration to a surface-based atlas of parcellated cortical regions (Fischl et al., 2004). Regional parcellations of the cortex are then interpolated back to voxels in the subject's image while constraining labeled voxels to be within the WM/cortex and cortex/CSF boundaries. In FreeSurfer, this process results in labeling of 35 cortical regions per hemisphere. The FreeSurfer segmentation workflow is outlined in Figure 2.4.

After segmentation voxels for each subcortical and cortical label can be summed to attain a measurement of volume for each brain region and can be used for input into subsequent statistical analysis. Importantly, automated segmentation methods are not error free and need to be inspected for accuracy prior to further analysis.

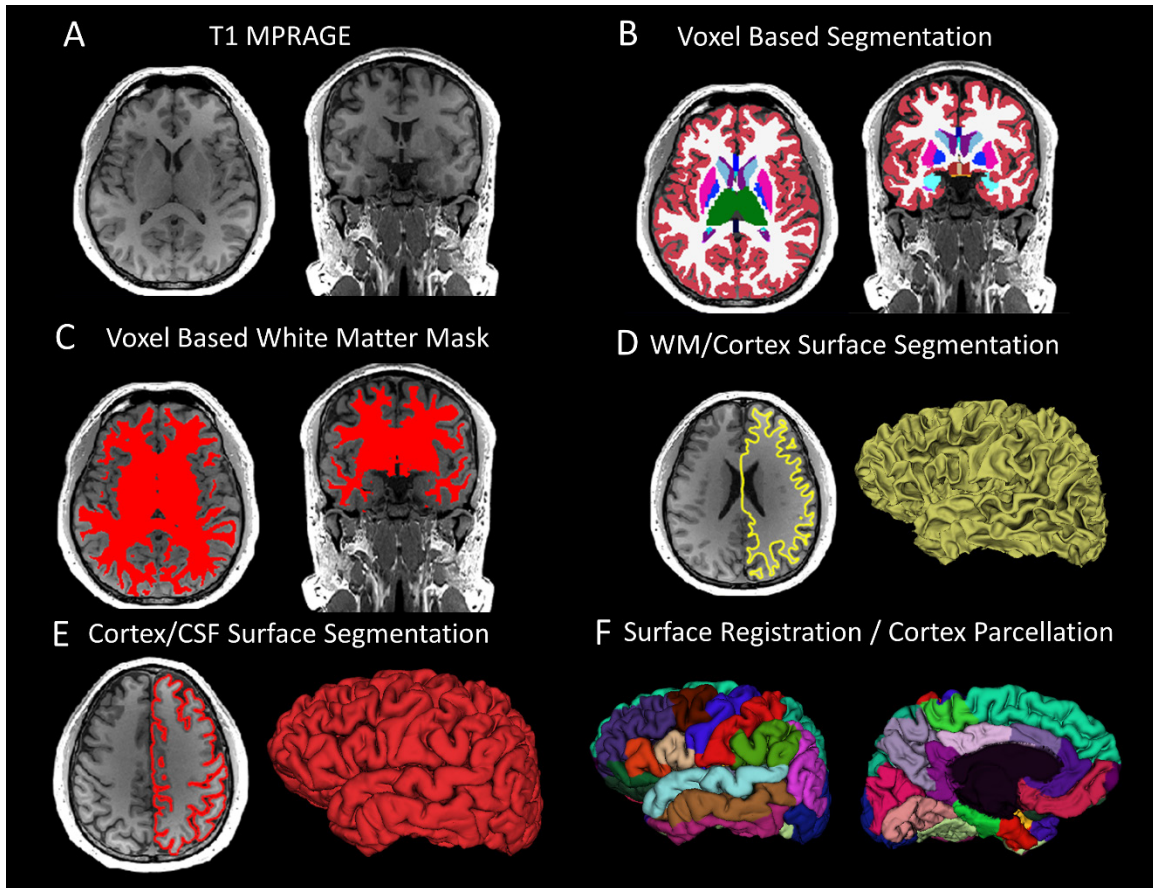


**Figure 2.4.** FreeSurfer segmentation pipeline using A) T1 MPRAGE whole brain acquisition. B) Each voxel is labeled using probabilistic modelling into one of a number of subcortical/tissue classes. C) A pseudo white matter (WM) mask is created containing all voxel labeled WM and some internal structures (e.g. ventricles). D) The WM mask is tessellated to create a 3D model and this surface is further corrected using successive surface deformations along the T1-weighted image gradient outputting a WM / Cortex surface. E) The WM / Cortex surface is expanded outward along the image gradient to the Cortex / CSF boundary. F) Surface based registration relying on measurements of sulcal depth and curvature is employed to parcellate the cortex into separate regions.

## 2.4 Echo Planar Imaging for Functional and Diffusion MRI

Many MRI techniques require the rapid acquisition of multiple images in a short amount of time. Echo planar imaging (EPI) was one of the first imaging sequences proposed (Mansfield, 1977; Stehling et al., 1991) and allows for the acquisition of an entire slice in a single excitation. The EPI sequence first selects a slice then immediately applies a phase encode gradient followed by a frequency encode gradient to read out a single line from the edge of k-space. Following the acquisition of an initial k-space line, a phase encode “blip” is applied followed by a frequency encode in the inverted direction to read out an adjacent line of k-space. Phase encode

“blips” combined with frequency encodes of alternating polarity are repeated until all of k-space is traversed in a zig-zag fashion after a single slice excitation (single-shot). The aforementioned gradient-echo EPI is typically used in functional MRI to rapidly acquire multiple T2\* weighted imaging volumes (~2-3 seconds per volume) over time but this technique is highly sensitive to susceptibility effects and spatial deformations present in the T2\* images. To reduce T2\* effects in diffusion weighted imaging (DWI), a 180° refocusing pulse can be added after the excitation pulse to create a spin-echo EPI image with T2 weighting. In spin-echo EPI the k-space readout is centered at the spin-echo resulting in a slightly longer imaging time relative to gradient-echo EPI, however in DWI a longer imaging time is usually accepted given the reduction in spatial distortion and susceptibility artifacts.

## 2.5 Functional Magnetic Resonance Imaging

Regional activation of neurons has been shown to be closely coupled with an influx of cerebral blood flow and the oxygenation of red blood cells in these regions (see the following for review of underlying physiology (Kim and Ogawa, 2012)). Specifically, under resting conditions regions of the brain will have steady flow of oxygenated hemoglobin into the arterioles of the capillaries. Neurons at rest will extract oxygen from the oxygenated hemoglobin creating a consistent ratio of oxygenated to deoxygenated hemoglobin in the venules of capillaries. When neurons activate the regional blood vessels will dilate creating an increase in oxygenated hemoglobin locally. This increase in oxygenated hemoglobin is more than needed to meet local metabolic demands thus neuronal activity is associated with an increase in the ratio of oxygenated to deoxygenated hemoglobin (Fox and Raichle, 1986). Given that deoxygenated hemoglobin is paramagnetic and oxygenated hemoglobin is diamagnetic an increase in signal is observed in T2\* weighted images at the site of neuronal activity relative to resting conditions. The measurable difference in signal between resting and active conditions is called the blood oxygen level dependent (BOLD) signal and was first reported in humans in multiple cortical regions (Bandettini et al., 1992; Frahm et al., 1992; Kwong et al., 1992; Ogawa et al., 1992) which lead to the popularity of task-based functional MRI (fMRI) studies. In task-based fMRI studies the BOLD signal is typically measured by acquiring multiple gradient-echo EPI images during the application of a stimulus (e.g. checkerboard or fingertap) and compared to measurements acquired during a baseline/rest condition (e.g. blank screen or no finger tap). However, it was later

observed that intrinsic patterns of functional connectivity were observed between regions of the motor cortex during the resting condition (Biswal et al., 1995) suggesting that measurements of fMRI signal fluctuations at rest relate to the intrinsic functional network structure of the brain. Regions of the brain that have strongly correlated resting-state fMRI signals are considered networks and multiple functional brain networks have been identified at rest (Damoiseaux et al., 2006) that relate to both lower level (e.g. visual and motor) and higher level (e.g. executive function) cognitive functions.

### **2.5.1 Resting-State Functional Magnetic Resonance Imaging Analysis**

During a resting-state fMRI (rs-fMRI) experiment multiple MRI volumes are acquired with gradient echo EPI over a period time with a relatively short TR (~2-3 s). To achieve whole brain coverage in a short acquisition, typical resolution of an EPI image is lower (~2-4 mm isotropic) relative to standard structural images. Thus, for the purpose of anatomical alignment between subjects an additional structural image (e.g. 1 mm isotropic MPRAGE) is usually acquired during the same scanning session. To account for subject motion functional images are first realigned (registered) across time, followed by registration to the structural imaging volume. Even after realignment, volumes that were acquired during severe patient motion (> 1 mm) will contain motion artifact and are typically removed in subsequent analysis. Respiratory related modulations and cardiac pulsations have been shown to correlate with the fMRI signal and thus post-processing methods have been developed to mitigate the impact of confounding physiological noise. The physiological noise reduction method used in this thesis CompCor (Behzadi et al., 2007) extracts fMRI timecourses from CSF and white matter segmentations where a signal related to brain function is not expected and removes (regresses) these signals from the fMRI time course at each voxel. Notably, this method has the advantage of not requiring the monitoring of a subject's physiology (e.g. heart rate monitoring) but has shown increased sensitivity to detect functional brain activity when compared to methods that utilize physiological monitoring. In cross-section studies fMRI volumes are typically registered to an anatomical template in a standard coordinate frame (e.g. Montreal Neurological Institute (MNI) space) so that group comparisons can be performed. The final step of pre-processing of fMRI images is spatial smoothing and is usually performed with a gaussian kernel larger than the acquired EPI voxel resolution to increase the SNR of the

BOLD signal across the image at the cost of reducing the effective spatial resolution of the images. The result of these pre-processing steps is a set of fMRI volumes registered to a standard template space where the time course of each voxel relates to the functional activation of that location over time.

Functional connectivity analysis of rs-fMRI data requires the correlation of time courses from separate regions of the brain. Several methods exist for analyzing fMRI to examine positive or negatively correlated brain regions. In the work presented in this thesis two methods based on regions of interest (ROI) are applied namely, seed-based analysis and ROI-to-ROI analysis (Figure 2.6). Seed-based analysis extracts a time course (e.g. average across voxels) from a region of interest (seed) and then correlates this time course to all other voxel time courses in the image outputting a connectivity map (correlations at each voxel) for that specific seed. Connectivity maps can be visualized to investigate regional patterns of positively and negatively (anti-correlated) connected regions with a given seed. For example, when a seed is placed in the precuneus the outputted connectivity map will have positive connectivity to regions of the prefrontal cortex and left/right lateral parietal lobe which are known regions of the default mode network (DMN). In ROI-to-ROI analysis time courses are extracted for multiple ROIs and each pair of ROI time courses are correlated resulting in a connectivity matrix consisting of correlations for every pairwise correlation between ROIs. Connectivity matrices can then be compared between groups by statistical analysis of individual connections (correlations). Rather than correlations (e.g. Spearman's correlation) functional connectivity analysis methods will apply a Fisher Z-transformation to correlations to normalize the distribution of values for statistical analysis. ROI-to-ROI analysis is useful to examine whole-brain functional connectivity rather than relying on a priori selection of a specific seed region in seed-based analysis. In Chapter 6 of this thesis seed-based connectivity analysis is used to ensure that the selected ROIs are similarly connected in both control and FASD groups. Whereas ROI-to-ROI analysis is used to investigate group differences in individual functional connections.

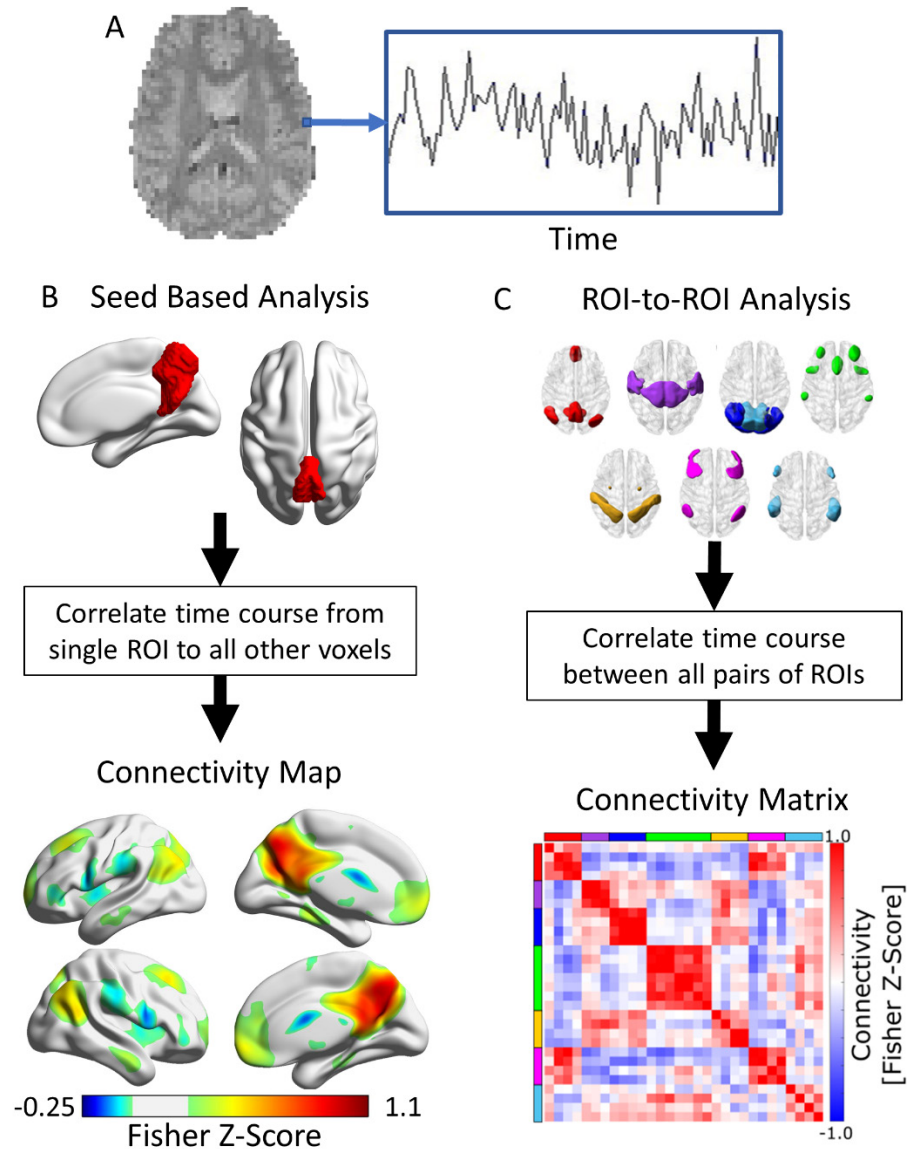


**Figure 2.5.** Visualization of the functional connectivity analysis techniques used in the current thesis. A) Firstly multiple EPI volumes are acquired over time resulting a 4D dataset where a time course in each voxel is related to the functional activity in that region. B) In seed-based analysis a time course is extracted from a single ROI and the correlated to all other time courses in the image resulting in a functional connectivity map. C) In ROI-to-ROI analysis time courses for multiple ROIs are extracted and correlated between all pairs of ROIs resulting in a connectivity matrix reflecting whole brain functional connectivity.

Two commonly used functional connectivity analysis strategies not used in the current thesis were analysis of global network properties (Rubinov and Sporns, 2010) and independent component analysis (ICA) (Calhoun et al., 2009). Global network properties based on graph theory (e.g. global efficiency, shortest path length) can be derived from connectivity matrices but rely on thresholding connectivity matrices (i.e. excluding weakly correlated

connections). Given that the amplitude of connectivity may be different between the four sites used in the current thesis work (see Chapter 5) global network properties may be confounded by site and thus were avoided for this work. ICA of rs-fMRI data aims to separate the 4-dimensional data into spatial components such that each component shares the same time course. Algorithms used to segregate the data into components in ICA are largely influenced by SNR and we show in Chapter 5 a large difference in SNR between the 4 sites used in the fMRI work precluding the use of ICA in these analyses.

## 2.6 Diffusion Magnetic Resonance Imaging

Diffusion describes the random Brownian motion of molecules in a fluid due to thermal collisions. The displacement ( $r$ ) is described in one dimension by equation 2.9 (Einstein, 1905) where  $t$  is time and  $D$  is the diffusion coefficient of the substance. Within substances without barriers such as CSF

$$\langle r \rangle = \sqrt{2Dt} \quad (2.9)$$

in the brain, water molecules will freely diffuse equally in all directions based on a random walk (isotropic diffusion). However, in regions of white matter axon bundles in the brain, water molecules are more likely to encounter cellular barriers perpendicular to the bundle rather than along to the bundle resulting in an increase in the displacement of water molecules along the tract relative to across the tract (anisotropic diffusion). The directional dependence of diffusion measurements in the brain allows for probing of the local microstructural environment of tissues using MRI.

In a typical diffusion MRI experiment the pulsed gradient spin echo (PGSE) technique (Stejskal and Tanner, 1965) is played out prior to the phase encode/readouts of a single-shot spin-echo EPI sequence to attain a diffusion-weighted image (DWI). The PGSE technique (visualized in Figure 2.7) requires the application of symmetric diffusion encoding gradients of the same duration, amplitude and direction. The first gradient is applied between the 90° excitation pulse and a 180° refocusing pulse, while the second gradient is applied between the 180° refocusing pulse and the EPI readout. During the application of the first diffusion encoding gradient, spins will acquire phase (dephase) in the direction of the applied gradient and stationary spins will be rephased after the

application of the refocusing pulse and second encoding gradient. However, spins that move along the gradient's axis during the PGSE technique will be exposed to asymmetric gradient dephasing and rephasing because gradient strength changes linearly across space. Hence, the PGSE technique is sensitive to signal loss resulting from the dephasing of spins that move along the direction of the diffusion encoding gradients. The measured signal loss due to diffusion in DWI images, follows equation 2.10 where the signal depends on the gradient amplitude ( $G$ ), gradient duration ( $\delta$ ), time between the onset of two diffusion gradients ( $\Delta$ ), and the apparent diffusion coefficient (ADC). Furthermore, this equation can be simplified in terms of b-value ( $b$ ) in equation 2.11.

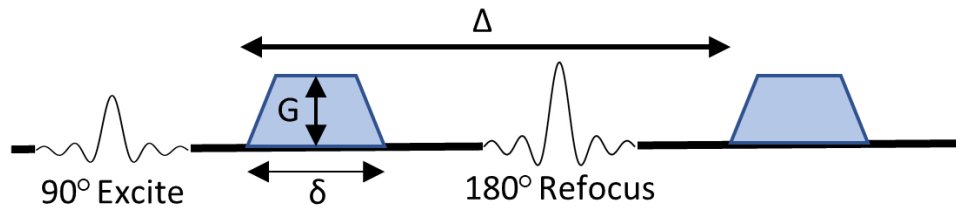


**Figure 2.6.** Stejskal and Tanner pulse spin echo sequence for diffusion encoding. Gradients of the same amplitude ( $G$ ) and duration ( $\delta$ ) are played out on either side of a refocusing pulse to attain diffusion weighting along the gradient direction. The time between the onset of the two gradients ( $\Delta$ ). Note that combinations of gradients in the X, Y and Z directions can be used to attain diffusion weighting in any possible direction.

$$\frac{S}{S_0} = e^{-\gamma^2 G^2 \delta^2 (\Delta - \frac{\delta}{3}) ADC} \quad (2.10)$$

$$\frac{S}{S_0} = e^{-bADC} \quad (2.11)$$

Here the diffusion coefficient is referred to as ADC because the diffusion measured is not the intrinsic diffusion coefficient of water but rather is affected by the degree of hindrances/restrictions by the tissue microstructure. Note that in order to solve for the ADC an additional measurement is needed ( $S_0$ ) which is the observed signal without any diffusion encoding. In MRI this is attained by acquiring a set of images (in addition to diffusion weighted images) with no diffusion encoding gradients (i.e.  $b_0$  image) but with all other sequence parameters consistent between diffusion weighted and  $b_0$  images. MRI gradients can be applied in any combination of X, Y and Z directions, thus diffusion encoding gradients can be applied to measure ADC along any 3-dimensional axis. In DWI in-vivo brain imaging the diffusion weighted signal is highly dependent on the direction

of the applied gradient relative to the orientation of the subject's head inside the scanner. Thus, rotationally invariant modelling of the diffusion signal was proposed based on the tensor model (Basser et al., 1994) which is a 3-dimensional ellipsoid. In diffusion tensor imaging (DTI), images are acquired for a minimum of 6 directions and stored in a diffusion matrix. An eigenvector decomposition of this matrix yields the 3 eigenvectors ( $\epsilon_1, \epsilon_2, \epsilon_3$ ) that describe the axes of the diffusion tensor ellipsoid and 3 eigenvalues ( $\lambda_1, \lambda_2, \lambda_3$ ) which describe the magnitude of diffusion along each axis (Figure 2.8). Here  $\epsilon_1$  is considered the primary eigenvector and composes the long axis of the tensor, whereas  $\epsilon_2$  and  $\epsilon_3$  are orthogonal to  $\epsilon_1$  and define the plane along the short axis of the ellipsoid. Typical, diffusion tensor imaging protocols will acquire multiple  $b_0$  images along with multiple diffusion weighted images each sampling a unique direction to model the tensor for each voxel within the image.

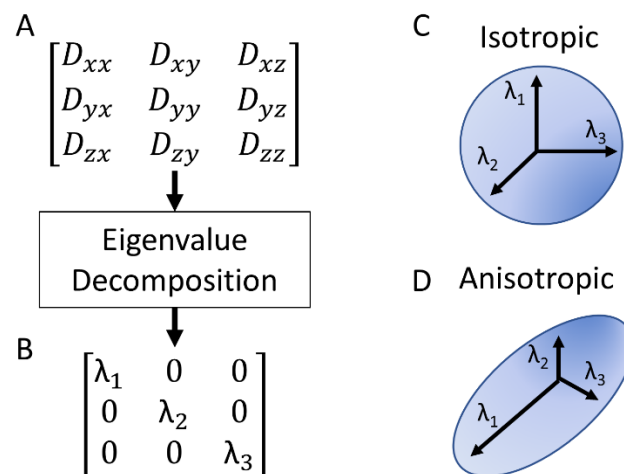


**Figure 2.7.** Measurements of the diffusion coefficient are made for multiple diffusion directions and stored in the diffusion matrix (A). After an eigenvalue decomposition the diffusion within each voxel can be modeled as a tensor by three eigenvectors that describe the axis of the tensor and (B) three eigenvalues ( $\lambda_1, \lambda_2, \lambda_3$ ) that describe the magnitude of diffusion along each axis. Isotropic (C) and anisotropic (D) diffusion tensors are shown.

In order to acquire multiple diffusion weighted and  $b_0$  volumes are acquired using a single shot EPI modified to include the PGSE technique after slice excitation (Turner et al., 1991). As described in Section 2.4, single shot EPI acquires an entire slice after a single slice excitation allowing for rapid acquisition of multiple whole brain images required for diffusion MRI. This rapid acquisition provides notable advantages for in-vivo diffusion

MRI. Given that diffusion MRI is sensitive to spin motion along the diffusion encoding direction, any subject motion in this direction can cause erroneous measurements of diffusion. The rapid slice acquisition of EPI reduces the time interval of the acquisition, in turn reducing motion artifacts and the probability of erroneous diffusion measurement. Given that alignment between acquired whole brain volumes is essential for modeling the diffusion tensor within each voxel, EPI allows for a relatively short total acquisition time decreasing the probability of inter volume subject motion during the acquisition. The beneficial rapid acquisition of EPI also has some notable disadvantages relating to spatial distortions of images. Local magnetic field inhomogeneities are created by susceptibility induced off resonance of precessional frequencies in areas of air tissue interfaces. Off resonance can result in either signal loss due to T2\* dephasing in some brain regions (e.g. medial temporal lobe) or positional errors that cause spatial deformation in other regions (e.g. anterior portions of the frontal lobe). As described above the PGSE technique requires gradients to be rapidly turned on and off causing eddy currents that result in spatial distortions unique to each diffusion weighted imaging direction. In order to model the diffusion tensor within each voxel, individual voxels need to be aligned across the multiple b0 and diffusion weighted volumes. Hence, post-processing techniques have been developed to simultaneously correct for subject motion and spatial distortions resulting from eddy currents (Andersson and Sotiropoulos, 2016).

In this thesis work, single shot spin-echo EPI images were acquired using a simultaneous multi-slice acquisition technique that allowed for a clinically relevant scan time of 3.5 minutes. The chosen protocol included the acquisition of 6 b0 images, along with 30 b1000 images (i.e. b-value of 1000) appropriate for modelling the diffusion tensor. Importantly, the diffusion imaging protocol used in the current thesis acquired images with a 1.5mm isotropic resolution enabling the segmentation and analysis of tensor properties of the cortical grey matter.

### **2.6.1 Diffusion Tensor Parameters**

From the tensor model parameters can be calculated that help to quantify the shape of the ellipsoid and relate to the microstructural environment in brain tissue. Mean diffusivity (MD) is calculated as the average of the 3 tensor eigen values over all directions (equation 2.11) and characterizes the mean ADC within a voxel. Fractional

anisotropy (FA) is a calculation of the standard deviation of the 3 tensor eigenvalues normalized to a value between 0 and 1 (equation 2.12) and describes the anisotropy of diffusion within a voxel (i.e. FA = 0 highly isotropic, FA = 1 highly anisotropic).

$$MD = \frac{\lambda_1 + \lambda_2 + \lambda_3}{3} \quad (2.11)$$

$$FA = \sqrt{\frac{3}{2}} \frac{\sqrt{(\lambda_1 - MD)^2 + (\lambda_2 - MD)^2 + (\lambda_3 - MD)^2}}{\sqrt{\lambda_1^2 + \lambda_2^2 + \lambda_3^2}} \quad (2.12)$$

These parameters are calculated for each voxel in DTI analysis creating diffusion parameter maps for MD and FA that show large differences between brain tissues (Figure 2.10). Water molecules in CSF diffuse freely unconstrained by microstructural barriers and thus have a high MD value relative to neighboring brain tissue. As previously mentioned, water within white matter encounter barriers perpendicular to axonal bundles but not parallel to the axon bundle making diffusion highly anisotropic in these regions and characterized by large FA values in parametric maps. The last tensor parameter used in this thesis work is the primary eigenvector ( $\epsilon_1$ ) which is a vector that describes the primary diffusion direction within a voxel. Typically, the primary eigenvector is used for tractography which is the process of segmenting the white matter into anatomically distinct tracts. However, in this thesis the primary eigenvector is extracted in cortical grey matter and the direction of this vector is measured relative to the cortical surface normal using the absolute value of the dot product between these vectors. This calculation is the radially of the primary diffusion direction relative to the cortex which is a measure thought to reflect the columnar microstructure of cortical grey matter.

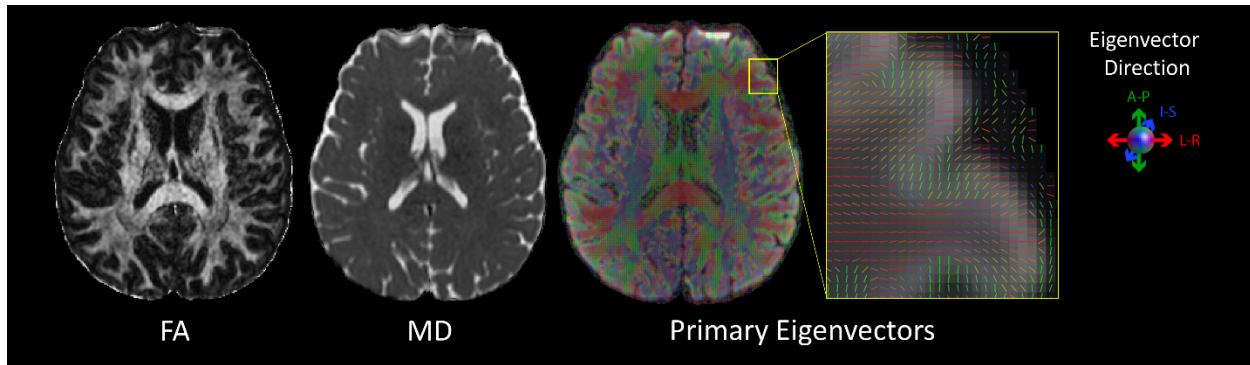


**Figure 2.8.** Example FA, MD and primary eigenvector maps. Increased FA is observed in the white matter of the brain because of the large anisotropy found in the white matter tracts of the brain, whereas MD is primarily high in the regions containing CSF because of the absence of boundaries to molecular diffusion. Primary eigenvectors show the orientational sensitivity of the diffusion tensor to the white matter tracts that project in a fanning orientation into the cortex.

## 2.7 Statistical Analysis

Multiple statistical methods are used in the thesis research chapters to test for relationships between independent (e.g. FASD or control group) and dependent (e.g. extracted imaging metrics) variables. In short conventional statistical tests (e.g. t-test, linear regression, correlation analysis) were used for the investigation of group differences in imaging metrics between FASD and controls, as well as relationships between imaging metrics and demographic / behavioral measures. In addition to more standard statistical techniques, measurement of intraclass correlations (ICC) allowed for quantification of the reproducibility and repeatability of imaging metrics across sites and scans. Finally, an advanced method of statistical modelling called machine learning was used to assess the predictive capacity of imaging metrics for classifying controls and FASD participants rather than conventional testing of statistical associations. The following sections give a general overview of the two non-conventional statistical techniques used in this thesis research namely, reproducibility/repeatability using ICC and machine learning analysis.

### 2.7.1 Measurement of Repeatability and Reproducibility

Reproducibility of scientific findings has been identified as an area of particular relevance to the field of neuroimaging (Poldrack et al., 2017). Measurements of brain structure (e.g. volume or microstructure) and

function (e.g. connectivity) should be repeatable and reproducible across scans and sites in order to maintain confidence in cross-sectional studies. Repeatability refers to the variation in a measurement taken multiple times under identical experimental conditions (e.g. test-retest imaging data of the same subject on the same scanner), whereas reproducibility refers to the variation in a measurement taken multiple times under varying experimental conditions (e.g. test-retest imaging data of the same subject but acquired using differing imaging protocols or scanners). In this thesis the reproducibility was evaluated for rs-fMRI functional connectivity measures and repeatability was evaluated for rs-fMRI functional connectivity and cortical microstructure by analyzing data acquired from the same subjects scanned multiple times. Intra class correlation (ICC) is a measure of repeatability (or reproducibility) and in the context of this thesis research is used to assess the consistency of imaging measures taken multiple times from the same individual. In general, the ICC measures the consistency or absolute agreement between measurements taken multiple times for the same subjects. Ten different variants of ICC exist and the particular model used is chosen to match the conditions of a reproducibility experiment (Koo and Li, 2016). For example, to quantify test-retest repeatability (functional connectivity Chapter 5, cortical diffusion measurement Chapter 7), the ICC(A, 1) two-way random, single-score model (Mcgraw and Wong, 1996) was used. Whereas, to test multisite reproducibility (functional connectivity Chapter 5), the ICC(A,1) two-way mixed, single-score model (Mcgraw and Wong, 1996) was used. ICC values range from 0 (no agreement between repeated measurements) to 1 (absolute agreement between repeated measurements) with values interpreted as poor (ICC < 0.5), fair (ICC 0.5 to 0.75), good (ICC 0.75 to 0.9), excellent (ICC > 0.9) (Koo and Li, 2016).

## **2.7.2 Machine Learning Approaches for Multivariate Analysis**

Typical volumetric analysis relies on univariate statistical analysis which examines volumes of individual structures separately. However, univariate analysis ignores complex relationships between brain structure that may be able to better differentiate groups of individuals (e.g. Controls and individuals with FASD) and identify patterns of brain pathology. Machine learning is a subfield of computer science which aims to build predictive models from datasets. In general, a machine learning algorithm takes multiple variables as input to build a multivariate predictive model that is either capable of separating groups (classification) or predicting a continuous

variable (regression) from provided input. Many machine learning algorithms exist that can be categorized into three overarching categories: supervised learning, unsupervised learning and reinforcement learning.

Supervised classification learning (the method used in the current thesis Chapter 4) takes multiple variables as input along with associated labels (e.g. patient or control) to train a model that is capable of predicting the label of data that was not originally included during training. In this thesis work, the support vector machine (SVM) classification model was chosen based on accurate performance in other neurological and psychiatric diseases (Orrù et al., 2012) and a linear kernel was used for increased interpretability of highly contributing brain regions to the model. The support vector classifier (SVC) aims to build a hyperplane (a plane in more than 3 dimensions) that is maximally distant from other points in multidimensional space such that points on opposing sides of the plane are classified into two distinct groups. The SVC maximizes the margin of the hyperplane (distance between plane and closest data point) based on the equation 2.7 and equation 2.8, where  $x$  is an input vector,  $w$  is a vector of feature weights and  $b$  is a bias vector.

$$w^T x - b = 1 \text{ (margin \#1, for all points above the hyperplane)} \quad (2.7)$$

$$w^T x - b = -1 \text{ (margin \#2, for all points below the hyperplane)} \quad (2.8)$$

Notably, the maximal distance for each margin is  $2/||w||$  (Figure 2.5) so the aim of an SVC is to minimize  $||w||$  with the constraint that no data points fall within the margin. However in “real-world” datasets, the data for two groups are unlikely to be completely separable by a hyperplane, thus this second constraint is typically relaxed (by a soft margin parameter “ $C$ ”) that allows data points to be within the margin boundaries which when chosen properly has the added advantage of ignoring potential outliers.

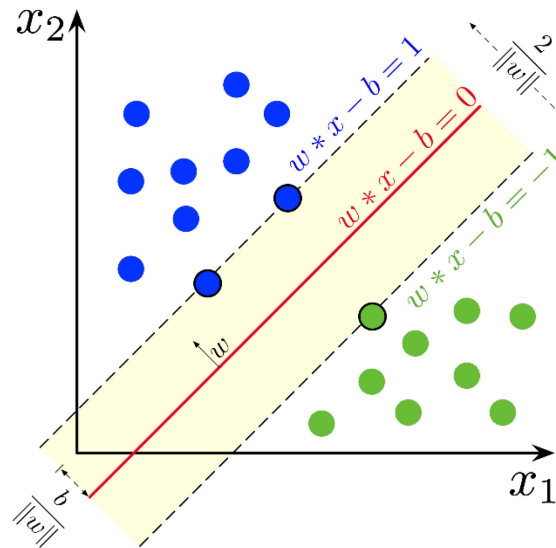


**Figure 2.9.** Plot of Support Vector Machine decision boundary (red line) based on two categories of data (blue and green dots). A decision boundary (red line) is fit to the data such that the margin (area between dashed lines) between the two categories is maximized. Image from Wikimedia Commons (public domain).

The process of optimizing the model weights ( $w$ ) and the soft margin parameter “ $C$ ” is considered the “training” step of machine learning algorithms requiring an additional “testing” procedure to evaluate the predictive performance of the model. The goal of machine learning classification algorithms is to generate predictive models that perform well on unseen data meaning data that was not included during the training of the model. Thus, classification models are typically evaluated using measures of accuracy on “test data” that is unseen at the time of training. When sufficient test data is unavailable, another approach called “k-fold cross validation” is used to emulate test data. In k-fold cross-validation the dataset is first broken into  $k$  number of subsets then a machine learning algorithm will train a predictive model on all but one subset and then test the predictive model on the left-out subset. This procedure is repeated  $k$  number of times while testing the model on a different subset each iteration resulting in measurements of accuracy for each subset. In Chapter 4 k-fold cross validation is used select the SVM soft margin parameter “ $C$ ” in the training of a predictive model and the resulting model is evaluated on a completely independent test dataset.

## **3 MRI in Fetal Alcohol Spectrum Disorder**

### **3.1 Volumetric / Classification Studies in FASD**

Studies of brain structure in children and adolescents with FASD have primarily relied on structural MRI segmentation to assess volumetric changes related to prenatal exposure to alcohol. Reductions in total brain volume associated to prenatal alcohol exposure have been consistently reported in children and adolescents with FASD (Archibald et al., 2001; Astley et al., 2009a). In studies that have analyzed brain tissue such as grey matter and white matter separately a larger reduction associated with prenatal alcohol exposure was observed in total grey matter volume (Archibald et al., 2001) and total cortical grey matter volume (Roussotte et al., 2012) relative to white matter and CSF volume suggesting that volumetric measurements of grey matter may be a sensitive measure to differentiate controls from those prenatally exposed to alcohol. Furthermore, studies of regional brain volumes have shown some subcortical brain volumes (e.g. putamen, caudate and hippocampus) are disproportionately reduced in children and adolescents with FASD (Nardelli et al., 2011; Roussotte et al., 2012). Notably, the caudate was the first reported region to have lower volume associated with prenatal alcohol exposure (Mattson et al., 1996), a finding that has since been consistently reported in the literature (Astley et al., 2009a; Inkelis et al., 2020; Treit et al., 2017). In addition, regions of the cortex have also shown regional differences in volumetric reduction associated to FASD in children and adolescents. Specifically, volume of the parietal, temporal and frontal lobes have all shown local decreased volume in FASD children/ adolescents relative to controls (Astley et al., 2009a; Chen et al., 2012). Since the publication of the thesis work presented in Chapter 4, one study has investigated age-related volumetric change in a cohort of adolescent control (n = 55) and FASD (n = 106) participants (Inkelis et al., 2020). This study primarily focused on developmental trajectories of these regional brain structures but also reported overall reductions in regional volumes in the FASD group for the caudate, putamen, corpus callosum and pallidum. Taken together, volumetric studies of children and adolescents with FASD suggest that volumetric reductions of multiple brain regions are associated with prenatal alcohol exposure, suggesting that these measurements may be useful in differentiating typically developing children and adolescents from those who were prenatally exposed to alcohol. However, these studies all use univariate analysis to detect

group differences which treats each brain region independently and ignores complex relationships (patterns) between structures that may be more suited to identifying individuals prenatally exposed to alcohol.

Few studies have combined multivariate analysis with biological based measurements to identify individuals prenatally exposed to alcohol (Table 3.1). Multimodal classification of FASD has been performed using features derived from psychometric and eye tracking data achieving an 83% accuracy (Zhang et al., 2019), and achieved relatively high classification accuracies using psychometric data (78% accuracy) and eye tracking data (76%) separately. Notably this study used a subset of the NeuroDevNet cohort used as the training data in Chapter 4 of this thesis. Another study used epigenetic DNA methylation features (again in a subset of the NeuroDevNet cohort) to classify FASD individuals and achieved a 83% accuracy in predicting FASD (Lussier et al., 2018). Facial features extracted from 3D laser scans achieved ~80%-90% accuracy identifying individuals with FAS (Fang et al., 2008), a subtype of FASD that exhibits sentinel facial features and is thought to be the “most affected” subgroup on the FASD spectrum. Three way classification has been attempted for groups of children and adolescents namely, FASD, ADHD and healthy controls, in a study using eye tracking data and achieved a 77% classification accuracy (Tseng et al., 2013). To our knowledge no study has attempted FASD classification using measures of regional brain volume reduction which have been the most consistently reported difference in structural MRI studies of FASD to date.

**Table 3.1.** Summary of FASD machine learning classification literature using biologically based measurements

Study	Sample	Age	Features	Classification Results
Fang et al. 2008	Dataset #1 (50 FAS, 32 Controls) Dataset #2 (36 FAS, 31 Controls)	Dataset #1 - mean $\sim 13.5 \pm 3.5$ years Dataset #2 - mean $\sim 5.0 \pm 2.0$ years	Pattern recognition techniques used to extract facial features from 3D laser scans for each subject.	$\sim 80$ -90% accuracy
Tseng et al. 2013	13 FASD, 21 ADHD, 18 Controls	FASD – mean $12.21 \pm 2.10$ years ADHD – mean $11.19 \pm 1.83$ years Control – mean $10.67 \pm 1.82$ years	Features extracted from eye tracking data while participants attended to videos	77% three-way classification accuracy
Lussier et al. 2018 <sup>A</sup>	Training: 83 FASD, 96 Controls Test: 24 FASD, 24 Controls	Training – range 5 - 18 years Test - range 3.5 - 18 years	Features extracted from genome wide analysis of DNA methylation patterns	83% accuracy
Zhang et al. 2019 <sup>A</sup>	45 FASD, 82 Controls	Range 5 – 18 years	Psychometric data plus antisaccade measurements extracted from eye tracking	83% accuracy
Zhang et al. 2019 <sup>A</sup> – dMRI features	22 FASD, 24 Controls	Range 5 – 18 years	Features extracted from DTI modelling of the corpus callosum	67% accuracy

<sup>A</sup> Sample includes subjects from the NeuroDevnet cohort used as the training data in Chapter 4 of this thesis

## 3.2 Functional MRI Studies in FASD

The majority of studies using MRI to study brain function in children and adolescents with FASD have used task-based fMRI designs to examine brain function of participants while performing a cognitive task. Altered brain function has been observed in FASD participants during a wide range of tasks spanning multiple cognitive domains (e.g. executive function, attention, and working memory) and results are summarized here. The go/no-go inhibition task has been shown to elicit a higher activation in child/adolescent FASD participants in regions of the frontal and parietal lobes (Fryer et al., 2007). Greater activation was also observed in young adults with FASD relative to controls during a sustained visual attention task with the larger activation localized to an occipital temporal region of the brain (Li et al., 2008). Similar regions (e.g. parietal, frontal, temporal regions) have also been reported to have greater activation in children with FASD during a number processing task (Meintjes et al., 2010). Similarly, greater activation in children/adolescents with FASD during spatial working memory in frontal/insular regions (Maliszka et al., 2005; Spadoni et al., 2009) and verbal working memory in frontal regions (O’Hare et al., 2009; Sowell et al., 2007). At the time of Chapter 6 being published, only studies using the conventional n-back task had reported contradictory findings in children with FASD with lower functional activation (Astley et al.,

2009b; Roussotte et al., 2011) and higher functional activation (Diwadkar et al., 2013) being reported in frontal, temporal and parietal regions. Notably, the consistent finding of greater activity during multiple tasks suggests a general increase in regional functional demand in children/adolescents with FASD. Since the work from Chapter 4 was published only one other task-based fMRI study has reported alterations in functional activity in children with FASD. This study used a non-symbolic number processing task and found decreased activation in the right parietal lobe of children with FASD compared to controls (Woods et al., 2018). Overall, task-based fMRI has provided a greater understanding of the relationship between brain function and cognitive performance in children/adolescents with FASD, however these studies are often confounded by the behavioral/cognitive differences that exist between individuals with FASD and typically developing controls. In addition, the practicalities of performing task-based fMRI in a clinical environment preclude the use of this technique for an assessment of brain function in a diagnostic setting.

Resting-state functional MRI studies assess the intrinsic functional architecture (i.e. “connectivity”) of the brain in absence of a cognitive task. At the time this thesis was initiated few studies had used rs-fMRI to investigate functional connectivity in individuals with FASD (Table 3.2). Early work investigated functional connectivity in FASD using ROI-to-ROI analysis to investigate the resting-state functional connectivity between a few a priori selected pairs of ROIs finding lower interhemispheric connectivity between para-central ROIs in children/ adolescents with FASD (Wozniak et al., 2011). In this same sample an analysis of global network properties revealed greater characteristic path length and less global efficiency in the FASD cohort (Wozniak et al., 2013) with additional studies demonstrating that these features also may be useful for identifying FASD participants that did not show striking facial dysmorphology patterns most commonly associated with FAS (Wozniak et al., 2016).

Other studies have attempted to examine altered functional connectivity associated with FASD in the context of established resting-state functional networks. For example lower functional connectivity was observed in young adults with FASD in connections of the default mode network (Santhanam et al., 2011) suggesting that functional alterations associated with prenatal alcohol exposure can be observed into early adulthood. Using ICA multiple functional connectivity networks (i.e. components) were investigated in a cohort of neonates prenatally

exposed to alcohol finding greater functional connectivity in a component related to motor function (Donald et al., 2016). At the time this thesis work was initiated no studies had investigated similar functional networks in children / adolescents prenatally exposed to alcohol but two reports other than the work in Chapter 6 have since been published. The first of these studies used ICA to investigate multiple functional networks in a cohort of 57 children / adolescents (19 FASD, 19 heavily exposed nonsymptomatic, 19 controls). Decreased connectivity was observed in the FASD group in five functional networks namely, the anterior DMN, salience network, dorsal attention network, ventral attention network, and right frontal-parietal network (Fan et al., 2017). The second work examined functional connectivity to the sensorimotor network in a cohort of individuals which primarily consisted of the same children / adolescents from the NeuroDevNet dataset analyzed in Chapter 6. In this study greater connectivity was observed in the FASD group between the sensorimotor network and the anterior cingulate cortex (ACC) and lower connectivity was observed in the FASD group between the sensorimotor network and regions of the DMN (Long et al., 2018). Even with the publication of these two studies the work in Chapter 6 is to date the only FASD study that investigates multiple functional networks in a relatively large sample of children/adolescents (n=127, 66 FASD, 67 controls).

**Table 3.2.** Summary of resting-state functional connectivity studies in FASD

Study	Sample	Age (years)	Analysis Method	Primary Finding
Wozniak et al. 2011 <sup>A</sup>	21 FASD, 23 Controls	10 – 17	ROI-to-ROI analysis of a priori selected pairs of ROIs	Decreased interhemispheric connectivity between para-central ROIs
Wozniak et al. 2013 <sup>A</sup>	24 FASD, 31 Controls	10 – 17	Global Network Properties	Greater characteristic path length and less global efficiency in the FASD cohort
Wozniak et al. 2016	75 PAE, 68 Controls	7 – 17	Global Network Properties	Global network properties (e.g. characteristic path length, global efficiency) were altered in a large proportion of individuals who were prenatally exposed to alcohol but could not be diagnosed by facial dysmorphic features alone.
Santhanam et al. 2011	21 Dysmorphic FASD 21 Non-dysmorphic FASD 22 Controls	9 – 24	ROI-to-ROI / Seed based analysis	Decreased connectivity in FASD between regions of the DMN
Donald et al. 2016	13 PAE, 14 Controls	2-4 weeks old (neonates)	ICA	Greater functional connectivity in the PAE group within the sensorimotor network
Fan et al. 2017	19 FASD, 19 heavily exposed nonsyndromal 19 Controls	11.3 ± 0.9	ICA	Decreased connectivity was observed in the FASD group in regions of five functional networks, the anterior DMN, salience network, dorsal attention network, ventral attention network, and right frontal-parietal network
Long et al. 2018 <sup>B</sup>	50 Controls, 59 PAE	5 - 18 years	Seed-Based Analysis of Sensorimotor network	Greater connectivity in the FASD group between the sensorimotor regions and the anterior cingulate cortex (ACC) and lower connectivity in FASD between the sensorimotor regions and the DMN

<sup>A</sup> The same subjects were included in the cohorts of both studies

<sup>B</sup> Cohort analyzed in this study primarily consisted of the NeuroDevNet cohort analyzed in Chapter 6 of this thesis

### 3.3 Studies of Cortical Microstructure in the Human Brain

Ex-vivo studies of diffusion magnetic resonance imaging (MRI) of the human cerebral cortex have shown sensitivity to underlying cortical microstructure, such as radial anisotropy reflecting the columnar structure of the cortex (McNab et al., 2013, 2009; Miller et al., 2011) and laminar specific patterns of radial and tangential diffusion relative to the cortex (Aggarwal et al., 2015; Leuze et al., 2014). Early in-vivo studies have attempted to characterize the measurements of the diffusion tensor in the cortical grey matter (GM), finding a negative relationship between a subject's age (~18-77 years old) and MD (Jeon et al., 2012) as well as sensitivity of cortical MD measurements to differentiate groups of individuals with neurological disorders such as Multiple Sclerosis (Rovaris et al., 2006) and mild cognitive impairment (Ray et al., 2006). Notably, these early studies relied on low-resolution DTI acquisitions (~3.0 mm isotropic) suggesting that increased MD measurements in the cortical GM

may be a result of partial volumes between GM and the large MD values of adjacent CSF. Thus, more recent studies of the cortex which is estimated to be ~1-5 mm thick have used high-resolution (~1mm isotropic) diffusion acquisitions that are less susceptible to partial volume measurements with neighboring CSF and superficial WM. In-vivo DTI with high-resolution (1mm isotropic) has shown sensitivity to microstructural properties of the cortex revealing diffusion anisotropy, albeit less than white matter, and a mostly radial orientation of the primary eigenvectors to the cortical surface with tangential orientation in somatosensory cortex in adults at 3T (McNab et al., 2013). Measurements of radially are also associated to cortical depth in 1mm isotropic DTI measurements at 7T with decreased radially observed at lower cortical and sulcal depths (Kleinnijenhuis et al., 2015). Other work at 7T (1.05mm isotropic) has shown a similar predominant radial orientation of the primary eigen vectors in the crowns of the gyri, but tangential orientation was observed in the sulcal fundus (Gulban et al., 2018).

To date, the majority of studies focused on diffusion MRI measurements of the cortex have utilized the publicly available imaging data from the Human Connectome Project (HCP) (Sotiropoulos et al., 2013; Van Essen et al., 2013) which includes high-resolution (1.25 mm isotropic) diffusion MRI at 3T (1 hour acquisition) from ~1000 subjects. Studies analyzing the HCP data have shown regional differences in neurite density (Fukutomi et al., 2018) and fibre orientation (Calamante et al., 2018). Additional work using the HCP data has shown promise in using diffusion MRI to discriminate cortical regions (Ganepola et al., 2018), suggesting that changes in the diffusion signal across the cortex correspond to differences in tissue microstructure between cortical regions. Another study using the HCP data, generated a three-dimensional coordinate system based on cortical folding patterns alone (Cottaar et al., 2018), finding that the ratio of radial to tangential diffusion across the cortex is fairly consistent but decreases in this ratio were observed in the sulcal fundi and the somatosensory cortex.

Note that all aforementioned studies rely on the acquisition of an additional structural image (e.g. 1mm isotropic T1 MPRAGE) to delineate the inner and outer cortical boundaries with available automated methods (Dale et al., 1999; Kim et al., 2005). 3D models of these cortical models are then coregistered to DTI images to extract diffusion measurements within the cortex. However, this registration of DTI to T1-weighted MPRAGE can be problematic, due to spatial distortions caused by eddy currents and susceptibility artifacts of EPI acquisitions. Additionally, all aforementioned high-resolution diffusion MRI studies of the cortex use acquisition protocols ~1

hour in length precluding their use in developmental or some clinical populations. In Chapter 7, a software analysis pipeline is presented that automatically segments the cortex in native DTI space bypassing the need for additional imaging and problematic registration. Additionally, in Chapter 7 an acquisition protocol is presented with a slightly lower resolution than previous cortical studies (1.5mm isotropic) but yields DTI measurements in line with high-resolution diffusion MRI cortical studies and is acquired in 3.5 minutes.

**Table 3.3.** Summary of high-resolution (~1mm isotropic) in-vivo diffusion MRI studies in adult human cortex

Study	Sample	Field Strength	Resolution	Diffusion Model	Primary Finding
McNab et al. 2013	6 healthy adults	3T	1mm isotropic slabs centered on the central sulcus	DTI	Primary eigen vector is oriented radially to the cortical surface except for tangential orientation in the post central sulcus.
Kleinnijenhuis et al. 2015	5 healthy adults	7T	1mm isotropic	DTI	Radiality measurements are dependent on both the cortical and sulcal depth.
Gulban et al. 2018 <sup>A</sup>	3T – 6 healthy adults 7T - 6 healthy adults	3T and 7T	1.25 mm isotropic	DTI and “Ball and Stick”	Tangential fibres observed in superficial cortical depths. Crossing fibres in deep cortical depths using “Ball and Stick” modeling
Fukutomi et al. 2018 <sup>A</sup>	505 healthy young adults	3T	1.25 mm isotropic	NODDI	Neurite density measures were high in areas known to have increased myelin content.
Calamante et al. 2018 <sup>A</sup>	8 healthy young adults	3T	1.25 mm isotropic	CSD	Average Fibre Orientation Distribution observed high in areas of increased myelin content.
Ganepola et al. 2018 <sup>A</sup>	40 healthy young adults	3T	1.25 mm isotropic	Diffusion signal measured relative to cortex	Diffusion MRI can be used to discriminate cortical regions with known architectonic differences
Cottaar et al. 2018 <sup>A</sup>	29 healthy young adults	3T	1.25 mm isotropic	Ball and Stick	Proposed 3D coordinate system based on the cortical surface that is highly predictive of diffusion in the cortex as well as superficial WM

<sup>A</sup> Uses publicly available HCP diffusion MRI data

# Research

## 4 Multivariate Models of Brain Volume for the Identification of Individuals Prenatally Exposed to Alcohol<sup>1</sup>

### Abstract

Magnetic resonance imaging (MRI) studies of fetal alcohol spectrum disorder (FASD) have shown reductions of brain volume associated with prenatal exposure to alcohol. Previous studies consider regional brain volumes independently but ignore potential relationships across numerous structures. This study aims (i) to identify a multivariate model based on regional brain volume that discriminates children/adolescents with FASD versus healthy controls, and (ii) to determine if FASD classification performance can be increased by building classification models separately for each sex. 3D T1-weighted MRI from two independent childhood/adolescent datasets were used for training (79 FASD, aged 5.7 - 18.9 years, 35 males; 81 Controls, aged 5.8 - 18.5 years, 32 males) and testing (67 FASD, aged 6.0 - 19.6 years, 38 males; 74 Controls, aged 5.2 - 19.5 years, 42 males) a classification model. Using FreeSurfer, 87 regional brain volumes were extracted for each subject and were used as input into a support vector machine generating a classification model from the training data. The model performed moderately well on the test data with accuracy 77%, sensitivity 64%, and specificity 88%. Regions that contributed heavily to prediction in this model included temporal lobe and subcortical gray matter. Further investigation of two separate models for males and females showed slightly decreased accuracy compared to the model including all subjects (male accuracy 70%; female accuracy 67%), but had different regional contributions suggesting sex differences. This work demonstrates the potential of multivariate analysis of brain volumes for discriminating children/adolescents with FASD and provides indication of the most affected regions.

---

<sup>1</sup> Chapter has been published elsewhere, Little G., Beaulieu C. "Multivariate models of brain volume for identification of children and adolescents with fetal alcohol spectrum disorder". *Hum Brain Mapp.* 2019;1–14

## 4.1 Introduction

A diagnosis of fetal alcohol spectrum disorder (FASD) relies on the identification of physical, cognitive, and behavioral impairments related to prenatal alcohol exposure (Popova et al., 2016). Quantitative structural magnetic resonance imaging (MRI) studies have consistently reported reductions of total brain, white matter, and gray matter volumes in individuals with prenatal exposure to alcohol who are often diagnosed with fetal alcohol spectrum disorder (FASD) (for reviews, see Donald et al., 2015; Lebel et al., 2011). Some structures may be disproportionately affected in FASD with larger proportional reductions in specific deep gray matter structures such as the caudate and putamen (Nardelli et al., 2011; Roussotte et al., 2012). These brain volume reductions have also been reported in infants and neonates with prenatal alcohol exposure for the corpus callosum (Jacobson et al., 2017) and gray matter (Donald et al., 2015). In addition, larger volume reductions have been observed in males with FASD suggesting sex differences (Chen et al., 2012; Dudek et al., 2014; Treit et al., 2017). However, most of these studies analyze each brain region separately (i.e. univariate analysis) and volumes have considerable overlap between groups making them unsuitable for individual FASD diagnosis.

Machine learning classification takes multiple variables as input to build a multivariate classification model capable of separating groups based on the provided input. In short, a multivariate classification model is a mathematical equation that describes a multidimensional boundary (e.g. a plane) where data points located on opposite sides of the boundary are classified into different groups (i.e. FASD versus control). Machine learning classification of neuroimaging features has shown promise to discriminate individuals with brain disorders from healthy controls (Arbabshirani et al., 2017). These techniques have been applied in pediatric populations to identify neurodevelopment disorders such as attention deficit hyperactivity disorder (ADHD) and autism (Levman and Takahashi, 2015). Multivariate classification studies with neuroimaging data typically rely on a large number of samples to achieve stable models (Nieuwenhuis et al., 2012) and to date ADHD classification studies have been performed most often on the same cohort of children and adolescents collected as part of the ADHD-200 consortium (Milham et al., 2012). Classification models on the ADHD-200 data have achieved accuracies ranging from 55% using structural brain features (Colby et al., 2012) to 81% using resting-state functional connectivity

features (Fair et al., 2013) in classifying children/adolescents with ADHD. Similar accuracies have been achieved in studies of large cohorts (> 100 participants) of children/adolescents with autism reporting classification accuracies of between 70% using a combination of regional brain volume and functional connectivity features (Zhou et al., 2014) to 91% using functional connectivity features alone (Chen et al., 2015). To our knowledge only one study focusing on eye tracking and psychometric data has attempted FASD classification using neuroimaging based features. This study extracted features from diffusion MRI of the corpus callosum, and achieved an accuracy of 65%-70% in classifying children/adolescents with FASD (41 individuals with FASD, 35 controls) (Zhang et al., 2019) that was a subset of the larger cohort used in the current study. However, to date no study has investigated the utility of multivariate classification models using regional brain volumes (notably the most consistent finding across FASD MRI studies) in FASD. Additionally, classification studies of neurodevelopmental disorders typically use a linear regression to reduce sex-related variation of input features, however in cases where there are group by sex interactions (e.g. those observed in FASD) this would be sub-optimal.

This study had two key aims: (i) to identify a multivariate model based on regional brain volume capable of discriminating children/adolescents with FASD and (ii) to determine if FASD classification performance can be increased by building classification models separately for each sex given the known volume differences between males and females as a group (Cahill, 2006; Cosgrove et al., 2007). The brain volume model was developed and then tested on independent FASD/un-exposed control cohorts from two studies – a four-site pan-Canadian “NeuroDevNet” cohort (79 FASD, 81 controls) and a local single-site “CIHR” cohort (67 FASD, 74 controls).

## 4.2 Materials and Methods

### 4.2.1 FASD / Typically Developing Subjects Training and Testing Datasets

Two previously collected independent MRI datasets were used to generate and validate a predictive model. The training data was collected at four different sites across Canada as part of the NeuroDevNet project on FASD (Reynolds et al., 2011a) and was selected as the training dataset so that outputted models were generalizable to different centres or scanners. One hundred and eighty-one childhood/adolescent healthy and FASD participants underwent brain MRI at four sites, but 21 subjects (11 FASD, 10 controls) were excluded for poor structural imaging quality. The remaining 160 subjects included 79 children with FASD ( $12.7 \pm 3.2$  years, 35 males) and 81 healthy un-exposed controls ( $11.9 \pm 3.4$  years, 32 males). Group analysis of brain volumes has been reported elsewhere for the healthy controls and FASD groups in this cohort (Zhou et al., 2017). FASD participants were recruited from six clinics across Canada and had an alcohol related disorder in accordance with the Canadian Guidelines for diagnosis of FASD (Chudley et al., 2005) or had confirmed prenatal alcohol exposure. The FASD participants in the training data included 7 fetal alcohol syndrome (FAS), 13 partial fetal alcohol syndrome (pFAS), 38 alcohol related neurodevelopmental disorder (ARND), and 21 confirmed prenatal alcohol exposure (PAE). In this study, subtypes were combined into two diagnostic groups, either 20 FASD with sentinel facial features (FAS or pFAS) or 38 FASD without sentinel facial features (ARND) in-line with updated diagnostic guidelines (Cook et al., 2016). PAE subjects remained in a single group as the diagnostic guidelines characterize this group as “at risk of neurodevelopmental disorder and FASD”. All FASD subtypes were labelled as a single group for machine learning classification.

The testing data for model validation was collected under a Canadian Institutes of Health Research (CIHR) project on brain development. Participants with brain MRI included 67 participants with FASD ( $12.1 \pm 3.3$  years, 38 males) and 74 controls ( $11.5 \pm 3.5$  years, 42 males). Notably, 57 FASD and 66 control participants were included in our previous study on volumes/DTI/cortical thickness (Treit et al., 2017). The other 10 FASD participants were included in a much earlier diffusion MRI study (Lebel et al., 2008), and were the participants that did not overlap the FASD participants from (Treit et al., 2017). An additional 8 controls were randomly selected males from a typical

development cohort (Narvacan et al., 2017) and were added to provide a similar ratio of males and females in the control and FASD groups. All three studies combined for the test data used the same 3D MPRAGE protocol on the same scanner at the University of Alberta. Participants from the FASD group were recruited primarily through an FASD diagnostic clinic at the Glenrose Rehabilitation Hospital in Edmonton, AB, and were diagnosed based on Canadian guidelines (Chudley et al., 2005) and the 4-digit diagnostic code (Astley, 2004). The FASD participants in the testing data included 10 FAS, 4 pFAS, 2 ARND, 1 fetal alcohol effect (FAE), 7 neurobehavioral disorder alcohol exposed (NBD:AE), 9 static encephalopathy alcohol exposed (SE:AE), 16 “FASD” without further specification, and 18 with no FASD diagnosis but confirmed prenatal alcohol exposure (PAE). As in the training data, subtypes were combined into two diagnostic groups, either 14 FASD with sentinel facial features (FAS or pFAS) or 35 FASD without sentinel facial features (ARND, FAE, NBD:AE, SE:AE, or FASD) consistent with updated diagnostic guidelines (Cook et al., 2016). All FASD subtypes were labelled as a single group for the testing of the machine learning classification model. Further demographic information for training and testing datasets was collected via questionnaire including ethnicity and current medication and are summarized for the training and testing cohorts in Tables 4.1 and 4.2, respectively.

This study was approved by the Human Research Ethics Boards at Queens’s University, University of Alberta, Children’s Hospital of Eastern Ontario, University of Manitoba and the University of British Columbia. Written informed consent was obtained from parent or legal guardian of children/adolescents. Assent was obtained from each child/adolescent before study participation.

### **4.2.2 Cognitive Testing**

Cognitive assessments were performed on the day of the MRI scan at all four sites by research assistants trained by the same neuropsychologist for between site consistency. Research assistants were not blinded to FASD diagnosis and participants took their medication as usual on the days of behavioral testing. The cognitive batteries performed for both the training and testing datasets were different but included evaluations of core functions affected in PAE such as math, reading, executive function, memory, and inhibition. For a full summary of the behavioral tests, see previously published work for training data (Zhou et al., 2017) and testing data (Treit et al., 2017). Only behavioral tests that were conducted in the majority of participants in both the training/testing cohorts were included for analysis in the current study: the Woodcock Johnson III Tests of Achievement (WJ-III ACH) evaluated mathematic and quantitative reasoning skills (Woodcock et al., 2001) and the Woodcock Reading Mastery Tests - Revised (WRMT-R) provided a comprehensive assessment of reading ability (Woodcock, 1998). Results for behavioral tests for the participants/cognitive tests in the current study are presented for both the training and testing groups in Tables 4.1 and 4.2, respectively.

**Table 4.1.** Participant characteristics and demographics for training “NeuroDevNet” data

	<b>Control</b>	<b>FASD</b>	<b>p-value<sup>a</sup></b>
<b>Participant Characteristics</b>	n = 81	n = 79	
Age (years)	11.9±3.4 (5.8 – 18.5)	12.7±3.2 (5.7 – 18.9)	0.138
Males (%)	32 (40%)	35 (44%)	0.540
<b>FASD Subtype (%)</b>			
FASD with sentinel facial features	0 (0%)	20 (25%)	< 0.001*
FASD without sentinel facial features	0 (0%)	38 (48%)	< 0.001*
Confirmed Prenatal Alcohol Exposure (PAE)	0 (0%)	21 (27%)	< 0.001*
<b>Ethnicity (%)</b>			
Indigenous	1 (1%)	41 (52%)	< 0.001*
Caucasian	74 (91%)	24 (30%)	< 0.001*
Other	5 (6%)	14 (18%)	0.024*
Unknown	1 (1%)	0 (0%)	0.323
<b>Medication (%)</b>			
Stimulants	1 (1%)	12 (15%)	0.001*
Antidepressants	0 (0%)	3 (4%)	0.078
Antipsychotics	0 (0%)	3 (4%)	0.078
Stimulants and Antipsychotics	0 (0%)	8 (10%)	0.003*
Stimulants, Antipsychotics & Antidepressants	0 (0%)	2 (3%)	0.151
Other	7 (9%)	24 (30%)	< 0.001*
No Medication	73 (90%)	38 (48%)	< 0.001*
<b>Comorbidities (%)</b>			
ADHD	1 (1%)	40 (50%)	<0.001*
Anxiety	0 (0%)	10 (13%)	0.001*
Depression	0 (0%)	4 (5%)	0.041*
Bipolar	0 (0%)	2 (3%)	0.151
Oppositional Defiant Disorder	0 (0%)	6 (8%)	0.012*
Conduct Disorder	0 (0%)	2 (3%)	0.151
Autism	0 (0%)	1 (1%)	0.311
Other Disorder	0 (0%)	23 (29%)	<0.001*
<b>Site (%)</b>			
University of Alberta	42 (52%)	34 (43%)	0.266
Queens University	18 (22%)	22 (28%)	0.413
University of Manitoba	8 (10%)	10 (13%)	0.579
University of British Columbia	13 (16%)	13 (16%)	0.945
<b>Cognitive Test (Age Standardized Score)</b>			
Woodcock Johnson - Quantitative Concepts 18A&B mathematics	<u>n = 80/81</u> 105±12 (69 – 129)	<u>n = 78/79</u> 83±19 (37 – 129)	<0.001*
Woodcock Reading Mastery Test Revised - Word ID	<u>n = 80/81</u> 106±13 (71 – 134)	<u>n = 78/79</u> 91±14 (52 – 126)	<0.001*

<sup>a</sup>Group differences of categorical variables (e.g. sex) assessed with Mann-Whitney U; continuous variable (e.g. age) assessed with independent samples t-test (\* p < 0.05).

**Table 4.2.** Participant characteristics and demographics for testing “CIHR” data

	<b>Control</b>	<b>FASD</b>	<b>p-value<sup>a</sup></b>
<b>Participant Characteristics</b>	n = 74	n = 67	
Age (years)	11.5±3.5 (5.2 – 19.5)	12.1±3.3 (6.0 – 19.6)	0.26
Males (%)	42 (57%)	38 (57%)	0.99
<b>FASD Subtype (%)</b>			
FASD with sentinel facial features	0 (0%)	14 (21%)	<0.001*
FASD without sentinel facial features	0 (0%)	35 (52%)	<0.001*
Confirmed Prenatal Alcohol Exposure (PAE)	0 (0%)	18 (27%)	<0.001*
<b>Ethnicity (%)</b>			
Indigenous	1 (1%)	19 (28%)	<0.001*
Caucasian	55 (74%)	15 (22%)	<0.001*
Other	8 (11%)	5 (7%)	<0.001*
Unknown	10 (14%)	28 (42%)	<0.001*
<b>Medication (%)</b>			
Stimulants	0 (0%)	19 (28%)	<0.001*
Atypical Antipsychotics	0 (0%)	22 (33%)	<0.001*
Antidepressants	0 (0%)	10 (15%)	<0.001*
Other	0 (0%)	9 (13%)	<0.001*
<b>Comorbidities (%)</b>			
ADHD	0 (0%)	33 (49%)	<0.001*
Anxiety	2 (3%)	12 (18%)	<0.001*
Reactive attachment disorder	0 (0%)	8 (12%)	<0.001*
Other Disorder	0 (0%)	17 (25%)	<0.001*
<b>Cognitive Test (Age Standardized Score)</b>			
Woodcock Johnson - Quantitative Concepts 18A&B mathematics	<u>n = 66/74</u> 107±13 (77 – 135)	<u>n = 52/67</u> 82±13 (53 – 118)	<0.001*
Woodcock Reading Mastery Test Revised - Word ID	<u>n = 66/74</u> 107±13 (81 – 147)	<u>n = 52/67</u> 89±14 (52 – 134)	<0.001*

<sup>a</sup>Group differences of categorical variables (e.g. sex) assessed with Mann-Whitney U; continuous variable (e.g. age) assessed with independent samples t-test (\* p < 0.05).

### 4.2.3 Image Acquisition

The training “NeuroDevNet” MRI data was acquired at four MR imaging centres: University of Alberta (1.5T Siemens Sonata), Queen’s University (3T Siemens Trio), University of Manitoba (3T Siemens Trio), and University of British Columbia (3T Philips Intera). 3D T1-weighted images were acquired with high-resolution (1 x 1 x 1 mm<sup>3</sup>) MPRAGE using 160 axial slices, TI = 1100 ms, and flip angle = 15°, but repetition (TR) and spin echo (TE) times were set individually per site given variations in scanner performance resulting in slightly different acquisition times: University of Alberta - TE = 4.38 ms, TR = 2180 ms, scan time 5:41 min; Queens University - TE = 3.45 ms, TR = 2180

ms, scan time 5:15 min; University of Manitoba - TE = 3.45 ms, TR = 2180 ms, scan time 5:15 min; University of British Columbia - TE = 3.6 ms, TR = 1858 ms, scan time 6:23 min. The testing “CIHR” data included 3D T1-weighted images exclusively acquired at the University of Alberta (1.5T Siemens Sonata) site using an MPRAGE sequence (1 x 1 x 1 mm<sup>3</sup>) with TE = 4.38 ms, TR = 1870 ms, TI = 1100 ms, flip angle = 15°, scan time 4:29 min. Other images were also acquired over 25 min included T2-weighted, fluid-attenuated inversion recovery (FLAIR), resting-state functional (for NeuroDevNet), and DTI; however, none of these are the focus of the current report on brain volumes.

#### **4.2.4 Automated Brain Segmentation**

In this study, only regional brain volumes rather than other imaging metrics were used as predictors for classification because reductions in regional brain volumes have been the most commonly reported differences in FASD populations relative to controls (Donald et al., 2015; Lebel et al., 2011). Regional brain volumes were extracted from T1-weighted structural images using the automated segmentation pipeline FreeSurfer version 5.3 (Fischl, 2012). Volumetric loss relating to FASD has been observed in numerous brain regions (Donald et al., 2015) with some regions being consistently reported including: regions of subcortical grey matter, total white matter, corpus callosum, and regions of the cortex. Hence, volumes of 87 regions were selected for classification analysis including subcortical gray matter (12 - 6 regions for left and right), left/right total white matter (2 - left and right), corpus callosum segmentations (5 regions), and cortical parcellations (68 - 34 regions for left and right). Note that left and right segmentations were kept separate for analysis. Notably, ventricular segmentations were excluded based on limited reports of volumetric differences in FASD, right/left nucleus accumbens were excluded based on the low scan-rescan reliability of FreeSurfer segmentations (Morey et al., 2010), and cerebellum/brain stem were excluded due to partial coverage in many participants. Each included volume was then standardized across training and test datasets (i.e. mean centered to zero and scaled to unit variance over entire training/testing datasets) as this is a requirement of the support vector learning algorithm used to build a classification model.

### 4.2.5 Predictive Model Training

Using the brain volumes from the training data as input, a linear support vector machine (SVM) was trained to predict FASD or control using the scikit-learn machine learning toolbox version 0.18.1 (Pedregosa et al., 2011). This SVM algorithm was selected based on accurate performance in other neurological and psychiatric disease classification studies (Orrù et al., 2012) and a linear kernel was used to allow for the identification of highly contributing brain regions to the model. The multisite data was selected for training so that the classification model generated by the SVM was robust to between site variation of regional brain volume measurements, and would perform consistently across different sites. A single classification model was generated by fitting the SVM hyperparameter “C” based on the training data using a combination of leave-one-out cross-validation with internal ten-fold validation for parameter selection. For each internal fold, the soft margin constant “C” was selected from a list of possible values ( $10^{-4}$ ,  $10^{-3}$ ,  $10^{-2}$ , 1, 10, 100) as the parameter with the highest average accuracy over the ten-fold internal validation. A single value of “C” for the training data was then chosen as the mode of all selected parameters from the leave-one-out folds and a single classification model was fit to the entire training data. This model was then used to predict FASD or control for each subject in the test data.

### 4.2.6 Model Evaluation / Interpretation

Three measures of model performance were calculated on both the leave-one-out cross-validation training results and the test dataset predictions, namely accuracy, sensitivity, and specificity. In addition, normalized feature weights (decision boundary weight divided by maximum weight in model) of the trained model were investigated to identify brain regions that contributed the most to FASD prediction. To compare the performance of the multivariate prediction model to more conventional univariate analysis, the same training/testing procedure was performed on each of the 87 individual brain volumes separately. Both cross-validation training and test set accuracies were compared between the multivariate model and all other univariate models. Permutation tests were performed on multivariate and univariate test accuracies by calculating the accuracy of the trained models on 2000 permutations of test data labels (FASD/Control). Note that because of the number of evaluations

performed, only multivariate/univariate models that performed higher than a multiple comparison corrected p-value ( $p < 0.0005 = 0.05/88$  tests) on the testing data permutation tests are presented.

#### **4.2.7 Sensitivity of Model to Participant Demographics**

To test for sensitivity of the classifier to FASD sub-group, the number of true positives and false negatives was compared between the 3 subtypes (FASD with sentinel facial features, FASD without sentinel facial features, and confirmed PAE without official FASD diagnosis). Next the distance from support vector decision boundary was calculated for each subject in the test data as a measure of how closely a subject matched the FASD prediction model. A positive boundary distance value indicates the subject was predicted "Control", whereas a negative value indicates the subject was predicted "FASD". For comparison between models, distance values were scaled by the maximum absolute distance of the test samples. Regional brain volumes are known to differ between males and females (Cahill, 2006; Cosgrove et al., 2007) and change throughout childhood / adolescence with regionally specific developmental trajectories (Giedd et al., 1999; Narvacan et al., 2017). Boundary distances were used to test for systematic classification errors related to sex (t-test), age (linear regression), and age-by-sex interaction (linear regression). To test for sensitivity of the classifier to a specific cognitive phenotype, linear regression was performed between boundary distance and two separate behavioral tests which were Woodcock Johnson Quantitative Concepts (mathematics) and Woodcock Johnson Word Identification (reading), notably these were the only tests performed in a majority of individuals from both the training and testing cohorts. All statistical tests were performed separately for FASD and Control groups and corrected for multiple comparisons (Bonferroni correction: 5 tests by 2 groups, 10 comparisons, effective  $p < 0.005$ ).

#### **4.2.8 Sex Specific Modelling**

Following these primary analyses, two approaches were taken to address sex related differences in model performance. Approach 1: The addition of sex as a control variable in a linear regression is a common approach for addressing sex related variation in classification studies (some examples; Fair et al., 2013; Nielsen et al., 2013).

In this study, the entire modelling procedure was repeated with brain volumes adjusted for sex using a linear regression prior to model training. Approach 2: The same modelling procedure was performed on raw brain volumes for males (n=35 FASD, n=32 controls) and females (n=44 FASD, n=49 controls) separately in the training cohort and then applied to the males (n=38 FASD, n=42 controls) and females (n=29 FASD, n=32 controls) in the test cohort. Both correction techniques were compared to the original model (which did not account for sex-related variation) using measures of accuracy, sensitivity, and specificity separately for males and females in the test cohort.

## **4.3 Results**

### **4.3.1 FASD Classification Model / Performance**

A binary classification model based on brain volumes was created to discriminate between typically developing individuals and those with FASD. The 10 most heavily weighted brain regions in the model included 3 subcortical gray matter regions (left globus pallidus, left and right caudate), 3 cortical gray matter regions located in the temporal lobe (right superior temporal gyrus, bank of the right superior temporal gyrus, and left inferior temporal gyrus), 2 cortical regions located in the frontal lobe (left and right pars triangularis), and 2 along the cingulate gyrus (right posterior cingulate and right isthmus of the cingulate). A visualization of all model weights for each segmented brain region is shown in Figure 4.1.

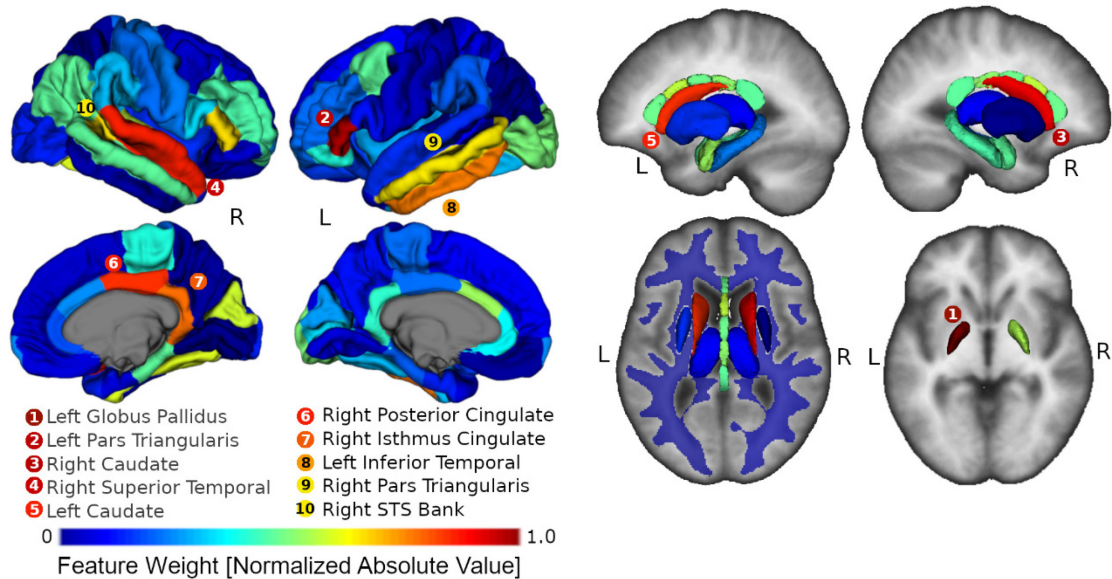


**Figure 4.1.** Visualization of model generated from brain volumes from the training dataset. All regions are displayed as 3D renderings, with the exception of left/right white matter segmentations displayed as a transparent overlay on an axial image from the FreeSurfer average template. For visualization purposes, globus pallidus renderings are displayed on a separate axial image. All regions of the brain are color coded by normalized support vector classifier weightings (weight divided by maximum absolute value weight in model). The 10 most heavily weighted regions are listed in order with corresponding colors. Model weightings were strongest for left/right regions of the temporal lobes, subcortical regions (left/right caudate and left globus pallidus), bilateral frontal lobe regions (left/right pars triangularis), and two regions in the cingulate of the right hemisphere.

The model showed moderate performance on the training data (NeuroDevNet) with accuracy 71%, sensitivity 58%, and specificity 84%, and achieved similar results on the independent test data (CIHR) with accuracy 77% ( $p$ -value = 0.0005), sensitivity 64%, and specificity 88%. Notably, the multivariate classification model outperformed all univariate classification models for accuracy in the test data (77% compared to the next highest 72% for the left caudate model), and in the training data (71% compared to 67% for the left caudate model). Accuracies for the multivariate and univariate classification models are presented in Figure 4.2. The multivariate classification model was more specific (88%) compared to all other univariate models that achieved higher than chance classification accuracy (58% right hippocampus - 85% right putamen), whereas sensitivity of the multivariate model (64%) was within range of the above chance univariate models (right putamen 46% - 79% left thalamus). Boundary distance, accuracy, sensitivity, and specificity for the multivariate classification model are presented alongside the left

caudate univariate model in Figure 4.3. Notably in both the univariate left caudate volume and multivariate model distance measurements there was a significant proportion of FASD participants minimally overlapping the controls. In total 17 FASD participants (10 females; age  $12.22 \pm 3.43$  years; 7 FASD with sentinel facial features, 4 without sentinel facial features and 6 prenatally exposed without official diagnosis) had a left caudate volume smaller than  $\sim 3.1 \text{ cm}^3$  whereas only 1 control had a left caudate volume below that threshold. No controls and 8 FASD participants had a left caudate volume lower than  $\sim 2.7 \text{ cm}^3$ . Similarly, the multivariate model had 20 FASD participants (9 females; age  $12.23 \pm 3.27$  years; 7 FASD with sentinel facial features, 6 FASD without sentinel facial features and 7 prenatally exposed without official diagnosis) with no overlapping controls below a distance from decision boundary value of -0.38 (the lowest control value). Of these 20 FASD participants that did not overlap controls in the multivariate model, 5 had a caudate volume larger than  $3.1 \text{ cm}^3$  demonstrating that the multivariate and univariate models are discriminating different individuals.

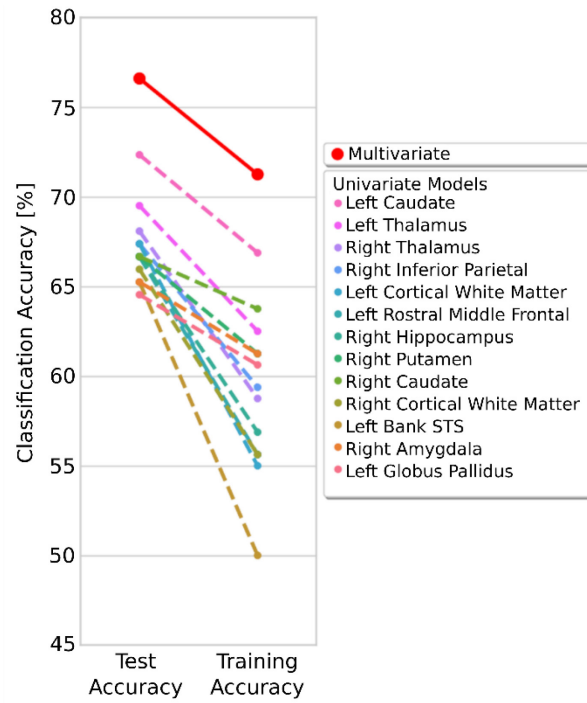


**Figure 4.2.** Performance of the multivariate brain volume prediction model (solid red line) compared to models generated using each brain region volume separately (dashed lines). Both the accuracy of the models on the test data and leave-one-out cross-validation accuracy on the training data are shown. Models are listed from highest to lowest accuracy and are presented if they performed significantly greater than chance (permutation test,  $p < 0.0005$ ) in the test cohort. The multivariate model outperformed all univariate models in both the training and testing data. Notably, 8 of these 13 regions are deep grey matter structures including bilateral caudate and bilateral thalamus.

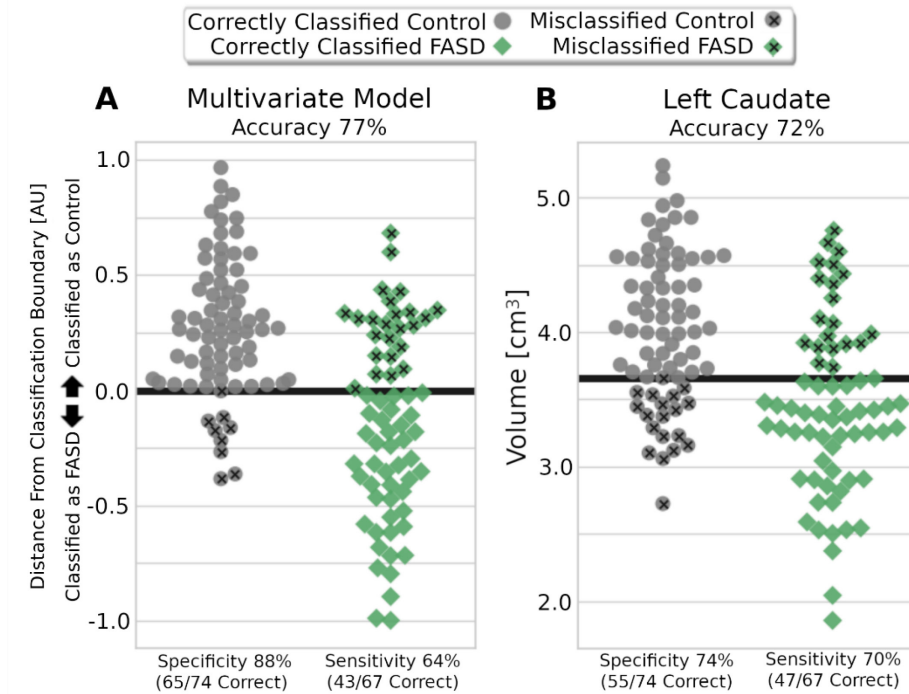


**Figure 4.3.** Distance from classification boundary for multivariate classification model (A) and raw volume for the top performing univariate model (B, left caudate) are presented for all subjects in the test “CIHR” cohort separated by group (FASD/Control). Values above the support vector machine decision boundary (black line) were classified as the control group whereas values below the decision boundary were classified as FASD. A large proportion of FASD participants had a distance from decision boundary that did not overlap any of the controls (20 FASD with boundary distance < -0.38), and similarly a large proportion of FASD had minimal overlap with controls below a left caudate volume of  $\sim 3.1$  cm<sup>3</sup> (1 control, 17 FASD).

### 4.3.2 Diagnostic, Demographic, and Cognitive Associations to FASD Classification Model

When separating classification performance in the FASD group by the 3 diagnostic subtypes, differences were observed between the proportion of true positives (TP) to false negatives (FN) between subtypes. Notably, almost all the FASD subjects with sentinel facial features were correctly classified (11 TP, 3 FN), whereas the other two subtypes, FASD without sentinel facial features (21 TP, 14 FN) and PAE (11 TP, 7 FN), had a lower proportion of TP relative to FN.

T-tests revealed a systematic difference in classification boundary distance between control males and females (t-statistic -3.67, p-value = 0.0005) indicating more false positives for females compared to males which may be a result of lower brain volumes observed in typical females relative to typical males, as a group. Linear regression results relating classification boundary distance to 4 demographic variables of interest, namely: age, age by sex, Woodcock Reading Mastery Test-Revised Word Identification (reading), and Woodcock Johnson Quantitative Concepts (mathematics) were not significant in the FASD or control groups.

### 4.3.3 Sex Specific Models

To further investigate the effect of sex on model performance, the original classification model was evaluated separately for males and females. The classification accuracies of the entire training set were similar for males (76%,  $p = 0.0005$ ) and females (77%,  $p = 0.0005$ ), but sensitivity was lower and specificity was greater for males (sensitivity 53%, specificity 98%) compared to females (sensitivity 79%, specificity 75%). In other words, 1/42 male controls were misclassified as FASD, whereas 8/32 female controls were misclassified as FASD. A larger difference in classification accuracy was observed in the FASD groups where 17/38 male FASD were misclassified as controls whereas only 6/29 female FASD were misclassified.

The first approach for reducing sex related bias in sensitivity/specificity was to fit a model based on sex adjusted volumes. This approach performed moderately well on the test data, however sensitivity remained low for males relative to females: male accuracy 72% ( $p$ -value = 0.0005), sensitivity 58%, specificity 86%; female accuracy 74% ( $p$ -value = 0.0005), sensitivity 72%, specificity 75%. The second approach for reducing sex-related bias in FASD prediction was to create separate models for males and females. Both models performed moderately well on the test data and had similar sensitivity and specificity between males and females: male accuracy 70% ( $p$ -value = 0.0005), sensitivity 68%, and specificity 71%; female accuracy 67% ( $p$ -value = 0.01), sensitivity 62%, and specificity 72%. Notably, sensitivity in the male FASD group was increased by creating separate models for males and females at the cost of decreased specificity and overall accuracy. Classification performance and classifier

boundary distance separated by sex and group is presented in Figure 4.4 for the original model, the model adjusted for sex and the models created separately for each sex.

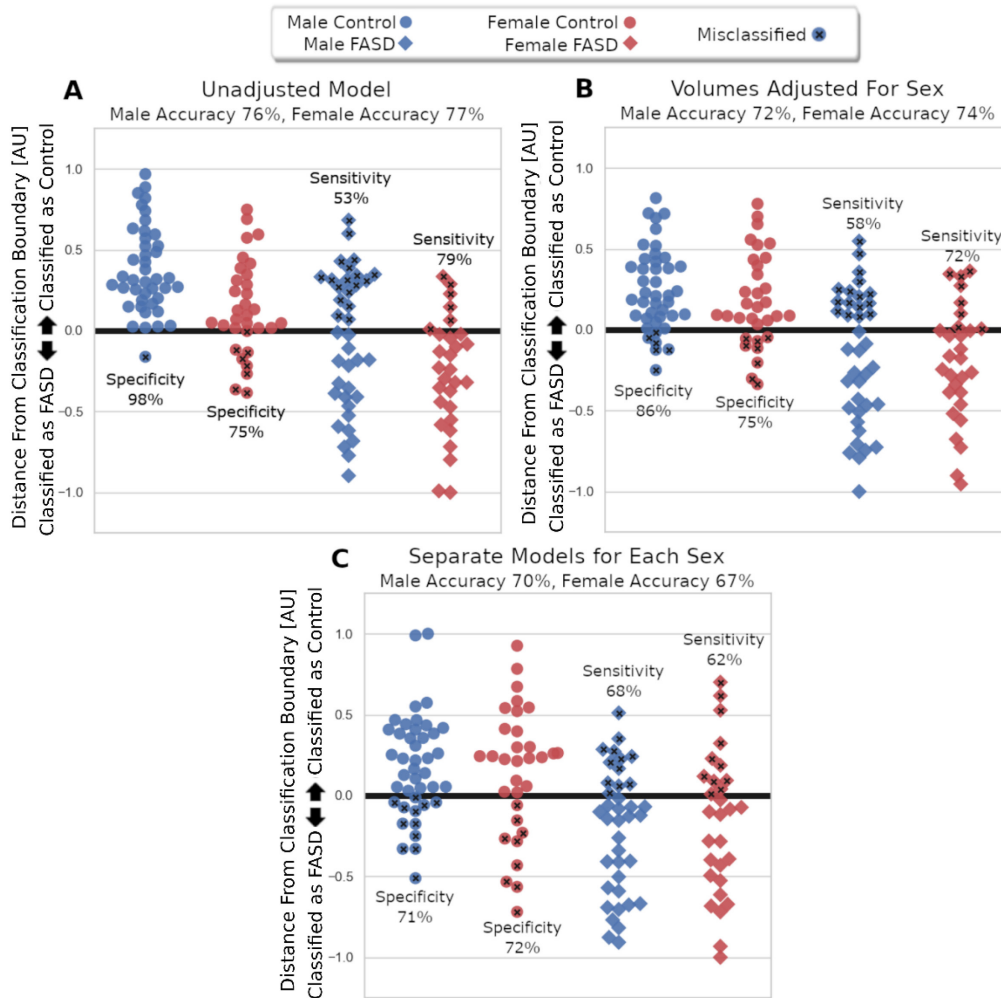


**Figure 4.4.** Distance from classification boundary is presented here for each subject in the test data separated by group (Control, circle / FASD, diamond) and sex (Male, blue / Female, red) for the unadjusted multivariate model (A), the multivariate model using regional brain volumes adjusted for sex (B), and creating separate classification models for males and females (C). Positive values indicate the subject was classified to the control group while negative values indicate the subject was classified to the FASD group. The most misclassifications in the unadjusted model were male FASD participants labelled as controls (18/38 misclassified) and a notable number of female controls were incorrectly labelled FASD (8/32 misclassified). Adjusting brain volumes for sex improved imbalance in specificity between males compared to females, whereas creating separate models improved the sex related imbalance in both specificity and sensitivity.

In general, the predictive models created separately for males and females had primary contributions from volumes of different brain regions. Of the 5 most heavily weighted regions in the male model, 4 were subcortical grey matter regions (left globus pallidus, left/right caudate, right hippocampus), and one was the right superior parietal region of the cortex. In contrast, of the 5 most heavily weighted regions in the female model, only one was subcortical grey matter (right amygdala), 3 were cortical regions (left superior parietal, right bank of the superior temporal gyrus, and right pars orbitalis), and 1 was the posterior part of the corpus callosum. The model weights for the male and female models are visualized in Figure 4.5.

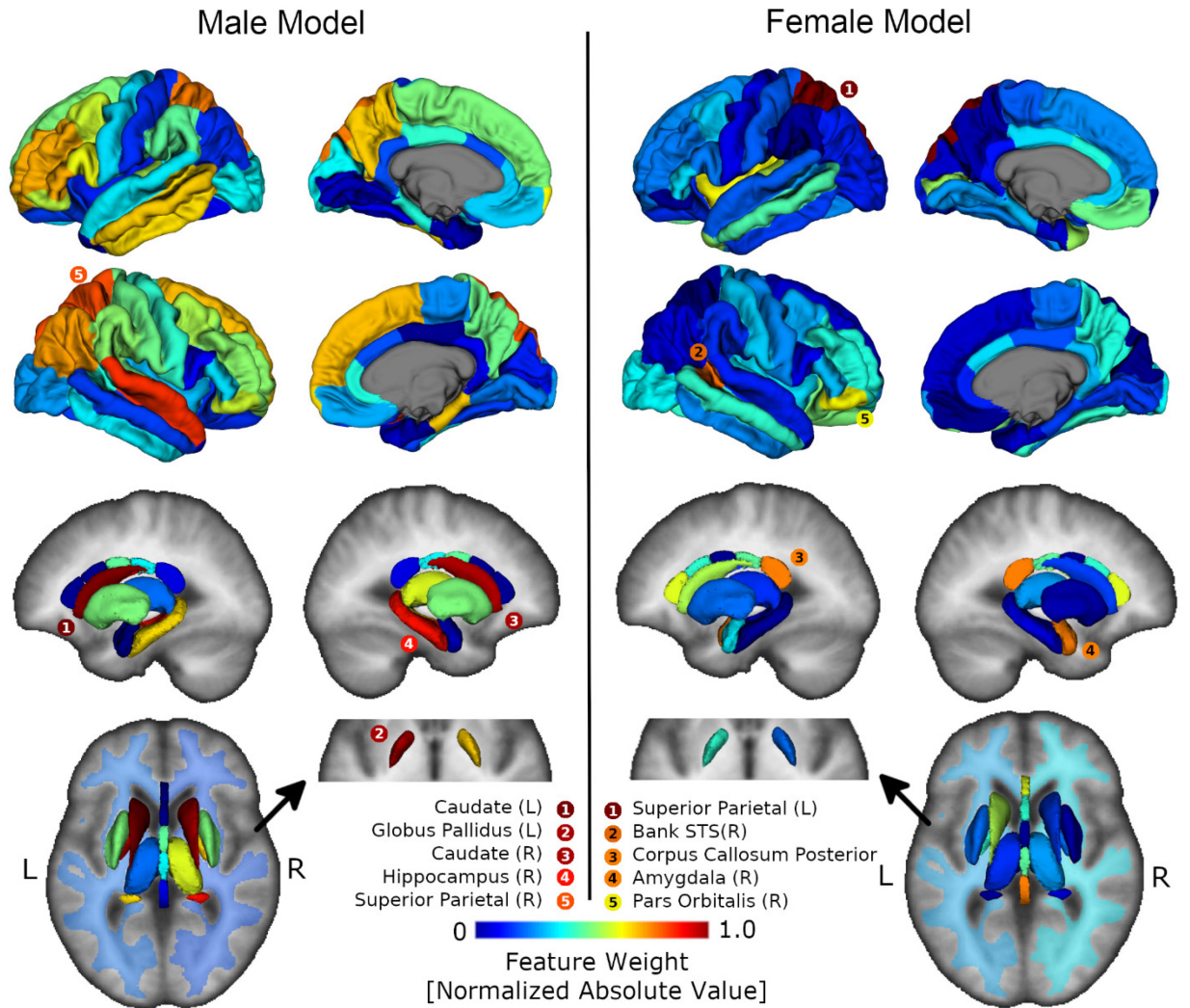


**Figure 4.5.** Visualization of prediction models generated on the training data for males (32 Controls, 35 FASD) and females (49 Controls, 44 FASD) separately. All regions are displayed as 3D renderings, with the exception of left/right white matter segmentations displayed as a transparent overlay on an axial image. All regions of the brain are color coded by support vector classifier weightings (feature importance). The 5 most heavily weighted regions in each model are listed in order with corresponding colors. Four of the 5 most heavily weighted regions in the male model are subcortical structures whereas 4 of the 5 most heavily weighted regions in the female model are cortical or corpus callosum regions.

## 4.4 Discussion

### 4.4.1 FASD Classification

This study reports a multivariate classification model based on brain volume that showed moderate accuracy (77% in test cohort) in identifying individuals with FASD from control participants. Notably, this classification accuracy is comparable to that reported in neuroimaging classification studies of other neurodevelopmental disorders such as ADHD (81% accuracy using resting state functional MRI measurements, Fair et al., 2013) and Autism (70% accuracy using brain volume and resting state functional MRI measurements, Zhou et al., 2014). To our knowledge, only one other study that primarily focused on eye tracking/psychometric data has attempted classification of FASD participants from controls using imaging data. In that study, an accuracy of 67% was achieved using features extracted from diffusion MRI of the corpus callosum on a relatively small sample (training: 19 controls, 11 FASD, testing: 22 controls, 24 FASD) of children/adolescents that partly overlapped the training cohort from the current study (also from NeuroDevNet) (Zhang et al., 2019). Notably, the accuracy using diffusion MRI features extracted from the corpus callosum was lower than the accuracy reported from the current study using brain volumes (77%), however the same study reported highest accuracies using features derived from other physiological/behavioral measurements (e.g. eye tracking data 76% and psychometric data 78%).

Other studies have classified FASD participants based on other modalities such as epigenetic DNA methylation features where a predictive model trained on an overlapping cohort from the training dataset in the current study achieved 83% accuracy in predicting FASD (Lussier et al., 2018). Additionally, features extracted from 3D facial laser scans achieved ~80%-90% accuracy identifying individuals with FAS (Fang et al., 2008), a subtype of FASD that exhibits sentinel facial features, the same subtype of FASD that had a high classification accuracy with multivariate brain volumes in the current study (11/14 FASD participants with sentinel facial features correctly classified in the test cohort). In a three way classification task of FASD, ADHD and control participants, a 77% classification accuracy was achieved using features extracted from eye tracking data collected while participants attended to videos (Tseng et al., 2013).

Taken together, these studies suggest that there may be value in combining multiple types of diagnostic and clinical features in future classification models to improve accuracy, including other modalities of MR imaging such as diffusion MRI and resting state functional MRI which were not part of this current analysis on brain volumes. Multimodal classification of FASD has been performed using features derived from psychometric and eye tracking data achieving 83% accuracy (Zhang et al., 2019), but showed no additional accuracy when including diffusion MRI; however the sample size was limited in that study (22 controls, 24 FASD).

Changes in total brain volume as well as unique regional trajectories of subcortical and cortical grey matter development during childhood / adolescence (Giedd et al., 1999; Narvacan et al., 2017) may impact classifier performance. In a supplementary analysis of classification performance (see Appendix A), no difference in age was observed between incorrectly/correctly classified controls or between incorrectly/correctly classified individuals with FASD in the test cohort, suggesting that classification performance was not confounded by age.

#### **4.4.2 Relating Multivariate and Univariate Analysis of FASD Regional Brain Volumes**

In this study, the multivariate FASD classification model outperformed all univariate models that were based on separate brain region volumes by ~5% in both the test and training cohorts. This result suggests that there is a pattern of volume change involving multiple brain structures that is more discriminative of children/adolescents with FASD relative to any one brain region independently. Of the univariate models with above chance accuracy, regions are consistent with previous studies reporting volume loss associated with FASD (Donald et al., 2015). Above chance univariate models consisted of 8 subcortical grey matter structures (left/right caudate, left/right thalamus, right putamen, right hippocampus, right amygdala, left globus pallidus), both left/right white matter volumes, and 3 cortical grey matter regions (right inferior parietal, left rostral middle frontal gyrus, left bank of the superior temporal sulcus). On the other hand, multivariate model weights indicated fewer subcortical regions as

heavily contributing to prediction (left/right caudate and left globus pallidus in the top ten), whereas cortical regions in the temporal lobe (left inferior temporal, bank of the right superior temporal sulcus, right superior temporal sulcus) and other subdivisions of the cortex (right posterior cingulate, right isthmus cingulate, right/ left pars triangularis) were more prominent. Taken together, univariate and multivariate results suggest that the increased accuracy of the multivariate model (relative to univariate models) may be a result of the inclusion of cortical regions.

In the current study a model trained using only the left caudate had a test accuracy only 5% lower than the model generated from all brain regions together. Notably, the caudate was one of the first reported brain structures with differences associated with prenatal alcohol exposure (Mattson et al., 1996). Since then, the caudate has been reported in animal models to be one of the more vulnerable regions to ethanol induced apoptosis (Young and Olney, 2006) which may underlie the observed volume reductions associated with prenatal exposure to alcohol in children and adolescents (Astley et al., 2009a; Cortese et al., 2006; Riihonen et al., 2005). Additionally, caudate volume has also been associated with deficits in both cognitive control and verbal learning/recall in children/adolescents with FASD (Fryer et al., 2012). In the current study, the classification model based solely on left caudate volume outperformed (72% test accuracy) the models based on other basal ganglia structures (e.g. left globus pallidus (64% accuracy), left putamen (63% accuracy), right putamen (67% accuracy), right caudate (67%)). The caudate takes input from the frontal eye fields and the frontal/parietal lobes, and has efferent pathways to the prefrontal cortex. Other basal ganglia structures such as the putamen and globus pallidus are implicated in neural pathways related to motor function. Hence, a larger effect of prenatal alcohol exposure on the caudate relative to other basal ganglia structures may reflect larger deficits in FASD to higher-order cognitive functions (e.g. executive function, problem solving) compared to motor functions. Additionally, a more recent study has demonstrated that shape-based features of caudate asymmetry can be combined with facial morphology features to better discriminate controls from those with FAS (Suttie et al., 2018). Taken together these findings suggest that the caudate is one of the most heavily impacted brain structures post prenatal alcohol exposure. In this study, a left caudate volume decision boundary of  $\sim 3.6 \text{ cm}^3$  (larger size indicating control) was generated from the training data

and performed adequately (accuracy 72%; sensitivity 70%; specificity 74%) on the test data. Notably, a large proportion of FASD participants (17/67) had left caudate volumes lower than all but one control at a threshold of  $3.1 \text{ cm}^3$  and suggests that a volume threshold could be used as a highly specific indicator of FASD. Similarly, distance from the decision boundary of the multivariate model is highly specific at values lower than -0.38 with 20/67 FASD participants and no controls having values below this threshold. Interestingly, at these lower values both left caudate volume and distance from the multivariate decision boundary were not sensitive to a particular sex or FASD diagnostic subtype, suggesting that both these measures may provide added value for further subdividing the FASD diagnosis based on brain structure alone. Importantly, the FASD model performed more accurately in the subtype of FASD with sentinel facial features relative to the other participants that did not display these features, suggesting a pattern of FASD brain volume change that is also likely to be associated with other structural changes in an individual. This finding is consistent with other univariate studies showing that facial dysmorphic features are related to more severe volumetric reductions in FASD (Astley et al., 2009a; Roussotte et al., 2012), and may reflect the timing of ethanol exposure between three to four weeks post gestation in humans when the brain and face are early in their development (Godin et al., 2011, 2010). Notably, more extensive volumetric reductions in the dysmorphic FASD participants could also be related to a higher level of prenatal ethanol exposure (although this was unavailable in our study) complicating the face-brain interpretation.

Along with ADHD, the participants in this study had a wide range of comorbid diagnoses (e.g. ADHD, Oppositional Defiant Disorder, etc). Importantly, to be of clear clinical use a classification model would be able to discriminate individuals with FASD from those with other neurodevelopmental disorders. Results from this study demonstrate that individuals with FASD can be discriminated from controls using regional brain volumes. However, it is unknown whether regional brain volumes or the same classification model could be used to discriminate individuals with FASD from those with other neurodevelopmental disorders.

The investigation of model weights can also aid in identifying regions that may be affected in FASD but that are not detected by univariate analysis alone. In this study, both the left and right pars triangularis of the frontal lobe

heavily contributed to the model. Notably, the volume of the bilateral pars triangularis has been associated with reading disorders such as dyslexia (Eckert et al., 2003) and deficits in language have been repeatedly observed in complex language tasks in participants with FASD (Becker et al., 1990; Mattson et al., 1998). Although the frontal lobe has shown volume loss in children/adolescents prenatally exposed to alcohol, to our knowledge pars triangularis volume has not been associated with FASD. Given that the pars triangularis regions were absent from the univariate models that performed higher than chance, this result implies that in the context of other FASD related regional volume change a multivariate model can extract additional information about structural change that is undetectable by univariate analysis alone.

#### **4.4.3 FASD Classification with Sex Specific Models**

To date, the most common approach for dealing with sex related variation in large classification studies of neurodevelopmental disorders is to perform classification on volumes adjusted for sex resulting from a multivariable linear regression with sex added as a covariate (Some examples being Fair et al. 2013; Zhou, Yu, and Duong 2014). However, in neurodevelopmental disorders such as FASD where reductions in regional brain volumes appear to be larger for males relative to females (Chen et al., 2012; Dudek et al., 2014; Treit et al., 2017) assuming the same effect of sex on volume between controls and FASD will have the effect of reducing but not eliminating between sex bias in sensitivity/specificity. Results from the current study demonstrate experimentally that when sex is not accounted for in FASD classification, sensitivity/specificity can differ greatly for males (sensitivity 53%, specificity 98%) compared to females (sensitivity 79%, specificity 75%) but this disparity can be reduced at the expense of accuracy by using sex adjusted volumes (male accuracy 72%, sensitivity 58%, specificity 86%; female accuracy 74%, sensitivity 72%, specificity 75%). Furthermore, this study proposes building FASD classification models separately for males and females which further reduced the imbalance in sensitivity/specificity, albeit at a larger decrease in accuracy (male accuracy 70%, sensitivity 68%, and specificity 71%; female accuracy 67%, sensitivity 62%, and specificity 72%). The observed decrease in accuracy of separate male/female models may be a result of the limited sample size for males/females in the training data and would likely be improved with the inclusion of more participants. An advantage of this technique is the ability to

investigate heavily contributing regions that are useful for prediction of FASD in males and females separately. Notably, subcortical regions heavily contributed to male FASD prediction (left/right caudate, left globus pallidus, right hippocampus) whereas cortical regions primarily contributed to female FASD prediction (left superior parietal cortex, right bank of the superior temporal gyrus, right pars triangularis), suggesting that patterns of volume change differ between males and females. The higher subcortical weightings in the male classification model likely reflects the greater relative volume reductions of subcortical grey matter regions in males compared to females with FASD (Dudek et al., 2014; Treit et al., 2017). Several neurophysiological/neurochemical effects of PAE are reported to be greater in males relative to females, including reductions in long term potentiation (Sickmann et al., 2014), increases in dopamine D1R binding (Converse et al., 2014), and reduced sensitivity to testosterone (Lan et al., 2009). More heavily weighted cortical regions in the female model is surprising, given that previous studies have reported no significant differences in the volume of cortical regions in females with FASD (Chen et al., 2012) and less pronounced effects of PAE on measures of cortical thickness relative to subcortical volume (Treit et al., 2017). It seems here that a pattern (i.e. multi-variate) of cortical volume reduction may more accurately discriminate females with FASD from controls compared to PAE related volume change within individual (i.e. univariate) cortical regions. Overall, results from this study suggest that there is value in modeling FASD related regional brain volume change separately for males and females. Notably, the classification differences reported here between males/females could be confounded by sex by group imbalances in demographics. However, no such group by sex interaction effects were observed in the test cohort for any of the demographic variables listed in Table 4.2 (data not shown), suggesting that demographic imbalances are not driving the observed classification differences between males and females. In the training cohort a small difference in age was observed between male control (age  $11.3 \pm 3.5$  years) and male FASD (age  $13.3 \pm 2.7$  years) participants, potentially impacting the weightings of the male FASD classification model. However, this male classification model heavily weighs subcortical regions whose volumes have been shown to change minimally over childhood/adolescence in both longitudinal and cross-sectional samples (Narvacan et al., 2017), suggesting that age differences are not influencing the model weightings presented in this study.

#### 4.4.4 Study Limitations and Future Directions

There are several limitations in this study, primarily related to the imbalanced distribution in demographics/comorbidities in the training/testing FASD groups relative to controls. The samples in this study consisted of control groups primarily of Caucasian descent, whereas about half the FASD participants self-identified as indigenous potentially confounding classification results. However, in a follow-up analysis, sensitivity to FASD classification differed minimally between the ethnic categories in the testing cohort (indigenous: 63%; Caucasian 67%; other 60%; unknown 64%) suggesting that ethnicity was not influencing classification performance. ADHD is a common comorbid diagnosis within FASD populations having an estimated prevalence of >70% (Burd et al., 2003) and was highly prevalent in the training/testing cohorts included in the current study (training FASD: 50%; testing FASD: 49%). Additionally, in this study a large proportion of FASD participants were on medication regimens that were highly discordant between individuals, and those participants were not asked to refrain from taking medication throughout the study. Such confounds in comorbid diagnosis and medications may impact reported cognitive scores and classification results in the FASD group. Again, a secondary analysis was conducted and showed minor differences between classification sensitivity between an ADHD-comorbid diagnosis (67% sensitivity) /no-ADHD diagnosis (62% sensitivity), as well as classification of FASD participants on different medications (stimulants 58%, atypical antipsychotics 59%, antidepressants 60%, and other medication 67%). This equally distributed sensitivity among demographic categories suggests that even though the FASD classification model was generated from imbalanced control/FASD training data, the model itself represents a discriminative pattern of brain volume difference that is associated with prenatal alcohol exposure and does not reflect differences based on ethnicity, comorbid diagnosis or medication regimen.

The training and testing FASD cohorts of the current study contained both individuals with a formal FASD diagnosis as well as those with confirmed alcohol exposure but non-diagnosed. Importantly, the classification results from the test cohort showed similar sensitivity between the FASD participants without sentinel facial features (test sensitivity 60%), and those in the PAE (non-diagnosed) group (test sensitivity 61%), suggesting that regional brain volumes were similarly affected in the diagnosed and undiagnosed individuals. In a secondary analysis excluding the PAE group (data not shown), decreased accuracy and sensitivity was observed in the test

cohort (accuracy 74%, sensitivity 53%, specificity 88%) relative to when PAE (non-diagnosed) were included (accuracy 77%, sensitivity 64%, and specificity 88%) warranting the inclusion of the PAE group in the analysis.

#### **4.4.5 Conclusions**

In this study a multivariate classification model was generated for discriminating children/adolescent controls from those with FASD. The model performed better than univariate analysis in discriminating FASD from controls and had predictive contributions from regions with known volumetric reduction in FASD. Additionally, a large proportion of FASD participants in the test data had little to no overlap with controls at negative distance from boundary values, and low left caudate volume values, suggesting that these measures should be investigated as a potential indicator of FASD. Classification accuracy of models generated separately for males and females had lower accuracy than the model containing all participants, but notably these models were more balanced in sensitivity and specificity suggesting that sex should be taken into account in brain volume based classification of FASD. Overall, this study shows the value in multivariate analysis of brain volume for the classification of FASD and identification of brain regions affected in children and adolescents prenatally exposed to alcohol.

## Appendix A

While Chapter 4 was in review, questions were raised about how the presented classification results are impacted by the age of individuals. Changes in total brain volume as well as unique regional trajectories of subcortical and cortical grey matter development during childhood / adolescence have been reported in a multitude of studies (Giedd et al., 1999; Narvacan et al., 2017). However, variability in developmental trajectories between brain regions as well as demonstration of continuous development across these ages suggest that dividing a sample into separate childhood vs early adolescent groups would be arbitrary. It is nonetheless important to determine whether the performance of the FASD/Control classification model differs by age of the subjects in either group.

In Chapter 4 we originally assessed age-related classification bias using a linear regression testing for an effect of age on the model distance from decision boundary (a measure of how closely a subject matched the FASD prediction model). In this analysis no age-related effect was observed supporting the notion that the model is unaffected by age. To increase confidence in this finding, we conducted a secondary analysis in response to reviewer feedback separating the testing cohort into groups of correctly/incorrectly classified controls (65 correct, 9 incorrect) and FASD (43 correct, 24 incorrect). Control and FASD groups separated by classification performance are plotted by age in Figure A1. Notably, correctly classified control as well as correctly classified FASD participants were equally distributed across the entire age range in the study, and no significant difference in age between correct and incorrectly classified subjects was found in either group, suggesting that correct classification does not differ by age from childhood to adulthood.

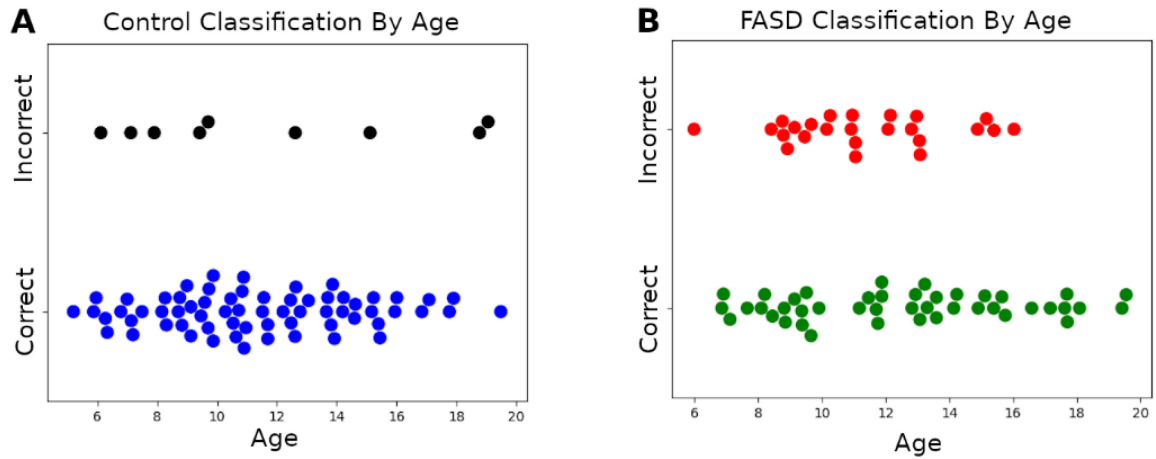


**Figure A1.** FASD classification model performance in the test cohort separately for A) Control (correctly classified age  $11.4 \pm 3.3$  years, incorrectly classified age  $11.8 \pm 4.6$  years) and B) FASD (correctly classified age  $12.5 \pm 3.6$  years, incorrectly classified age  $11.3 \pm 2.5$  years) groups. Notably, correctly classified Control and FASD participants were well distributed across the entire age range. Additional analysis did not detect a difference in age between incorrectly/correctly classified Control (t-test,  $p = 0.76$ ) or FASD (t-test,  $p = 0.14$ ) participants. These results suggest that the FASD classification model is not biased towards any particular age range.

## 5 Inter-site Reproducibility of Functional Connectivity Relative to Intra-site Repeatability

### Abstract

Multi-site resting state functional MRI (rsfMRI) studies are commonly used to enable larger sample sizes over diverse populations. Few multisite rsfMRI reproducibility studies have been conducted that have included participants repeatedly scanned at multiple sites to address between-site reproducibility and within-site repeatability in the same cohort. This study aimed to i) investigate the multi-site reproducibility and within-site repeatability of rsfMRI functional connectivity data acquired on the same individuals scanned two times at multiple sites, and ii) evaluate the effectiveness of correcting for between-site variation using the commonly applied technique of including site as a covariate in statistical analysis. Participants included 8 individuals scanned twice at four sites as part of the NeuroDevNet imaging study. Seven core functional networks with 30 regions of interest (ROIs) were examined using ROI-to-ROI analyses. Intraclass correlations for individual connections demonstrated poor between site reproducibility (ICC ~0.2) and higher but poor repeatability (ICC ~0.4) however, this was in line with previous intra-site and inter-site reproducibility studies that used comparable methods. Site-correction of functional connectivity values resulted in increased reproducibility measures of (increase of ICC > 0.05) in 49/435 whereas the majority of connections (380/435) had minimal changes in reliability (ICC change between -0.05 to 0.05) and only 6 functional connections had changes in reproducibility < -0.05. Data presented in this reproducibility study help aid in the analysis and interpretation of results when using the rsfMRI data from the NeuroDevNet cohort and supports the use of multisite correction using a linear mean shift (i.e. using site as a covariate) in multisite functional connectivity studies. Notably, the method for correcting between site variability developed here was applied to the cross-sectional FASD analysis in Chapter 6.

## 5.1 Introduction

Resting state functional magnetic resonance imaging (rsfMRI) enables the study of the intrinsic functional connectivity between regions while a subject is at rest. Given the absence of a cognitive task during acquisition, rsfMRI analysis has become a popular method for assessing alterations in functional connectivity associated with typical or atypical neural development (Hull et al., 2017; Konrad and Eickhoff, 2010) as well as various neuropsychiatric disorders (Greicius, 2008). The widespread use of rsfMRI has led to studies of its test-retest reliability (repeatability) to quantify the stability of functional connectivity measures acquired from multiple scans under the same experimental conditions (i.e. repeatability). Repeatability studies have aimed to quantify the test-retest consistency of functional connectivity measures and have generally reported poor agreement between scans (see (Noble et al., 2019) for review). While rsfMRI functional connectivity studies are typically conducted at a single site with the same MRI hardware and protocol, multi-site studies are commonly employed to enable larger sample sizes over diverse populations; some examples include healthy (n=1414 over 35 sites, 3T/1.5T (Biswal et al., 2010)) and ADHD (n=776 over 8 sites, 3T/1.5T (Fair et al., 2012)). In these studies, site differences in connectivity values do exist, but investigations of between-site variability are precluded due to different populations (and protocols) per site. Early work on the multisite reproducibility of task-based fMRI has proposed using participants repeatedly scanned at multiple sites to address multi-site reproducibility for the task-related BOLD signal (Forsyth et al., 2014; Friedman et al., 2008; Zou et al., 2005). More recently, multisite reproducibility has been assessed for rsfMRI connectivity measurements using the same approach.

In a study of ten subjects scanned repeatedly on two same-vendor 3T MRI functional connectivity values extracted using an independent component analysis revealed highly reliable (Intra Class Correlation (ICC) > ~0.9) connectivity values in regions of intra-network connectivity (Jann et al., 2015). Other work analyzed rsfMRI images with an ROI-to-ROI (connectivity matrix) approach from eight participants scanned repeatedly on eight different 3T MRI scanners with different vendors (5 Siemens, 3 GE) reporting poor reproducibility (ICC = 0.07 - 0.17) with a 5 minute acquisition and higher but still poor reproducibility (ICC = 0.21 - 0.36) using a longer 25 minute acquisition. Importantly, this study observed no effect of site or vendor on measures of functional connectivity suggesting that low reproducibility is a result of test-retest repeatability of the functional connectivity measurements. More recent

work has analyzed multisite reproducibility of multivariate measures of functional connectivity in a single subject scanned on 3T MRI systems from 13 different sites across 3 vendors. In this study, both site and vendor related effects were reported in connectivity measures as well as a difference in the ability to detect (“fingerprinting”) this subject among others scanned at the 13 sites (Badhwar et al., 2020). Given the limited study of between-site reproducibility of rsfMRI functional connectivity measures, further work is needed to address the inconsistencies of previously reported measures of multisite reproducibility.

To date, the most common approach to reducing between-site variance in multisite functional connectivity studies is to use site as a covariate in a multiple linear regression. More recent work has proposed more complex corrections for between site variability based on statistical harmonization techniques (Yamashita et al., 2019; Yu et al., 2018), as well as a method based on principle component analysis (Bari et al., 2019). Although these techniques show promising gains in harmonizing functional connectivity across sites the studies did not address modelling site as a covariate in linear regression. Thus, more work is needed to assess the utility of correcting for between-site effects by using site as a covariate in a linear regression or in other words applying a mean shift in connectivity values specific to each site and connection.

This study has two aims: 1) to investigate multi-site reproducibility of ROI-to-ROI functional connectivity by examining the same healthy participants scanned at four imaging sites (2 x 3T Siemens, 1.5T Siemens, 3T Philips) across Canada, as part of the NeuroDevNet study on childhood development (Reynolds et al., 2011b); 2) to evaluate the utility of using site-corrections that are based on the average connectivity values calculated for each site.

## **5.2 Materials and Methods**

### **5.2.1 Participants / Image Acquisition**

This study was approved by the Human Research Ethics Boards at Queens’s University, University of Alberta, Children’s Hospital of Eastern Ontario, University of Manitoba and the University of British Columbia. Written

informed consent was obtained from each individual before study participation. For assessing between site reproducibility of functional connectivity measures, eight healthy young adults (age  $28 \pm 6$  years, 2 males/6 females) underwent two sequential imaging sessions at each of the four sites (mean 102 days from first to last scan). Structural and functional images were collected for each participant at four MR imaging centres: University of Alberta (1.5T Siemens Sonata, one channel receive coil), Queen's University (3T Siemens Trio, 32 channel receive coil), University of Manitoba (3T Siemens Trio, 32 channel receive coil), and University of British Columbia (3T Philips Intera, 32 channel receive coil). Each session had a total acquisition time of approximately 25 min including anatomical T1-weighted, T2-weighted, fluid-attenuated inversion recovery (FLAIR), and DTI imaging. For this study resting-state functional imaging was acquired using an echo planar imaging gradient-echo sequence with: 3 mm isotropic voxels, 40 axial slices, FOV =  $192 \times 192 \text{ mm}^2$ , TR = 2.5 s, TE = 30 ms (3T scanners)/ 40 ms (1.5T scanner), phase encode direction anterior-posterior (Siemens Scanners) / posterior-anterior (Philips scanner), flip angle = 90 deg, 140 time points, 6 min total acquisition. Additionally, T1-weighted images used for anatomical registration were acquired with a high-resolution ( $1 \times 1 \times 1 \text{ mm}^3$ ) magnetization prepared rapid acquisition gradient echo (MPRAGE) sequence with: 160 axial slices, FOV =  $256 \times 256 \text{ mm}^2$ , inversion time (TI) = 1100 ms, flip angle = 15 deg, TR ~ 2100 ms, TE ~ 3.5 ms, and acquisition time ~ 5:30 min.

## 5.2.2 Pre-Processing

All study participants and scans were processed separately and analyzed using the same standard pipeline from the Functional Connectivity Toolbox (version 17.a <https://www.nitrc.org/projects/conn>). Functional volumes were realigned, unwarped, and co-registered to the anatomical images using the statistical parametric mapping toolbox (SPM 12b). The artifact detection toolbox was employed for scrubbing and removing time points with corrupted data greater than 0.5 mm in movement or with changes in mean signal intensity greater than 2 standard deviations (conservative settings 95<sup>th</sup> percentile). Masks of white matter and cerebrospinal fluid were generated using SPM segmentations of anatomy. Principal component analysis was performed on voxel by time series matrices from each mask. For the purpose of removing unwanted signal from the fMRI time course per voxel, the first five components from the white matter and cerebrospinal fluid masks were used as nuisance regressors in a

multiple linear regression. Anatomical images were then spatially normalized to the MNI306 template, and the calculated transformation was used to spatially normalize the preprocessed functional volumes to the MNI306 template (SPM 12b). Spatially normalized functional volumes were then smoothed with an 8mm (~3 times voxel size) full width half max gaussian kernel (SPM12b) as has been suggested to increase sensitivity in group inference experiments (Mikl et al., 2008).

### **5.2.3 Functional Connectivity ROI Based Analysis**

Regions of interest (ROIs) were taken from the network specific mask included in the functional connectivity toolbox version 17.a (Whitfield-Gabrieli and Nieto-Castanon, 2012). These ROIs were generated from an independent component analysis of 497 healthy individuals from the Human Connectome Project. Included in this toolbox are labels that specify the functional network (e.g. DMN, Dorsal Attention) for each ROI. In this study regions of interest from 7 a priori defined networks were used: default mode network (4 ROIs), dorsal attention network (4 ROIs), language network (4 ROIs), frontal-parietal network (4 ROIs), salience network (7 ROIs), sensorimotor network (3 ROIs) and visual network (4 ROIs). ROIs from the cerebellum were excluded in the analysis because a large proportion of the participants had missing coverage. Correlations between ROI time courses (averaged across voxels within each ROI) were calculated between all 30 ROIs for each subject and scan, resulting in a connectivity matrix per subject for each scan. Correlations from each connectivity matrix were then Fisher z-transformed.

### **5.2.4 Repeatability and Reproducibility Analysis of Functional Connectivity**

A qualitative analysis was performed to assess regional variability of signal amplitude and temporal signal to noise ratio (SNR) in native imaging space. Both mean signal intensity (average across time) and temporal SNR (mean amplitude divided by standard deviation over time) maps were calculated for each subject and scan. Both maps were inspected for general patterns of regional differences between sites for individual subjects. A quantitative analysis of reproducibility was performed on ROI-to-ROI connectivity matrices for all pairwise connections from the

30 ROIs used in this study. For each connection (z-scored correlation) measurements of repeatability (test-retest within site) and reproducibility (inter-site reliability) were calculated (MATLAB) using intraclass correlation (ICC) a measure that assesses the fraction of total variance caused by between-subject rather than within-subject measurement error. Within-site repeatability (two-raters) was calculated per site using the ICC(A, 1) two-way random, single-score model (Mcgraw and Wong, 1996). Inter-site reproducibility was calculated using only the first scan from each subject with the ICC(A,1) two-way mixed, single-score model (Mcgraw and Wong, 1996) and was calculated across all 4 Sites (4 raters). ICC values range from 0 (no agreement between repeated measurements) to 1 (absolute agreement between repeated measurements) with values interpreted as poor (ICC < 0.5), fair (ICC 0.5 to 0.75), good (ICC 0.75 to 0.9), excellent (ICC > 0.9) (Koo and Li, 2016). As a summary measure of between-site reproducibility and repeatability for each ROI used in the study, ICC values were averaged for all connections for each of the 30 ROIs.

### **5.2.5 Evaluation of Proposed Site Correction Technique**

Typically, multisite studies use site as a covariate in a multiple linear regression to model the between site variance between scanners / sites. To test whether linearly modelling site is an appropriate procedure we calculated a site correction factor and applied these corrections in a leave one out framework as to not overfit the dataset used in the current study. Firstly, between site correction factors (linear mean shift) were calculated for each site in the following way for each connectivity matrix. First, a site correction matrix ( $\Delta$ ) was calculated for each site by subtracting the site mean correlation matrix (average of a site's connectivity matrices) from the total mean correlation matrix across all traveling subjects and sites (average all connectivity matrices). The inverse of this  $\Delta$  matrix was then applied to each individual's correlation matrix within each site/scan. This approach would be analogous to covarying by site in a linear regression. Notably, this correction technique would ultimately reduce between-site variability if applied to all subjects in the test-retest cohort and would amount to an overfitting of the dataset and not accurately reflect the generalizability of this technique to unseen data. Hence, to appropriately test the technique we applied the correction in a leave-one-out framework where site corrections are calculated

from 7 subjects (56 functional images) and applied to the left-out subject (8 functional images). This process is repeated for all 8 subjects resulting in a site corrected connectivity matrix for each scan / subject. ICCs were calculated as previously done across all 4 scanners for each corrected ROI-to-ROI z-scored correlation and compared to the initial ICC values attained prior to between-site correction. As performed in the initial reproducibility analysis ICC values were averaged across all connections for each of the 30 ROIs and compared to ROI summary measures prior to application of the proposed site correction technique.

## 5.3 Results

### 5.3.1 Temporal Signal to Noise Ratio and Qualitative Reproducibility Analysis

Mean rsfMRI signal intensity (average over time) maps as well as tSNR images were extracted for each scan and subject and are displayed for a single subject at all four sites in Figure 5.1. Mean intensity maps displayed a similar grey to white matter contrast and anatomical detail across site however, variability in the spatial distortions between sites were observed in anterior regions of the brain that are prone to magnetic susceptibility. Temporal SNR values varied substantially between sites with markedly lower tSNR observed for images acquired with the 1.5T Siemens Sonata system relative to the three other higher field strength systems. Of the 3.0T systems the Philips Intera had higher tSNR values compared to two Siemens Trio scanners that had much more comparable tSNR values. In addition, the tSNR values on the 1.5T Siemens Sonata system were homogeneous across the brain whereas tSNR values at the 3 other higher field systems varied regionally. These observations were consistent for all subjects and scans in the study.

Functional connectivity (Fisher z-score) matrices were extracted for each subject / scan using 30 ROIs from 7 different functional networks. Example connectivity matrices are displayed for a single subject for all scans and sites in Figure 5.2. The expected pattern of intra/inter-network functional connectivity (strong intra network connectivity, weaker inter network connectivity) was observed in the majority of scans within the study regardless of site; however, connectivity matrices extracted from the images acquired on the 1.5T Siemens Sonata displayed a more distributed pattern of connectivity with smaller differences between inter-network and intra-network

connectivity values. This discrepancy could be explained by the lower tSNR observed in the 1.5T Siemens Sonata images.

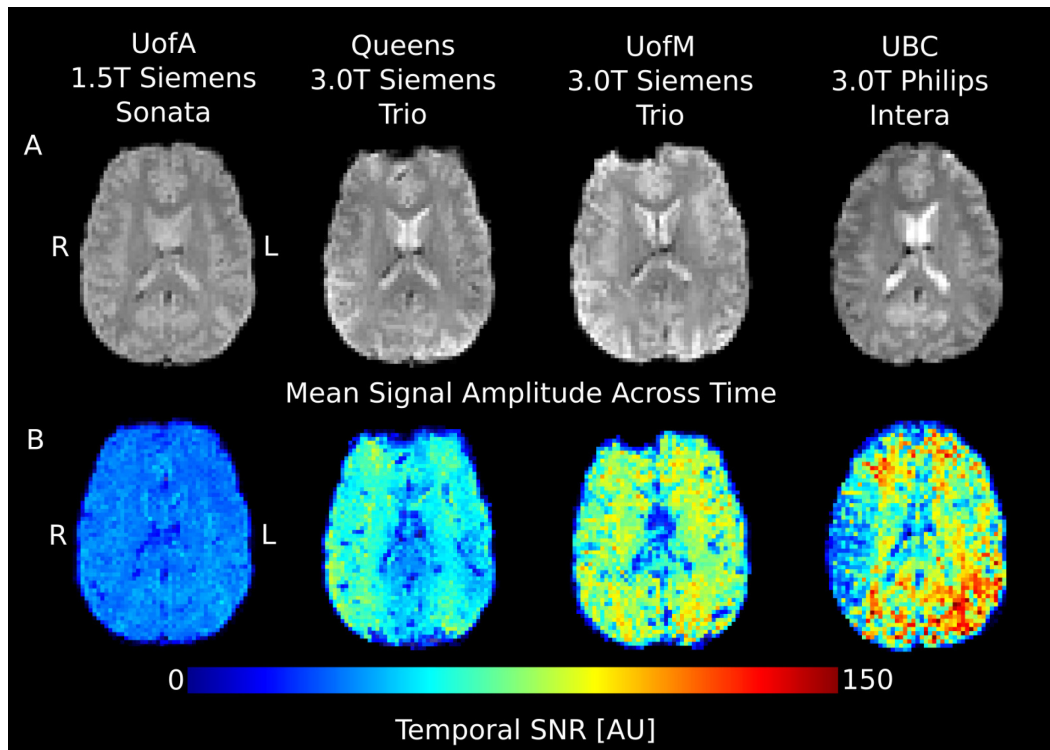


**Figure 5.1.** Single slice from (A) mean resting state functional MR images over time (after pre-processing but before smoothing and MNI registration) and (B) temporal signal to noise ratio (tSNR, mean signal divided by standard deviation over time) images acquired from a single subject at the four different sites from the NeuroDevNet imaging study. Large differences in tSNR were observed between sites with markedly lower tSNR observed at a lower field strength (1.5T Siemens Sonata) whereas greater tSNR was observed on the 3.0T Philips Intera. Regional differences in tSNR were not observed on the 1.5T Siemens Sonata suggesting that field strength rather than the single channel coil setup was driving the tSNR differences between sites.

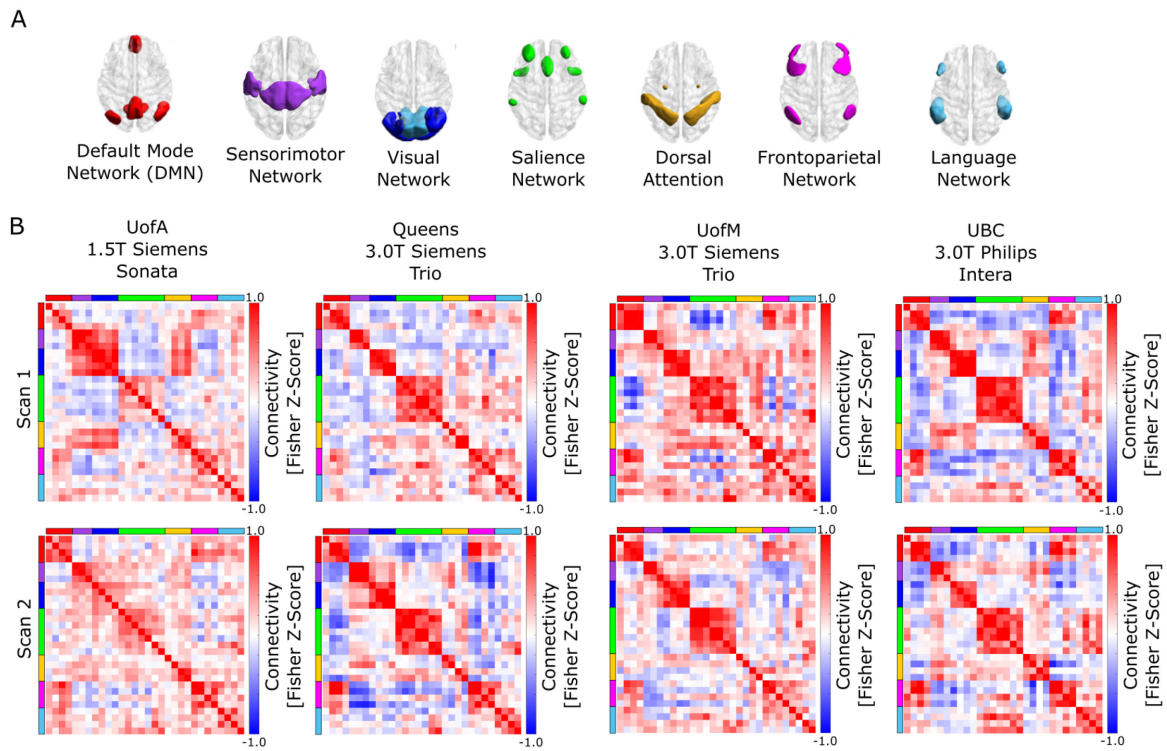


**Figure 5.2.** Functional network specific ROIs used in the current study (A) as well as functional connectivity matrices with rows and columns color coded by network association (B) extracted from the same subject for each scan at all four sites. Seven of the eight scans demonstrate expected patterns of intra/inter-network connectivity (strong intra network connectivity, weaker inter network connectivity) with scan 2 from the 1.5T Siemens Sonata displaying a more distributed pattern of connectivity. In addition, the contrast between positive intra-network connectivity and weaker inter-network connectivity was less apparent on connectivity matrices acquired on the 1.5T Siemens Sonata.

### 5.3.2 Within-site Repeatability Analysis

Intraclass correlation (ICC) values were calculated for each ROI-to-ROI connectivity value as a measurement of within-site repeatability and are presented in Figure 5.3. ICC values across the ROI-to-ROI matrix ranged from less than 0 (poor repeatability) to ~0.8 (good repeatability) and showed lower reliability at the 1.5T Siemens Sonata site compared to the 3.0T sites (see Figure 5.3b). In general, ICC values for the 3.0T sites were within the same range for all three sites however, the spatial patterns of ICC values over the connectivity matrices were different across the 3.0T sites and showed no strikingly consistent patterns of increased repeatability in areas of intra-network or inter-network connectivity.

Summary measures of within-site repeatability are displayed in Table 5.1 and were calculated as the average ICC across all 29 connections for each ROI for each site. Notably, there was little agreement in the most reliable regions between sites. For example, the 1.5T scanner had highest repeatability values (mean ICC 0.30-0.35) for the left / right posterior superior temporal lobe (ICC  $0.30 \pm 0.38$ , ICC  $0.30 \pm 0.32$  respectively) of the language network, the right supramarginal gyrus (ICC  $0.30 \pm 0.33$ ) and left/right rostral prefrontal gyrus (ICC  $0.35 \pm 0.24$ , ICC  $0.30 \pm 0.32$  respectively) of the salience network and the left lateral parietal cortex (ICC  $0.30 \pm 0.31$ ) of the default mode network. Whereas, the 3.0T Philips Intera site had highest repeatability (mean ICC 0.41 to 0.55) in the left / right inferior frontal gyrus (ICC  $0.50 \pm 0.28$ , ICC  $0.55 \pm 0.20$  respectively) of the language network, the left lateral prefrontal cortex (ICC  $0.42 \pm 0.25$ ) of the frontal parietal network, the left /right lateral sensorimotor network regions (ICC  $0.44 \pm 0.28$ , ICC  $0.41 \pm 0.32$  respectively) and the left lateral parietal cortex (ICC  $0.46 \pm 0.20$ ) of the default mode network.

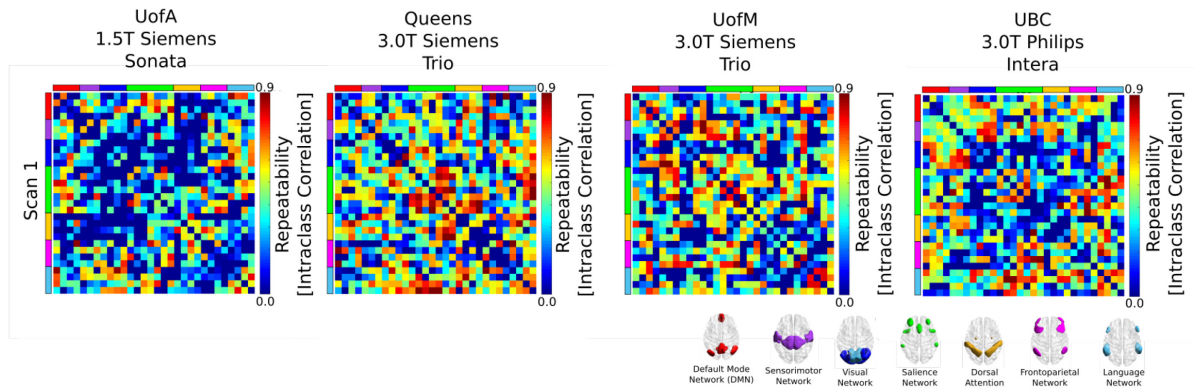


**Figure 5.3** Within-site reproducibility of ROI-to-ROI connectivity matrices calculated as the Intra-class correlation (ICC) for functional connectivity values for each site. Repeatability was markedly higher on the 3.0T systems compared to the 1.5T scanner. In general, among the 3.0T sites the patterns of reliability are more similar between the two Siemens Trio sites relative to 3.0T Philips Intera site.

**Table 5.1.** Within-site repeatability measured as the average intraclass correlation (ICC) across all connections for each ROI for each site.

Network	Region	UofA	Queens	Winn	UBC
		1.5T Siemens	3.0T Siemens Trio	3.0T Siemens Trio	3.0T Philips Intera
Default Mode Network	Medial Prefrontal	0.28 ± 0.33	0.29 ± 0.33	0.32 ± 0.20	0.36 ± 0.26
	Lateral Parietal (L)	0.30 ± 0.31	0.31 ± 0.27	0.25 ± 0.31	0.46 ± 0.20
	Lateral Parietal (R)	0.29 ± 0.30	0.29 ± 0.27	0.46 ± 0.29	0.39 ± 0.27
	Posterior Cingulate	0.18 ± 0.34	0.36 ± 0.32	0.19 ± 0.36	0.24 ± 0.30
Visual	Primary	0.13 ± 0.33	0.37 ± 0.26	0.12 ± 0.38	0.25 ± 0.30
	Ventral	0.09 ± 0.35	0.40 ± 0.35	0.14 ± 0.34	0.23 ± 0.35
	Dorsal (L)	0.20 ± 0.36	0.40 ± 0.26	0.33 ± 0.36	0.32 ± 0.30
	Dorsal (R)	0.14 ± 0.38	0.30 ± 0.33	0.32 ± 0.41	0.25 ± 0.32
Sensorimotor	Lateral (L)	0.22 ± 0.35	0.38 ± 0.24	0.41 ± 0.30	0.44 ± 0.28
	Lateral (R)	0.17 ± 0.31	0.41 ± 0.25	0.38 ± 0.30	0.41 ± 0.32
	Superior	0.21 ± 0.31	0.28 ± 0.29	0.43 ± 0.34	0.35 ± 0.28
Salience	Anterior Cingulate	0.11 ± 0.42	0.41 ± 0.28	0.32 ± 0.38	0.33 ± 0.24
	Anterior Insula (L)	0.08 ± 0.37	0.48 ± 0.25	0.40 ± 0.29	0.34 ± 0.27
	Anterior Insula (R)	0.20 ± 0.32	0.49 ± 0.21	0.44 ± 0.31	0.32 ± 0.33
	Rostral prefrontal (L)	0.35 ± 0.24	0.42 ± 0.34	0.36 ± 0.33	0.35 ± 0.37
	Rostral prefrontal (R)	0.30 ± 0.32	0.48 ± 0.31	0.39 ± 0.36	0.26 ± 0.34
	Supramarginal Gyrus (L)	0.22 ± 0.29	0.45 ± 0.28	0.28 ± 0.38	0.37 ± 0.36
	Supramarginal Gyrus (R)	0.30 ± 0.33	0.43 ± 0.27	0.37 ± 0.28	0.37 ± 0.26
Dorsal	Frontal Eye Field (L)	-0.05 ± 0.33	0.39 ± 0.36	0.28 ± 0.33	0.07 ± 0.38
	Frontal Eye Field (R)	0.14 ± 0.33	0.40 ± 0.29	0.30 ± 0.31	0.27 ± 0.29
	Intraparietal sulcus (L)	0.24 ± 0.29	0.42 ± 0.28	0.23 ± 0.32	0.35 ± 0.28
	Intraparietal sulcus (R)	0.07 ± 0.33	0.39 ± 0.30	0.14 ± 0.37	0.28 ± 0.31
Frontal Parietal	Lateral Prefrontal (L)	0.19 ± 0.42	0.21 ± 0.34	0.25 ± 0.31	0.42 ± 0.25
	Posterior Parietal (L)	0.24 ± 0.32	0.30 ± 0.35	0.27 ± 0.38	0.28 ± 0.31
	Lateral Prefrontal (R)	0.25 ± 0.26	0.27 ± 0.35	0.28 ± 0.27	0.34 ± 0.38
	Posterior Parietal (R)	0.18 ± 0.37	0.31 ± 0.32	0.47 ± 0.34	0.16 ± 0.40
Language	Inferior Frontal Gyrus (L)	0.22 ± 0.41	0.42 ± 0.29	0.25 ± 0.37	0.50 ± 0.28
	Inferior Frontal Gyrus (R)	0.28 ± 0.33	0.36 ± 0.30	0.16 ± 0.39	0.55 ± 0.20
	Posterior Superior Temporal Gyrus (L)	0.30 ± 0.38	0.54 ± 0.20	0.30 ± 0.31	0.32 ± 0.34
	Posterior Superior Temporal Gyrus (R)	0.30 ± 0.32	0.52 ± 0.27	0.45 ± 0.19	0.29 ± 0.26

ROI, region of interest, L left, R right

### 5.3.3 Between-site Reproducibility Analysis and Multisite Correction

Intraclass correlation (ICC) values were calculated for each ROI-to-ROI connectivity value as a measurement of between-site reproducibility and are presented in Figure 5.4. ICC values across the ROI-to-ROI matrix ranged from less than 0 (poor reproducibility) to  $\sim 0.6$  (fair reproducibility) and showed elevated reproducibility in connections between specific networks (see Figure 5.4b). In general, compared to other ROI-to-ROI connections between site-reproducibility was relatively greater ( $\sim 0.3$  to  $\sim 0.6$ ) in inter-network connections between the salience network and other functional networks namely, the default mode network, the sensorimotor network, the frontoparietal network, and the language network. Intra-network connections displayed relatively lower reproducibility relative to inter-network connections except for greater reproducibility in connections within the sensorimotor network (ICC  $\sim 0.40$ ) and the language network (ICC of  $\sim 0.60$ ). Summary measures of reproducibility are displayed in Table 5.2 and were calculated as the average ICC across all 29 connections for each ROI. Of the 7 most reproducible (mean ICC  $> 0.27$ ) regions 3 were from the salience network (right supramarginal gyrus ICC  $0.34 \pm 0.22$ , left supramarginal gyrus ICC  $0.29 \pm 0.13$ , left rostral prefrontal cortex ICC  $0.27 \pm 0.20$ ), 1 was from the language network (right posterior superior temporal gyrus ICC  $0.27 \pm 0.21$ ), 1 was from the frontal parietal network (right lateral prefrontal cortex ICC  $0.27 \pm 0.20$ ), 1 was from the sensorimotor network (superior motor region ICC  $0.29 \pm 0.21$ ) and 1 was from the dorsal attention network (left intraparietal sulcus ICC  $0.28 \pm 0.16$ ). Of the 6 least reliable (ICC  $< 0.17$ ) regions, 2 were from the DMN (medial prefrontal ICC  $0.13 \pm 0.18$ , left lateral parietal cortex ICC  $0.14 \pm 0.19$ ), 2 were from the dorsal attention network (right frontal eye field  $0.17 \pm 0.12$ , left frontal eye field ICC  $0.09 \pm 0.15$ ), 1 from the visual network (primary visual cortex ICC  $0.16 \pm 0.11$ ) and 1 from the frontal parietal network (left posterior parietal cortex ICC  $0.16 \pm 0.15$ ).

A site-correction technique (linear mean shift) was used to reduce between site variability in functional connectivity measures and was applied in a leave-one-out framework so that the site-corrections were not overfit to the dataset. After the application of the site-correction technique, the majority of connections (380/435) showed minimal change in ICC values (change in ICC  $-0.05$  to  $0.05$ ). Of the remaining connections 49/435 showed larger ICC increases  $> 0.05$  whereas only 6/435 connections had decreased in reliability  $< -0.05$  indicating that the site-correction technique reduces between site variance in connections (see Figure 5.3c). In addition, larger

increases in reproducibility (increase of ICC  $\sim 0.2$ ) were observed in specific network connections namely, intra-network salience connections, as well as dorsal attention to default mode network connections, and somatosensory to visual network connections. Notably, ranking of regions based on average reproducibility across connections yielded the same top 6 and bottom 6 regions before and after site-correction (See Table 5.2).

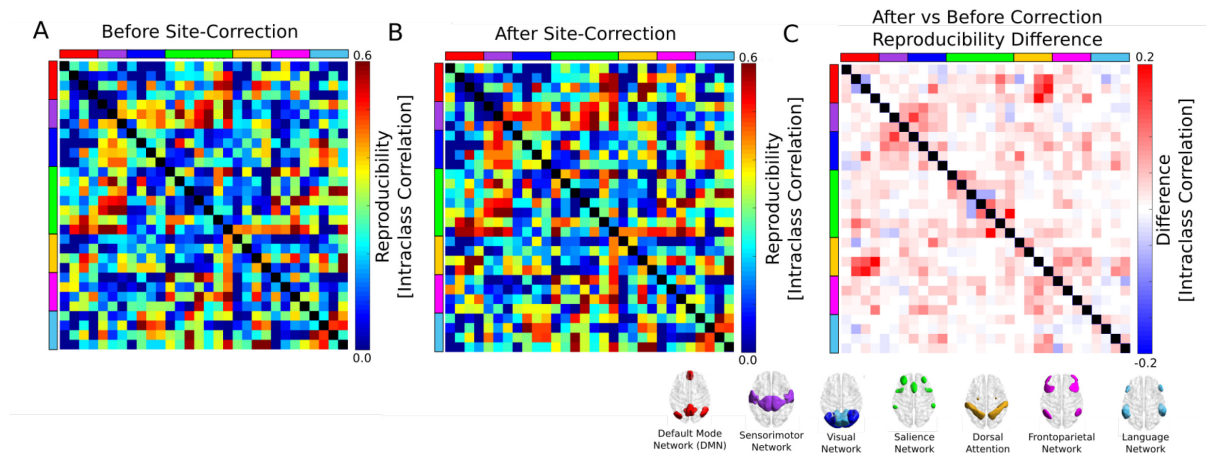


**Figure 5.4.** Between-site reproducibility of ROI-to-ROI connectivity matrices calculated as the Intra-class correlation (ICC) for functional connectivity values before (A) and after the application of site-correction (B). The difference between the two reproducibility matrices (After site-correction minus before site-correction) is displayed (C). Compared to other ROI-to-ROI connections between site-reproducibility was relatively greater ( $\sim 0.3$  to  $\sim 0.6$ ) in inter-network connections between the salience network and other functional networks namely, the default mode network, the sensorimotor network, the frontoparietal network, and the language network. Intra-network connections displayed relatively lower reproducibility relative to other connections except for the sensorimotor network and the language network which showed poor to fair (ICC of  $\sim 0.4$  to  $\sim 0.6$ ) reproducibility. Small gains in between-site reproducibility were observed after the application of the site-correction technique for almost all ROI-to-ROI connections (D, red/pink colored connections) with larger increases (ICC  $\sim 0.2$ ) observed for intra-network salience connections, as well as dorsal attention to default mode network connections, and sensorimotor to visual network connections.

**Table 5.2.** Between-site reproducibility measured as the average intraclass correlation (ICC) across all connections for each ROI. ICC values are presented before and after the application of the proposed between-site correction technique.

Network	Region	ICC Before Site-Correction	ICC After Site-Correction
Default	Medial Prefrontal	0.13 ± 0.18	0.13 ± 0.19
Mode	Lateral Parietal (L)	0.14 ± 0.19	0.16 ± 0.23
Network	Lateral Parietal (R)	0.24 ± 0.19	0.27 ± 0.22
	Posterior Cingulate	0.18 ± 0.18	0.21 ± 0.21
Visual	Primary	0.16 ± 0.11	0.19 ± 0.13
	Ventral	0.22 ± 0.20	0.25 ± 0.21
	Dorsal (L)	0.25 ± 0.16	0.27 ± 0.18
	Dorsal (R)	0.22 ± 0.16	0.24 ± 0.18
Sensorimotor	Lateral (L)	0.26 ± 0.18	0.27 ± 0.18
	Lateral (R)	0.26 ± 0.22	0.28 ± 0.23
	Superior	0.27 ± 0.20	0.29 ± 0.21
Salience	Anterior Cingulate	0.21 ± 0.22	0.22 ± 0.23
	Anterior Insula (L)	0.23 ± 0.16	0.25 ± 0.16
	Anterior Insula (R)	0.23 ± 0.20	0.23 ± 0.22
	Rostral prefrontal (L)	0.27 ± 0.20	0.29 ± 0.21
	Rostral prefrontal (R)	0.23 ± 0.20	0.24 ± 0.21
	Supramarginal Gyrus (L)	0.29 ± 0.13	0.32 ± 0.14
	Supramarginal Gyrus (R)	0.34 ± 0.22	0.37 ± 0.22
Dorsal	Frontal Eye Field (L)	0.09 ± 0.15	0.11 ± 0.17
	Frontal Eye Field (R)	0.17 ± 0.12	0.19 ± 0.12
	Intraparietal sulcus (L)	0.28 ± 0.16	0.32 ± 0.19
	Intraparietal sulcus (R)	0.22 ± 0.20	0.26 ± 0.23
Frontal	Lateral Prefrontal (L)	0.18 ± 0.23	0.19 ± 0.25
Parietal	Posterior Parietal (L)	0.16 ± 0.15	0.18 ± 0.17
	Lateral Prefrontal (R)	0.27 ± 0.20	0.29 ± 0.20
	Posterior Parietal (R)	0.21 ± 0.16	0.23 ± 0.17
Language	Inferior Frontal Gyrus (L)	0.24 ± 0.18	0.25 ± 0.18
	Inferior Frontal Gyrus (R)	0.21 ± 0.23	0.21 ± 0.24
	Posterior Superior	0.23 ± 0.21	0.25 ± 0.22
	Temporal Gyrus (L)		
	Posterior Superior	0.27 ± 0.21	0.28 ± 0.23
	Temporal Gyrus (R)		

ROI, region of interest, L left, R right

## 5.4 Discussion

### 5.4.1 Reproducibility of Functional Connectivity Measures Between Sites

Functional connectivity matrices across site and scan showed expected patterns of functional connectivity (i.e. strongly positive intra-network connectivity, weak/strongly negative inter-network connectivity) despite large variations in tSNR between sites. However, connectivity matrices extracted for individual scans from the 1.5T scanner showed a reduction in the contrast between inter-network and intra-network connections that was likely a result from the observed lower tSNR at the lower field strength. This result is unsurprising given that the SNR of the fMRI signal has been experimentally observed to increase with field strength (Gati et al., 1997).

Within-site repeatability measures of functional connectivity calculated for each ROI were considered poor ( $ICC < 0.5$ ) for all sites which is in line with other test-retest studies using similar methods and has been estimated at 0.29 in a meta-analysis (Noble et al., 2019). ICC values were markedly lower for the 1.5T siemens sonata relative to the 3.0T systems, which again likely reflects the lower SNR at this site. In previous studies intra-network connections have been observed to have greater repeatability (Shah et al., 2016; Shehzad et al., 2009), whereas another study reported greater reliability in inter-network connections (Wisner et al., 2013). Notably, no striking relationship was observed between connectivity strength and reliability in the current study.

Average between-site reproducibility for each ROI had ICC values of  $\sim 0.2$  in line with test-retest reliability discussed above and comparable to the reproducibility range detected for 25 minute scans acquired in an eight site multisite reproducibility study at 3.0T using a similar ROI-to-ROI functional connectivity analysis (Noble et al., 2017). Notably, both the aforementioned study and the current study report lower ICC values compared to a study of multisite reproducibility of functional connectivity between two different 3.0T Siemens TRIM Trio systems (Jann et al., 2015) that used an independent component analysis and only investigated strongly positively connected regions ( $ICA\ z\text{-score} > 2.0$ ) which may explain the discrepancy in reproducibility measurements between these studies. In the current study, differences in multisite reproducibility existed between connections of specific networks. Internetwork connections to the salience network were observed to have higher reproducibility than

other connections except for intra-network connections in the sensorimotor and language networks where the majority of connections within each network had a greater reproducibility ( $ICC > \sim 0.4$ ) suggesting that these networks are stable across site.

### **5.4.2 Multisite Correction**

This study applied a site correction metric equivalent to covarying by site in a linear regression to reduce between site variance in functional connectivity measures. Increases in multi-site reproducibility measurements were observed after correction for most connections in the ROI-to-ROI connectivity matrix suggesting that mean correction of functional connectivity values based on site is an appropriate technique to reduce between-site variability. However, observed increases in reproducibility were minimal ( $ICC$  increase  $\sim 0.05$ ) after site corrections were applied suggesting that although site-correction will not bias the measurement of functional connectivity values, this technique has limited use for completely removing between site variance in this data. Other more complex techniques that consider the distribution of values across site rather than simply the mean may be more advantageous for reducing between-site variance in functional connectivity measures. For example techniques based on statistical harmonization (Yamashita et al., 2019; Yu et al., 2018) and a previously proposed method based on principle component analysis (Bari et al., 2019) have both shown value in reducing between site variance in functional connectivity measurement, thus future work could evaluate the efficacy of these methods on using data acquired at multiple sites from the same subjects.

### **5.4.3 Limitations**

Although efforts were made to harmonize rsfMRI acquisition protocols between sites a few differences remained. Firstly, the phase encode direction on the Philips Intera system was reverse (posterior to anterior) compared to the Siemens systems (anterior to posterior) causing EPI spatial distortions to manifest in opposite directions between vendors in this data. In addition, field maps as are typically acquired in fMRI data were not acquired here precluding the correction for the differing spatial distortions between sites. In data presented here the distortions

were primarily observed in the prefrontal cortex which may explain the poor reproducibility (ICC 0.181) observed in connections to this region.

Apart from the ROI-to-ROI connectivity analysis used in the current study, a multitude of techniques exist for analyzing rsfMRI images outside of the scope of the current study including but not limited to graph theory analysis (Bullmore and Sporns, 2009) and independent component analysis (Beckmann et al., 2005). Graph theory analysis takes connectivity matrices as input and calculates measures relating to the network properties of the connectivity matrix. Notably, this category of network analysis relies on the connectivity matrices themselves so we anticipate that the reproducibility results presented here could help inform multisite graph theory analysis in the future, especially considering the highest reproducibility was primarily observed in weak inter-network connections that would normally be removed during the thresholding step of graph theory analysis. On the other hand, relating the results from the current study to studies using ICA remains difficult given that the conventional ICA decomposes the rsfMRI signal into multiple network components and removes components deemed artifact based on their spatial/temporal properties. When ICA was applied separately per site on data collected from the current study, the spatial characteristics of the components differed between sites (data not shown) likely due to the differing tSNR profiles between sites and precluded a proper comparison of ICA functional connectivity metrics across site. Thus, further work could investigate how to best mitigate the tSNR differences observed between sites during post-processing (e.g. filtering, denoising) to enable ICA analysis across site to study functional connectivity.

## 5.5 Conclusions

Here we present functional connectivity reproducibility data from 8 subjects scanned twice at 4 separate sites across Canada. Reproducibility values for individual connections demonstrated similar between site reproducibility (ICC  $\sim$ 0.2) to previous multisite reproducibility study of 8 subjects scanned at 8 different sites. Correction for multisite variability was performed using a procedure identical to using site as a covariate in a linear regression and evaluated in a leave-one-out framework. Site-correction of functional connectivity values resulted in minimal changes to reproducibility measures in the majority of connections, with only a few connections (6/435) showing a

decrease in reproducibility lower than -0.05. These findings support the application of the multisite correction technique in future rsfMRI studies of the multisite NeuroDevNet cohort (See Chapter 6).

## 6 Altered Functional Connectivity Observed at Rest in Children and Adolescents Prenatally Exposed to Alcohol<sup>2</sup>

### Abstract

Studies of brain structure in fetal alcohol spectrum disorder (FASD) have shown the global and focal effects that prenatal alcohol exposure has on the brain, suggesting but not measuring altered function in FASD. This study aimed to i) identify resting-state functional networks in children and adolescents with FASD, ii) investigate functional connectivity differences compared to healthy controls, and iii) assess the links to cognitive deficits. Participants included 66 children/adolescents with FASD (aged 5.5 – 18.9 years) and 67 healthy controls (aged 5.8 – 18.5 years) scanned across four sites as part of the NeuroDevNet study. Six core functional networks with 27 regions of interest (ROIs) were examined using seed-based and ROI-to-ROI analyses. Average seed-based connectivity maps showed significant spatial overlap of positively correlated regions for all six core networks between FASD and controls, but there was less overlap for negatively correlated regions. ROI-to-ROI matrices demonstrated lower inter-network connectivity between regions primarily associated with the salience network (anterior cingulate cortex, bilateral insula), frontal-parietal network (bilateral posterior parietal cortex), and language network (right posterior superior temporal gyrus). Post-hoc correlations of the FASD participants without medication revealed a relationship between functional connectivity and performance on two cognitive tests associated with math ability and attention. Even though participants with prenatal alcohol exposure exhibit very similar intra-network functional connectivity patterns as controls, their lower inter-network functional connectivity suggests underlying deficits in the functional network brain architecture that may be related to cognitive impairment.

---

<sup>2</sup> Chapter has been published elsewhere, Little G., Reynolds J., Beaulieu C. “Altered Functional Connectivity Observed at Rest in Children and Adolescents Prenatally Exposed to Alcohol”. *Brain Connectivity*. 2018;8(8):503-15

## 6.1 Introduction

The prevalence of fetal alcohol spectrum disorder (FASD) has been estimated as high as ~1 in 100 and is characterized by a wide range of physical, cognitive and behavioral impairments (May et al., 2009). Behavioral deficits in FASD are not limited to a single cognitive domain and include deficits in motor function, attention, learning and memory, expressive and receptive language, executive function and visuospatial skills (Riley and McGee, 2005). The impact of prenatal alcohol exposure on behavior provides insight into potential widespread neurological damage and motivates the study of anatomical and functional brain abnormalities in this debilitating disorder.

Findings from structural magnetic resonance imaging (MRI) include abnormal regional brain volumes, cortical thickness, and white matter microstructure in FASD (for review see (Donald et al., 2015)). Results from these studies suggest, but do not explicitly measure, altered brain function in FASD. Task-based functional magnetic resonance imaging (fMRI) studies of children / adolescents with FASD have reported differences in functional activity while performing a variety of cognitive tasks. Studies of inhibition tasks (Fryer et al., 2007; O'Brien et al., 2013) have shown higher activation in participants with FASD in regions of the frontal and parietal lobes as well as the cingulate gyrus. A task-based study of sustained attention reported greater activation in an occipital-temporal region (Li et al., 2008). Children with FASD showed greater activation in parietal, frontal and inferior temporal regions while performing a number processing task (Meintjes et al., 2010). Several studies have investigated functional activation related to working memory in FASD, as follows. Studies utilizing a conventional n-back working memory task have reported both lower (Astley et al., 2009b; Roussotte et al., 2011) and higher (Diwadkar et al., 2013) functional activation in frontal, temporal, and parietal regions. Studies into subdomains such as spatial working memory (Malisza et al., 2005; Spadoni et al., 2009) have been more consistent reporting greater activation in inferior frontal lobe and insular cortex. Studies of verbal working memory (O'Hare et al., 2009; Sowell et al., 2007) have also shown greater activation of frontal regions. Studies of young adults with FASD have shown differences in functional activation during spatial working memory (Malisza et al., 2005) and number processing

(Santhanam et al., 2011) suggesting that functional abnormalities persist into adulthood. Taken together task-based fMRI studies suggest more regional functional demand in children/adolescents with FASD.

Resting-state functional MRI (rsfMRI) has provided insight into typical brain development (Stevens, 2016) and a variety of neurodevelopmental disorders such as Autism (Hull et al., 2017) and ADHD (Konrad and Eickhoff, 2010), but has had limited study in FASD. Studies of global network properties have suggested widespread functional network differences in FASD such as greater characteristic path length and less global efficiency in children and adolescents prenatally exposed to alcohol (Wozniak et al., 2013), with the potential for identifying FASD participants from controls who could not be classified based on facial dysmorphology features alone (Wozniak et al., 2016). Other studies have investigated specific functional connections in FASD populations using region of interest (ROI) based analysis. Children and adolescents prenatally exposed to alcohol (same sample as (Wozniak et al., 2013)) had lower inter-hemispheric connectivity between para-central ROIs (Wozniak et al., 2011). In an investigation of default mode network (DMN) connections, lower connectivity was observed at rest, as well as reduced task-related deactivation of the DMN in young adults with FASD (Santhanam et al., 2011). Rather than investigating individual functional connections between regions or global network properties, other work has investigated the impact of prenatal alcohol exposure on connectivity in multiple functional networks simultaneously using independent component analysis. Greater connectivity of motor related networks was observed in neonates prenatally exposed to alcohol (Donald et al., 2016), that may indicate a delayed development of the functional compartmentalization of these brain networks.

To our knowledge, only one study has investigated multiple functional networks in a sample of children/adolescents with FASD (Fan et al., 2017). In a group of 57 participants (19 FASD, 19 heavily exposed nonsyndromal, 19 controls), independent component analysis showed lower within-network connectivity in FASD compared to controls in five regions of five separate functional networks: anterior default mode (right post-central), salience (right middle frontal), dorsal attention (left precentral), ventral attention (right precentral), and right fronto-parietal (left crus II of the cerebellum) networks. Results in rsfMRI studies suggest that the functional organization of the brain is altered in FASD and differences are widespread manifesting in multiple networks at

various stages in development. Given the limited study of functional networks in large samples of children / adolescents prenatally exposed to alcohol more work is needed to evaluate the consistency of previous findings as well as to explore differences in inter-network connectivity and the relationship of functional connectivity to cognitive deficits in this population.

This study investigated alterations in functional connectivity of resting state networks in children / adolescents with FASD. Specifically, the study aims were to: 1) identify the spatial overlap of positively- and negatively-connected regions of 6 core networks, namely the default mode, visual, fronto-parietal, salience, language, and ventral attention networks in a relatively large cohort of 66 children/adolescents prenatally exposed to alcohol relative to 67 controls, 2) investigate differences of functional connectivity between the nodes of these 6 networks in FASD, and 3) determine whether functional connectivity alterations in FASD are associated with cognitive deficits.

## **6.2 Materials and Methods**

### **6.2.1 FASD / Typically Developing Participants**

This study was approved by the Human Research Ethics Boards at Queens's University, University of Alberta, Children's Hospital of Eastern Ontario, University of Manitoba and the University of British Columbia. Written informed consent was obtained from a parent or legal guardian and assent was obtained from each child before study participation.

Participants (healthy control and FASD) were recruited as part of the NeuroDevNet multi-site imaging project on FASD (Reynolds et al., 2011a). Structural and functional MRI were acquired for 178 participants with 45 (22 FASD, 23 Controls) being excluded for poor structural / functional imaging quality or excessive motion during the rsfMRI scan, and individuals with less than 5 minutes of scan time after artifact detection and removal. The remaining 133 participants included 66 children with FASD ( $12.9 \pm 3.4$  years, 37 males) and 67 healthy controls ( $12.3 \pm 3.4$  years, 40

males). Participants were scanned at 4 sites across Canada, namely University of Alberta (24 FASD, 30 Controls), Queens University (18 FASD, 14 Controls), University of Manitoba, (10 FASD, 8 Controls), and University of British Columbia (14 FASD, 15 Controls). Children/adolescents in the FASD group had either formal diagnoses according to the Canadian guidelines (Chudley et al., 2005) as fetal alcohol syndrome (FAS, n=5), partial FAS (pFAS, n=10), and alcohol related neurodevelopmental disorder (ARND, n=33), or confirmed prenatal alcohol exposure without a formal diagnosis (PAE, n=18). All FASD subtypes were combined into one group for statistical analysis.

Socioeconomic status (SES) was calculated using Hollingshead's Four-factor Index of Social Status [Hollingshead, 2011]. Further demographic information was collected via questionnaire including ethnicity, current medication, and comorbid psychiatric disorders (Table 6.1).

**Table 6.1.** Participant characteristics and demographics for FASD and control groups

	<b>FASD</b>	<b>Control</b>	<b>p-value<sup>a</sup></b>
Participant characteristics	n = 66	n = 67	
Age (years)	12.9±3.4 (5.5 – 18.9)	12.3±3.4 (5.8 – 18.5)	ns
Males (%)	37 (56)	40 (60)	ns
Ethnicity (%)			
Aboriginal	37 (59)	1 (1)	< 0.001
Caucasian	20 (29)	60 (88)	< 0.001
Other	9 (12)	6 (10)	ns
Medication (%)			
Antidepressants	1 (2)	0 (0)	ns
Antipsychotics	2 (3)	0 (0)	ns
Stimulants	4 (6)	1 (2)	ns
Stimulants and Antipsychotics	7 (11)	0 (0)	0.006
Stimulants, Antipsychotics & Antidepressants	2 (3)	0 (0)	ns
Simulants and Other Medication	7 (11)	0 (0)	0.006
Other	7 (11)	3 (4)	0.006
No Medication	36 (55)	63 (94)	< 0.001
Comorbidities (%)			
ADHD	32 (48)	1 (1)	<0.001
Anxiety	9 (14)	0 (0)	0.002
Depression	4 (6)	0 (0)	0.042
Bipolar	2 (3)	0 (0)	ns
Oppositional Defiant Disorder	6 (9)	0 (0)	0.012
Conduct Disorder	2 (3)	0 (0)	ns
Autism	1 (2)	0 (0)	ns
Other Disorder	16 (24)	0 (0)	0.001
SES	43±15 (11 – 66)	48±8 (22 – 66)	0.012
Site (%)			
University of Alberta	24 (36)	30 (45)	ns
Queens University	18 (27)	14 (21)	ns
University of Manitoba	10 (15)	8 (12)	ns
University of British Columbia	14 (21)	15 (22)	ns
% removed volumes during preprocessing	6± 4 (0 - 16)	5± 4 (0 - 17)	ns

<sup>a</sup> Group differences of categorical variables (e.g. sex) assessed with Mann-Whitney U; continuous variable (e.g. age) assessed with independent samples t-test (at p < 0.05).

## 6.2.2 Cognitive Testing

Research assistants trained by a single neuropsychologist for consistency across the four sites performed a battery of cognitive assessments. The test battery included five major evaluations of core functions affected in PAE such as math, reading, executive function, memory, and inhibition as follows. The Woodcock Johnson III Tests of Achievement (WI-III ACH) evaluated mathematic and quantitative reasoning skills (Woodcock et al., 2001). The Woodcock Reading Mastery Tests - Revised (WRMT-R) provided a comprehensive assessment of reading ability (Woodcock, 1998). The Behavior Rating Inventory of Executive Function (BRIEF) assessed executive function with greater scores indicating a higher level of dysfunction in a particular sub-domain of executive function. The Working Memory Test Battery for Children (WMTB-C) was assessed to evaluate working memory (Pickering and Gathercole, 2001). Seven subtests of the Developmental Neuropsychological Assessment (NEPSY-II) (Korkman et al., 2007) were administered to assess basic concept formation, selective/sustained attention, inhibition, and short-term/long-term memory of verbal information. Notably, the cognitive results presented here are from a subset of a larger cohort of participants in the NeuroDevNet study on FASD (Paolozza et al., 2014a, 2014b).

## 6.2.3 Image Acquisition

Structural and functional images were collected for each participant at four MR imaging centres: University of Alberta (1.5T Siemens Sonata), Queen's University (3T Siemens Trio), University of Manitoba (3T Siemens Trio), and University of British Columbia (3T Philips Intera). Each session had a total acquisition time of approximately 25 min including anatomical T1-weighted, T2-weighted, fluid-attenuated inversion recovery (FLAIR), and DTI imaging. For this study resting-state functional imaging was acquired using an echo planar imaging gradient-echo sequence with: 3 mm isotropic voxels, 40 axial slices, FOV = 192 x 192 mm<sup>2</sup>, TR = 2.5 s, TE = 30 ms (3T scanners)/ 40 ms (1.5T scanner), phase encode direction anterior-posterior (Siemens Scanners) / posterior-anterior (Philips scanner), flip angle = 90 deg, 140 time points, 6 min total acquisition. Additionally, T1-weighted images used for anatomical registration were acquired with a high-resolution (1 x 1 x 1 mm<sup>3</sup>) magnetization prepared rapid acquisition

gradient echo (MPRAGE) sequence with: 160 axial slices, FOV = 256 x 256 mm<sup>2</sup>, inversion time (TI) = 1100 ms, flip angle = 15 deg, TR ~ 2100 ms, TE ~ 3.5 ms, and acquisition time ~ 5:30 min.

## 6.2.4 Intersite Correction Participants

For assessing between site reproducibility of functional connectivity measures, eight healthy young adults (age 28 ± 6 years, 2 males/6 females) prospectively underwent two sequential imaging sessions at each of the four sites (mean 102 days from first to last scan).

## 6.2.5 Pre-Processing

All study participants were processed and analyzed using the same standard pipeline from the Functional Connectivity Toolbox (version 17.a <https://www.nitrc.org/projects/conn>). Functional volumes were realigned, unwarped, and co-registered to the anatomical images using the statistical parametric mapping toolbox (SPM 12b). The artifact detection toolbox was employed for scrubbing and removing time points with corrupted data greater than 0.5 mm in movement or with changes in mean signal intensity greater than 2 standard deviations (conservative settings 95<sup>th</sup> percentile). After removing time points with corrupted data, participants with less than 5 minutes (120 volumes) remaining were excluded from analysis (5 Controls, 6 FASD). Masks of white matter and cerebrospinal fluid were generated using SPM segmentations of anatomy. Principal component analysis was performed on voxel by time series matrices from each mask. For the purpose of removing unwanted signal from the fMRI time course per voxel, the first five components from the white matter and cerebrospinal fluid masks were used as nuisance regressors in a multiple linear regression. Anatomical images were then spatially normalized to the MNI306 template, and the calculated transformation was used to spatially normalize the preprocessed functional volumes to the MNI306 template (SPM 12b). Spatially normalized functional volumes were then smoothed with an 8mm full width half max gaussian kernel (SPM12b).

## 6.2.6 Functional Connectivity ROI Based Analysis

Regions of interest (ROIs) were taken from the network specific mask included in the functional connectivity toolbox version 17.a (Whitfield-Gabrieli and Nieto-Castanon, 2012). These ROIs were generated from an independent component analysis of 497 healthy individuals from the human connectome project and are detailed in Table 6.2. Included in this toolbox are labels that specify the functional network (e.g. DMN, Dorsal Attention) for each ROI. In this study regions of interest from 6 a priori defined networks were used: default mode network (4 ROIs), dorsal attention network (4 ROIs), language network (4 ROIs), frontal-parietal network (4 ROIs), salience network (7 ROIs), and visual network (4 ROIs). ROIs from the sensorimotor and cerebellar networks were excluded in the analysis because a large proportion of the participants had missing coverage. First, for the purpose of investigating spatial connectivity patterns between groups, seed-based connectivity maps were created for each individual by extracting a mean time series across all voxels of a given ROI, and correlating the time series to all voxels in the subject's image resulting in 27 seed-based connectivity maps per subject for the six networks. By investigating multiple seed-based connectivity maps within a given network, this analysis remained sensitive to differences related to specific network ROIs. Secondly, correlations between average ROI time courses were calculated between all 27 ROIs for each subject, resulting in a connectivity matrix per subject. Correlations from seed-based maps and connectivity matrices were then fisher z-transformed. The same analysis was performed on the images acquired from the 8 travelling control participants from the multisite reproducibility data.

**Table 6.2.** Regions of interest are listed for the six core networks for both seed-based and ROI-based analysis (center of mass in MNI coordinates) that were taken from the network specific mask included in functional connectivity toolbox version 17.a (*Whitfield-Gabrieli and Nieto-Castanon, 2012*).

Network	Region Number	Region	Center of Mass (x,y,z)	ROI size (mm <sup>3</sup> )
Default Mode Network	1	Medial Prefrontal	(1,55,-3)	10770
	2	Lateral Parietal (L)	(-39,-77,33)	8328
	3	Lateral Parietal (R)	(47,-67,29)	10610
	4	Posterior Cingulate	(1,-61,38)	38660
Visual	1	Primary	(2,-79,12)	73660
	2	Ventral	(0,-93,-4)	41710
	3	Dorsal (L)	(-37,-79,10)	24830
	4	Dorsal (R)	(38,-72,13)	33970
Salience	1	Anterior Cingulate	(0,22,35)	8504
	2	Anterior Insula (L)	(-44,13,1)	3568
	3	Anterior Insula (R)	(47,14,0)	3104
	4	Rostral prefrontal (L)	(-32,45,27)	9328
	5	Rostral prefrontal (R)	(32,46,27)	4648
	6	Supramarginal Gyrus (L)	(-60,-39,31)	1864
	7	Supramarginal Gyrus (R)	(62,-35,32)	2272
Dorsal	1	Frontal Eye Field (L)	(-27,-9,64)	704
	2	Frontal Eye Field (R)	(30,-6,64)	432
	3	Intraparietal sulcus (L)	(-39,-43,52)	26280
	4	Intraparietal sulcus (R)	(39,-42,54)	25100
Frontal Parietal	1	Lateral Prefrontal (L)	(-43,33,28)	13620
	2	Posterior Parietal (L)	(-46,-58,49)	6656
	3	Lateral Prefrontal (R)	(41,38,30)	14060
	4	Posterior Parietal (R)	(52,-52,45)	6696
Language	1	Inferior Frontal Gyrus (L)	(-51,26,2)	3856
	2	Inferior Frontal Gyrus (R)	(54,28,1)	4296
	3	Posterior Superior Temporal Gyrus (L)	(-57,-47,15)	18100
	4	Posterior Superior Temporal Gyrus (R)	(59,-42,13)	13500

ROI, region of interest, L left, R right

### **6.2.7 Multisite Correction**

To account for variability in connectivity measures between sites the travelling control data was used to generate correction factors (linear mean shift) for each connectivity matrix in the childhood/adolescent cohort using the following process. First, a site correction matrix ( $\Delta$ ) was calculated for each site by subtracting the site mean correlation matrix (average of 16 functional images) from the total mean correlation matrix across all traveling subjects and sites (average of 64 functional images). The inverse of this  $\Delta$  matrix was then applied to each individual's correlation matrix within each site. This approach would be analogous to covarying by site in a linear regression, except the site estimates per connection are taken from an independent sample of 8 travelling control participants scanned twice at each site.

### **6.2.8 Spatial Overlap of Connected Regions**

Average seed-based connectivity maps were calculated separately for control and FASD groups for all 27 seeds and were thresholded to fisher z-scores greater than 0.25 and less than 0. Positively and negatively connected regions between corresponding control and FASD maps were visually compared to assess general between group spatial agreement of connected regions. Positively connected (z-score >0.25) and negatively connected (z-score < 0) group average maps were created and binarized where 1 indicates values other than zero. As a quantitative measure of voxel-wise spatial agreement between groups, dice coefficients were calculated between average control and FASD binarized maps resulting in a measure of overlap between groups separately for positive and negative connectivity maps for each seed. The dice coefficient used in this instance is calculated as 2 times the number of voxels intersecting FASD and control maps, divided by the sum of all voxels in the control map plus all voxels in the FASD map.

## **6.2.9 Group Comparison / Network Matrices Analysis**

Connectivity matrices per subject were used to test for group differences in individual functional connections between controls and FASD participants. A general linear model was used to assess between group differences for every connection between ROIs, covarying for effects of age, sex, number of removed timepoints during scrubbing, and average motion during scanning session. Results were then corrected for multiple comparisons (27 ROIs, 351 connections) using false-discovery rate (FDR) correction and results (t-statistics, FDR-corrected p-value) were reported for connections with group differences exceeding an FDR corrected p-value  $< 0.05$ . To assess whether potential confounds influenced the group effect observed between FASD and controls, four potential confounding variables were selected for further analysis, namely diagnosis of ADHD, aboriginal ethnicity, currently on medication including stimulants, and currently on medication other than stimulants. The effects of confounders on connections surviving FDR-correction were assessed within the FASD group using separate multivariate linear models ( $p < 0.05$ ) for each potential confounder including covariates previously included in the between-group analysis. Furthermore, a within-group (non-medicated FASD group and control group separated) correlation analysis was performed to test for relationships (uncorrected for multiple comparisons  $p < 0.05$ ) between cognitive scores and functional connectivity of the connections that show between group differences surviving FDR-correction.

## **6.3 Results**

### **6.3.1 Cognitive and Behavioral Differences in FASD**

Relative to controls, the FASD group had lower cognitive scores as well as higher BRIEF scores for all tests (Table 6.3). The cognitive tests with the greatest differences were related to response inhibition, whereas the largest difference in BRIEF scores were related to working memory and behavioral regulation.

**Table 6.3.** The FASD group showed poorer cognitive test performance in all tests relative to controls, as well as greater deficits in executive function (BRIEF) in all parent reported behaviors.

Cognitive Test	Subtest/Domain	FASD			Controls			% Change	p-value <sup>a</sup>
		N (/66)	Standard Score	Range	N (/67)	Standard Score	Range	FASD from Control	
<b>Woodcock Johnson</b>	Quantitative concepts 18A&B (mathematics)	65	84±20	37-129	66	105±12	69-129	-20%	<0.001
<b>Woodcock reading mastery test-revised</b>	Word ID	65	92±14	52-118	66	106±13	71-134	-13%	<0.001
<b>NEPSY II</b>	Animal sorting	59	8±3	2-18	60	10±4	1-18	-20%	<0.001
	Auditory attention	60	8±4	1-13	65	11±3	3-18	-27%	<0.001
	Response set	58	10±3	1-14	60	12±3	5-14	-20%	0.018
	Inhibition naming	59	7±4	1-17	64	10±3	3-16	-30%	<0.001
	Inhibition inhibition	57	7±3	1-15	64	10±4	2-19	-30%	<0.001
	Inhibition switching	54	8±4	1-19	59	10±2	4-15	-20%	<0.001
	Memory for names + delay	59	7±3	1-16	65	9±3	2-15	-22%	<0.001
<b>BRIEF parent form</b>	Inhibition	57	68±13	42-100	63	49±9	37-76	+28%	<0.001
	Shift	57	67±14	38-95	63	48±8	36-73	+28%	<0.001
	Emotional Control	57	64±12	43-91	63	48±10	24-78	+25%	<0.001
	Behavioral Regulation Index	57	69±12	45-97	63	48±9	36-80	+30%	<0.001
	Initiate	57	65±12	40-86	63	50±10	36-73	+23%	<0.001
	Working Memory	57	70±12	40-90	63	49±10	36-79	+30%	<0.001
	Plan	57	267±12	38-84	63	50±11	35-81	+5%	<0.001
	Organize	57	58±9	37-72	63	51±9	34-71	+12%	<0.001
	Monitor	57	65±12	36-82	63	49±11	31-81	+25%	<0.001
	Metacognition index	57	64±10	42-85	63	55±15	33-91	+14%	<0.001
	Global Executive Composite	57	70±11	43-94	63	50±13	6-92	+29%	<0.001

<sup>a</sup> Group differences assessed with independent samples t-test (at p < 0.05).

### 6.3.2 Spatial Characteristics of Connectivity in FASD

All six networks, namely the default mode, dorsal attention, language, frontal parietal, salience and visual networks, had similar connectivity patterns between healthy controls and participants with FASD for all 27 seeds. Average connectivity maps per group are presented for 6 seeds, one per network (Figure 6.1). In general, average connectivity maps for both the control and FASD groups demonstrated excellent spatial agreement in positively connected regions ( $z$ -score  $> 0.25$ ) for all seeds, given high dice coefficients ( $0.85 \pm 0.04$ ) with 25 of the 27 seeds greater than 0.8 (as high as 0.89). However, the dice coefficient between controls and FASD maps were notably lower for negative correlations ( $0.71 \pm 0.06$ ) with only 1 of 27 seeds being greater than 0.8 (left posterior parietal seed of the frontal parietal network) and the lowest being 0.55 for the anterior cingulate seed of the salience network.

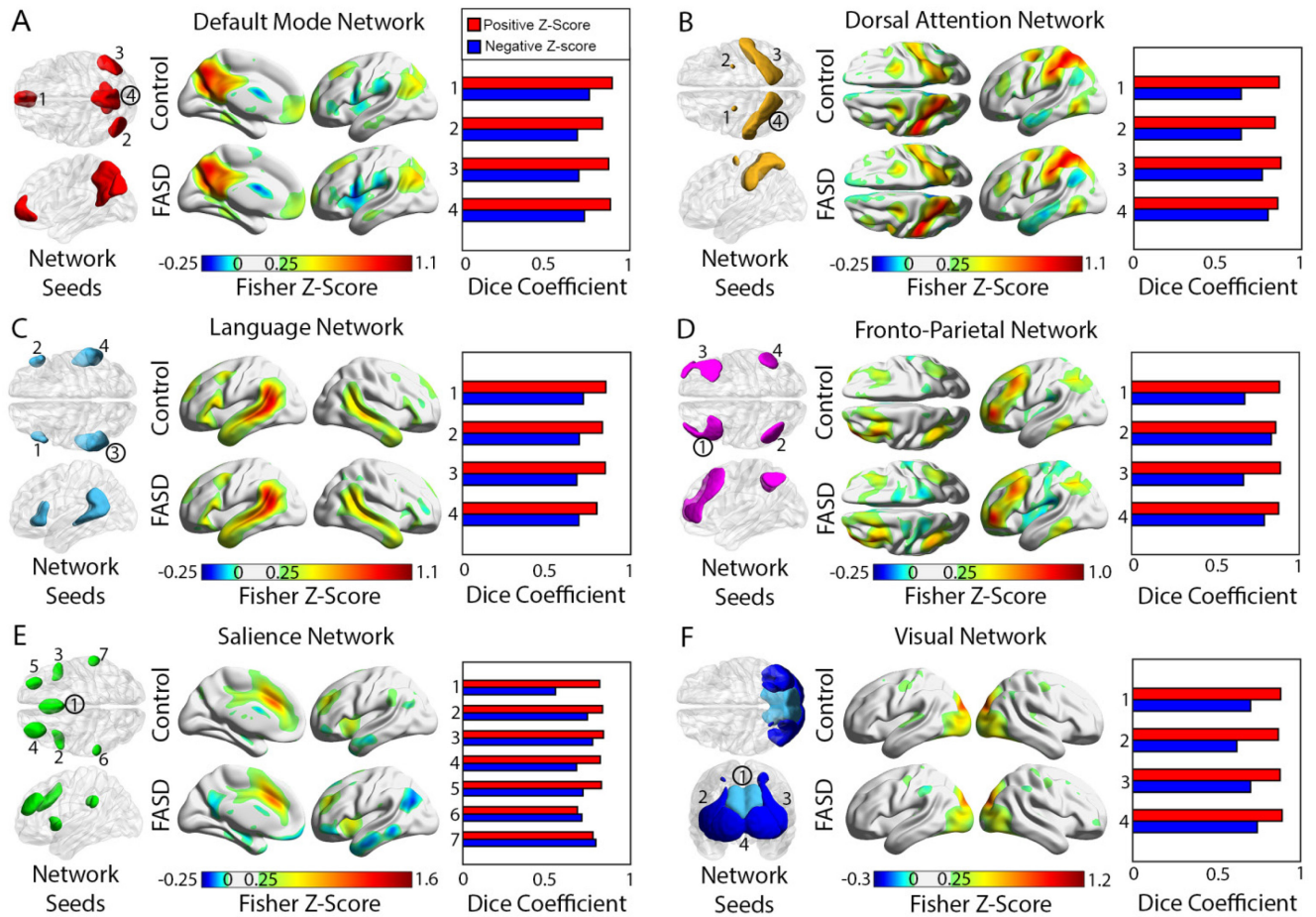


**Figure 6.1.** ROIs used for seed-based connectivity analysis are visualized separately for six functional networks (A-F). Average connectivity maps for control (N=67) and FASD (N=66) groups are presented for only one select seed (circled) within each network. Strong spatial agreement was observed between group average maps of positively and negatively connected regions in all seeds suggesting that the spatial organization of these functional networks is similar in FASD. Quantitatively, dice coefficients for positive regions (red bars) were  $0.85 \pm 0.04$  with 25 of 27 seeds yielding greater than 0.8, with the exception of the two posterior supramarginal gyrus seeds of the salience network (ROIs 6 and 7 in E). Dice coefficients for negatively connected regions (blue bars) indicated less overlap between controls and PAE with  $0.71 \pm 0.06$  and only 1 of 27 regions with values greater than 0.8. The lowest dice coefficient was 0.55 from negatively connected regions to the anterior cingulate cortex seed (ROI 1 in E) of the salience network.

### 6.3.3 Functional Connectivity Differences in FASD:

The three connections that had statistically significant between-group differences of altered connectivity (FDR-corrected  $p < 0.05$ ) in FASD are rendered in 3D and displayed along with bee-swarm plots of individual z-scores for each connection (Figure 6.2). Relative to controls, all 3 connections in FASD showed different inter-network connectivity to regions within the salience network. Relative to controls, functional connectivity was lower for the anterior cingulate cortex (ACC) to the left posterior parietal cortex (PPC), the right insula to the right posterior parietal cortex (PPC) and the left insula to the right posterior superior temporal gyrus (pSTG). The absolute differences of between group averages in functional connectivity ranged from 0.140 to 0.176 for all three connections. In the control group all connections had positive average fisher z-scores, whereas the FASD average connectivity qualitatively had a trend of negative or close to zero connectivity in the 2 connections between the salience and the frontal parietal network. Notably, a more robust group effect was observed ( $T(127) = 4.40$ ,  $p = 0.0078$ ) in the connection between the anterior cingulate and left posterior parietal cortices relative to the other two connections.

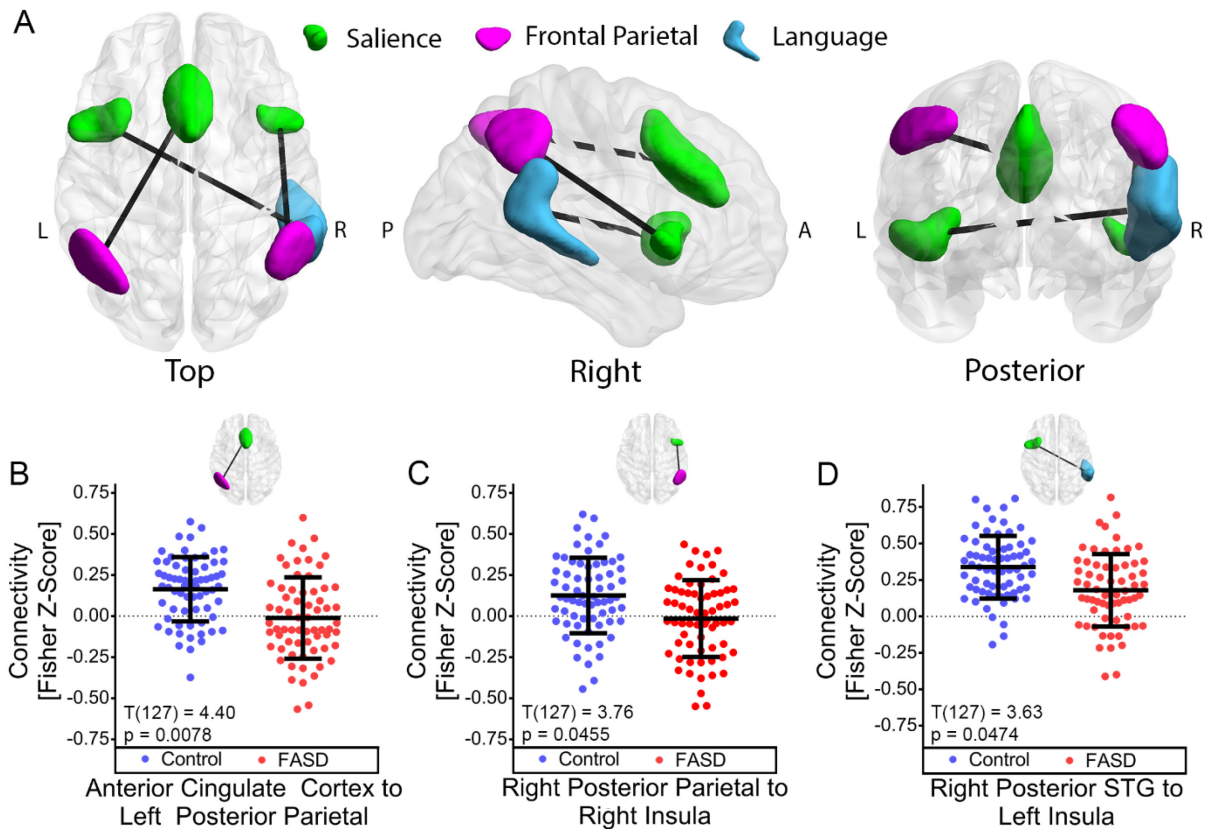


**Figure 6.2.** (A) Three network connections that involve the salience (green ROIs), frontal parietal (pink ROIs), and language (blue ROI) networks show (B-D) significant ( $p < 0.05$  FDR corrected for all network edges) lower functional connectivity between FASD,  $N=66$  (red) and Control,  $N=67$  (blue) groups. Three different views are shown for the same three connections in (A) that all involve reduced inter-network connectivity from salience network regions including (B) ACC to the left PPC, (C) right PPC to the right insula, and (D) the right pSTG to the left insula. Note that the three views shown in (A) are oriented axial left to right (L/R), sagittal posterior to anterior (P/A), and coronal left to right (L/R) respectively. ACC anterior cingulate cortex; PPC, posterior parietal cortex; pSTG, posterior superior temporal gyrus.

### 6.3.4 Potential Confounding Variables and Cognitive Associations

Results of post-hoc analysis of the 3 connections with observed group differences are reported in Table 6.4. No significant ( $p < 0.05$ ) effects related to diagnosis of ADHD, aboriginal ethnicity, and medication not including stimulants were observed between functional connectivity of the 3 remaining connections in the FASD group. A positive effect on functional connectivity ( $p < 0.05$ ) was observed between the FASD group on at least one stimulant relative to the non-medicated FASD group in connectivity between the right pSTG and the left insula. Functional connectivity values are presented for this connection as bee-swarm plots (Figure. 6.3) separating the FASD group by medication class. The FASD group on at least one stimulant had an observed increase in functional connectivity ( $p < 0.05$ ) relative to the non-medicated FASD group.

**Table 6.4.** Post-hoc analysis of potential confounds in the FASD group for the three connections with lower functional connectivity in the FASD group relative to controls.

	<i>N</i>	ACC to Left PPC			Right PPC to Right Insula			Right pSTG to Left Insula		
		<i>Beta</i>	<i>T-stat</i>	<i>p-val</i> <sup>a</sup>	<i>Beta</i>	<i>T-stat</i>	<i>p-val</i> <sup>a</sup>	<i>Beta</i>	<i>T-stat</i>	<i>p-val</i> <sup>a</sup>
<b>Medicated including at least one stimulant</b>	20	-0.28	-0.338	0.737	0.076	1.005	0.320	<b>0.197</b>	<b>2.551</b>	<b>0.014*</b>
<b>Medicated with Non-Stimulants</b>	10	0.126	1.125	0.267	0.115	1.161	0.252	0.98	0.953	0.346
<b>Aboriginal Ethnicity</b>	37	0.009	0.138	0.891	0.053	0.895	0.375	0.009	0.137	0.892
<b>ADHD Comorbidity</b>	32	0.009	0.139	0.890	0.002	0.025	0.980	0.091	1.415	0.162

<sup>a</sup> Statistical differences were assessed with a multivariate linear regression (\* and bolded text for  $p < 0.05$ ) adjusting for age, sex, number of volumes removed during scrubbing, and average motion per subject.

Connectivity values for the 3 connections surviving FDR-correction were carried forward to test for relationships to cognitive scores in the non-medicated FASD group and control group separately. In the non-medicated FASD group a positive correlation ( $r = 0.472$ ,  $p = 0.006$ ) was observed between scores on the NEPSY II Auditory Attention subtest and functional connectivity between the left insula and right pSTG (Figure 6.4A). Additionally, in the non-medicated FASD group a negative correlation ( $r = -0.356$ ,  $p = 0.036$ ) was observed between performance on Woodcock Johnson Quantitative Concepts Subtest and functional connectivity between the left PPC and the ACC (Figure 6.4B). Within the control group no statistically significant correlations were observed between z-scores from the 3 connections investigated and cognitive scores.

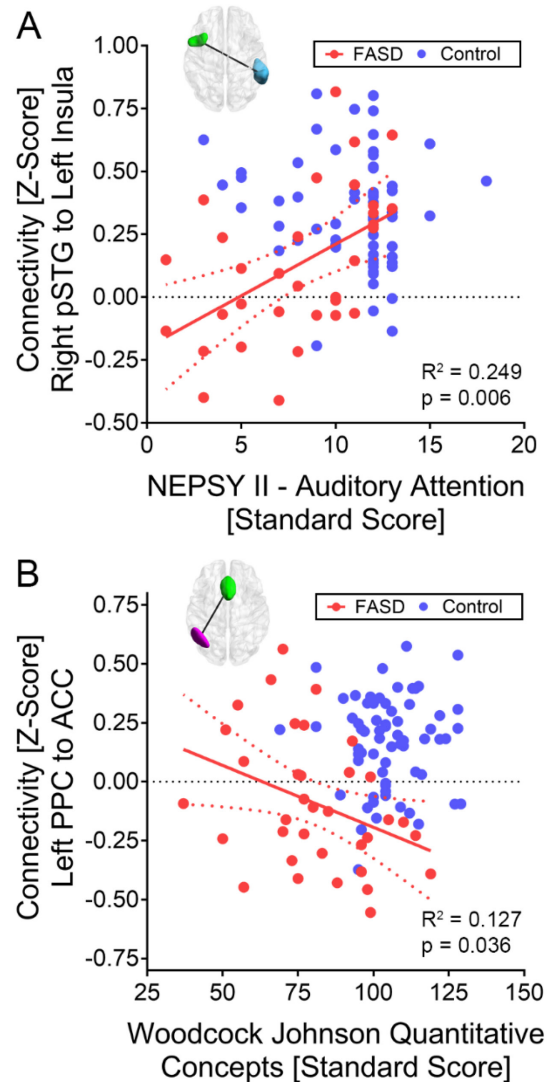


**Figure 6.3.** Statistically significant (uncorrected  $p < 0.05$ ) correlations (red lines) between two inter-network connections and cognitive scores in the non-medicated FASD group (red) are presented along with 95% confidence intervals (red dotted lines). A) A positive correlation was observed in the non-medicated FASD group,  $N=32$ , between standard scores on the NEPSY II – auditory attention subtest and functional connectivity between the right posterior superior temporal gyrus (pSTG) and the left insula. B) A negative correlation was observed in the non-medicated FASD group,  $N = 35$ , between the standardized score on the Woodcock Johnson Quantitative Concepts subtest of math ability and functional connectivity between the left posterior parietal cortex (PCC) and the anterior cingulate cortex (ACC). Correlations were not observed in the control group (blue). NEPSY II standard scores have an expected value (population average) of 10, whereas the Woodcock Johnson Quantitative Concepts standard scores have an expected value (population average) of 100. Note that the black dotted lines indicate a functional connectivity value of zero. pSTG, posterior superior temporal gyrus.

## **6.4 Discussion**

### **6.4.1 Spatial Patterns of Resting State Networks in FASD**

This study reports six resting-state functional networks in children/adolescents with FASD that share strong spatial agreement with controls in positively connected regions and slightly weaker spatial agreement of negatively connected regions; namely the default mode, fronto-parietal, salience, dorsal attention, language, and visual networks. These results suggest that spatial patterns of connectivity remain intact in FASD, and that the ROIs can be confidently used for between-group analysis in this study. This is in agreement with one study that showed similar connectivity patterns in FASD of the salience, default mode, visual, somatosensory, fronto-parietal, and dorsal/ventral attention networks (Fan et al., 2017). In addition, similar functional connectivity patterns have been shown in adults with FASD in a seed-based analysis of the default mode network (Santhanam et al., 2011), and in an independent component analysis of neonates with FASD (Donald et al., 2016) in motor regions. These results are unsurprising given that regional functional connectivity patterns have been shown to be highly replicable in large samples (Yeo et al., 2011), and different rsfMRI analysis techniques have been applied successfully in many studies of other neurodevelopmental disorders such as Autism (Hull et al., 2017) and ADHD (Konrad and Eickhoff, 2010).

### **6.4.2 Functional Connectivity Differences in FASD**

In this study, functional connectivity differences were primarily observed in connections to the salience network, a network thought to be involved in identifying stimuli that are meaningful or important for behavior. Functional connectivity differences were also observed in connections to the frontal-parietal network that plays a role in executive function, a known cognitive deficit in FASD (Rasmussen, 2005). More recently it has been suggested that the salience network modulates the switching between the default mode network and the executive function network (Goulden et al., 2014), suggesting that the lower connectivity in FASD in both the salience and fronto-parietal networks could be interrelated. Moreover, abnormal connectivity in any of these networks could result in more widespread cognitive deficits observed in FASD rather than deficits related to a specific cognitive domain.

Functional connectivity was lower in three inter-network connections for the FASD participants, in agreement with other work reporting lower functional connectivity in children /adolescents with FASD in both the bilateral posterior parietal cortices (Wozniak et al., 2011), and in other networks including the salience and fronto-parietal networks (Fan et al., 2017). Importantly, these results differed with the current findings as the previous studies showed functional connectivity differences within strongly correlated (intra-network) regions whereas differences in this study were observed between weakly connected (inter-network) regions. Relative to controls, lower connectivity between networks may indicate decreased between network integration in these disorders. To our knowledge, functional connectivity studies of FASD have only investigated intra-network connectivity making a comparison to previous findings difficult. However, FASD diagnosis is highly comorbid with ADHD (note: 48% of our FASD participants, Table 6.1) where studies have shown lower inter-network connectivity primarily related to the Default Mode Network connections in adults with ADHD (Castellanos et al., 2008) and children and adolescents with ADHD (Sripada et al., 2014). More specifically these studies report lower connectivity to the cingulate cortex (Castellanos et al., 2008) as well as regions related to both salience and frontal parietal networks (Sripada et al., 2014) overlapping regions with lower connectivity in our study. This suggests that inter-network connectivity deficits could be common in populations with neurodevelopmental disorders rather than specific to FASD.

Two connections were observed to have positive average connectivity in the control group and negative average connectivity in the FASD group. Negative correlations have been an area of controversy in the field and distributions of positive and negative correlations have been shown to change based on varying preprocessing steps (Chai et al., 2012), and may have a vascular basis in large cerebral veins (Bianciardi et al., 2011), thus a proper interpretation based purely on these quantitative values is not yet feasible. Future work investigating anticorrelations and their physiological basis could provide a better understanding of how negative and positive connectivity manifest in FASD.

The analysis from this study did not use slice timing correction as a preprocessing step. A secondary ROI-to-ROI analysis was performed while including slice timing correction as a preprocessing step and this resulted in the same three connections showing similar group differences (data not shown). In addition, most multi-site rs-fMRI

studies use site as a covariate to correct for inter-site systematic differences (Di Martino et al., 2014; Fair et al., 2013). This is necessary practically since most studies don't usually acquire prospective scans from the same traveling subjects at each site. A reanalysis of our data using the conventional "site as a covariate" approach showed the same FASD versus control group difference for the anterior cingulate cortex to right posterior parietal connection. However, of the three connections with group differences from the original analysis, there were small systematic decreases in group difference T-statistics when using site as a covariate resulting in two of the three connections having a slightly larger p-value than the statistical threshold of  $p < 0.05$  (see Appendix B Table B1). This suggests that the traveling participant correction technique may improve sensitivity to detect group differences across site. For a secondary analysis demonstrating the consistency of these findings across site see Appendix B Figures B1 and B2.

### **6.4.3 Regional Functional Alterations in FASD**

A large number of fMRI studies have reported alterations of brain activation in FASD during tasks related to working memory, executive function, sustained attention, and number processing. Of these studies, many have shown alterations in functional activity of the anterior cingulate cortex, both parietal lobes, posterior superior temporal gyrus, and both insular cortices, the same regions that showed robust lower resting functional connectivity in our study. Task-related fMRI studies of working memory and verbal learning have reported lower activation in FASD of the right posterior parietal cortex during a 2-back task related to working memory (Astley et al., 2009b), greater activation in FASD in the right inferior parietal cortex during a spatial working memory task (Diwadkar et al., 2013), greater activation in FASD in the left inferior parietal lobe during a verbal working memory task (O'Hare et al., 2009) and greater activation in FASD in right superior parietal cortex during a verbal learning task (Sowell et al., 2007). Additionally, the anterior cingulate has shown greater activity in FASD in a go/no-go (executive function) task (O'Brien et al., 2013), and decreased activity in a working memory task (Roussotte et al., 2011). Insular cortices have shown differential functional activation in PAE participants during tasks related to working memory (Norman et al., 2013; Roussotte et al., 2011; Spadoni et al., 2009) and number processing

(Meintjes et al., 2010), while the posterior superior temporal gyrus has shown greater activation in FASD participants during a working memory task (O'Hare et al., 2009). Even though the relationship is unclear between resting functional connectivity and task-related functional activity, resting state functional connectivity has been shown to predict task-related activation patterns of a variety of cognitive tasks in healthy participants (Tavor et al., 2016). Given that both task-related activity and resting-state functional connectivity of similar regions are reported to be altered in FASD, a relationship between greater functional demand and lower functional connectivity could exist in this disorder.

#### **6.4.4 Functional Connectivity may be Associated with Structural/Metabolic Alterations in FASD**

Structural MRI studies of volume have shown abnormal regional cortical volumes in FASD. Cortical thickness studies of FASD have shown thicker (Sowell et al., 2008b; Yang et al., 2012) and thinner cortex (Zhou et al., 2011) in the parietal lobe, as well as thinner cortex in the posterior superior temporal gyrus (Chen et al., 2012). Diffusion MRI studies of children/adolescents with FASD have revealed alterations to white matter structure in long range tracts that connect regions with reduced functional connectivity in the current study. Specifically, the lateral splenium of corpus callosum (Sowell et al., 2008a) and bilateral superior longitudinal fasciculus (Lebel et al., 2008) showed lower fractional anisotropy in their respective tracts suggesting that structural "connectivity" may explain the lower functional connectivity in FASD from this study. One MR spectroscopy study has shown lower metabolic ratios of NAA/Cho and NAA/Cr in both the right parietal cortex and anterior cingulate of adolescents/young adults (ages 14-21) with FASD (Fagerlund et al., 2006). Converging results from multiple imaging modalities in similar regions may indicate an underlying structural and metabolic explanation for the functional connectivity results observed in this study; many studies have shown structural and metabolic differences in FASD participants in other brain regions, so another possible interpretation is that non-local structural/metabolic differences could have indirect effects on functional connectivity differences reported in this paper.

### 6.4.5 Correlations to Cognitive Scores

Within group correlations with cognitive test scores indicated a positive correlation between performance on the NEPSY II auditory attention subtest and functional connectivity between the left insula and the right posterior superior temporal gyrus only in the non-medicated FASD group. Interestingly, it has been suggested that the anterior insula is involved in high-level cognitive tasks such as attention and may be responsible for mediating the switching between other task-related networks (Menon and Uddin, 2010). The posterior superior temporal gyrus is thought to be involved in auditory language processing (Friederici et al., 2000) a necessary component of the auditory attention task in this study. This suggests that this inter-network connection may be functionally specific to the observed auditory attention task performance in the FASD group. Additionally, a negative correlation was observed between the average connectivity from the left posterior parietal region of interest to the anterior cingulate and math ability (Woodcock Johnson Quantitative Concepts 18A&B) only in the FASD group. Previous work has revealed a relationship between white matter structure in the left parietal lobe and math ability in healthy young adults (Matejko et al., 2013) and in children/adolescents with FASD (Lebel et al., 2010). Interestingly, in both these studies, math ability was positively correlated to measures of fractional anisotropy (white matter “integrity”) contrary to the negative correlation with left parietal lobe functional connectivity observed in this study. Taken together, these studies show that larger fractional anisotropy and less functional connectivity of the left parietal lobe are predictors of positive math outcomes in children/adolescents with FASD. Furthermore, this may indicate that lower functional connectivity is a compensatory change related to underlying structural deficits in FASD. Notably, brain-behavior relationships were only found in a subgroup of medically naive FASD participants. A secondary analysis including all FASD participants yielded no such relationships (data not shown), suggesting that separating groups by medication status may be desired to be sensitive to brain-behavior relationships.

### 6.4.6 Limitations

Several limitations exist in the current study, primarily associated with unknown environmental exposures. Animal studies have shown a dose-dependent effect of developmental alcohol on neurodegeneration (Ikonomidou et al., 2000). The patients in the current study were recruited long after birth and many were adopted from a young age so an accurate characterization of maternal alcohol consumption was not available. Even though socioeconomic status was characterized from a child's current household, children prenatally exposed to alcohol often experience adverse environmental events at a young age (McCrorry et al., 2010) that could have a varying effect on the development of functional connectivity patterns in children and adolescents. To control for these confounds, future work may be able to characterize the level and timing of exposure as well as adverse life events to better assess the effect of prenatal alcohol exposure on functional connectivity.

In our sample, participants with FASD had a variety of comorbid diagnosis including ADHD, Anxiety, Depression, Bipolar, Oppositional Defiant Disorder, Conduct Disorder, or Autism. Comorbidities in this population are quite common and thus developmental effects of various medications, treatments and diagnosis are difficult to separate. In this study, post-hoc testing revealed that greater connectivity between the left insula and the right posterior superior temporal gyrus in the FASD group was associated with current use of stimulant medication (Figure 6.3). Importantly, an analysis of the entire cohort showed lower connectivity in this same connection for the FASD group relative to controls. Taken together these results suggest that the group difference was not driven by stimulant, and if anything the effect of stimulant weakened the observed group difference. To our knowledge, no studies have investigated the effect of stimulant use on brain function in an FASD cohort. However, increased insular connectivity may be comparable to task-based studies of children with ADHD that show different salience network activity in the right insula and anterior cingulate associated with stimulant use (Rubia et al., 2014).

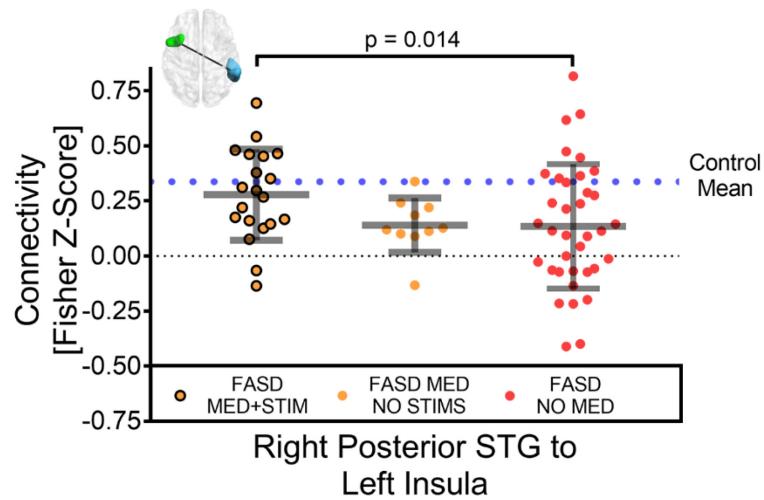


**Figure 6.4.** Difference between functional connectivity of FASD participants who were medicated with at least one stimulant (N=20, orange/black MED+STIM), medicated without stimulants (N=10, orange MED NO STIMS) and not medicated (N=36, red NO MED). Relative to the no stimulants or non-mediated FASD, functional connectivity was greater in one connection (out of the three tested from Figure 6.2), namely between the right posterior superior temporal gyrus (STG) and the left insula, in the FASD participants medicated with at least one stimulant. Notably this latter connectivity was near the control mean (dashed blue line). Note that the black dotted line marks a functional connectivity value of zero.

### **6.4.7 Conclusions**

In this study of children/adolescents aged 5-18 years, functional connectivity of 6 resting-state networks were identified in the FASD participants that were spatially consistent with the same functional networks in the control group. Functional connectivity was lower in inter-network connections between salience network regions and regions of the fronto-parietal and language networks. This suggests abnormal network to network functional communication in FASD. Functional connectivity of two connections in the non-medicated FASD group were associated with math ability and performance on an attention task indicating that these changes may underlie cognitive deficits. Overall, individuals with prenatal alcohol exposure demonstrate functional differences in regions spanning multiple networks of the brain.

## Appendix B

During peer review of the manuscript presented in Chapter 6 additional analysis was conducted to justify the use of the site-correction technique and to demonstrate the robustness of the results across site. This Appendix includes some of the work included for that response to reviewers.

To account for site variability, this study prospectively acquired images for eight healthy adults scanned twice at all four sites. We repeated the analysis from the original manuscript to investigate the effect of adding site as a covariate to uncorrected ROI-to-ROI matrices. In general, covarying by site made little difference to our significant findings between the two groups, but the t-statistics were systematically smaller when covarying by site (~0.1 lower) than when using site corrections from travelling phantoms (Table B1). As a result, of the three functional connections that had statistically significant group differences in FASD, only one connection (anterior cingulate to right posterior parietal) surpassed the statistical threshold of  $p < 0.05$ . This could either be explained by a combination of two factors: 1) corrections based on traveling subjects are more accurately reducing between site variance in functional connectivity values or 2) the degrees of freedom are reduced when adding site as a covariate reducing the sensitivity of this technique to detect group differences.

**Table B1.** Results of linear regressions for an effect of group (FASD versus controls) calculated using two different site correction techniques independently.

Functional Connection	Site Correction Using Traveling Subjects		Site as a Covariate	
	T-stat (127)	FDR Correct P-val	T-stat (124)	FDR Correct P-val
Saliency Anterior insula (R) to Frontal Parietal PPC (R)	3.76	0.0455	3.68	0.0615
Saliency Anterior insula (L) to Language pSTG (R)	3.63	0.0474	3.53	0.0683
Frontal Parietal PPC (L) to Saliency ACC	4.40	0.0078	4.31	0.0113

Secondary analysis was conducted separating participants by site: 1.5T Siemens University of Alberta (24 FASD, 30 Controls), 3.0T Siemens Queens University (18 FASD, 14 Controls), 3.0T Siemens University of Manitoba (10 FASD, 8 Controls), 3.0T Philips University of British Columbia (14 FASD, 15 Controls). Average seed-based connectivity maps were generated with the anterior cingulate seed for each site for the childhood/adolescent control and FASD groups separately (Figure B1). The anterior cingulate seed was chosen for this example because analysis of the entire group showed distinct differences in FASD relative to controls. Average connectivity maps from the 1.5T scanner showed a pattern of weaker positive and negative functional connectivity compared to the other sites. Even with these notable differences across sites, lower connectivity was located in the left temporal lobe and left parietal cortex in the average connectivity maps of the FASD group at each site.

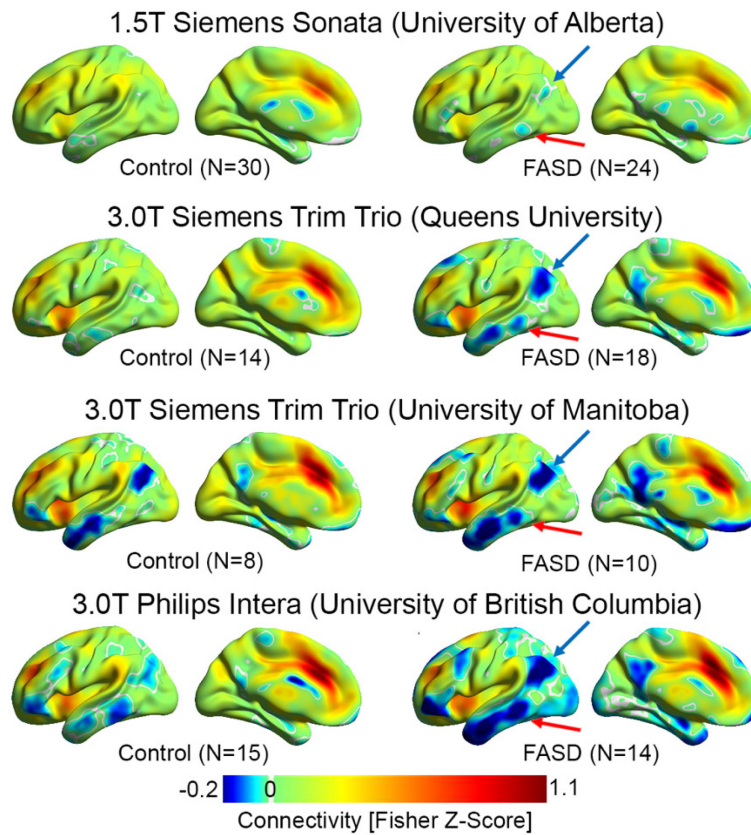


**Figure B1.** Average connectivity maps (anterior cingulate cortex seed) separated by site and group. Absolute functional connectivity was lower at the 1.5T site compared to the 3T sites. Functional connectivity was lower in the FASD group in the posterior parietal cortex (blue arrow) and the temporal lobe (red arrow) at all 4 sites.

Secondly, the three connections that had statistically significant group differences when considering participants across all sites were examined separately at all four sites to see if lower connectivity in the FASD group was consistent across all sites (Figure B2). Mean functional connectivity appeared lower in the FASD groups across all sites, adding to the robustness and confidence of our primary findings.

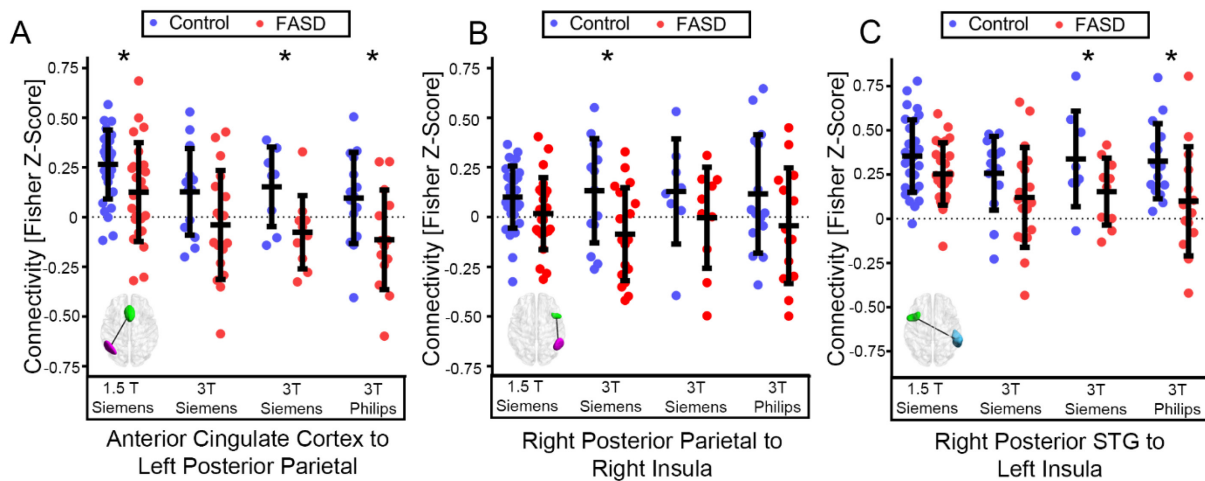


**Figure B2.** Comparison of functional connectivity values per site for the three ROI-to-ROI connections that showed statistically significant FASD versus control group differences over the entire sample. Functional connectivity values (uncorrected for site) are shown for three connections (A-C) for FASD (red) and Control (blue) at all four sites: 1.5T Siemens Sonata (University of Alberta), 3T Siemens Trim Trio (Queens University), 3T Siemens Trim Trio (University of Manitoba), and 3T Philips Intera (University of British Columbia). Average functional connectivity appeared lower in FASD in all three connections at all 4 sites. When separating the sample by site, statistically significant differences (\* t-test uncorrected  $p < 0.05$ ) indicated lower connectivity in FASD at three sites for the anterior cingulate cortex to the left posterior parietal cortex connection (A), at one 3T site for the right posterior parietal cortex to right insula connection (B) and at two 3T sites for the right posterior STG to left insula connection (C). ROI, region of interest; STG, superior temporal gyrus.

## 7 Anisotropy of the Human Cerebral Cortex Segmented on Diffusion MRI<sup>3</sup>

### Abstract

Diffusion tensor imaging (DTI) of the cerebral cortex reveals diffusion anisotropy, albeit less than white matter, with mostly a radial orientation of the primary eigenvectors to the cortical surface. The inner and outer boundaries of the cortex are usually defined on 3D-T1-weighted images and then applied to the co-registered DTI, but this is prone to registration errors given distortion of diffusion images acquired with the typical 2D-EPI. Given the thickness of the cortex, typical segmentation methods require high-resolution imaging with sufficient gray-white matter contrast to delineate the cortical boundaries. Here an automatic cortical boundary segmentation method was developed to work directly only on the native DTI images by using fractional anisotropy (FA), mean diffusivity (MD) and mean diffusion weighted images (DWI), the latter with excellent gray-white matter image contrast. This new method was applied to 15 healthy young adults (10 cross-sectional, 5 test-retest) to measure FA, MD, and radially of the primary eigenvector across the cortex on whole-brain 1.5 mm isotropic images acquired at 3T. The proposed method accurately segmented the cortical boundaries for all individuals in the cross-sectional and test-retest cohorts. Both FA ( $\sim 0.15$ ) and MD ( $\sim 0.75 \times 10^{-3} \text{ mm}^2/\text{s}$ ) were relatively stable across the cortex, although focal regions such as the post-central sulcus, anterior insula, and medial temporal lobe showed higher FA. The primary eigenvectors were primarily oriented radially to the cortex surface, but there were tangential orientations in the sulcal fundi as well as in the post-central sulcus. The proposed method demonstrates the feasibility and accuracy of cortical analysis in native DTI space while avoiding the acquisition and potentially problematic registration of other imaging types like 3D T1-weighting.

---

<sup>3</sup> submitted currently in review

## 7.1 Introduction

There has been growing interest in diffusion magnetic resonance imaging (MRI) of the cerebral cortex given improvements in scanner hardware and acquisition methods that enable the necessary high spatial resolution (see recent reviews – (Assaf, 2019; Kroenke, 2018)). Early on, diffusion MRI yielded interesting observations of high anisotropy with primary eigenvectors perpendicular to the cortical surface in neonates, followed by a reduction of this anisotropy with development (see review – (Neil and Smyser, 2018)). Although those studies showed that this anisotropy diminished with age, ex vivo and in vivo studies listed below suggested that cortical anisotropy persisted to adulthood, albeit less than that observed in the more commonly investigated and highly anisotropic white matter (WM) tracts.

Ex vivo diffusion MRI studies with much higher spatial resolution (e.g.  $0.5 \times 0.5 \times 0.5 \text{ mm}^3$ ,  $0.8 \times 0.8 \times 0.8 \text{ mm}^3$ , or  $0.94 \times 0.94 \times 0.94 \text{ mm}^3$ ) than typically used in vivo have demonstrated radial anisotropy in the adult human cortex (McNab et al., 2013, 2009; Miller et al., 2011), likely reflecting the orientation of the radial glia that provide the scaffolding for neural migration during development. Lamina specific patterns of radial and tangential diffusion relative to the cortex (Aggarwal et al., 2015; Leuze et al., 2014) and dependence of fractional anisotropy (FA) and mean diffusivity (MD) on cortical depth (Kleinnijenhuis et al., 2013) have also been shown in ex vivo human cortex. Variability in the diffusion signal across the cortex has enabled segmentation of cortical layers that are in agreement with histology (Bastiani et al., 2016). Radiality in the cortex was associated with microstructure of the cortical columns in multiple sclerosis post-mortem (McKavanagh et al., 2019) suggesting sensitivity to neuropathology.

In vivo studies with high spatial resolution ( $\sim 1 \times 1 \times 1 \text{ mm}^3$ ) have also observed diffusion anisotropy in the adult cortex, with a predominantly radial orientation relative to the cortical surface (Gulban et al., 2018; Heidemann et al., 2010; McNab et al., 2013), in agreement with the ex-vivo studies. In addition, a primarily tangential diffusion orientation relative to the cortex surface has been observed in the post-central sulcus (McNab et al., 2013), the sulcal fundi (Gulban et al., 2018), and regions of the parietal and occipital lobes (Golay et al.,

2002). Microscopic FA in the cortical grey matter (GM) has persisted even when minimizing WM signal via inversion recovery, suggesting that cortical anisotropy is not driven by adjacent WM (Lawrenz and Finsterbusch, 2019). The diffusion tensor is changed with proximity to the cortical surface such that decreased radiality, decreased MD and increased FA is associated with deeper cortical and sulcal depths using varying resolutions such as 3 mm isotropic at 3T (Kang et al., 2012), more moderate resolution (0.6 mm x 0.6 mm x 3 mm) at 3T (Truong et al., 2014), or high resolution (1 mm isotropic) at 7T (Kleinnijenhuis et al., 2015). Notably, radiality of the primary diffusion direction peaks in the middle of the cortex (Kleinnijenhuis et al., 2015; Truong et al., 2014) reflecting either partial volume measurements with superficial white matter and surrounding cerebrospinal fluid (CSF) or may reflect differences in laminar microstructure across the cortex. Diffusion MRI has been able to parcellate the cortex (Ganepola et al., 2018; Nagy et al., 2013), suggesting sensitivity to regional cytoarchitectonic differences. The Human Connectome Project (1.25 mm isotropic, multi-shell, hour long scan) diffusion imaging studies of the human cortex have shown regional differences of neurite density (Fukutomi et al., 2018), fibre orientation distribution patterns across the cortex that correspond with known patterns of myeloarchitecture (Calamante et al., 2018), and a gyral coordinate system to predict fibre orientations (Cottaar et al., 2018).

Notably, the majority of these in-vivo diffusion MRI studies of the cortex typically use an additional anatomical image (e.g. 3D T1-weighted) for delineation of the inner and outer cortical boundaries with available methods (Dale et al., 1999; Kim et al., 2005), which is then transferred to the co-registered diffusion images. However, this is prone to registration errors given the spatial distortions of diffusion images acquired with 2D single-shot echo planar imaging (EPI), as has been previously discussed (Cottaar et al., 2018). There would be a number of advantages to identify the cortex on the diffusion images/maps directly. Previous studies have shown promise in using diffusion MRI to segment brain tissue (i.e. WM, GM, CSF) using measurements extracted from both the diffusion tensor (Hasan et al., 2007; Yap et al., 2015) and models requiring the acquisition of multiple shells (Jeurissen et al., 2014). However, to investigate diffusion measurements relative to the cortex, GM tissue must be further segmented into cortical / non-cortical GM and then modelled as a 3D surface to calculate radiality.

Here an automatic cortical boundary segmentation method is presented that follows the same framework as previously proposed cortical segmentation algorithms, but it is applied directly on the DTI images and maps. The proposed method requires whole-brain diffusion MRI acquired at a high enough spatial resolution to clearly delineate the cortex on a mean DWI. The new method uses a surface deformation procedure similar to those previously proposed for cortical segmentation of anatomical T1/T2 weighted images (Dale et al., 1999; Kim et al., 2005), but uses quantitative parameters calculated from the diffusion tensor (i.e. FA and MD) along with the image intensity of the mean DWI image to first classify brain tissue and then deform a 3D surface model to the inner and outer cortical boundaries. This new method was evaluated for segmentation accuracy on whole-brain 1.5 mm isotropic diffusion images acquired in 3.5 minutes at 3T. FA, MD, and radially were extracted from parcellations of the cortical regions in a cross-sectional cohort of 10 healthy young adults. Test-retest reliability of the cortical diffusion measurements were assessed in a separate cohort of 5 healthy young adults.

## **7.2 Materials and Methods**

### **7.2.1 Participants, Data Acquisition and Pre-processing**

This study was approved by the Human Research Ethics Boards at the University of Alberta and written informed consent was obtained from all individuals prior to study participation. For cross-sectional analysis, 10 healthy adult participants ( $26.5 \pm 6.1$ , 20-38 years; 3 females) underwent diffusion tensor imaging (DTI) on a 3T Siemens Prisma (64 channel head coil). For reliability analysis, 5 additional participants ( $24.9 \pm 3.8$ , 22-31 years; 3 females) underwent 2 imaging sessions ( $2.0 \pm 2.2$ , 1-6 days between imaging sessions). Diffusion tensor imaging was acquired with a single-shot EPI spin-echo sequence: multi-band=2, GRAPPA R=2, 6/8 partial Fourier, 6 b0, 30 b1000 s/mm<sup>2</sup>, 30 b2000 s/mm<sup>2</sup> (not used here), TR=4700 ms, TE=64 ms, FOV=220 mm, 90 1.5 mm slices with no gap, 1.5x1.5 mm<sup>2</sup> zero-filled to 0.75x0.75 mm<sup>2</sup> in-plane, and 6 min scan (although only 3.5 min for just b0 and b1000). A brain mask was generated on the mean b0 image (BET, FSL v6.0.2) and image volumes were corrected for eddy current distortions/motion (FSL v6.0.2, eddy). Tensor models were fit (DIPY v0.15.0) outputting fractional anisotropy (FA), mean diffusivity (MD), and primary eigenvector maps. Additionally, a mean b1000 diffusion

weighted image (DWI) was output and was normalized using N4 correction based on the spatial variations of signal intensity estimated from the mean b0 image. The diffusion weighted image and diffusion parameter maps are visualized in Figure 7.1. Striking WM / GM contrast is observed on the mean DWI with a contrast to noise ratio (CNR) of 40. CNR was calculated from a single subject as the average GM voxel intensity minus average WM voxel intensity divided by the standard deviation of the intensity from a noise ROI represented by a cube on the corner of the image.

## 7.2.2 Voxel-Based White Matter Segmentation

Previously proposed cortical segmentation algorithms (Dale et al., 1999; Kim et al., 2005; Schuh et al., 2017) on T1 or T2 weighted images (not used here) first require a pseudo white matter mask of voxels identified as WM, subcortical GM (excluding hippocampus and amygdala) and ventricles. Here a pseudo white matter mask is generated based on FA and MD parametric maps and the mean b1000 DWI. To initialize a region growing algorithm, a subset of voxels on the mean b1000 DWI were initially labeled as one of the following three tissue categories, either GM, WM, or non-brain tissue (includes cerebro-spinal fluid). Voxels were labelled using tensor parameters as WM ( $FA > 0.25$ ), GM ( $FA = 0.05 - 0.15$  or  $MD = 1.0 - 1.2 \times 10^{-3} \text{ mm}^2/\text{s}$ ) or non-brain tissue ( $MD > 1.2 \times 10^{-3} \text{ mm}^2/\text{s}$ ). Notably the lower and upper MD bounds chosen for GM will label voxels that reflect partial volume measurements of CSF and GM but was selected to ensure that GM voxels fully enclose the perimeter of the cerebrum. Mean brain intensity and standard deviation was calculated on the mean b1000 DWI across all labeled GM and WM voxels. These intensity values were used to correct misclassified voxels from the tensor-based segmentation. Voxels with high intensity primarily located in the cortex (mean DWI intensity  $>$  mean brain intensity  $+ 2$  standard deviations) were labelled GM and voxels with low intensity values exterior to the cortex (mean DWI intensity  $<$  mean brain intensity  $- 2$  standard deviations) were labelled as non-brain tissue. This initial voxel labelling creates a segmented image where most voxels are labeled except for in regions adjacent to GM/WM boundary and medial/lower depths of the cortex which are labelled in the following steps.

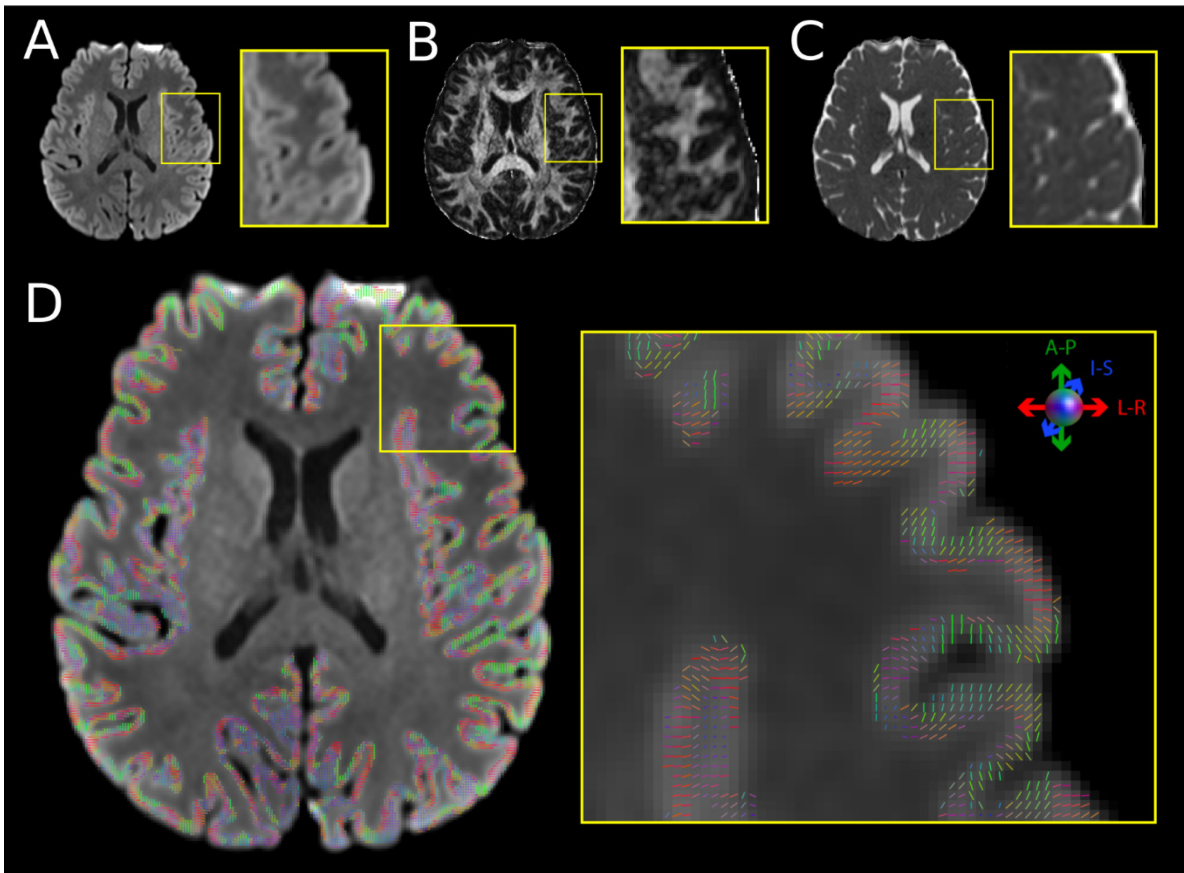


**Figure 7.1.** (A) Mean b1000 DWI, (B) FA map and (C) MD map acquired with  $1.5 \times 1.5 \times 1.5 \text{ mm}^3$  resolution (zero-filled in-plane by two in these images) at 3T in 3.5 minutes for whole brain. The mean b1000 DWI shows excellent grey-white matter contrast whereas the FA and MD maps highlight the white matter and outer cortical surface, respectively. (D) Primary eigenvectors from tensors are overlaid on a cortical segmentation of the mean b1000 image. Radial orientation normal to the curvature of the cortex was primarily observed in the crown of gyri.

In order to generate a pseudo-white matter mask, all WM and brain structure contained within the cortex of the cerebrum must be identified; the presented method accomplishes this by using a non-linear transformation from MNI space to the subject's native image space by registering the FSL Human Connectome 1065 FA template (included in FSLv6.0.2) to the subject's FA map (FLIRT/FNIRT FSLv6.0.2). Three masks were generated for the cerebellum, subcortical grey matter, and hippocampus/amygdala in MNI space by merging associated FreeSurfer anatomical segmentation labels provided in the Human Connectome processing pipeline (Glasser et al., 2013). The masks were then transformed from MNI space to each subject's native image space using the previously calculated transformation. Voxels in the subcortical mask were then labelled WM whereas hippocampus/amygdala were labelled GM. Finally, unlabeled voxels were then labelled either GM or WM using the intensity of the mean b1000 image as input to a random walker algorithm (scikit-image v0.16) outputting a singular cluster of WM voxels. This WM segmentation was then split into left and right hemispheres using an additional mask of the medial boundary. Initial tissue segmentations and an initial voxel-wise WM segmentation are shown for a single subject in Figure 7.2B and 7.2C, respectively. A surface model consisting of vertices (~175000) and edges was generated for each hemisphere with the Medical Imaging Registration Toolbox (MIRTK v2.0.0) along the boundary of the voxel-based WM segmentation. This surface was then smoothed (Laplacian smoothing, 300 iterations, relaxation factor of 0.1) and the topology of the surface corrected to be consistent with a sphere using FreeSurfer v6.0 (Fischl, 2012).

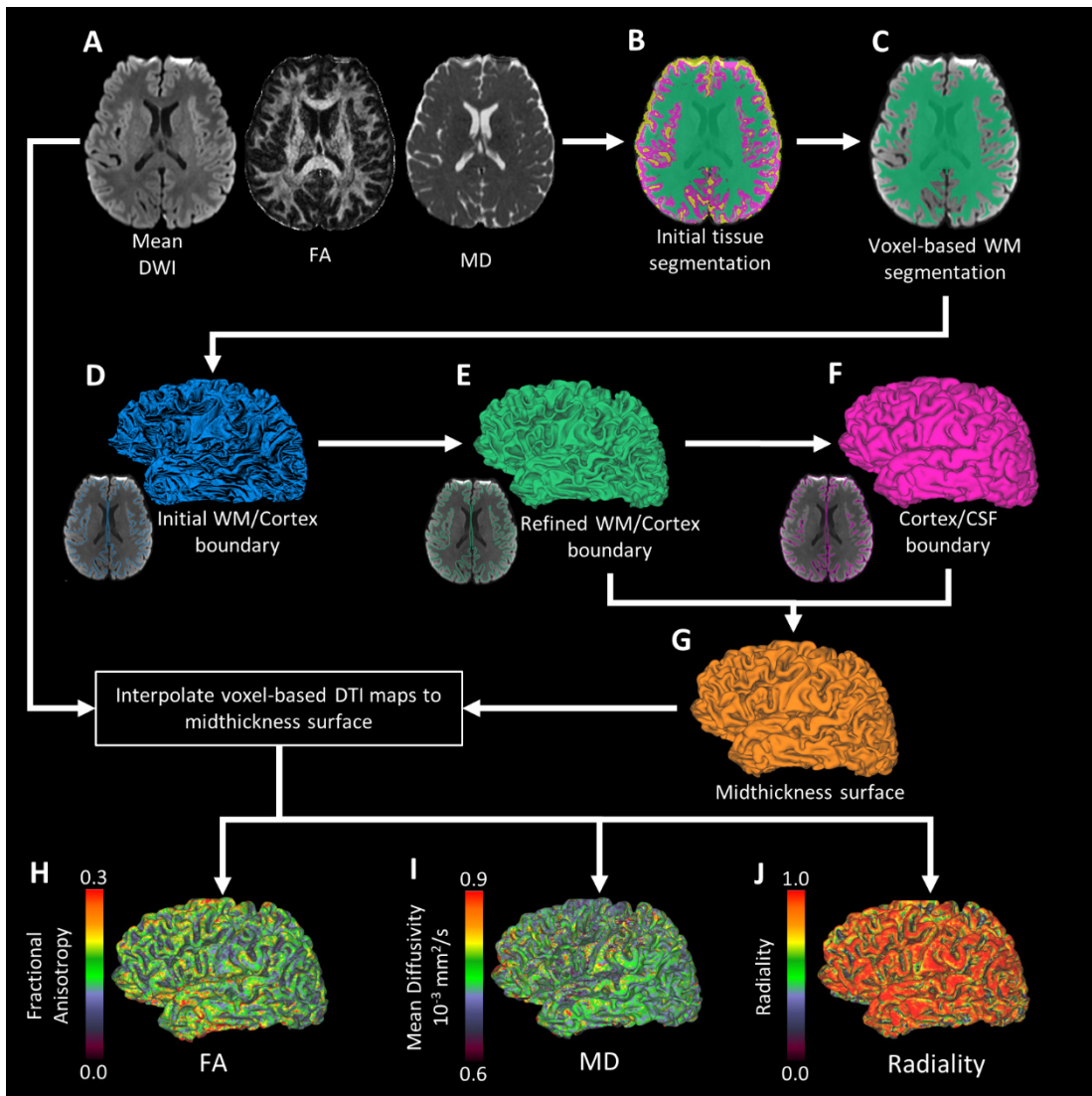


**Figure 7.2.** Cortical segmentation workflow in native DTI space using mean b1000 images, and FA/MD maps. (A, B) Voxels are classified from FA/MD into white matter (WM), grey matter (GM), and cerebrospinal fluid (CSF), and then filling subcortical grey matter/ ventricles with registration to brain atlas. (C) Unlabeled voxels are then filled using a random walker algorithm outputting a singular cluster of WM voxels that is then separated into left and right hemispheres. (D) The WM segmentation is tessellated and then smoothed to create an initial WM /cortex surface that is deformed to closest edge on the mean DWI while using the tensor-based force yielding a (E) refined WM / cortex boundary. (F) The refined WM / cortex surface is moved outward along the surface normal to the low intensity edge on the mean b1000 DWI to generate the cortex / CSF boundary surface. (G) A midthickness surface is generated halfway between the WM/ cortex and cortex / CSF surfaces and is used to extract (H) FA, (I) MD, and (J) radiality from within the cortical boundaries.

### 7.2.3 Surface-Based Inner and Outer Cortical Boundary Segmentation

Typically used cortical segmentation algorithms (Dale et al., 1999; Kim et al., 2005) on T1 or T2-weighted images (neither one used here) take a surface model as input and move vertices to high contrast regions along the white/grey matter and grey/CSF (pial) boundaries while constraining the curvature and self-intersection properties of the surface. In general, these algorithms iteratively apply surface deformations based on external/internal forces calculated per vertex upon each iteration. In conventional methods, external forces are based on the image intensities of a T1 or T2-weighted image and are used to move the surface to a target boundary along the cortex. In contrast, internal forces are calculated based on the properties of the surface itself (i.e. internally) such as local curvature or vertex position relative to the surface. Internal forces are used to regulate the curvature (i.e. prefer a smooth surface) and promote equidistant spacing between vertices.

Here, a method is proposed that uses the excellent WM/GM contrast on the mean b1000 DWI, as well as FA and MD parametric maps to segment the cortex. Here the WM / cortex and cortex / CSF surfaces are obtained in each participant by deforming the initial WM surface model using the MIRTk with external/internal forces (for details on surface deformation using internal/external forces see (Schuh et al., 2017)). Each force requires the selection of force weights (i.e. the contribution of force to surface deformation) and various parameters that are specific to each external/internal force. The developmental Human Connectome Project (dHCP) cortical segmentation pipeline designed for use with T1 and T2 weighted images (Makropoulos et al., 2018) has validated the parameters chosen for each force through visual inspection of resulting surfaces and for this reason, where possible, parameters were matched to those from the dHCP pipeline, whereas weights were chosen experimentally based on the accuracy of the resulting surfaces.

In the current work, two external forces were used for surface deformation. First, as in previously proposed methods for cortical segmentation (Kim et al., 2005; Schuh et al., 2017), an edge distance force was calculated. However, rather than T1 or T2-weighted images, the mean b1000 DWI intensity is used to identify image edges (weight 1.4, parameters: edge smoothing 1 mm, closest maximum of gradient calculated along surface normal). To restrict the movement of the surface across large sulcal gaps (e.g. central sulcus) where the

intensity gradient is the same for the WM / cortex and opposing cortex / CSF boundary, a second force is applied based on FA, MD and mean DWI intensity. For this force a tensor-based force map is generated by multiplying the FA map by -1 adding an offset of 0.2 (the target FA value for the WM /cortex boundary) and setting CSF voxels ( $MD > 1.2 \times 10^{-3} \text{ mm}^2/\text{s}$  or mean DWI intensity  $< \text{mean brain intensity} - 2 \text{ standard deviations}$ ) to a value of 1.0. An example tensor-based map is visualized in Figure 7.3A and has negative values (where surface is pushed outward) within white matter regions, positive values (where surface is pushed inward) in areas of cortex / CSF and a value of  $\sim 0$  in areas adjacent to the WM / cortex boundary. A force is calculated for each vertex/iteration as the distance to the minimum value along the surface normal on the tensor-based force map (weight 1.6, smoothing 1 mm). Effectively, when applied together the edge distance force and tensor-based force will favor WM / cortex edges on the mean b1000 DWI with an FA of 0.2 (the FA offset on the tensor-based force map), while discouraging deformations into regions of CSF or GM that have positive values in the tensor-based force map. Notably, without the addition of the tensor-based force, surface deformations will propagate across large sulcal gaps (e.g. central sulcus) where the intensity gradient of the WM /cortex boundary is similar to the CSF / cortex boundary on the opposing side of the sulci (Figure 7.3B). As performed in the dHCP pipeline (Makropoulos et al., 2018) and to avoid overfitting of the surface to local anomalies in mean DWI intensity, external forces were applied using 3 levels of averaging from neighboring vertices (level 1 neighboring forces averaged 4 times, level 2: neighboring forces averaged 2 times, and level 1: neighboring forces averaged once).

Internal forces used here, namely repulsion, mean curvature and gaussian curvature forces, are the same as those used for the dHCP cortical segmentation pipeline (Makropoulos et al., 2018). In the current study, parameters for these internal forces match those in the dHCP pipeline; however, weights for internal forces were chosen experimentally to ensure that the resulting surfaces followed the WM/cortex boundary. Internal forces used were: repulsion force (weight 4.0, parameters: front facing radius 0.5 mm, back facing radius 1.0 mm), mean curvature force (weight 4.0), gaussian curvature force (weight 1.0, parameters: minimum 0.1, maximum 0.2, outside 0.5).

Internal and external forces are applied using 100 iterations for each level of the external force averaging which provided the iterations necessary for the surfaces to deform into the WM/cortex boundary. Surface self-intersection was avoided by preventing vertices from moving closer than a distance of 0.1 mm to the surface. To constrain the distance between neighboring vertices upon each iteration, the surface is resampled such that each vertex is between 0.5 mm to 1.0 mm to all neighboring vertices. Following this initial surface deformation, 300 iterations are performed without the tensor-based force but with all other previously used forces/parameters, allowing the surface to expand into the WM/cortex boundary within some gyral crowns where the target FA value of the tensor-based force (0.2) is not accurate (Figure 7.3C).

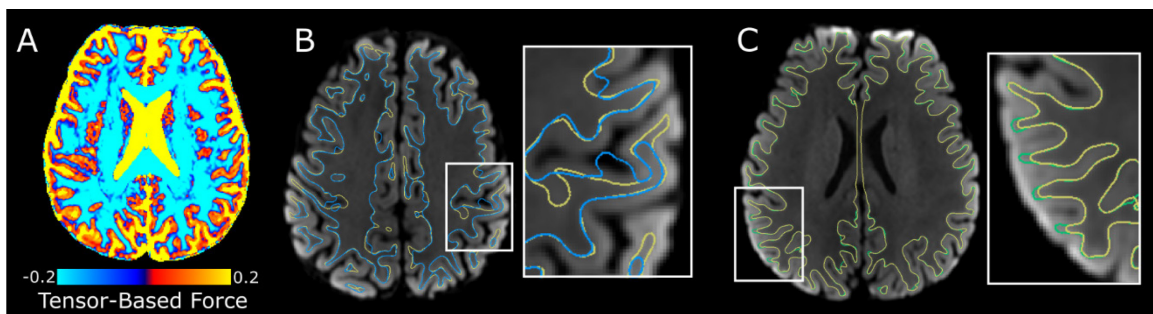


**Figure 7.3.** (A) Tensor-based force generated from FA / MD maps and mean DWI intensities. Areas in blue / light blue (force amplitude  $< 0$ ) indicate regions with an outward force, whereas yellow/red areas (force amplitude  $> 0$ ) indicate regions with an inward force. (B) Visualization of WM / cortex surfaces generated while using both an edge-based force and the tensor-based force (yellow) compared to surfaces generated using only the edge-based force (blue). Without the application of the tensor-based force, the surface deformations propagate over large sulcal gaps to areas where signal intensities change from low to high on the opposing side of the surface. (C) Visualization of the final surface deformation where the WM / cortex surface generated while using both an edge-based force and the tensor-based force (yellow) is further refined using only the edge-based force (green) to allow the surface to expand properly into the WM / cortex boundary of the gyral crowns.

To generate the cortex / CSF surface, the WM / cortex surface is first expanded 1.5 mm outwards along the surface normal (normal force 0.25, 500 iterations, max displacement 1.5 mm) while using the same internal forces used previously. This intermediate surface is then deformed to the cortex / CSF boundary by optimizing the edge distance force on the mean b1000 DWI (weight 1.0, smoothing 1 mm, edge force averaging levels/iterations: 4:100, 2:100, 1:200), again using the same internal forces used for the WM / cortex deformations. Both WM / cortex and cortex / CSF surfaces were projected to axial, coronal, and sagittal image slices and qualitatively inspected for segmentation accuracy.

### **7.2.4 Surface-based Diffusion Measurements**

To minimize diffusion measurements from non-cortical voxels, a medial surface was created by finding the half-way point between the inner/outer cortical boundaries (i.e. the Euclidean mean of corresponding WM / cortex and cortex / CSF vertex coordinates). FA, MD, and primary eigenvector values were interpolated onto mid-thickness surface vertices using the value of the enclosing voxel. The radially index measures how aligned a tensor is relative to the normal of a surface and is calculated here as the absolute value of the dot product of the mid-thickness surface normal and the primary eigenvector interpolated at each mid-thickness vertex.

### **7.2.5 Spherical Registration and Regional Analysis**

Patterns of cortical folding especially in large sulci (e.g. central sulcus) are consistent between healthy individuals, thus surface-based registration techniques predominantly rely on measurements of sulcal depth to align a subject's cortical surface to a template. To calculate sulcal depth, the WM / cortex surface model was inflated using FreeSurfer v6.0. For registration purposes, the inflated surface was mapped to a sphere using FreeSurfer v6.0 (Fischl, 2012). The subjects were then registered to the population average template (Van Essen et al., 2012) using the Multimodal Surface Matching algorithm (Robinson et al., 2014) by minimizing the difference between sulcal depth maps of the subject and template on corresponding spheres. To qualitatively assess regional

differences in surface-based diffusion measurements, maps of FA, MD, and radiality were resampled to the template and then averaged. Brodmann's areas distributed with the population average template (Van Essen et al., 2012) were combined to create parcellations of the temporal lobe (Brodmann's areas, 20, 21, 22, 27, 28, 35, 36, 37, 38), occipital lobe (Brodmann's areas, 17, 18, 19), parietal lobe (Brodmann's areas, 1, 2, 3, 5, 7, 23, 26, 29, 30, 31, 39, 40), frontal lobe (Brodmann's areas, 4, 6, 8, 9, 10, 11, 24, 25, 32, 33, 44, 45, 46, 47), and insula (Brodmann's areas, 41, 42, unlabeled portion of the insula). These parcellations were dilated so that all surface vertices of the template were labeled while restricting the dilation along the medial wall which contains non-cortical structures (e.g. corpus callosum and ventricles). Regional parcellations were then resampled to the subject's native space and measurements of FA, MD and radiality were extracted in native imaging space and averaged per lobe for each region. Whole-hemisphere measurements of FA, MD, and radiality were also extracted separately for the left and right hemispheres of each subject. Mean and standard deviations were calculated for FA, MD and radiality for each region per hemisphere across all 10 subjects in the cross-sectional cohort. To test for statistical differences between regions, measurements were averaged across hemispheres and regional differences were assessed by multiple pairwise t-tests (SPSS v2.4) using a Bonferroni corrected p-value ( $p\text{-value} < 0.003 = 0.05 / 15$  i.e. 3 measurements by 5 regions). Secondly, statistical differences between hemispheres were assessed separately for FA, MD, and radiality with a paired t-test (SPSS v2.4) using a Bonferroni corrected p-value ( $p\text{-value} < 0.017 = 0.05 / 3$  measurements).

### **7.2.6 Test-retest Analysis**

Segmentations of WM /cortex and cortex /CSF boundaries, along with surface-based FA, MD, and radiality maps were visually inspected for between scan consistency. Measures of FA, MD, and radiality were extracted for each regional parcellation (left and right hemisphere separate) and repeatability of each regional measure was calculated as the intraclass correlation (ICC) across the 5 subjects and 2 scans, the ICC(A, 1) two-way random, single-score model (Mcgraw and Wong, 1996). ICC values range from 0 (no agreement between repeated measurements) to 1 (absolute agreement between repeated measurements) with values interpreted as poor (ICC

< 0.5), fair (ICC 0.5 to 0.75), good (ICC 0.75 to 0.9), excellent (ICC > 0.9) (Koo and Li, 2016). Additionally, the difference between scan 1 and scan 2 (delta) was calculated for FA, MD, and radiality for each region per hemisphere as the value at scan 1 minus value at scan 2.

## **7.3 Results**

### **7.3.1 Cortical Segmentations on Native DTI**

The proposed automated cortical segmentation method applied to 1.5 mm isotropic DTI images/maps alone generated inner (WM / cortex) and outer (cortex / CSF) boundaries for all 15 subjects included in the study (10 cross-sectional, 5 test-retest). The entire segmentation pipeline takes ~3 hours when executed in a high-performance computing environment (Hardware: 16 cores, AMD Ryzen thread ripper 2990wx, 64 GB Ram, Linux Ubuntu 18.04 operating system). Example segmentations of inner and outer cortical boundaries for 3 subjects are visualized in Figure 7.4. Segmentations were qualitatively assessed and deemed accurate for most of the cortex for all subjects included in the study. Only cortical areas prone to magnetic susceptibility in the temporal lobes had noticeably poor segmentations due to distortions and image intensity shifts that negated any WM / cortex or cortex / CSF distinction on the mean b1000 DWI.

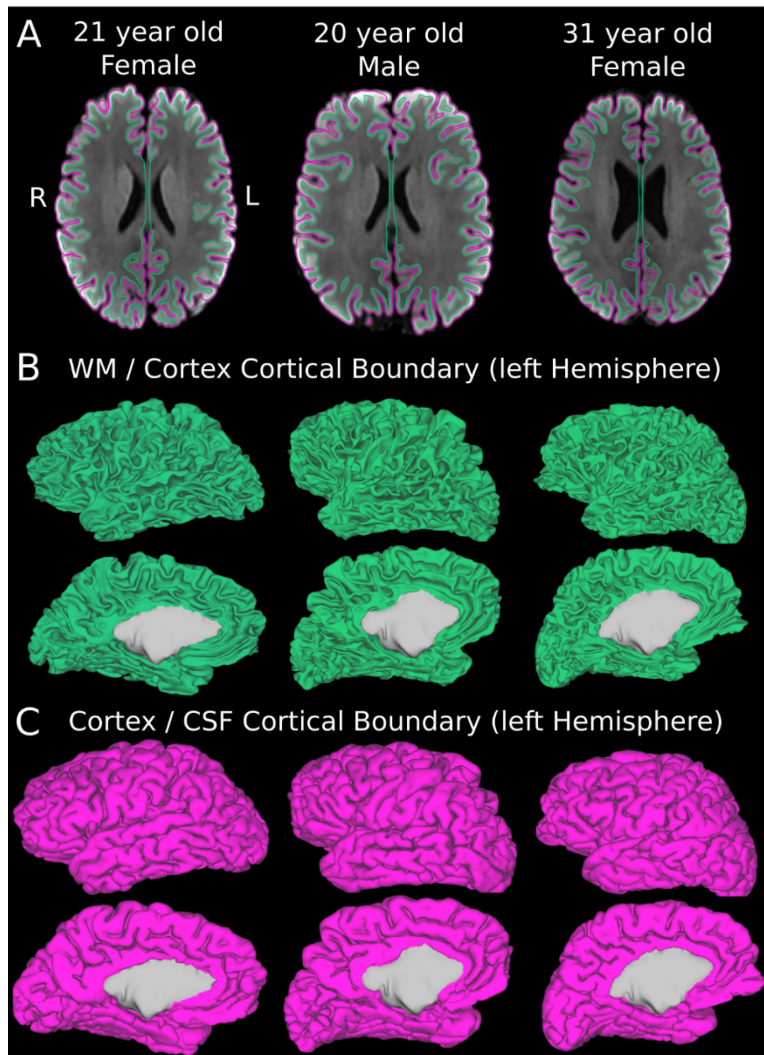


**Figure 7.4.** White matter (WM) / cortex inner boundary (green) and cortex / CSF outer boundary (pink) derived from the DTI cortical segmentation workflow displayed for three of the subjects from the cross-sectional cohort. Cortical surfaces are displayed on (A) a single slice of the mean b1000 diffusion weighted images and for the left hemisphere as 3D surfaces for (B) WM/cortex and (C) cortex/CSF. Grey regions indicate the mask of the medial wall used to restrict vertex movement and separate hemispheres. Even with substantial subject variability in cortical folding and brain size/shape, reasonably accurate cortical segmentations were generated in all cases. R – right hemisphere, L – left hemisphere.

### 7.3.2 Diffusion Measurements in Native Imaging Space

Surface-based maps of FA, MD, and radiality were generated for all 10 subjects. FA, MD, and radiality maps are displayed along with histograms for an example subject in Figure 7.5A, 7.5C, and 7.5E. FA and MD were within range of expected values for grey matter for all subjects (histogram peaks at FA  $\sim 0.15$ , MD  $\sim 0.75 \times 10^{-3} \text{ mm}^2/\text{s}$ ), suggesting that the mid-thickness surface was located within the cortical boundaries. Histograms of radiality across the cortex had a highly skewed distribution towards a radiality value of 1.0 (indicating that the primary eigenvector is perpendicular to the surface). Lower FA (FA  $\sim 0.12$ ) was observed in lateral portions of the parietal and frontal lobes relative to other regions (FA  $\sim 0.15$ ). Additionally, markedly higher FA values (FA  $> 0.3$ ) were observed along the bank of the post-central sulcus (Figure 7.5A), notably a thinner cortical area, as well as the anterior portion of the insula and medial portions of the temporal lobe. In contrast, there were no striking regional differences on MD maps. Additionally, in all subjects an increase in radiality was observed in the crowns of the gyrus (FA  $> 0.15$ ) relative to the fundus (FA  $< 0.15$ ), as well as a low radiality ( $\sim 0$ ) along the post-central sulcus where FA values were  $> 0.3$ . Average surface maps of FA, MD, and radiality were generated for the 10 subjects and are displayed on the average template in Figure 7.5B, 7.5D, and 7.5F. Consistent with regional difference observations in subject level maps, average maps showed decreased FA values in portions of the parietal and frontal lobes relative to the rest of the cortex. Additionally, areas of high FA ( $> 0.3$ ) corresponded to regions with low radiality ( $< 0.2$ ) and were observed along the post-central sulcus.

As outlined in the methods, average regional measurements of FA, MD and radiality were extracted for each subject using parcellations of the insula, temporal, occipital, frontal and parietal lobes with each hemisphere measured separately. Average FA, MD and radiality values of the 10 cross-sectional subjects are displayed for the 5 regions for each hemisphere in Figure 7.6. Pairwise t-tests (left/right averaged) indicated FA values were higher ( $p < 0.003$ ) in the temporal lobe ( $0.167 \pm 0.005$ ) and insular region ( $0.156 \pm 0.006$ ) relative to all other regions, and FA in the frontal lobe ( $0.147 \pm 0.004$ ) was higher compared to the parietal ( $0.136 \pm 0.003$ ) lobes. The observed regional difference in radiality was primarily driven by statistically higher ( $p < 0.003$ ) radiality in the frontal lobe ( $0.72 \pm 0.03$ ) compared to the occipital ( $0.65 \pm 0.02$ ) and parietal ( $0.66 \pm 0.03$ ) lobes, whereas no statistical difference was observed in radiality values for the insula ( $0.70 \pm 0.03$ ), and temporal lobe ( $0.68 \pm 0.03$ ) relative to

any other regions. MD values were largely consistent across most regions namely, the frontal ( $0.77 \pm 0.01 \times 10^{-3}$  mm<sup>2</sup>/s), temporal ( $0.76 \pm 0.01 \times 10^{-3}$  mm<sup>2</sup>/s), and occipital ( $0.77 \pm 0.02 \times 10^{-3}$  mm<sup>2</sup>/s) lobes, with higher ( $p < 0.003$ ) MD values observed in the parietal lobe ( $0.78 \pm 0.01 \times 10^{-3}$  mm<sup>2</sup>/s) relative to the insula ( $0.76 \pm 0.01 \times 10^{-3}$  mm<sup>2</sup>/s). Paired t-tests indicated small but statistically significant differences ( $p < 0.017$ ) between left and right hemispheres in measures of MD and radiality. Lower MD values were observed in the left hemisphere ( $0.763 \pm 0.012 \times 10^{-3}$  mm<sup>2</sup>/s) compared to the right hemisphere ( $0.775 \pm 0.012 \times 10^{-3}$  mm<sup>2</sup>/s). whereas higher radiality was observed in the left ( $0.689 \pm 0.025$ ) hemisphere relative to the right ( $0.682 \pm 0.029$ ) hemisphere.

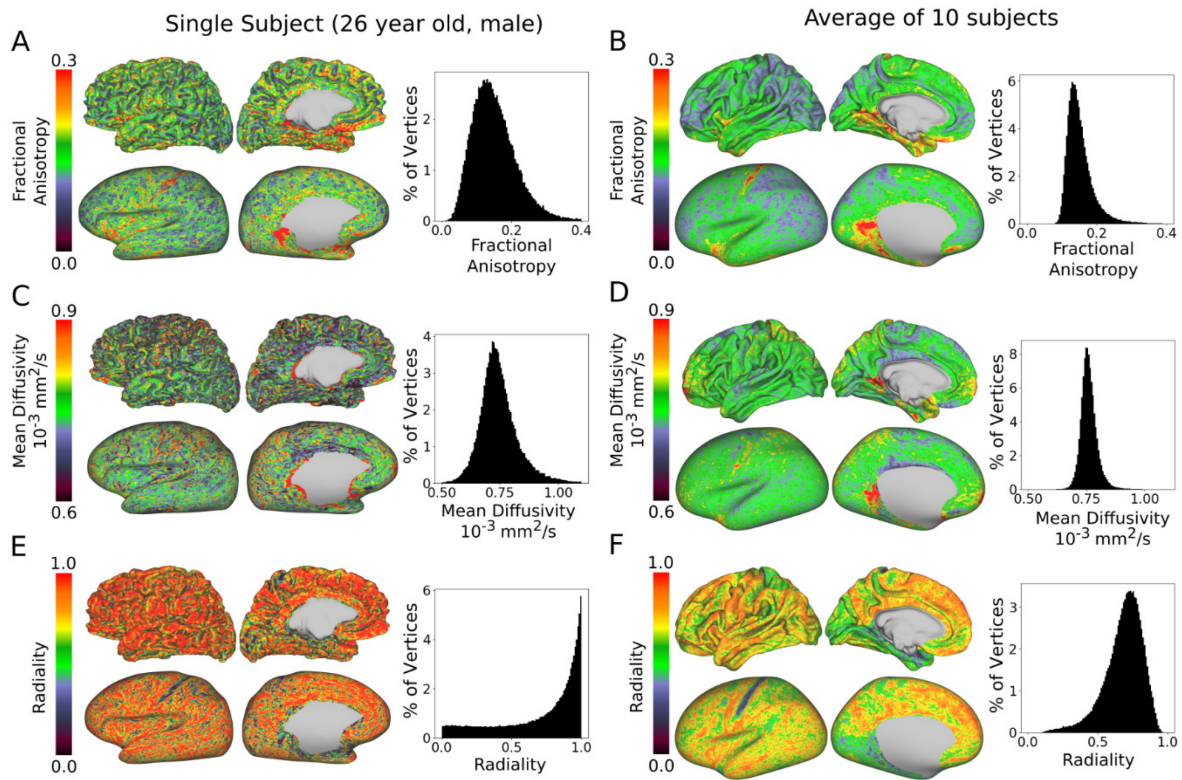


**Figure 7.5.** Diffusion parameter surface visualization on midthickness and inflated surfaces for (A, C and E) a single subject (left) and (B, D and F) average of ten subjects on the template (right). Surface-based FA, MD and radiality maps are displayed for the left hemisphere as well as corresponding histograms across the hemisphere. In both subject-level and average maps, FA/MD were generally homogeneous and within range of expected cortical grey matter values, except high FA values were observed along the somatosensory cortex, the medial temporal lobe and in the anterior portion of the insula. Radiality maps showed predominantly high radiality values with increased radiality in the crown of the gyri relative to the sulcal fundi, and a markedly lower radiality was observed along the central sulcus.

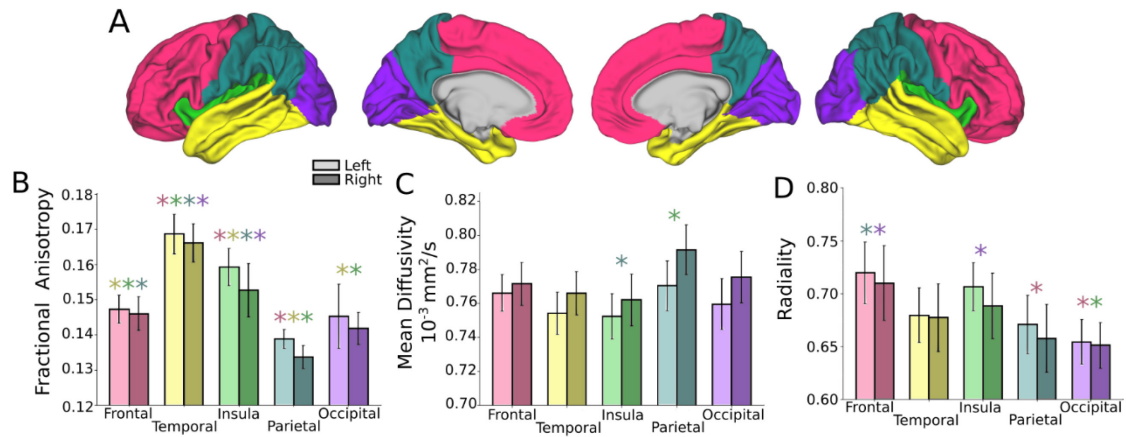


**Figure 7.6.** Average (B) FA, (C) MD, and (D) radiality across the 10 individuals in the cross-sectional cohort, along with (A) lobe parcellations displayed on the midthickness surface of the template. Color of asterisk indicate a statistical difference in pairwise t-test ( $p < 0.003$ ) with the corresponding lobe. FA values were variable between regions with the temporal lobe ( $\sim 0.17$ ) and insula ( $\sim 0.16$ ) having higher values compared to all other regions whereas frontal lobe ( $\sim 0.15$ ) had statistically higher values than the parietal lobe ( $\sim 0.14$ ). Similar MD values were observed across all regions with values  $\sim 0.77 \times 10^{-3} \text{ mm}^2/\text{s}$ , with higher MD values were observed in the parietal lobe ( $\sim 0.78 \times 10^{-3} \text{ mm}^2/\text{s}$ ) compared to the insula ( $\sim 0.76 \times 10^{-3} \text{ mm}^2/\text{s}$ ). Radiality was higher (\*,  $p < 0.003$ ) in the frontal lobe ( $\sim 0.71$ ) relative to the parietal ( $\sim 0.66$ ) and occipital lobes ( $\sim 0.65$ ).

### 7.3.3 Test-retest repeatability

Surface-based maps of FA, MD, and radiality were generated for all 5 subjects in the test-retest cohort. Maps of FA, MD, and radiality for an example subject scanned twice are visualized in Figure 7.7. Maps of FA, MD and radiality had consistent patterns of regional variation between repeat scans of the same individuals. Regional measurements of FA, MD, and radiality for all 5 participants in the test-retest cohort are presented per hemisphere in Figure 7.8, along with corresponding ICC and delta (scan 1 minus scan 2) values. Regional measures of radiality had the highest ICC values relative to repeatability measurements of FA and MD with all regional radiality measurements ranging from fair (ICC 0.5 to 0.75) to excellent (ICC > 0.9). Excellent repeatability was observed for radiality in the left (ICC 0.96) / right (ICC 0.97) frontal lobes, left (ICC 0.99) / right (ICC 0.98) parietal lobes, left insula (ICC 0.97), and right occipital (ICC 0.92) lobes, whereas good (ICC 0.75 to 0.9) reliability was observed in the right insula (ICC 0.88) and left (ICC 0.73) / right (ICC 0.85) temporal lobes. Repeatability ranged from poor (ICC < 0.5) to excellent for regional measurements of both FA and MD. Excellent repeatability for FA was observed in left (ICC 0.90) / right (0.90) frontal lobes and for MD in the left temporal lobe (ICC 0.93). Poor repeatability was observed for FA in the left (ICC 0.03) / right (ICC -0.54) temporal lobes largely reflecting the large delta (scan 1 minus scan 2) from a single subject, resulting from a poor segmentation in the inferior temporal lobe that caused overestimated FA bilaterally for this scan. Poor repeatability was observed in MD measurements of the right frontal (ICC 0.33) and right occipital (ICC 0.28) lobes.

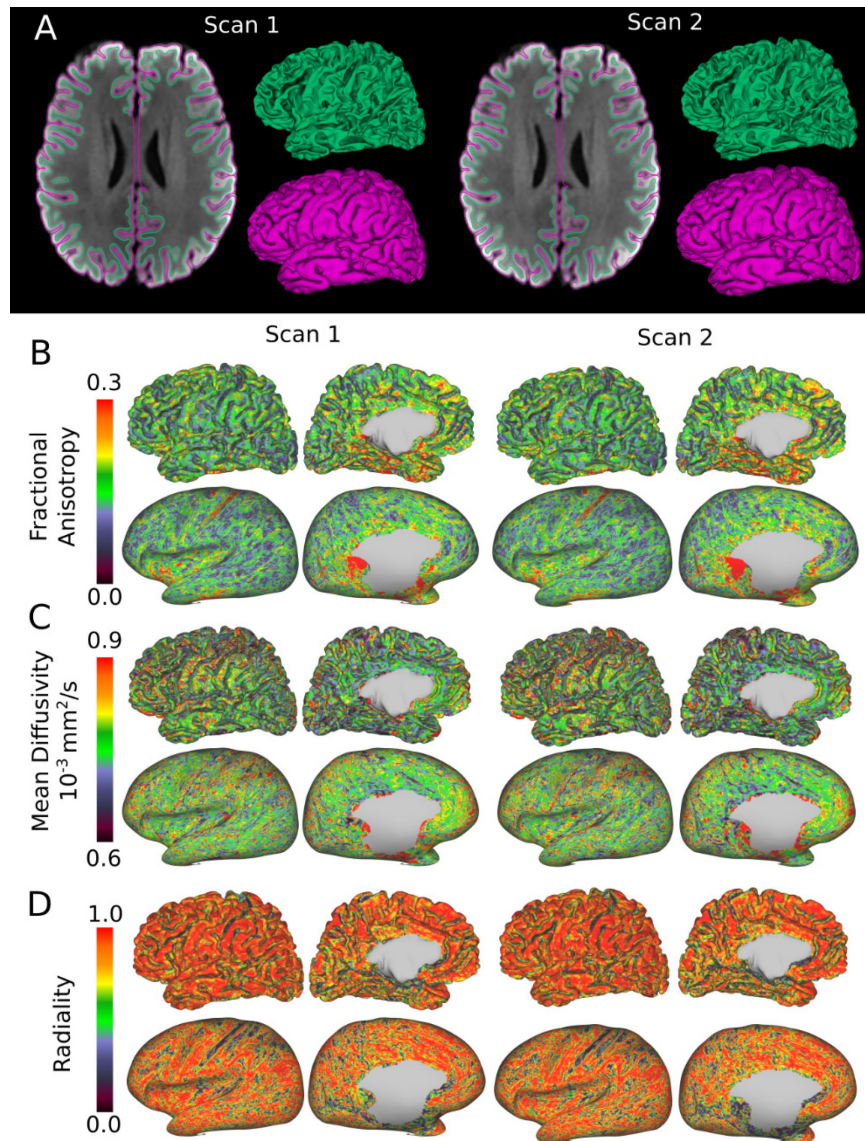


**Figure 7.7.** (A) White matter (WM) / cortex inner boundary (green) and cortex / CSF outer boundary (pink) derived from the DTI cortical segmentation for the same subject scanned twice. Surface-based (B) FA, (C) MD, and (D) radiality maps for the mid-thickness surface of the left hemisphere from the same subject. Consistent cortical segmentations and patterns for all three DTI derived maps were observed between scan 1 (left) and scan 2 (right).

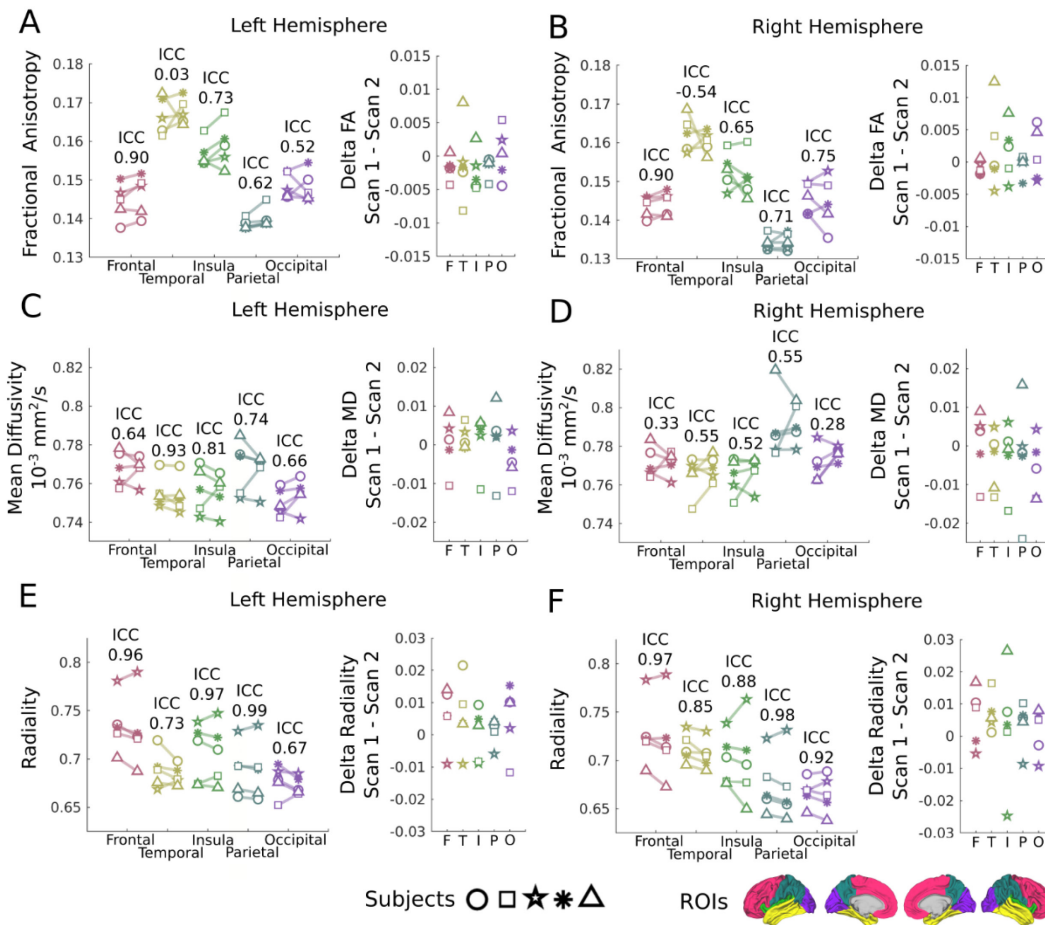


**Figure 7.8.** Average (A and B) FA, (C and D) MD, and (E and F) radiality within lobe parcellations separated by hemisphere for the 5 individuals (different shapes) in the test-retest cohort. Intraclass correlation (ICC) values are a measure of test-retest repeatability and are shown along with deltas (scan 1 minus scan 2) for each measure per lobe. FA values had excellent (ICC > 0.90) repeatability for the left/right frontal lobes whereas poor (ICC < 0.50) repeatability was observed in the temporal lobes (ICC left: 0.03, right: -0.54) that was primarily driven by markedly different FA values for a single subject (yellow triangle). MD repeatability ranged from poor to excellent with lowest repeatability, along with a smaller range of MD values, being observed in the occipital and frontal lobes. Repeatability values for radiality ranged from good (ICC 0.75 to 0.90) to excellent in 8 of the 10 regions with fair (ICC 0.5 to 0.75) repeatability in the left temporal lobe (ICC 0.73) and left occipital lobe (ICC 0.67).

## 7.4 Discussion

### 7.4.1 Cortical Segmentation on Native DTI

This study proposes a novel surface-based cortical segmentation method that is applied directly on DTI images removing the need for registration to an additional anatomical image. The method utilizes the mean b1000 DWI image which was acquired at a 1.5mm isotropic resolution to attain excellent GM/WM contrast along the cortical boundaries. Other surface-based cortical segmentation methods rely on T1 or T2 weighted image intensities. However, these methods would fail if applied to a mean b1000 DWI because of the suppressed CSF signal. Thus, we propose using a combination of mean DWI signal intensity and FA / MD values during both the tissue classification and surface-based deformation steps of the segmentation algorithm. By using DTI measurements in conjunction with image intensities, the algorithm avoids surface-deformations into the large sulcal gaps that would otherwise occur by using image intensities alone (Figure 7.3b). Using this method, accurate segmentations were generated in all cases except in areas of known increased magnetic susceptibility (e.g. lateral temporal lobe) resulting from the lack of visible WM / cortex contrast in this region. Conventional algorithms used to register DWI to anatomical images such as boundary-based registration (Greve and Fischl, 2009) rely on GM / WM contrast, thus registration with a conventional T1-weighted image would also be problematic in this region.

Diffusion measurements reported here are in the range of expected grey matter values (FA  $\sim$  0.15, MD  $\sim$   $0.75 \times 10^{-3}$  mm<sup>2</sup>/s) suggesting that tensor measurements are being extracted from the cortex and not from superficial WM or exterior CSF. Additionally, measurements of the radially of the primary eigenvectors relative to the cortex in individual subjects were high across the cortex ( $\sim$ 1.0) and histograms were in agreement with in-vivo and ex-vivo measurements of the radial orientation of the cortex using higher resolution diffusion imaging at 1 mm isotropic resolutions (Gulban et al., 2018; McNab et al., 2013), furthering support that the proposed segmentation pipeline is accurately delineating the cortex. Segmentations as well as surface-based patterns of FA, MD, and radially for each of the 5 test-retest subjects were also largely consistent between scans. Although surface segmentations on high-resolution (1mm isotropic) T1-weighted images benefit from undistorted anatomy

it is problematic to assume that cortical boundaries generated on such an image will translate properly to a typically much lower resolution (not to mention distorted) DTI scan (Kang et al., 2012). This consideration is particularly important when calculating radially (McNab et al., 2013) or orientationally invariant features (Ganepola et al., 2018; Nagy et al., 2013) which both require an accurate measurement of the direction of the cortical surface normal.

The proposed cortical segmentation algorithm requires the a priori selection of FA and MD parameters for the generation of the initial voxel-based tissue classification and the tensor-based force used in surface-deformations for the initial location of the WM/ cortex boundary. Notably both steps are subsequently updated using the image intensity on the mean b1000 DWI such that the segmentations are not biased by the selection of these initial parameters. When applied to healthy controls in this study, the a priori selected FA and MD values produced adequate initial tissue classification and WM / cortex boundaries for input into the subsequent steps. However, the current study was on neurotypical young adults, and the algorithm parameters will need to be assessed for different ages and those with clinical disorders given changes in DTI parameters.

Importantly, the proposed segmentation pipeline relied on the selection of multiple parameters specific to each internal / external force and were chosen experimentally based on the resulting cortical segmentations through visualization on 2D image slices. Similarly, previous cortical segmentation algorithms for T1-weighted images such as those included in FreeSurfer (Dale et al., 1999), CIVET (Kim et al., 2005), and dHCP cortical segmentation pipeline (Schuh et al., 2017) have also optimized force and smoothing parameters based on the accuracy of the resulting surfaces. Although the parameters reported here may be specific to the proposed data acquisition technique, it is speculated that these parameters could be optimized for other diffusion MRI protocols.

## 7.4.2 Regional Variation in Surface-Based Diffusion Measurements

Surface-based FA, MD, and radiality maps provide insight into variations of the diffusion tensor measures across the cortex. Radiality was observed to be high across the majority of cortical regions, with the exception of low values being observed in sulcal fundi and post-central sulcus. Previous studies have observed lower radiality in the sulcal fundi relative to the rest of the cortex with whole brain 1 mm isotropic diffusion MRI acquisitions in vivo at 7T (Gulban et al., 2018; Kleinnijenhuis et al., 2015) and numerous studies have reported diffusion primarily oriented tangentially to the cortical surface along the post-central sulcus in high-resolution (1 mm-1.25 mm isotropic) diffusion MRI in-vivo at 3T (Cottaar et al., 2018; McNab et al., 2013). Importantly, in this study higher FA in the expected range of white matter ( $> 0.3$ ) was observed in portions of this region suggesting that radiality measurements of the post-central sulcus measurements may reflect measurements from a lower cortical depth or potentially measurement of a partial volume effect with superficial WM and should be interpreted with caution.

In other regions, FA was largely within the expected range of grey matter ( $\sim 0.15$ ) that has been previously reported for the cortex in-vivo at b1000 at 3T (Fukutomi et al., 2019; McNab et al., 2013) acquired using 1 mm and 1.25 mm isotropic resolutions, respectively. Elevated FA values were observed in a region in the anterior portion of the insula, and in the medial regions of the temporal lobe similar to previously reported surface-based FA measurements at b1000 (Fukutomi et al., 2019). This was confirmed by regional analysis where higher FA values were observed for cortical parcellations of the insula and temporal lobe compared to all other regions and frontal lobes showed statistically higher values compared to the parietal and occipital lobes.

Repeatability of cortical FA ranged from between fair and excellent with only the temporal lobe having poor repeatability ( $ICC < 0.5$ ). To our knowledge, only one other DTI study has reported surface-based measurements of repeatability (coefficient of repeatability) and cortical patterns that suggest lower repeatability in temporal lobe, insula and regions surrounding the medial wall in an analysis using all shells (b1000, b2000, and b3000) from the HCP data (Fukutomi et al., 2018). Large methodological differences exist between these repeatability experiments including, but not limited to, cortical segmentation method, number and choice of b-values, image resolution, ROI or vertice-based measurement, and choice of repeatability measure, all of which could potentially

impact repeatability measurement. Values for MD were largely consistent ( $\sim 0.75 \times 10^{-3} \text{ mm}^2/\text{s}$ ) across the cortex in line with previously reported cortical MD values (McNab et al., 2013); however, more regional variability between cortical regions has been previously reported using the HCP b1000 data (Fukutomi et al., 2019) and may reflect the noted methodological differences between the two studies. Repeatability for MD was also poor to fair for 6 of 10 regions in the cortex that may reflect sensitivity of MD to partial volume measurement, a known issue in cortical DTI studies (Kang et al., 2012).

Regional differences in FA and radiality could be explained by regional differences in cytoarchitecture across the cortex; for example the frontal lobe is primarily composed of regions with agranular structure (relatively thicker, larger pyramidal neurons, lacking clear granular layers) whereas the occipital, and parietal lobes contain a higher proportion of regions containing granular structure (thinner, predominantly tangentially oriented myelinated fibre bands) (Triarhou, 2013; von Economo and Koskinas, 1925). Thus, these results suggest that FA and radiality may be a sensitive marker to the underlying microstructural variation of the cortex. Note that given the limited sample size of the cross-section cohort in this study ( $n=10$ ), large regional parcellations were selected to reduce the number of multiple comparisons between regions. However, the number of cortical regions in humans has been estimated to be  $\sim 150$  to  $200$  (Van Essen et al., 2012), and suggests that the regional measurements presented here could be more specific in finely defined cortical regions.

### **7.4.3 Diffusion MRI Acquisition Considerations for Measuring Cortical Anisotropy**

In this study, the proposed automatic segmentation method was applied to images acquired at 3T with a 90 slice, 1.5 mm isotropic voxels, whole brain, single b1000 shell, 30 direction DTI protocol with a scan time of 3.5 minutes (note 6-minutes here with the extra b2000 shell not used in the current pipeline) enabled by using a simultaneous multi-slice acceleration factor of 2. Previous studies have used higher b-values (e.g. b2000, b3000) to extract diffusion measures sensitive to cortical microstructure such as neurite density (Fukutomi et al., 2018; Schmitz et al., 2019), fibre orientation distribution patterns across the cortex that correspond with known patterns of

myeloarchitecture (Calamante et al., 2018) and for cortical parcellation (Ganepola et al., 2018). Future work will attempt to use the proposed segmentation pipeline along with the unused b2000 shell from the presented diffusion acquisition to model more complex structures (e.g. fibre crossings) in the cortex.

Although the resolution was lower than the 1 mm isotropic resolution used in more recent cortical diffusion studies in vivo acquired in about ~1 hour (only b1000 shell) at 3T (Gulban et al., 2018; Kleinnijenhuis et al., 2015; McNab et al., 2013), the clinically relevant scan time of 3.5 min used here makes this acquisition suitable to studies of cortical microstructure in neurodevelopmental or clinical populations. In fact, radiality measurements in this study agreed with those from higher-field and higher-resolution studies demonstrating that 1.5 mm isotropic resolution is high enough to extract such basic properties relating to cortical microstructure. Importantly, typically used cortical segmentation algorithms such as those implemented in FreeSurfer (Fischl, 2012) and CIVET-CLASP (Kim et al., 2005) analysis pipelines recommend using high resolution (1 mm isotropic) T1-weighted / T2-weighted images for cortical delineation (reflecting its thickness of 1 mm – 5 mm), and their accuracy can be improved with sub-millimeter (0.5 mm isotropic) imaging resolution (Lüsebrink et al., 2013). It is anticipated that the proposed method would benefit from similar high resolution imaging, however inherent challenges with 2D-EPI preclude straight forward implementation of 1 mm isotropic acquisitions for whole brain. For instance increased echo time, combined with smaller voxel results in a large decrease in SNR that is typically counter balanced by much longer scan times as done previously to measure DTI in the cortex (Gulban et al., 2018; Kleinnijenhuis et al., 2015; McNab et al., 2013). Novel techniques have been proposed to reduce the trade off in scan time such as 3D DTI acquisitions (Song et al., 2014) or super-resolution imaging techniques (Ning et al., 2016). Thus, future work is needed to investigate novel imaging methods in the context of cortical diffusion analysis to examine the effect of higher resolution on these measurements.

Importantly, the images used in the current study were acquired using a 64 channel receive coil, which was accounted for by bias field correcting the mean DWI image prior to segmentation. Notably, all other diffusion images were left uncorrected, so bias fields were unaccounted for while modelling the tensor. Given that the cortex is located on the perimeter of the brain the 64-channel coil is expected to provide increased SNR in the

cortex. However, this may result in subtle alterations in diffusion parameters as a function of cortical depth, as such future studies may investigate the role SNR plays at varying cortical depths, or crowns versus deep sulci.

#### **7.4.4 Conclusions**

Here, a novel cortical segmentation and analysis method applied directly to diffusion images was presented to yield diffusion parametric maps and regional DTI measures of the healthy human cortex in vivo. Cortical boundary segmentation was performed in native DTI space using a surface deforming algorithm relying on the mean DWI image WM/GM contrast combined with FA and MD maps. Accurate segmentation of the cortex was obtained for all healthy participants. FA, MD, and radially of the primary eigenvector relative to the cortex were within range of expected values and their regional variability was in agreement with higher spatial resolution studies that require longer scans and registration to an additional anatomical image. The proposed method segments the cortex in native DTI space and will benefit from more accurate measurements of cortical diffusion properties in studies of neurodevelopment and clinical populations.

## 8 Summary & Conclusions

The novel research presented in this thesis adds considerable knowledge to various fields of MRI and neuroimaging FASD research. In Chapter 4 and Chapter 6 novel data is presented that adds to the understanding of structural and functional changes associated with prenatal alcohol exposure. Chapter 5 presents novel data analysis methods of functional connectivity reproducibility across multiple sites and Chapter 7 presents a novel strategy for analyzing diffusion metrics in the cortex.

In Chapter 4, a machine learning approach was used to build a predictive model that achieved a 77% accuracy in classifying controls from participants with FASD. Given that all previous volumetric studies in FASD studied brain regions independently it was particularly interesting to see that there was large agreement between regions of the brain heavily weighted in the predictive model (e.g. caudate, temporal lobe) and brain regions that have been commonly reported to have reduced volume in FASD from earlier studies. In addition, the multivariate predictive model outperformed all other univariate analysis suggesting that there is a value in classifying FASD based on patterns of volumetric change rather than single structure. Finally, this study presented separate FASD classification models for males and females showing large difference in both performance and regional weighting of models. This result further supports analyzing males and females separately in FASD studies in agreement with recent studies (Inkelis et al., 2020; Treit et al., 2017). Although a 77% accuracy in identifying individuals with FASD is in the range of other studies that have attempted FASD classification using biologically based measures, it is certainly not accurate enough to be applied clinically. Thus, the model has potential to be used in conjunction with other FASD diagnostic measures (e.g. behavioral, facial measurements). Given that other studies have shown value in classifying FASD based on epigenetic (Lussier et al., 2018), facial image (Fang et al., 2008), eye tracking (Tseng et al., 2013) and psychometric (Zhang et al., 2019) data, further machine learning studies could attempt to combine features from multiple sources to train a more accurate classification model. In fact, the NeuroDevNet imaging dataset has enabled an ongoing research project that aims to investigate whether diffusion parameters extracted from WM and/or measurements of cortical thickness can be combined with the regional volumes presented in Chapter 4 to boost the accuracy of the FASD classification model.

The primary purpose of the research in Chapter 5 was to assess variability of functional connectivity measures across the four sites to further support the findings resulting from the analysis of the multisite control/FASD cohort in Chapter 6. However, two findings from this multisite reproducibility study have broader implications for multisite rs-fMRI research. Firstly, modest between site reproducibility ( $ICC \sim 0.2$ ) was observed in functional connectivity measurements which is in line with the only other study to report ICC values using similar analysis methods (Noble et al., 2017). Secondly, using linear site correction (i.e. covarying by site in linear regression) improves between site reproducibility by small margins in an overwhelming majority of the functional connections used in this study. This result suggests that covarying by site is an appropriate method for accounting for some of the between site variability observed in functional connectivity measurements. However given the limited effectiveness of linear site correction, future studies may examine the use of more complex site correction techniques such as statistical harmonization that have been shown to better account for between site variability in functional connectivity measures.

Alterations in functional connectivity were observed in the FASD cohort in the research presented in Chapter 6. Notably, to date, only a handful of studies have investigated functional connectivity with rs-fMRI in individuals with FASD. The primary results from the work showed decreased connectivity in the FASD group in connectivity in internetwork connections of the salience network, and further supports other studies that have observed decreased functional connectivity in FASD (Fan et al., 2017; Wozniak et al., 2011). In conjunction with an additional somatosensory study published in the same year on the same NeuroDevNet FASD cohort (Long et al., 2018) these works were the first to report alterations in functional internetwork connectivity. Considering that internetwork connectivity is often ignored in favor of focusing on strongly connected intranetwork connections, these results suggest that FASD functional connectivity studies may benefit from expansion of functional connectivity analysis to internetwork connections as well.

Recruitment in FASD studies is a challenging prospect resulting in notable limitations relating to the clinical and demographic characteristics of FASD cohorts. Firstly, large demographic imbalances are typically observed in FASD studies. In Chapter 4 and Chapter 6 of this thesis, a large proportion of individuals with FASD

were aboriginal (referred to as indigenous in Chapter 6), were on some form of medication, had a comorbid diagnosis, were living in adopted homes or in foster care. On the other hand, our control group was primarily Caucasian, unmedicated, and had no other diagnosis which potentially confounds this image analyses. Future studies would benefit from attempts to control for recruitment reducing these biases between groups. However, one of the benefits of large multisite cohorts like those used in Chapter 4 and Chapter 6 is the ability to test for within-group effects of these potential confounds. In Chapter 4 subsequent analysis was performed that showed no difference in classification accuracy in the FASD group relating to ethnicity, medication status or comorbid diagnosis, suggesting that the classification model represented a pattern of volumetric change in FASD and was not sensitive to potential confounding variables. In Chapter 6 subsequent analysis was performed to test for a relationship between functional connectivity of the connections found to be different in the FASD group and potential confounds. In that analysis only stimulant use and not any other potential confounding variables, related to the functional connectivity in the FASD group. Notably, stimulant use was associated with increased functional connectivity suggesting that the effect of stimulants “mitigated” the decreased functional connectivity observed in the group effect rather than being the source of the effect.

In Chapter 7 of this thesis a method is presented to extract in-vivo diffusion measurements of diffusion from the cortex. Very few studies have investigated cortical microstructure with diffusion MRI to date and the majority have used long acquisitions (~1 hour long) at high-resolution (~1mm isotropic) such as the publicly available HCP diffusion imaging data. Previous studies have also relied on registration of diffusion MRI to an additional structural image acquired for the purpose of delineating the cortical boundaries. The technique proposed in Chapter 7 utilizes diffusion data (~1.5mm isotropic) acquired in 3.5 minutes and proposes a surface-based cortical segmentation algorithm performed on native DTI removing the need for additional structural imaging and problematic registration between modalities. Notably, cortical segmentations presented in Chapter 7 were accurate on all ten subjects in the study. Interestingly, resulting surface-based diffusion metrics showed predominantly radially oriented primary eigenvectors and showed regional differences in FA values that may relate to underlying microstructure across the cortex. Given the short scan time and the added benefit of foregoing

registration to a structural image, the proposed method has the potential for use in large scale studies of development and clinical populations.

The primary limitation of the research presented in Chapter 7 is the resolution of the data relative to the size of cortex (1mm-5mm thick) which could result in cortical diffusion measurements to be skewed by partial volumes of the superficial white matter or exterior CSF. Importantly, the results presented in Chapter 7 are in line with higher resolution (1mm isotropic) studies that attempt DTI of the cortex (McNab et al., 2013). However, to more thoroughly address resolution as a limitation to this type of analysis future studies should investigate how surface-based DTI parametric maps change as a function of resolution. Importantly, the analysis framework presented in this thesis is analogous to resolution (as long as the edge of the cortex can be detected) meaning that it could be applied to higher resolution data as well, opening the possibility of applying this cortical analysis framework to high resolution in-vivo data in the future.

Although the projects presented here tackle three diverse areas of research, all aforementioned work adds to the scientific fields of MRI applications and/or MRI methods for the study of brain development. The first study of machine learning classification of FASD using regional brain volumes is presented and resulted in a predictive model that achieved a moderately high classification accuracy (77%) in identifying individuals with FASD. A multisite study of functional connectivity alterations in FASD showed decreased functional connectivity in FASD and to date is one of only two studies that utilized cohorts consisting of more than 100 subjects. Finally, a new method is proposed to study DTI in the cortex that has the potential for application in a multitude large scale diffusion MRI studies in developmental or clinical populations.

## References

- Aggarwal, M., Nauen, D.W., Troncoso, J.C., Mori, S., 2015. Probing region-specific microstructure of human cortical areas using high angular and spatial resolution diffusion MRI. *NeuroImage* 105, 198–207. <https://doi.org/10.1016/j.neuroimage.2014.10.053>
- Andersson, J.L.R., Sotiropoulos, S.N., 2016. An integrated approach to correction for off-resonance effects and subject movement in diffusion MR imaging. *Neuroimage* 125, 1063–1078. <https://doi.org/10.1016/j.neuroimage.2015.10.019>
- Arbabshirani, M.R., Plis, S., Sui, J., Calhoun, V.D., 2017. Single subject prediction of brain disorders in neuroimaging: Promises and pitfalls. *NeuroImage, Individual Subject Prediction* 145, 137–165. <https://doi.org/10.1016/j.neuroimage.2016.02.079>
- Archibald, S.L., Fennema-Notestine, C., Gamst, A., Riley, E.P., Mattson, S.N., Jernigan, T.L., 2001. Brain dysmorphology in individuals with severe prenatal alcohol exposure. *Developmental Medicine and Child Neurology* 43, 148–154. <https://doi.org/10.1017/S0012162201000299>
- Assaf, Y., 2019. Imaging laminar structures in the gray matter with diffusion MRI. *NeuroImage* 197, 677–688. <https://doi.org/10.1016/j.neuroimage.2017.12.096>
- Astley, S.J., 2004. Diagnostic guide for fetal alcohol spectrum disorders: The 4-digit diagnostic code. University of Washington.
- Astley, S.J., Aylward, E.H., Olson, H.C., Kerns, K., Brooks, A., Coggins, T.E., Davies, J., Dorn, S., Gendler, B., Jirikowic, T., Kraegel, P., Maravilla, K., Richards, T., 2009a. Magnetic resonance imaging outcomes from a comprehensive magnetic resonance study of children with fetal alcohol spectrum disorders. *Alcoholism: Clinical and Experimental Research* 33, 1671–1689. <https://doi.org/10.1111/j.1530-0277.2009.01004.x>
- Astley, S.J., Aylward, E.H., Olson, H.C., Kerns, K., Brooks, A., Coggins, T.E., Davies, J., Dorn, S., Gendler, B., Jirikowic, T., others, 2009b. Functional magnetic resonance imaging outcomes from a comprehensive magnetic resonance study of children with fetal alcohol spectrum disorders. *Journal of neurodevelopmental disorders* 1, 61.
- Badhwar, A., Collin-Verreault, Y., Orban, P., Urchs, S., Chouinard, I., Vogel, J., Potvin, O., Duchesne, S., Bellec, P., 2020. Multivariate consistency of resting-state fMRI connectivity maps acquired on a single individual over 2.5 years, 13 sites and 3 vendors. *NeuroImage* 205, 116210. <https://doi.org/10.1016/j.neuroimage.2019.116210>
- Bandettini, P.A., Wong, E.C., Hinks, R.S., Tikofsky, R.S., Hyde, J.S., 1992. Time course EPI of human brain function during task activation. *Magnetic Resonance in Medicine* 25, 390–397. <https://doi.org/10.1002/mrm.1910250220>
- Bari, S., Amico, E., Vike, N., Talavage, T.M., Goñi, J., 2019. Uncovering multi-site identifiability based on resting-state functional connectomes. *NeuroImage* 202, 115967. <https://doi.org/10.1016/j.neuroimage.2019.06.045>
- Basser, P.J., Mattiello, J., Lebihan, D., 1994. Estimation of the Effective Self-Diffusion Tensor from the NMR Spin Echo. *Journal of Magnetic Resonance, Series B* 103, 247–254. <https://doi.org/10.1006/jmrb.1994.1037>
- Bastiani, M., Oros-Peusquens, A.-M., Seehaus, A., Brenner, D., Möllenhoff, K., Celik, A., Felder, J., Bratzke, H., Shah, N.J., Galuske, R., Goebel, R., Roebroek, A., 2016. Automatic Segmentation of Human Cortical Layer-Complexes and Architectural Areas Using Ex vivo Diffusion MRI and Its Validation. *Front Neurosci* 10. <https://doi.org/10.3389/fnins.2016.00487>

- Becker, M., Warr-Leeper, G.A., Leeper, H.A., 1990. Fetal alcohol syndrome: A description of oral motor, articulatory, short-term memory, grammatical, and semantic abilities. *Journal of Communication Disorders* 23, 97–124. [https://doi.org/10.1016/0021-9924\(90\)90016-R](https://doi.org/10.1016/0021-9924(90)90016-R)
- Beckmann, C.F., DeLuca, M., Devlin, J.T., Smith, S.M., 2005. Investigations into resting-state connectivity using independent component analysis. *Philosophical Transactions of the Royal Society of London B: Biological Sciences* 360, 1001–1013.
- Behzadi, Y., Restom, K., Liu, J., Liu, T.T., 2007. A Component Based Noise Correction Method (CompCor) for BOLD and Perfusion Based fMRI. *Neuroimage* 37, 90–101.
- Bianciardi, M., Fukunaga, M., Van Gelderen, P., De Zwart, J.A., Duyn, J.H., 2011. Negative BOLD-fMRI signals in large cerebral veins. *Journal of Cerebral Blood Flow & Metabolism* 31, 401–412.
- Biswal, B., Yetkin, F.Z., Haughton, V.M., Hyde, J.S., 1995. Functional connectivity in the motor cortex of resting human brain using echo-planar mri. *Magnetic Resonance in Medicine* 34, 537–541. <https://doi.org/10.1002/mrm.1910340409>
- Biswal, B.B., Mennes, M., Zuo, X.-N., Gohel, S., Kelly, C., Smith, S.M., Beckmann, C.F., Adelstein, J.S., Buckner, R.L., Colcombe, S., others, 2010. Toward discovery science of human brain function. *Proceedings of the National Academy of Sciences* 107, 4734–4739.
- Bloch, F., 1946. Nuclear Induction. *Phys. Rev.* 70, 460–474. <https://doi.org/10.1103/PhysRev.70.460>
- Bullmore, E., Sporns, O., 2009. Complex brain networks: graph theoretical analysis of structural and functional systems. *Nature Reviews Neuroscience* 10, 186–198. <https://doi.org/10.1038/nrn2575>
- Burd, L., Klug, M.G., Martsof, J.T., Kerbeshian, J., 2003. Fetal alcohol syndrome: neuropsychiatric phenomics. *Neurotoxicology and Teratology, The Four State Fetal Alcohol Consortium: Clinical and Epidemiologic Findings* 25, 697–705. <https://doi.org/10.1016/j.ntt.2003.07.014>
- Cahill, L., 2006. Why sex matters for neuroscience. *Nature Reviews Neuroscience* 7, 477–484. <https://doi.org/10.1038/nrn1909>
- Calamante, F., Jeurissen, B., Smith, R.E., Tournier, J.-D., Connelly, A., 2018. The role of whole-brain diffusion MRI as a tool for studying human in vivo cortical segregation based on a measure of neurite density. *Magnetic Resonance in Medicine* 79, 2738–2744. <https://doi.org/10.1002/mrm.26917>
- Calhoun, V.D., Liu, J., Adalı, T., 2009. A review of group ICA for fMRI data and ICA for joint inference of imaging, genetic, and ERP data. *NeuroImage, Mathematics in Brain Imaging* 45, S163–S172. <https://doi.org/10.1016/j.neuroimage.2008.10.057>
- Castellanos, F.X., Margulies, D.S., Kelly, C., Uddin, L.Q., Ghaffari, M., Kirsch, A., Shaw, D., Shehzad, Z., Di Martino, A., Biswal, B., Sonuga-Barke, E.J.S., Rotrosen, J., Adler, L.A., Milham, M.P., 2008. Cingulate-Precuneus Interactions: A New Locus of Dysfunction in Adult Attention-Deficit/Hyperactivity Disorder. *Biological Psychiatry, Impulse Control: Aggression, Addiction, and Attention Deficits* 63, 332–337.
- Chai, X.J., Castañón, A.N., Öngür, D., Whitfield-Gabrieli, S., 2012. Anticorrelations in resting state networks without global signal regression. *Neuroimage* 59, 1420–1428.
- Chen, C.P., Keown, C.L., Jahedi, A., Nair, A., Pflieger, M.E., Bailey, B.A., Müller, R.-A., 2015. Diagnostic classification of intrinsic functional connectivity highlights somatosensory, default mode, and visual regions in autism. *NeuroImage: Clinical* 8, 238–245. <https://doi.org/10.1016/j.nicl.2015.04.002>
- Chen, X., Coles, C.D., Lynch, M.E., Hu, X., 2012. Understanding specific effects of prenatal alcohol exposure on brain structure in young adults. *Hum. Brain Mapp.* 33, 1663–1676. <https://doi.org/10.1002/hbm.21313>
- Chudley, A.E., Conry, J., Cook, J.L., Looock, C., Rosales, T., LeBlanc, N., 2005. Fetal alcohol spectrum disorder: Canadian guidelines for diagnosis. *Canadian Medical Association Journal* 172, S1–S21.

- Clarren, S.K., Alvord, E.C., Sumi, S.M., Streissguth, A.P., Smith, D.W., 1978. Brain malformations related to prenatal exposure to ethanol. *The Journal of Pediatrics* 92, 64–67. [https://doi.org/10.1016/S0022-3476\(78\)80072-9](https://doi.org/10.1016/S0022-3476(78)80072-9)
- Colby, J.B., Rudie, J.D., Brown, J.A., Douglas, P.K., Cohen, M.S., Shehzad, Z., 2012. Insights into multimodal imaging classification of ADHD. *Front. Syst. Neurosci.* 6. <https://doi.org/10.3389/fnsys.2012.00059>
- Converse, A.K., Moore, C.F., Holden, J.E., Ahlers, E.O., Moirano, J.M., Larson, J.A., Resch, L.M., DeJesus, O.T., Barnhart, T.E., Nickles, R.J., Murali, D., Christian, B.T., Schneider, M.L., 2014. Moderate level prenatal alcohol exposure induces sex differences in dopamine D1 receptor binding in adult rhesus monkeys. *Alcohol Clin Exp Res* 38, 2934–2943. <https://doi.org/10.1111/acer.12575>
- Cook, J.L., Green, C.R., Lilley, C.M., Anderson, S.M., Baldwin, M.E., Chudley, A.E., Conry, J.L., LeBlanc, N., Look, C.A., Lutke, J., Mallon, B.F., McFarlane, A.A., Temple, V.K., Rosales, T., 2016. Fetal alcohol spectrum disorder: a guideline for diagnosis across the lifespan. *CMAJ* 188, 191–197. <https://doi.org/10.1503/cmaj.141593>
- Cortese, B.M., Moore, G.J., Bailey, B.A., Jacobson, S.W., Delaney-Black, V., Hannigan, J.H., 2006. Magnetic resonance and spectroscopic imaging in prenatal alcohol-exposed children: Preliminary findings in the caudate nucleus. *Neurotoxicology and Teratology* 28, 597–606. <https://doi.org/10.1016/j.ntt.2006.08.002>
- Cosgrove, K.P., Mazure, C.M., Staley, J.K., 2007. Evolving knowledge of sex differences in brain structure, function and chemistry. *Biol Psychiatry* 62, 847–855. <https://doi.org/10.1016/j.biopsych.2007.03.001>
- Cottaar, M., Bastiani, M., Chen, C., Dikranian, K., Van Essen, D., Behrens, T.E., Sotiropoulos, S.N., Jbabdi, S., 2018. A gyral coordinate system predictive of fibre orientations. *Neuroimage* 176, 417–430. <https://doi.org/10.1016/j.neuroimage.2018.04.040>
- Dale, A.M., Fischl, B., Sereno, M.I., 1999. Cortical surface-based analysis. I. Segmentation and surface reconstruction. *Neuroimage* 9, 179–194. <https://doi.org/10.1006/nimg.1998.0395>
- Damoiseaux, J., Rombouts, S., Barkhof, F., Scheltens, P., Stam, C., Smith, S.M., Beckmann, C., 2006. Consistent resting-state networks across healthy subjects. *Proceedings of the national academy of sciences* 103, 13848–13853.
- Daugherty, A.M., Raz, N., 2016. Accumulation of iron in the putamen predicts its shrinkage in healthy older adults: A multi-occasion longitudinal study. *NeuroImage* 128, 11–20. <https://doi.org/10.1016/j.neuroimage.2015.12.045>
- Di Martino, A., Yan, C.-G., Li, Q., Denio, E., Castellanos, F.X., Alaerts, K., Anderson, J.S., Assaf, M., Bookheimer, S.Y., Dapretto, M., Deen, B., Delmonte, S., Dinstein, I., Ertl-Wagner, B., Fair, D.A., Gallagher, L., Kennedy, D.P., Keown, C.L., Keysers, C., Lainhart, J.E., Lord, C., Luna, B., Menon, V., Minshew, N.J., Monk, C.S., Mueller, S., Müller, R.-A., Nebel, M.B., Nigg, J.T., O’Hearn, K., Pelphrey, K.A., Peltier, S.J., Rudie, J.D., Sunaert, S., Thioux, M., Tyszka, J.M., Uddin, L.Q., Verhoeven, J.S., Wenderoth, N., Wiggins, J.L., Mostofsky, S.H., Milham, M.P., 2014. The autism brain imaging data exchange: towards a large-scale evaluation of the intrinsic brain architecture in autism. *Molecular Psychiatry* 19, 659–667.
- Diwadkar, V.A., Meintjes, E.M., Goradia, D., Dodge, N.C., Warton, C., Molteno, C.D., Jacobson, S.W., Jacobson, J.L., 2013. Differences in cortico-striatal-cerebellar activation during working memory in syndromal and nonsyndromal children with prenatal alcohol exposure. *Human brain mapping* 34, 1931–1945.
- Donald, K.A., Eastman, E., Howells, F.M., Adnams, C., Riley, E.P., Woods, R.P., Narr, K.L., Stein, D.J., 2015. Neuroimaging effects of prenatal alcohol exposure on the developing human brain: a magnetic resonance imaging review. *Acta neuropsychiatrica* 27, 251–269.
- Donald, K.A., Ipser, J.C., Howells, F.M., Roos, A., Fouche, J.-P., Riley, E.P., Koen, N., Woods, R.P., Biswal, B., Zar, H.J., others, 2016. Interhemispheric functional brain connectivity in neonates with prenatal alcohol exposure: preliminary findings. *Alcoholism: Clinical and Experimental Research* 40, 113–121.

- Dudek, J., Skocic, J., Sheard, E., Rovet, J., 2014. Hippocampal abnormalities in youth with alcohol-related neurodevelopmental disorder. *Journal of the International Neuropsychological Society* 20, 181–191. <https://doi.org/10.1017/S1355617713001343>
- Eckert, M.A., Leonard, C.M., Richards, T.L., Aylward, E.H., Thomson, J., Berninger, V.W., 2003. Anatomical correlates of dyslexia: frontal and cerebellar findings. *Brain* 126, 482–494. <https://doi.org/10.1093/brain/awg026>
- Einstein, A., 1905. On the motion required by the molecular kinetic theory of heat of small particles suspended in a stationary liquid. *Annalen der physik* 17, 549–560.
- Eugene Hoyme, H., May, P.A., Kalberg, W.O., Kodituwakku, P., Phillip Gossage, J., Trujillo, P.M., Buckley, D.G., Miller, J.H., Aragon, A.S., Khaole, N., Viljoen, D.L., Jones, K.L., Robinson, L.K., 2005. A Practical Clinical Approach to Diagnosis of Fetal Alcohol Spectrum Disorders: Clarification of the 1996 Institute of Medicine Criteria. *Pediatrics* 115, 39–47. <https://doi.org/10.1542/peds.2004-0259>
- Fagerlund, Å., Heikkinen, S., Autti-Rämö, I., Korkman, M., Timonen, M., Kuusi, T., Riley, E.P., Lundbom, N., 2006. Brain Metabolic Alterations in Adolescents and Young Adults With Fetal Alcohol Spectrum Disorders. *Alcoholism: Clinical and Experimental Research* 30, 2097–2104. <https://doi.org/10.1111/j.1530-0277.2006.00257.x>
- Fair, D., Nigg, J.T., Iyer, S., Bathula, D., Mills, K.L., Dosenbach, N.U., Schlaggar, B.L., Mennes, M., Gutman, D., Bangaru, S., Buitelaar, J.K., Dickstein, D.P., Di Martino, A., Kennedy, D.N., Kelly, C., Luna, B., Schweitzer, J.B., Velanova, K., Wang, Y.-F., Mostofsky, S.H., Castellanos, F.X., Milham, M.P., 2013. Distinct neural signatures detected for ADHD subtypes after controlling for micro-movements in resting state functional connectivity MRI data. *Front. Syst. Neurosci.* 6.
- Fair, D.A., Nigg, J.T., Iyer, S., Bathula, D., Mills, K.L., Dosenbach, N.U., Schlaggar, B.L., Mennes, M., Gutman, D., Bangaru, S., others, 2012. Distinct neural signatures detected for ADHD subtypes after controlling for micro-movements in resting state functional connectivity MRI data. *Frontiers in systems neuroscience* 6.
- Fan, J., Taylor, P.A., Jacobson, S.W., Molteno, C.D., Gohel, S., Biswal, B.B., Jacobson, J.L., Meintjes, E.M., 2017. Localized reductions in resting-state functional connectivity in children with prenatal alcohol exposure. *Hum Brain Mapp* 38, 5217–5233.
- Fang, S., McLaughlin, J., Fang, J., Huang, J., Autti-Rämö, I., Fagerlund, Å., Jacobson, S.W., Robinson, L.K., Hoyme, H.E., Mattson, S.N., Riley, E., Zhou, F., Ward, R., Moore, E.S., Foroud, T., 2008. Automated diagnosis of fetal alcohol syndrome using 3D facial image analysis. *Orthodontics & Craniofacial Research* 11, 162–171. <https://doi.org/10.1111/j.1601-6343.2008.00425.x>
- Fischl, B., 2012. FreeSurfer. *NeuroImage, 20 YEARS OF fMRI* 62, 774–781. <https://doi.org/10.1016/j.neuroimage.2012.01.021>
- Fischl, B., Salat, D.H., Busa, E., Albert, M., Dieterich, M., Haselgrove, C., van der Kouwe, A., Killiany, R., Kennedy, D., Klaveness, S., Montillo, A., Makris, N., Rosen, B., Dale, A.M., 2002. Whole Brain Segmentation: Automated Labeling of Neuroanatomical Structures in the Human Brain. *Neuron* 33, 341–355. [https://doi.org/10.1016/S0896-6273\(02\)00569-X](https://doi.org/10.1016/S0896-6273(02)00569-X)
- Fischl, B., Sereno, M.I., Dale, A.M., 1999. Cortical Surface-Based Analysis: II: Inflation, Flattening, and a Surface-Based Coordinate System. *NeuroImage* 9, 195–207. <https://doi.org/10.1006/nimg.1998.0396>
- Fischl, B., van der Kouwe, A., Destrieux, C., Halgren, E., Ségonne, F., Salat, D.H., Busa, E., Seidman, L.J., Goldstein, J., Kennedy, D., Caviness, V., Makris, N., Rosen, B., Dale, A.M., 2004. Automatically Parcellating the Human Cerebral Cortex. *Cereb Cortex* 14, 11–22. <https://doi.org/10.1093/cercor/bhg087>
- Forsyth, J.K., McEwen, S.C., Gee, D.G., Bearden, C.E., Addington, J., Goodyear, B., Cadenhead, K.S., Mirzakhania, H., Cornblatt, B.A., Olvet, D.M., others, 2014. Reliability of functional magnetic resonance imaging

- activation during working memory in a multi-site study: Analysis from the North American Prodrome Longitudinal Study. *NeuroImage* 97, 41–52.
- Fox, P.T., Raichle, M.E., 1986. Focal physiological uncoupling of cerebral blood flow and oxidative metabolism during somatosensory stimulation in human subjects. *Proc. Natl. Acad. Sci. U.S.A.* 83, 1140–1144. <https://doi.org/10.1073/pnas.83.4.1140>
- Frahm, J., Bruhn, H., Merboldt, K.-D., Hänicke, W., 1992. Dynamic MR imaging of human brain oxygenation during rest and photic stimulation. *Journal of Magnetic Resonance Imaging* 2, 501–505. <https://doi.org/10.1002/jmri.1880020505>
- Friederici, A.D., Meyer, M., von Cramon, D.Y., 2000. Auditory Language Comprehension: An Event-Related fMRI Study on the Processing of Syntactic and Lexical Information. *Brain and Language* 74, 289–300.
- Friedman, L., Stern, H., Brown, G.G., Mathalon, D.H., Turner, J., Glover, G.H., Gollub, R.L., Lauriello, J., Lim, K.O., Cannon, T., others, 2008. Test–retest and between-site reliability in a multicenter fMRI study. *Human brain mapping* 29, 958–972.
- Friedman, L.A., Rapoport, J.L., 2015. Brain development in ADHD. *Current Opinion in Neurobiology, SI: Neuropsychiatry* 30, 106–111. <https://doi.org/10.1016/j.conb.2014.11.007>
- Fryer, S.L., Mattson, S.N., Jernigan, T.L., Archibald, S.L., Jones, K.L., Riley, E.P., 2012. Caudate volume predicts neurocognitive performance in youth with heavy prenatal alcohol exposure. *Alcoholism: Clinical and Experimental Research* 36, 1932–1941. <https://doi.org/10.1111/j.1530-0277.2012.01811.x>
- Fryer, S.L., Tapert, S.F., Mattson, S.N., Paulus, M.P., Spadoni, A.D., Riley, E.P., 2007. Prenatal Alcohol Exposure Affects Frontal–Striatal BOLD Response During Inhibitory Control. *Alcoholism: Clinical and Experimental Research* 31, 1415–1424. <https://doi.org/10.1111/j.1530-0277.2007.00443.x>
- Fukutomi, H., Glasser, M.F., Murata, K., Akasaka, T., Fujimoto, K., Yamamoto, T., Autio, J.A., Okada, T., Togashi, K., Zhang, H., Van Essen, D.C., Hayashi, T., 2019. Diffusion Tensor Model links to Neurite Orientation Dispersion and Density Imaging at high b-value in Cerebral Cortical Gray Matter. *Scientific Reports* 9, 1–12. <https://doi.org/10.1038/s41598-019-48671-7>
- Fukutomi, H., Glasser, M.F., Zhang, H., Autio, J.A., Coalson, T.S., Okada, T., Togashi, K., Van Essen, D.C., Hayashi, T., 2018. Neurite imaging reveals microstructural variations in human cerebral cortical gray matter. *NeuroImage, Microstructural Imaging* 182, 488–499. <https://doi.org/10.1016/j.neuroimage.2018.02.017>
- Ganepola, T., Nagy, Z., Ghosh, A., Papadopoulou, T., Alexander, D.C., Sereno, M.I., 2018. Using diffusion MRI to discriminate areas of cortical grey matter. *Neuroimage* 182, 456–468. <https://doi.org/10.1016/j.neuroimage.2017.12.046>
- Gati, J.S., Menon, R.S., Ugurbil, K., Rutt, B.K., 1997. Experimental determination of the BOLD field strength dependence in vessels and tissue. *Magn Reson Med* 38, 296–302. <https://doi.org/10.1002/mrm.1910380220>
- Giedd, J.N., Blumenthal, J., Jeffries, N.O., Castellanos, F.X., Liu, H., Zijdenbos, A., Paus, T., Evans, A.C., Rapoport, J.L., 1999. Brain development during childhood and adolescence: a longitudinal MRI study. *Nat. Neurosci.* 2, 861–863. <https://doi.org/10.1038/13158>
- Glasser, M.F., Sotiropoulos, S.N., Wilson, J.A., Coalson, T.S., Fischl, B., Andersson, J.L., Xu, J., Jbabdi, S., Webster, M., Polimeni, J.R., Van Essen, D.C., Jenkinson, M., 2013. The Minimal Preprocessing Pipelines for the Human Connectome Project. *Neuroimage* 80, 105–124. <https://doi.org/10.1016/j.neuroimage.2013.04.127>
- Godin, E.A., Dehart, D.B., Parnell, S.E., O’Leary-Moore, S.K., Sulik, K.K., 2011. Ventromedian forebrain dysgenesis follows early prenatal ethanol exposure in mice. *Neurotoxicol Teratol* 33, 231–239. <https://doi.org/10.1016/j.ntt.2010.11.001>

- Godin, E.A., O'Leary-Moore, S.K., Khan, A.A., Parnell, S.E., Ament, J.J., Dehart, D.B., Johnson, B.W., Allan Johnson, G., Styner, M.A., Sulik, K.K., 2010. Magnetic resonance microscopy defines ethanol-induced brain abnormalities in prenatal mice: effects of acute insult on gestational day 7. *Alcohol. Clin. Exp. Res.* 34, 98–111. <https://doi.org/10.1111/j.1530-0277.2009.01071.x>
- Golay, X., Jiang, H., Zijl, P.C.M. van, Mori, S., 2002. High-resolution isotropic 3D diffusion tensor imaging of the human brain. *Magnetic Resonance in Medicine* 47, 837–843. <https://doi.org/10.1002/mrm.10143>
- Goodlett, C.R., Horn, K.H., Zhou, F.C., 2005. Alcohol Teratogenesis: Mechanisms of Damage and Strategies for Intervention. *Exp Biol Med (Maywood)* 230, 394–406. <https://doi.org/10.1177/15353702-0323006-07>
- Goulden, N., Khusnulina, A., Davis, N.J., Bracewell, R.M., Bokde, A.L., McNulty, J.P., Mullins, P.G., 2014. The salience network is responsible for switching between the default mode network and the central executive network: replication from DCM. *Neuroimage* 99, 180–190.
- Greicius, M., 2008. Resting-state functional connectivity in neuropsychiatric disorders. *Current Opinion in Neurology* 21, 424–430. <https://doi.org/10.1097/WCO.0b013e328306f2c5>
- Greve, D.N., Fischl, B., 2009. Accurate and robust brain image alignment using boundary-based registration. *NeuroImage* 48, 63–72. <https://doi.org/10.1016/j.neuroimage.2009.06.060>
- Guerra, C., Bazinet, A., Riley, E.P., 2009. Foetal Alcohol Spectrum Disorders and Alterations in Brain and Behaviour. *Alcohol Alcohol* 44, 108–114. <https://doi.org/10.1093/alcalc/agn105>
- Gulban, O.F., Martino, F.D., Vu, A.T., Yacoub, E., Uğurbil, K., Lenglet, C., 2018. Cortical Fibers Orientation Mapping using in-vivo Whole Brain 7 Tesla Diffusion MRI. *Neuroimage* 178, 104–118. <https://doi.org/10.1016/j.neuroimage.2018.05.010>
- Ha, S., Sohn, I.-J., Kim, N., Sim, H.J., Cheon, K.-A., 2015. Characteristics of Brains in Autism Spectrum Disorder: Structure, Function and Connectivity across the Lifespan. *Exp Neurobiol* 24, 273–284. <https://doi.org/10.5607/en.2015.24.4.273>
- Hasan, K.M., Halphen, C., Sankar, A., Eluvathingal, T.J., Kramer, L., Stuebing, K.K., Ewing-Cobbs, L., Fletcher, J.M., 2007. Diffusion Tensor Imaging Based Tissue Segmentation: Validation and Application to the Developing Child and Adolescent Brain. *Neuroimage* 34, 1497–1505. <https://doi.org/10.1016/j.neuroimage.2006.10.029>
- Heidemann, R.M., Porter, D.A., Anwender, A., Feiweier, T., Heberlein, K., Knösche, T.R., Turner, R., 2010. Diffusion imaging in humans at 7T using readout-segmented EPI and GRAPPA. *Magnetic Resonance in Medicine* 64, 9–14. <https://doi.org/10.1002/mrm.22480>
- Heuvel, M.P. van den, Mandl, R.C.W., Kahn, R.S., Pol, H.E.H., 2009. Functionally linked resting-state networks reflect the underlying structural connectivity architecture of the human brain. *Human Brain Mapping* 30, 3127–3141. <https://doi.org/10.1002/hbm.20737>
- Hull, J.V., Jacokes, Z.J., Torgerson, C.M., Irimia, A., Van Horn, J.D., 2017. Resting-State Functional Connectivity in Autism Spectrum Disorders: A Review. *Front Psychiatry* 7.
- Ikonomidou, C., Bittigau, P., Ishimaru, M.J., Wozniak, D.F., Koch, C., Genz, K., Price, M.T., Stefovská, V., Hörster, F., Tenkova, T., Dikranian, K., Olney, J.W., 2000. Ethanol-Induced Apoptotic Neurodegeneration and Fetal Alcohol Syndrome. *Science* 287, 1056–1060. <https://doi.org/10.1126/science.287.5455.1056>
- Inkelis, S.M., Moore, E.M., Bischoff-Grethe, A., Riley, E.P., 2020. Neurodevelopment in adolescents and adults with fetal alcohol spectrum disorders (FASD): A magnetic resonance region of interest analysis. *Brain Research* 1732, 146654. <https://doi.org/10.1016/j.brainres.2020.146654>
- Jacobson, S.W., Jacobson, J.L., Molteno, C.D., Warton, C.M.R., Wintermark, P., Hoyme, H.E., De Jong, G., Taylor, P., Warton, F., Lindinger, N.M., Carter, R.C., Dodge, N.C., Grant, E., Warfield, S.K., Zöllei, L., van der Kouwe,

- A.J.W., Meintjes, E.M., 2017. Heavy prenatal alcohol exposure is related to smaller corpus callosum in newborn MRI scans. *Alcohol Clin Exp Res* 41, 965–975. <https://doi.org/10.1111/acer.13363>
- Jann, K., Gee, D.G., Kilroy, E., Schwab, S., Smith, R.X., Cannon, T.D., Wang, D.J.J., 2015. Functional connectivity in BOLD and CBF data: Similarity and reliability of resting brain networks. *Neuroimage* 106, 111–122. <https://doi.org/10.1016/j.neuroimage.2014.11.028>
- Jeon, T., Mishra, V., Uh, J., Weiner, M., Hatanpaa, K.J., White, C.L., Zhao, Y.D., Lu, H., Diaz-Arrastia, R., Huang, H., 2012. Regional changes of cortical mean diffusivities with aging after correction of partial volume effects. *Neuroimage* 62, 1705–1716. <https://doi.org/10.1016/j.neuroimage.2012.05.082>
- Jeurissen, B., Tournier, J.-D., Dhollander, T., Connelly, A., Sijbers, J., 2014. Multi-tissue constrained spherical deconvolution for improved analysis of multi-shell diffusion MRI data. *NeuroImage* 103, 411–426. <https://doi.org/10.1016/j.neuroimage.2014.07.061>
- Jones, K.L., Smith, D.W., 1973. Recognition of the fetal alcohol syndrome in early infancy. *Lancet* 302, 999–1001. [https://doi.org/10.1016/s0140-6736\(73\)91092-1](https://doi.org/10.1016/s0140-6736(73)91092-1)
- Jones, K.L., Smith, D.W., Ulleland, C.N., Streissguth, P., 1973. Pattern of malformation in offspring of chronic alcoholic mothers. *Lancet* 1, 1267–1271. [https://doi.org/10.1016/s0140-6736\(73\)91291-9](https://doi.org/10.1016/s0140-6736(73)91291-9)
- Kang, X., Herron, T.J., Turken, U., Woods, D.L., 2012. Diffusion properties of cortical and pericortical tissue: regional variations, reliability and methodological issues. *Magnetic Resonance Imaging* 30, 1111–1122. <https://doi.org/10.1016/j.mri.2012.04.004>
- Kim, J.S., Singh, V., Lee, J.K., Lerch, J., Ad-Dab'bagh, Y., MacDonald, D., Lee, J.M., Kim, S.I., Evans, A.C., 2005. Automated 3-D extraction and evaluation of the inner and outer cortical surfaces using a Laplacian map and partial volume effect classification. *Neuroimage* 27, 210–221. <https://doi.org/10.1016/j.neuroimage.2005.03.036>
- Kim, S.-G., Ogawa, S., 2012. Biophysical and Physiological Origins of Blood Oxygenation Level-Dependent fMRI Signals. *J Cereb Blood Flow Metab* 32, 1188–1206. <https://doi.org/10.1038/jcbfm.2012.23>
- Kleinnijenhuis, M., van Mourik, T., Norris, D.G., Ruiter, D.J., van Cappellen van Walsum, A.-M., Barth, M., 2015. Diffusion tensor characteristics of gyrencephaly using high resolution diffusion MRI in vivo at 7T. *NeuroImage* 109, 378–387. <https://doi.org/10.1016/j.neuroimage.2015.01.001>
- Kleinnijenhuis, M., Zerbi, V., Küsters, B., Slump, C.H., Barth, M., van Cappellen van Walsum, A.-M., 2013. Layer-specific diffusion weighted imaging in human primary visual cortex in vitro. *Cortex* 49, 2569–2582. <https://doi.org/10.1016/j.cortex.2012.11.015>
- Konrad, K., Eickhoff, S.B., 2010. Is the ADHD brain wired differently? A review on structural and functional connectivity in attention deficit hyperactivity disorder. *Human Brain Mapping* 31, 904–916.
- Koo, T.K., Li, M.Y., 2016. A Guideline of Selecting and Reporting Intraclass Correlation Coefficients for Reliability Research. *Journal of Chiropractic Medicine* 15, 155–163. <https://doi.org/10.1016/j.jcm.2016.02.012>
- Korkman, M., Kirk, U., Kemp, S., 2007. NEPSY-II. Pearson San Antonio, TX.
- Kroenke, C.D., 2018. Using diffusion anisotropy to study cerebral cortical gray matter development. *Journal of Magnetic Resonance* 292, 106–116. <https://doi.org/10.1016/j.jmr.2018.04.011>
- Kwong, K.K., Belliveau, J.W., Chesler, D.A., Goldberg, I.E., Weisskoff, R.M., Poncelet, B.P., Kennedy, D.N., Hoppel, B.E., Cohen, M.S., Turner, R., 1992. Dynamic magnetic resonance imaging of human brain activity during primary sensory stimulation. *PNAS* 89, 5675–5679. <https://doi.org/10.1073/pnas.89.12.5675>
- Lan, N., Hellems, K.G.C., Ellis, L., Viau, V., Weinberg, J., 2009. Role of testosterone in mediating prenatal ethanol effects on hypothalamic-pituitary-adrenal activity in male rats. *Psychoneuroendocrinology* 34, 1314–1328. <https://doi.org/10.1016/j.psyneuen.2009.04.001>

- Lauterbur, P.C., 1973. Image Formation by Induced Local Interactions: Examples Employing Nuclear Magnetic Resonance. *Nature* 242, 190–191. <https://doi.org/10.1038/242190a0>
- Lawrenz, M., Finsterbusch, J., 2019. Detection of microscopic diffusion anisotropy in human cortical gray matter in vivo with double diffusion encoding. *Magnetic Resonance in Medicine* 81, 1296–1306. <https://doi.org/10.1002/mrm.27451>
- Lebel, C., Rasmussen, C., Wyper, K., Andrew, G., Beaulieu, C., 2010. Brain Microstructure Is Related to Math Ability in Children With Fetal Alcohol Spectrum Disorder. *Alcoholism: Clinical and Experimental Research* 34, 354–363. <https://doi.org/10.1111/j.1530-0277.2009.01097.x>
- Lebel, C., Rasmussen, C., Wyper, K., Walker, L., Andrew, G., Yager, J., Beaulieu, C., 2008. Brain diffusion abnormalities in children with fetal alcohol spectrum disorder. *Alcoholism: Clinical and Experimental Research* 32, 1732–1740. <https://doi.org/10.1111/j.1530-0277.2008.00750.x>
- Lebel, C., Roussotte, F., Sowell, E.R., 2011. Imaging the impact of prenatal alcohol exposure on the structure of the developing human brain. *Neuropsychol Rev* 21, 102–118. <https://doi.org/10.1007/s11065-011-9163-0>
- Leuze, C.W.U., Anwender, A., Bazin, P.-L., Dhital, B., Stüber, C., Reimann, K., Geyer, S., Turner, R., 2014. Layer-Specific Intracortical Connectivity Revealed with Diffusion MRI. *Cereb Cortex* 24, 328–339. <https://doi.org/10.1093/cercor/bhs311>
- Levman, J., Takahashi, E., 2015. Multivariate analyses applied to fetal, neonatal and pediatric MRI of neurodevelopmental disorders. *NeuroImage: Clinical* 9, 532–544. <https://doi.org/10.1016/j.nicl.2015.09.017>
- Li, Z., Coles, C.D., Lynch, M.E., Ma, X., Peltier, S., Hu, X., 2008. Occipital-temporal Reduction and Sustained Visual Attention Deficit in Prenatal Alcohol Exposed Adults. *Brain Imaging and Behavior* 2, 39–48. <https://doi.org/10.1007/s11682-007-9013-0>
- Long, X., Little, G., Beaulieu, C., Lebel, C., 2018. Sensorimotor network alterations in children and youth with prenatal alcohol exposure. *Human Brain Mapping* 39, 2258–2268. <https://doi.org/10.1002/hbm.24004>
- Lüsebrink, F., Wollrab, A., Speck, O., 2013. Cortical thickness determination of the human brain using high resolution 3T and 7T MRI data. *NeuroImage* 70, 122–131. <https://doi.org/10.1016/j.neuroimage.2012.12.016>
- Lussier, A.A., Morin, A.M., MacIsaac, J.L., Salmon, J., Weinberg, J., Reynolds, J.N., Pavlidis, P., Chudley, A.E., Kobor, M.S., 2018. DNA methylation as a predictor of fetal alcohol spectrum disorder. *Clinical Epigenetics* 10, 5. <https://doi.org/10.1186/s13148-018-0439-6>
- Makropoulos, A., Robinson, E.C., Schuh, A., Wright, R., Fitzgibbon, S., Bozek, J., Counsell, S.J., Steinweg, J., Vecchiato, K., Passerat-Palmbach, J., Lenz, G., Mortari, F., Tenev, T., Duff, E.P., Bastiani, M., Cordero-Grande, L., Hughes, E., Tusor, N., Tournier, J.-D., Hutter, J., Price, A.N., Teixeira, R.P.A.G., Murgasova, M., Victor, S., Kelly, C., Rutherford, M.A., Smith, S.M., Edwards, A.D., Hajnal, J.V., Jenkinson, M., Rueckert, D., 2018. The Developing Human Connectome Project: a Minimal Processing Pipeline for Neonatal Cortical Surface Reconstruction. *Neuroimage* 173, 88–112. <https://doi.org/10.1101/125526>
- Malisza, K.L., Allman, A.-A., Shiloff, D., Jakobson, L., Longstaffe, S., Chudley, A.E., 2005. Evaluation of Spatial Working Memory Function in Children and Adults with Fetal Alcohol Spectrum Disorders: A Functional Magnetic Resonance Imaging Study. *Pediatr Res* 58, 1150–1157. <https://doi.org/10.1203/01.pdr.0000185479.92484.a1>
- Mansfield, P., 1977. Multi-planar image formation using NMR spin echoes. *J. Phys. C: Solid State Phys.* 10, L55–L58. <https://doi.org/10.1088/0022-3719/10/3/004>
- Matejko, A.A., Price, G.R., Mazzocco, M.M.M., Ansari, D., 2013. Individual differences in left parietal white matter predict math scores on the Preliminary Scholastic Aptitude Test. *NeuroImage* 66, 604–610. <https://doi.org/10.1016/j.neuroimage.2012.10.045>

- Mattson, S.N., Riley, E.P., Gramling, L., Delis, D.C., Jones, K.L., 1998. Neuropsychological comparison of alcohol-exposed children with or without physical features of fetal alcohol syndrome. *Neuropsychology* 12, 146–153.
- Mattson, S.N., Riley, E.P., Sowell, E.R., Jernigan, T.L., Sobel, D.F., Jones, K.L., 1996. A decrease in the size of the basal ganglia in children with fetal alcohol syndrome. *Alcoholism: Clinical and Experimental Research* 20, 1088–1093. <https://doi.org/10.1111/j.1530-0277.1996.tb01951.x>
- May, P.A., Gossage, J.P., Kalberg, W.O., Robinson, L.K., Buckley, D., Manning, M., Hoyme, H.E., 2009. Prevalence and epidemiologic characteristics of FASD from various research methods with an emphasis on recent in-school studies. *Developmental disabilities research reviews* 15, 176–192.
- McCrary, E., De Brito, S.A., Viding, E., 2010. Research Review: The neurobiology and genetics of maltreatment and adversity. *Journal of Child Psychology and Psychiatry* 51, 1079–1095. <https://doi.org/10.1111/j.1469-7610.2010.02271.x>
- Mcgraw, K., Wong, S.P., 1996. Forming Inferences About Some Intraclass Correlation Coefficients. *Psychological Methods* 1, 30–46. <https://doi.org/10.1037/1082-989X.1.1.30>
- McKavanagh, R., Torso, M., Jenkinson, M., Kolasinski, J., Stagg, C.J., Esiri, M.M., McNab, J.A., Johansen-Berg, H., Miller, K.L., Chance, S.A., 2019. Relating diffusion tensor imaging measurements to microstructural quantities in the cerebral cortex in multiple sclerosis. *Hum Brain Mapp* 40, 4417–4431. <https://doi.org/10.1002/hbm.24711>
- McNab, J.A., Jbabdi, S., Deoni, S.C.L., Douaud, G., Behrens, T.E.J., Miller, K.L., 2009. High resolution diffusion-weighted imaging in fixed human brain using diffusion-weighted steady state free precession. *NeuroImage* 46, 775–785. <https://doi.org/10.1016/j.neuroimage.2009.01.008>
- McNab, J.A., Polimeni, J.R., Wang, R., Augustinack, J.C., Fujimoto, K., Player, A., Janssens, T., Farivar, R., Folkerth, R.D., Vanduffel, W., Wald, L.L., 2013. Surface Based Analysis of Diffusion Orientation for Identifying Architectonic Domains in the In Vivo Human Cortex. *Neuroimage* 69, 87–100. <https://doi.org/10.1016/j.neuroimage.2012.11.065>
- Meintjes, E.M., Jacobson, J.L., Molteno, C.D., Gatenby, J.C., Warton, C., Cannistraci, C.J., Hoyme, H.E., Robinson, L.K., Khaole, N., Gore, J.C., Jacobson, S.W., 2010. An fMRI Study of Number Processing in Children With Fetal Alcohol Syndrome. *Alcoholism: Clinical and Experimental Research* 34, 1450–1464. <https://doi.org/10.1111/j.1530-0277.2010.01230.x>
- Menon, V., Uddin, L.Q., 2010. Saliency, switching, attention and control: a network model of insula function. *Brain Struct Funct* 214, 655–667. <https://doi.org/10.1007/s00429-010-0262-0>
- Mikl, M., Mareček, R., Hlušík, P., Pavlicová, M., Drastich, A., Chlebus, P., Brázdil, M., Krupa, P., 2008. Effects of spatial smoothing on fMRI group inferences. *Magnetic Resonance Imaging* 26, 490–503. <https://doi.org/10.1016/j.mri.2007.08.006>
- Milham, M.P.P.D., Fair, D.P.-C., Mennes, M.P.D., Mostofsky, S.H.M.D., 2012. The adhd-200 consortium: a model to advance the translational potential of neuroimaging in clinical neuroscience. *Front. Syst. Neurosci.* 6. <https://doi.org/10.3389/fnsys.2012.00062>
- Miller, K.L., Stagg, C.J., Douaud, G., Jbabdi, S., Smith, S.M., Behrens, T.E.J., Jenkinson, M., Chance, S.A., Esiri, M.M., Voets, N.L., Jenkinson, N., Aziz, T.Z., Turner, M.R., Johansen-Berg, H., McNab, J.A., 2011. Diffusion imaging of whole, post-mortem human brains on a clinical MRI scanner. *Neuroimage* 57, 167–181. <https://doi.org/10.1016/j.neuroimage.2011.03.070>
- Morey, R.A., Selgrade, E.S., Wagner, H.R., Huettel, S.A., Wang, L., McCarthy, G., 2010. Scan–rescan reliability of subcortical brain volumes derived from automated segmentation. *Hum Brain Mapp* 31, 1751–1762. <https://doi.org/10.1002/hbm.20973>

- Morrison, J.H., Hof, P.R., 1997. Life and Death of Neurons in the Aging Brain. *Science* 278, 412–419. <https://doi.org/10.1126/science.278.5337.412>
- Mugler, J.P., Brookeman, J.R., 1991. Rapid three-dimensional T1-weighted MR imaging with the MP-RAGE sequence. *Journal of Magnetic Resonance Imaging* 1, 561–567. <https://doi.org/10.1002/jmri.1880010509>
- Nagy, Z., Alexander, D.C., Thomas, D.L., Weiskopf, N., Sereno, M.I., 2013. Using High Angular Resolution Diffusion Imaging Data to Discriminate Cortical Regions. *PLoS One* 8. <https://doi.org/10.1371/journal.pone.0063842>
- Nardelli, A., Lebel, C., Rasmussen, C., Andrew, G., Beaulieu, C., 2011. Extensive deep gray matter volume reductions in children and adolescents with fetal alcohol spectrum disorders. *Alcoholism: Clinical and Experimental Research* 35, 1404–1417. <https://doi.org/10.1111/j.1530-0277.2011.01476.x>
- Narvacan, K., Treit, S., Camicioli, R., Martin, W., Beaulieu, C., 2017. Evolution of deep gray matter volume across the human lifespan. *Human Brain Mapping* 38, 3771–3790. <https://doi.org/10.1002/hbm.23604>
- Neil, J.J., Smyser, C.D., 2018. Recent Advances in the Use of MRI to Assess Early Human Cortical Development. *J Magn Reson* 293, 56–69. <https://doi.org/10.1016/j.jmr.2018.05.013>
- Nielsen, J.A., Zielinski, B.A., Fletcher, P.T., Alexander, A.L., Lange, N., Bigler, E.D., Lainhart, J.E., Anderson, J.S., 2013. Multisite functional connectivity MRI classification of autism: ABIDE results. *Front Hum Neurosci* 7. <https://doi.org/10.3389/fnhum.2013.00599>
- Nieuwenhuis, M., van Haren, N.E.M., Hulshoff Pol, H.E., Cahn, W., Kahn, R.S., Schnack, H.G., 2012. Classification of schizophrenia patients and healthy controls from structural MRI scans in two large independent samples. *NeuroImage* 61, 606–612. <https://doi.org/10.1016/j.neuroimage.2012.03.079>
- Ning, L., Setsompop, K., Michailovich, O., Makris, N., Shenton, M.E., Westin, C.-F., Rathi, Y., 2016. A joint compressed-sensing and super-resolution approach for very high-resolution diffusion imaging. *NeuroImage* 125, 386–400. <https://doi.org/10.1016/j.neuroimage.2015.10.061>
- Noble, S., Scheinost, D., Constable, R.T., 2019. A decade of test-retest reliability of functional connectivity: A systematic review and meta-analysis. *Neuroimage* 203, 116157. <https://doi.org/10.1016/j.neuroimage.2019.116157>
- Noble, S., Scheinost, D., Finn, E.S., Shen, X., Papademetris, X., McEwen, S.C., Bearden, C.E., Addington, J., Goodyear, B., Cadenhead, K.S., Mirzakhani, H., Cornblatt, B.A., Olvet, D.M., Mathalon, D.H., McGlashan, T.H., Perkins, D.O., Belger, A., Seidman, L.J., Thermenos, H., Tsuang, M.T., van Erp, T.G.M., Walker, E.F., Hamann, S., Woods, S.W., Cannon, T.D., Constable, R.T., 2017. Multisite Reliability of MR-Based Functional Connectivity. *Neuroimage* 146, 959–970. <https://doi.org/10.1016/j.neuroimage.2016.10.020>
- Norman, A.L., O'Brien, J.W., Spadoni, A.D., Tapert, S.F., Jones, K.L., Riley, E.P., Mattson, S.N., 2013. A functional magnetic resonance imaging study of spatial working memory in children with prenatal alcohol exposure: contribution of familial history of alcohol use disorders. *Alcohol. Clin. Exp. Res.* 37, 132–140. <https://doi.org/10.1111/j.1530-0277.2012.01880.x>
- O'Brien, J.W., Norman, A.L., Fryer, S.L., Tapert, S.F., Paulus, M.P., Jones, K.L., Riley, E.P., Mattson, S.N., 2013. Effect of predictive cuing on response inhibition in children with heavy prenatal alcohol exposure. *Alcoholism: Clinical and Experimental Research* 37, 644–654.
- Ogawa, S., Tank, D.W., Menon, R., Ellermann, J.M., Kim, S.G., Merkle, H., Ugurbil, K., 1992. Intrinsic signal changes accompanying sensory stimulation: functional brain mapping with magnetic resonance imaging. *PNAS* 89, 5951–5955. <https://doi.org/10.1073/pnas.89.13.5951>
- O'Hare, E.D., Lu, L.H., Houston, S.M., Bookheimer, S.Y., Mattson, S.N., O'Connor, M.J., Sowell, E.R., 2009. Altered frontal-parietal functioning during verbal working memory in children and adolescents with heavy prenatal alcohol exposure. *Human brain mapping* 30, 3200–3208.

- Orrù, G., Pettersson-Yeo, W., Marquand, A.F., Sartori, G., Mechelli, A., 2012. Using support vector machine to identify imaging biomarkers of neurological and psychiatric disease: A critical review. *Neuroscience & Biobehavioral Reviews* 36, 1140–1152. <https://doi.org/10.1016/j.neubiorev.2012.01.004>
- Paolozza, A., Rasmussen, C., Pei, J., Hanlon-Dearman, A., Nikkel, S.M., Andrew, G., McFarlane, A., Samdup, D., Reynolds, J.N., 2014a. Working memory and visuospatial deficits correlate with oculomotor control in children with fetal alcohol spectrum disorder. *Behavioural Brain Research* 263, 70–79. <https://doi.org/10.1016/j.bbr.2014.01.024>
- Paolozza, A., Rasmussen, C., Pei, J., Hanlon-Dearman, A., Nikkel, S.M., Andrew, G., McFarlane, A., Samdup, D., Reynolds, J.N., 2014b. Deficits in response inhibition correlate with oculomotor control in children with fetal alcohol spectrum disorder and prenatal alcohol exposure. *Behavioural Brain Research* 259, 97–105. <https://doi.org/10.1016/j.bbr.2013.10.040>
- Pedregosa, F., Varoquaux, G., Gramfort, A., Michel, V., Thirion, B., Grisel, O., Blondel, M., Prettenhofer, P., Weiss, R., Dubourg, V., Vanderplas, J., Passos, A., Cournapeau, D., Brucher, M., Perrot, M., Duchesnay, É., 2011. Scikit-learn: Machine learning in python. *Journal of Machine Learning Research* 12, 2825–2830.
- Pickering, S., Gathercole, S.E., 2001. Working memory test battery for children (WMTB-C). Psychological Corporation.
- Poldrack, R.A., Baker, C.I., Durnez, J., Gorgolewski, K.J., Matthews, P.M., Munafò, M.R., Nichols, T.E., Poline, J.-B., Vul, E., Yarkoni, T., 2017. Scanning the horizon: towards transparent and reproducible neuroimaging research. *Nature Reviews Neuroscience* 18, 115–126. <https://doi.org/10.1038/nrn.2016.167>
- Popova, S., Lange, S., Shield, K., Mihic, A., Chudley, A.E., Mukherjee, R.A.S., Bekmuradov, D., Rehm, J., 2016. Comorbidity of fetal alcohol spectrum disorder: a systematic review and meta-analysis. *The Lancet* 387, 978–987. [https://doi.org/10.1016/S0140-6736\(15\)01345-8](https://doi.org/10.1016/S0140-6736(15)01345-8)
- Rasmussen, C., 2005. Executive Functioning and Working Memory in Fetal Alcohol Spectrum Disorder. *Alcoholism: Clinical and Experimental Research* 29, 1359–1367. <https://doi.org/10.1097/01.alc.0000175040.91007.d0>
- Ray, K.M., Wang, H., Chu, Y., Chen, Y.-F., Bert, A., Hasso, A.N., Su, M.-Y., 2006. Mild Cognitive Impairment: Apparent Diffusion Coefficient in Regional Gray Matter and White Matter Structures. *Radiology* 241, 197–205. <https://doi.org/10.1148/radiol.2411051051>
- Reynolds, J.N., Weinberg, J., Clarren, S., Beaulieu, C., Rasmussen, C., Kobor, M., Dube, M.-P., Goldowitz, D., 2011a. Fetal alcohol spectrum disorders: gene-environment interactions, predictive biomarkers, and the relationship between structural alterations in the brain and functional outcomes, in: *Seminars in Pediatric Neurology*. Elsevier, pp. 49–55.
- Reynolds, J.N., Weinberg, J., Clarren, S., Beaulieu, C., Rasmussen, C., Kobor, M., Dube, M.-P., Goldowitz, D., 2011b. Fetal alcohol spectrum disorders: gene-environment interactions, predictive biomarkers, and the relationship between structural alterations in the brain and functional outcomes. *Seminars in Pediatric Neurology* 18, 49–55.
- Riikonen, R.S., Nokelainen, P., Valkonen, K., Kolehmainen, A.I., Kumpulainen, K.I., Könönen, M., Vanninen, R.-L.S., Kuikka, J.T., 2005. Deep serotonergic and dopaminergic structures in fetal alcoholic syndrome: A study with nor-β-CIT-single-photon emission computed tomography and magnetic resonance imaging volumetry. *Biological Psychiatry* 57, 1565–1572. <https://doi.org/10.1016/j.biopsych.2005.01.029>
- Riley, E.P., McGee, C.L., 2005. Fetal alcohol spectrum disorders: an overview with emphasis on changes in brain and behavior. *Experimental biology and medicine* 230, 357–365.
- Robinson, E.C., Jbabdi, S., Glasser, M.F., Andersson, J., Burgess, G.C., Harms, M.P., Smith, Stephen.M., Van Essen, D.C., Jenkinson, M., 2014. MSM: a new flexible framework for Multimodal Surface Matching☆. *Neuroimage* 100, 414–426. <https://doi.org/10.1016/j.neuroimage.2014.05.069>

- Roussotte, F.F., Bramen, J.E., Nunez, S.C., Quandt, L.C., Smith, L., O'connor, M.J., Bookheimer, S.Y., Sowell, E.R., 2011. Abnormal brain activation during working memory in children with prenatal exposure to drugs of abuse: the effects of methamphetamine, alcohol, and polydrug exposure. *Neuroimage* 54, 3067–3075.
- Roussotte, F.F., Sulik, K.K., Mattson, S.N., Riley, E.P., Jones, K.L., Adnams, C.M., May, P.A., O'Connor, M.J., Narr, K.L., Sowell, E.R., 2012. Regional brain volume reductions relate to facial dysmorphology and neurocognitive function in fetal alcohol spectrum disorders. *Human Brain Mapping* 33, 920–937. <https://doi.org/10.1002/hbm.21260>
- Rovaris, M., Judica, E., Gallo, A., Benedetti, B., Sormani, M.P., Caputo, D., Ghezzi, A., Montanari, E., Bertolotto, A., Mancardi, G., Bergamaschi, R., Martinelli, V., Comi, G., Filippi, M., 2006. Grey matter damage predicts the evolution of primary progressive multiple sclerosis at 5 years. *Brain* 129, 2628–2634. <https://doi.org/10.1093/brain/awl222>
- Rubia, K., Alegria, A.A., Cubillo, A.I., Smith, A.B., Brammer, M.J., Radua, J., 2014. Effects of Stimulants on Brain Function in Attention-Deficit/Hyperactivity Disorder: A Systematic Review and Meta-Analysis. *Biological Psychiatry* 76, 616–628.
- Rubinov, M., Sporns, O., 2010. Complex network measures of brain connectivity: Uses and interpretations. *NeuroImage, Computational Models of the Brain* 52, 1059–1069. <https://doi.org/10.1016/j.neuroimage.2009.10.003>
- Santhanam, P., Coles, C.D., Li, Z., Li, L., Lynch, M.E., Hu, X., 2011. Default mode network dysfunction in adults with prenatal alcohol exposure. *Psychiatry Research: Neuroimaging* 194, 354–362.
- Schenker C, Meier D, Wichmann W, Boesiger P, Valavanis A, 1993. Age distribution and iron dependency of the T2 relaxation time in the globus pallidus and putamen. *Neuroradiology* 35, 119–124. <https://doi.org/10.1007/bf00593967>
- Schmitz, J., Fraenz, C., Schlüter, C., Friedrich, P., Jung, R.E., Güntürkün, O., Genç, E., Ocklenburg, S., 2019. Hemispheric asymmetries in cortical gray matter microstructure identified by neurite orientation dispersion and density imaging. *NeuroImage* 189, 667–675. <https://doi.org/10.1016/j.neuroimage.2019.01.079>
- Schuh, A., Makropoulos, A., Wright, R., Robinson, E.C., Tusor, N., Steinweg, J., Hughes, E., Cordero Grande, L., Price, A., Hutter, J., Hajnal, J.V., Rueckert, D., 2017. A deformable model for the reconstruction of the neonatal cortex, in: 2017 IEEE 14th International Symposium on Biomedical Imaging (ISBI 2017). Presented at the 2017 IEEE 14th International Symposium on Biomedical Imaging (ISBI 2017), pp. 800–803. <https://doi.org/10.1109/ISBI.2017.7950639>
- Shah, L.M., Cramer, J.A., Ferguson, M.A., Birn, R.M., Anderson, J.S., 2016. Reliability and reproducibility of individual differences in functional connectivity acquired during task and resting state. *Brain and Behavior* 6, e00456. <https://doi.org/10.1002/brb3.456>
- Shehzad, Z., Kelly, A.M.C., Reiss, P.T., Gee, D.G., Gotimer, K., Uddin, L.Q., Lee, S.H., Margulies, D.S., Roy, A.K., Biswal, B.B., Petkova, E., Castellanos, F.X., Milham, M.P., 2009. The Resting Brain: Unconstrained yet Reliable. *Cereb Cortex* 19, 2209–2229. <https://doi.org/10.1093/cercor/bhn256>
- Sickmann, H.M., Patten, A.R., Morch, K., Sawchuk, S., Zhang, C., Parton, R., Szlavik, L., Christie, B.R., 2014. Prenatal ethanol exposure has sex-specific effects on hippocampal long-term potentiation. *Hippocampus* 24, 54–64. <https://doi.org/10.1002/hipo.22203>
- Song, A.W., Chang, H.-C., Petty, C., Guidon, A., Chen, N.-K., 2014. Improved Delineation of Short Cortical Association Fibers and Gray/White Matter Boundary Using Whole-Brain Three-Dimensional Diffusion Tensor Imaging at Submillimeter Spatial Resolution. *Brain Connectivity* 4, 636–640. <https://doi.org/10.1089/brain.2014.0270>

- Sotiropoulos, S.N., Jbabdi, S., Xu, J., Andersson, J.L., Moeller, S., Auerbach, E.J., Glasser, M.F., Hernandez, M., Sapiro, G., Jenkinson, M., Feinberg, D.A., Yacoub, E., Lenglet, C., Ven Essen, D.C., Ugurbil, K., Behrens, T.E., 2013. Advances in diffusion MRI acquisition and processing in the Human Connectome Project. *Neuroimage* 80, 125–143. <https://doi.org/10.1016/j.neuroimage.2013.05.057>
- Sowell, E.R., Johnson, A., Kan, E., Lu, L.H., Van Horn, J.D., Toga, A.W., O'Connor, M.J., Bookheimer, S.Y., 2008a. Mapping white matter integrity and neurobehavioral correlates in children with fetal alcohol spectrum disorders. *Journal of Neuroscience* 28, 1313–1319.
- Sowell, E.R., Lu, L.H., O'hare, E.D., McCourt, S.T., Mattson, S.N., O'connor, M.J., Bookheimer, S.Y., 2007. Functional magnetic resonance imaging of verbal learning in children with heavy prenatal alcohol exposure. *Neuroreport* 18, 635–639.
- Sowell, E.R., Mattson, S.N., Kan, E., Thompson, P.M., Riley, E.P., Toga, A.W., 2008b. Abnormal cortical thickness and brain–behavior correlation patterns in individuals with heavy prenatal alcohol exposure. *Cerebral Cortex* 18, 136–144.
- Spadoni, A.D., Bazinet, A.D., Fryer, S.L., Tapert, S.F., Mattson, S.N., Riley, E.P., 2009. BOLD Response During Spatial Working Memory in Youth With Heavy Prenatal Alcohol Exposure. *Alcoholism: Clinical and Experimental Research* 33, 2067–2076. <https://doi.org/10.1111/j.1530-0277.2009.01046.x>
- Sripada, C., Kessler, D., Fang, Y., Welsh, R.C., Kumar, K.P., Angstadt, M., 2014. Disrupted network architecture of the resting brain in attention-deficit/hyperactivity disorder. *Human Brain Mapping* 35, 4693–4705.
- Stehling, M.K., Turner, R., Mansfield, P., 1991. Echo-planar imaging: magnetic resonance imaging in a fraction of a second. *Science* 254, 43–50. <https://doi.org/10.1126/science.1925560>
- Stejskal, E.O., Tanner, J.E., 1965. Spin Diffusion Measurements: Spin Echoes in the Presence of a Time-Dependent Field Gradient. *J. Chem. Phys.* 42, 288–292. <https://doi.org/10.1063/1.1695690>
- Stevens, M.C., 2016. The contributions of resting state and task-based functional connectivity studies to our understanding of adolescent brain network maturation. *Neuroscience & Biobehavioral Reviews, The Adolescent Brain* 70, 13–32.
- Sulik, K.K., 2005. Genesis of Alcohol-Induced Craniofacial Dysmorphism. *Exp Biol Med (Maywood)* 230, 366–375. <https://doi.org/10.1177/15353702-0323006-04>
- Suttie, M., Wozniak, J.R., Parnell, S.E., Wetherill, L., Mattson, S.N., Sowell, E.R., Kan, E., Riley, E.P., Jones, K.L., Coles, C., Foroud, T., Hammond, P., 2018. Combined face-brain morphology and associated neurocognitive correlates in fetal alcohol spectrum disorders. *Alcohol Clin Exp Res* 42, 1769–1782. <https://doi.org/10.1111/acer.13820>
- Tavor, I., Jones, O.P., Mars, R.B., Smith, S.M., Behrens, T.E., Jbabdi, S., 2016. Task-free MRI predicts individual differences in brain activity during task performance. *Science* 352, 216–220. <https://doi.org/10.1126/science.aad8127>
- Treit, S., Chen, Z., Zhou, D., Baugh, L., Rasmussen, C., Andrew, G., Pei, J., Beaulieu, C., 2017. Sexual dimorphism of volume reduction but not cognitive deficit in fetal alcohol spectrum disorders: A combined diffusion tensor imaging, cortical thickness and brain volume study. *Neuroimage Clin* 15, 284–297. <https://doi.org/10.1016/j.nicl.2017.05.006>
- Triarhou, L.C., 2013. The Cytoarchitectonic Map of Constantin von Economo and Georg N. Koskinas, in: Geyer, S., Turner, R. (Eds.), *Microstructural Parcellation of the Human Cerebral Cortex*. Springer Berlin Heidelberg, Berlin, Heidelberg, pp. 33–53. [https://doi.org/10.1007/978-3-662-45766-5\\_2](https://doi.org/10.1007/978-3-662-45766-5_2)
- Truong, T.-K., Guidon, A., Song, A.W., 2014. Cortical Depth Dependence of the Diffusion Anisotropy in the Human Cortical Gray Matter In Vivo. *PLoS ONE* 9, 1–10. <https://doi.org/10.1371/journal.pone.0091424>

- Tseng, P.-H., Cameron, I.G.M., Pari, G., Reynolds, J.N., Munoz, D.P., Itti, L., 2013. High-throughput classification of clinical populations from natural viewing eye movements. *J Neurol* 260, 275–284.  
<https://doi.org/10.1007/s00415-012-6631-2>
- Turner, R., Bihan, D.L., Chesnicks, A.S., 1991. Echo-planar imaging of diffusion and perfusion. *Magnetic Resonance in Medicine* 19, 247–253. <https://doi.org/10.1002/mrm.1910190210>
- Van Essen, D.C., Glasser, M.F., Dierker, D.L., Harwell, J., Coalson, T., 2012. Parcellations and Hemispheric Asymmetries of Human Cerebral Cortex Analyzed on Surface-Based Atlases. *Cereb Cortex* 22, 2241–2262.  
<https://doi.org/10.1093/cercor/bhr291>
- Van Essen, D.C., Smith, S.M., Barch, D.M., Behrens, T.E., Yacoub, E., Ugurbil, K., Consortium, W.-M.H., others, 2013. The WU-Minn human connectome project: an overview. *Neuroimage* 80, 62–79.
- Vanderah, T., Gould, D.J., 2015. *Nolte's The Human Brain E-Book: An Introduction to its Functional Anatomy*. Elsevier Health Sciences.
- von Economo, C.F., Koskinas, G.N., 1925. Die cytoarchitektonik der hirnrinde des erwachsenen menschen. J. Springer.
- Whitfield-Gabrieli, S., Nieto-Castanon, A., 2012. Conn: a functional connectivity toolbox for correlated and anticorrelated brain networks. *Brain connectivity* 2, 125–141.
- Wisner, K.M., Atluri, G., Lim, K.O., MacDonald, A.W., 2013. Neurometrics of intrinsic connectivity networks at rest using fMRI: Retest reliability and cross-validation using a meta-level method. *NeuroImage* 76, 236–251.  
<https://doi.org/10.1016/j.neuroimage.2013.02.066>
- Woodcock, R.W., 1998. *Woodcock Reading Mastery Tests, Revised, Examiner's Manual*. American Guidance Service.
- Woodcock, R.W., McGrew, K., Mather, N., 2001. *Woodcock-Johnson tests of achievement*. Itasca, IL: Riverside Publishing.
- Woods, K.J., Jacobson, S.W., Molteno, C.D., Jacobson, J.L., Meintjes, E.M., 2018. Altered Parietal Activation during Non-symbolic Number Comparison in Children with Prenatal Alcohol Exposure. *Front. Hum. Neurosci.* 11.  
<https://doi.org/10.3389/fnhum.2017.00627>
- Wozniak, J.R., Mueller, B.A., Bell, C.J., Muetzel, R.L., Hoecker, H.L., Boys, C.J., Lim, K.O., 2013. Global functional connectivity abnormalities in children with fetal alcohol spectrum disorders. *Alcoholism: Clinical and experimental research* 37, 748–756.
- Wozniak, J.R., Mueller, B.A., Mattson, S.N., Coles, C.D., Kable, J.A., Jones, K.L., Boys, C.J., Lim, K.O., Riley, E.P., Sowell, E.R., Cifas, T., 2016. Functional connectivity abnormalities and associated cognitive deficits in fetal alcohol Spectrum disorders (FASD). *Brain Imaging and Behavior* 1–14.
- Wozniak, J.R., Mueller, B.A., Muetzel, R.L., Bell, C.J., Hoecker, H.L., Nelson, M.L., Chang, P.-N., Lim, K.O., 2011. Inter-Hemispheric Functional Connectivity Disruption in Children With Prenatal Alcohol Exposure. *Alcoholism: Clinical and Experimental Research* 35, 849–861.
- Yamashita, A., Yahata, N., Itahashi, T., Lisi, G., Yamada, T., Ichikawa, N., Takamura, M., Yoshihara, Y., Kunimatsu, A., Okada, N., Yamagata, H., Matsuo, K., Hashimoto, R., Okada, G., Sakai, Y., Morimoto, J., Narumoto, J., Shimada, Y., Kasai, K., Kato, N., Takahashi, H., Okamoto, Y., Tanaka, S.C., Kawato, M., Yamashita, O., Imamizu, H., 2019. Harmonization of resting-state functional MRI data across multiple imaging sites via the separation of site differences into sampling bias and measurement bias. *PLoS Biol* 17.  
<https://doi.org/10.1371/journal.pbio.3000042>
- Yang, Y., Roussotte, F., Kan, E., Sulik, K.K., Mattson, S.N., Riley, E.P., Jones, K.L., Adnams, C.M., May, P.A., O'Connor, M.J., others, 2012. Abnormal cortical thickness alterations in fetal alcohol spectrum disorders and their relationships with facial dysmorphology. *Cerebral cortex* 22, 1170–1179.

- Yap, P.-T., Zhang, Y., Shen, D., 2015. Brain Tissue Segmentation Based on Diffusion MRI Using  $\ell_0$  Sparse-Group Representation Classification. *Med Image Comput Comput Assist Interv* 9351, 132–139.
- Yeo, B.T., Krienen, F.M., Sepulcre, J., Sabuncu, M.R., Lashkari, D., Hollinshead, M., Roffman, J.L., Smoller, J.W., Zöllei, L., Polimeni, J.R., others, 2011. The organization of the human cerebral cortex estimated by intrinsic functional connectivity. *Journal of neurophysiology* 106, 1125–1165.
- Young, C., Olney, J.W., 2006. Neuroapoptosis in the infant mouse brain triggered by a transient small increase in blood alcohol concentration. *Neurobiology of Disease* 22, 548–554.  
<https://doi.org/10.1016/j.nbd.2005.12.015>
- Yu, M., Linn, K.A., Cook, P.A., Phillips, M.L., McClinnis, M., Fava, M., Trivedi, M.H., Weissman, M.M., Shinohara, R.T., Sheline, Y.I., 2018. Statistical harmonization corrects site effects in functional connectivity measurements from multi-site fMRI data. *Human Brain Mapping* 39, 4213–4227. <https://doi.org/10.1002/hbm.24241>
- Zhang, C., Paolozza, A., Tseng, P.-H., Reynolds, J.N., Munoz, D.P., Itti, L., 2019. Detection of children/youth with fetal alcohol spectrum disorder through eye movement, psychometric, and neuroimaging data. *Front. Neurol.* 10. <https://doi.org/10.3389/fneur.2019.00080>
- Zhou, D., Lebel, C., Lepage, C., Rasmussen, C., Evans, A., Wyper, K., Pei, J., Andrew, G., Massey, A., Massey, D., others, 2011. Developmental cortical thinning in fetal alcohol spectrum disorders. *Neuroimage* 58, 16–25.
- Zhou, D., Rasmussen, C., Pei, J., Andrew, G., Reynolds, J.N., Beaulieu, C., 2017. Preserved cortical asymmetry despite thinner cortex in children and adolescents with prenatal alcohol exposure and associated conditions. *Hum. Brain Mapp.* 39, 72–88. <https://doi.org/10.1002/hbm.23818>
- Zhou, Y., Yu, F., Duong, T., 2014. Multiparametric MRI characterization and prediction in autism spectrum disorder using graph theory and machine Learning. *PLOS ONE* 9, e90405.  
<https://doi.org/10.1371/journal.pone.0090405>
- Zou, K.H., Greve, D.N., Wang, M., Pieper, S.D., Warfield, S.K., White, N.S., Manandhar, S., Brown, G.G., Vangel, M.G., Kikinis, R., others, 2005. Reproducibility of Functional MR Imaging: Preliminary Results of Prospective Multi-institutional Study Performed by Biomedical Informatics Research Network 1. *Radiology* 237, 781–789.